MODELLING GASTROINTESTINAL SMOOTH MUSCLE MECHANICS

CHUNG CHEUK WANG

(B. Eng. (Hons.), NUS)

(M. Sc., NUS)

A THESIS SUBMITTED

FOR THE DEGREE OF DOCTOR OF PHILOSOPHY

DEPARTMENT OF BIOENGINEERING

NATIONAL UNIVERSITY OF SINGAPORE

2013

DECLARATION

I hereby declare that the thesis is my original work and it has been written by me in its entirety. I have duly acknowledged all the sources of information which have been used in the thesis.

This thesis has also not been submitted for any degree in any university previously.

_____

Chung Cheuk Wang

25 January 2013

Acknowledgements

I would like to express my heartfelt gratitude towards many unsung heroes in my PhD journey.

I am indebted to my thesis supervisor, Dr Martin Buist. He is a gentleman and a competent guide from the first day. His calm demeanour, clear-thinking, quick-wit and open-mindedness make difficult problems look easy. He is a joy to share ideas with, and encouraging when the work does not go well. He has provided me with numerous opportunities for professional development in terms of research, teaching and supervising. He is an example of a good mentor.

Professor Lim Chwee Teck, my thesis co-supervisor, has supported my experimental exploration in cell biomechanics. He is a world-renowned scientist. Nevertheless, he is humble, sincere and respectful in his interaction with me and other students. He is willing to share the honours and celebrate his achievements with his research groups. His cheerfulness and enthusiasm towards science have a positive influence on me.

My journey would be less fulfilling without the valuable members of the Computational Bioengineering Laboratory, past and present. David was a research fellow with profound computing knowledge and experience. His smile and jovial manner often brightened the lab. Alberto was a PhD student when I started and is now a lecturer in NUS. He has inspired me with his success through hard work and dedication. Viveka, May Ee and Aishwariya told me their personal stories, which have taught me that there are bigger things in life than research. Yong Cheng is an all-rounded talent as shown in his work and organisation of student activities. His drive for excellence has impressed me. Nicholas and Jing Wui are young and bright PhD students. Their

curiosity and eagerness to learn remind me of the attitudes that I should always carry with me. I am also fortunate to co-supervise a few undergraduate students, Mingqi, Bernice and Gokula, whose work has contributed to this thesis.

The Department of Bioengineering has offered me a generous scholarship and an exciting opportunity to conduct my research. I have gained tremendous knowledge in cell mechanics from the dedicated staff and students in the Nanobiomechanics Laboratory. I would also want to thank the Control and Mechatronics Laboratory, Impact Mechanics Laboratory and Bioengineering Design Studio for allowing me to use their equipment. I wish to make special mentions of external collaborators, Dr Zhao Jingbo, Dr Liao Donghua and Dr Robert Kirton, who have supported my work by sharing their experimental data.

My parents are neither highly educated nor wealthy. Nevertheless, they instil good values in my sister and me, and believe in giving us the best education they can afford. My sister takes a larger share of housework and spends more time with my parents during my absence. Wan Hua, my wife, gives her unwavering support while I pursue my dream. The thesis is especially dedicated to them for their unconditional love and sacrifice.

Table of Contents

Thesis summary

Prevalence of gastrointestinal (GI) diseases is a socio-economical burden to our society. To improve the effectiveness and efficacy of treatments, it is paramount to advance our understanding of GI physiology and pathophysiology.

The mechanical properties of GI smooth muscle are an integral component of GI motility which is responsible for important digestive processes. Studies have also shown that the geometric and mechanical properties of GI smooth muscle change when the GI tract are afflicted with diseases. GI smooth muscle passive viscoelasticity and Ca^{2+}-dependent contractile properties influence its overall mechanical responses. The GI smooth muscle passive and active mechanics are modifiable, and can be regulated by mechanical stimulations. The smooth muscle mechanical capabilities assist GI organ to fulfil its physiological roles and adapt to pathological conditions.

A nonlinear viscoelastic solid (NVS) model is developed to demonstrate uniaxial passive mechanics of GI smooth muscle. The compact model can simulate passive viscoelastic response of mammalian fundus and jejunum tissues under isokinetic, isometric and isotonic loading conditions. Furthermore, the NVS is extended to accept piecewise constitutive relations for its components. This permits the encapsulation of tensile and compressive smooth muscle material properties into a single model.

An active nonlinear viscoelastic solid (ANVS) model is derived to simulate the one-dimensional mechanics of active GI smooth muscle. The versatile ANVS can be connected to other strain-dependent and Ca^{2+}-dependent active force generation models to extend its capability. The parameterised model can simulate the periodic contraction and dynamic stiffness of active GI smooth muscle. The ANVS can also

demonstrate isotonic shortening during phasic and tonic contractions in antrum smooth muscle and the results agree with the Hill's force-velocity relation.

A length-adaptive active nonlinear viscoelastic solid (LANVS) model is constructed to illustrate the dynamics of the smooth muscle active and passive mechanics. The LANVS can simulate the regulation of passive and active stress-strain relations in response to prolonged deformation. It can also exhibit the transient of isometric active force recovery and passive tension decay under electrical stimulation. The model illustrates a possible mechanism which allows GI smooth muscle to operate in extended range of strain. It also demonstrates a plausible feedback control loop which modulates smooth muscle mechanics under the influence of deformation.

The GI smooth muscle structure, mechanical properties and functions are connected to the GI physiological objective and stimulus through a suggested adaptive mechanical framework. The framework demonstrates a proposed multi-scale control processes in which GI smooth muscle perceives the mechanical signals, alters its structure and mechanical properties, and influences the effectiveness of the gastric reservoir and gastric emptying functions. It also illustrates a plausible mechanism in which the intestinal wall tissue can respond to pseudo-obstruction by adapting its structure through a sequence of intra-cellular, cellular and extra-cellular measures. In both cases, it is hypothesised that the GI tract and its constituent components seek to achieve mechanical homeostasis.

Collectively, this work shows a plausible notion that mechanical functions of GI tract are determined by the structure and properties of its constituents. It also establishes that the constituent components regulate their responses according to physical and chemical factors, which consequently affect the GI physiology.

List of Tables

List of Figures

Chapter 1 Introduction

1.1 Prevalence, treatment and future of GI diseases

In 2004, for every 100 US residents, there were 35.7 outpatient visits and 4.6 hospitalisations in which a digestive diagnosis was involved (Everhart and Ruhl, 2009). The numbers have risen from 22.4 and 4.2 per 100, respectively, in 1985 (Everhart, 1994). The total cost, which comprises direct medical expenses and indirect loss of productivity, amounted to US$141.8 billion in 2004 alone.

Examples of gastrointestinal (GI) diseases, or digestive diseases, include gastroesophageal reflux disease, gastroparesis, pseudo-obstruction, chronic constipation and inflammatory bowel disease. On an individual level, patients with GI diseases endure a reduced quality of life in terms of pain and inconvenience caused by the disease symptoms such as vomiting, diarrhoea and constipation (Agarwal and Spiegel, 2011). Absenteeism and presenteeism in workplaces and schools reduce the patients' and caretakers' productivities which translate to lower family incomes (Toghanian *et al.*, 2010). Coupled with higher health insurance premiums, these families have fewer resources and opportunities to progress in society.

For pharmaceutical firms, a large patient population is a huge business prospect. However, developing a remedy for an illness is a time-consuming, capital intensive and risky process. Research and development of a novel drug often lasts more than a decade with the mean cost of delivering a new medicine at about US$1.8 billion (Paul *et al.*, 2010). Several drugs such as rofecoxib and isotretinoin, which were previously approved by U. S. Food and Drug Administration (FDA), have

been withdrawn from the market after reported adverse side-effects on GI tract such as perforation, ulceration, and bleeding (Jaksch *et al.*, 2008; Shale *et al.*, 2009). A cost-effective procedure, such as computational modelling, to single out probable drug candidates and study their likely physiological effects on human bodies can improve drug safety, increase the efficacy of medicine development and provide affordable means of treatment to a less affluent population.

GI diseases are set to have escalating impact in the future. Apart from rising incidence in US, Singapore and other Asian countries recorded an increasing occurrence of colorectal cancer and gastro-oesophageal reflux disease over the years due to changes in lifestyle and living environment (Sung, 2004; Goh, 2007). To reverse this trend, knowledge of GI tract physiology and pathophysiology are important for devising appropriate public health policies, prevention methods and treatment processes.

In this thesis, a mathematical model is developed to quantify the mechanical properties of GI smooth muscle. The modelling work aims to integrate existing theories, quantitatively explain the biomechanics of GI motility and advance our understanding of the anatomy, functional roles and pathologies of the GI tract.

1.2 Physiology of GI tract

1.2.1 Functional anatomy of GI tract

The GI tract, also called the alimentary canal, is a multi-organ and continuous channel that starts from the mouth and ends at anus. The main functions of the GI tract include breaking down ingested food physically and enzymatically, absorbing nutrients and ejecting waste (Liao *et al.*, 2009a). To perform these functions, each organ in the

system is responsible for some or all of the following roles: absorption, secretion and motility. Table 1.1 shows the roles of each organ in the digestive system.

Table 1.1 Absorption, secretion and motility-related roles of digestive organs.

Organs in alimentary canal	Accessory organs	Secretion	Absorption	Motility
Mouth	Tongue, teeth, lips, cheeks and palate	Saliva, secreted from salivary gland, comprises electrolytes, amylase, lysozyme and Immunoglobulin A (De Almeida Pdel *et al.*, 2008).	-	The mouth and all accessory organs help in mixing food with saliva, chewing and grinding food. Tongue presses food into a bolus, ready for swallowing (Miller, 1982; Woda *et al.*, 2006).
Pharynx and Oeso-phagus	-	-	-	Contractions of muscles create peristaltic wave which propels the food bolus to stomach (Goyal and Chaudhury, 2008).

Organs in alimentary canal	Accessory organs	Secretion	Absorption	Motility
Stomach	-	Gastric juice consists of pepsin and mucus produced by the gastric glands (Kong and Singh, 2008).	Stomach absorbs some fat-soluble substances (Marieb, 2004).	Stomach contractions press, stretch and mix food with gastric juice. Gastric motility is responsible for emptying the stomach (Soybel, 2005).
Small intestine	Liver, gallbladder and pancreas	Gallbladder releases bile which consists of bile salts and phospholipids which assist in the emulsion and absorption of dietary fats and liposoluble vitamins (Monte *et al.*, 2009). Pancreas secretes pancreatic juice, which contains substances such as proteases, amylase, lipases and nucleases, to the small intestine (Marieb, 2004).	Absorption of carbohydrates, proteins, fats, vitamins, electrolytes and water occurs in small intestine. Liver filters harmful substances from the absorbed materials (Drozdowski and Thomson, 2006).	Motility of small intestine mixes chyme with bile and pancreatic juice. Segmenting movements divide chyme into sections for mixing and absorptions. Peristaltic waves propel the food in aboral direction (Cheng *et al.*, 2001).

Organs in alimentary canal	Accessory organs	Secretion	Absorption	Motility
Large intestine	-	Large intestine secretes mucus, NaCl and KCl to maintain hydration of residue and ionic homeostasis (Geibel, 2005).	The large intestine absorbs water, electrolytes and vitamins produced by bacteria (Geibel, 2005).	Slow haustral contractions segment the food residue and aid water absorption. Mass movements propel the residues to the rectum for defecation (Bassotti *et al.*, 1995).

GI organs are regulated by intrinsic and extrinsic control mechanisms (Marieb, 2004). The intrinsic control mechanisms depend mainly on the responses of enteric nervous system (ENS) while the extrinsic mechanisms involve communication with the central nervous system (CNS). In both mechanisms, nerve plexuses in GI tract wall tissues can be stimulated by distensions, concentrations of solutes, and pH values. However, the intrinsic nerve plexuses are solely responsible for effecting responses such as altering gland secretions and organ motility. Extrinsic impulses are sent from excited receptors to CNS which then signals the GI nerve plexuses to respond. The CNS can also be activated by external stimuli, such as the smell and taste of food, and can exert changes on GI tract through extrinsic mechanisms.

1.2.2 Structure of GI tract wall tissue

To study the biomechanics of GI tract, it is imperative to examine the structure of its wall tissue. GI wall tissue is a composite material which can be subdivided into four layers: the mucosa, submucosa, muscularis externa and serosa as shown in Figure 1.1.

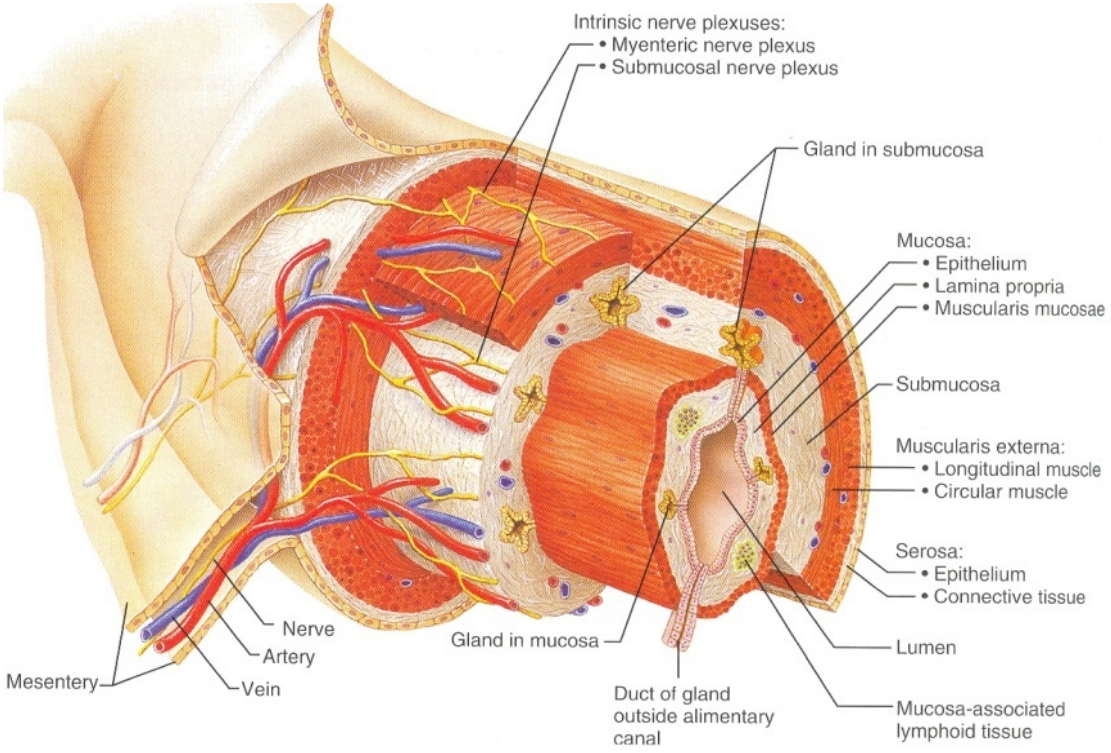

Figure 1.1 Structure of gastrointestinal wall tissue. (Source: Marieb, 2004)

The mucosal layer is closest to the lumen and it constitutes epithelium, lamina propria and muscularis mucosae. To facilitate individual GI organ functions, the epithelium is lined with distinct specialist cells while the lamina propria contains different secretory glands. For instance, the oesophagus lumen is covered with squamous epithelial cells that are resistant to abrasion by food particles during swallowing (Long and Orlando, 2010). The lining of stomach is undulating with steep openings of gastric glands which secrete mucus, water and gastric juice which facilitates mixing, lubrication and

digestion (Semrin and Russo, 2010). The intestinal mucosa layer is deeply folded with villi protruding perpendicularly out of the surface. Blood capillaries and lacteal are found inside each villus and they carry the absorbed nutrients to the liver. Crypts are situated between villi for intestinal juice secretion (Kahn and Daum, 2010). All these features are essential for the intestinal absorption of nutrients by slowing down the passing of food mass and providing extra surface contact area. Crypts are also found at the colonic lumen epithelium. They are spaced uniformly and wide, and extend from the lumen surface to the muscularis mucosae (Dahl and Greenson, 2007). The muscularis mucosae is a thin layer of smooth muscle which prevents distortion of mucosa and regulates the orientations of villi (Gramlich and Petras, 2007).

In most parts of GI tract, the submucosal layer consists of connective tissue containing blood vessels, lymphatic vessels, lymphoid follicles and nerve fibres (Pabst, 1987). It consists of a large proportion of elastic fibres that enable the digestive organ to vary its size according to the content. The submucosa nerve plexus regulates glands and muscularis mucosae.

The muscularis externa of alimentary canal is largely bi-layered, having an inner circular layer and an outer longitudinal layer (Figure 1.1). Spindle-shaped smooth muscle cells (SMC), which are capable of shortening when activated, are arranged in parallel in both layers. The long axes of the SMC align to the circumferential direction and length of the GI tract in the circular and longitudinal layers, respectively. The stomach has an additional innermost oblique smooth muscle layer (Semrin and Russo, 2010). All layers affect gastrointestinal motility. Distinctions arise at the oesophagus and the anus where part of the organ contains striated muscle regions for voluntary control of swallowing and defecation, respectively (Clouse and Diamant, 2006; Sarna and Shi, 2006).

The myenteric nerve plexus is sandwiched between the circumferential and longitudinal smooth muscle layers (Komuro, 2006). It contains the enteric nervous system together with the submucosal nerve plexus, and controls the motility and secretion in GI tract. ENS neurons are also connected to the central nervous system through visceral and motor fibres. In this way, the CNS can influence the response of the neurons in both submucosal and myenteric nerve plexuses.

The outermost tissue layer of the oesophagus is the adventitia (Long and Orlando, 2010) while stomach, small intestine and large intestine are covered by serosa (Andrews and Blackshaw, 2010; Cook *et al.*, 2010; Semrin and Russo, 2010).

1.2.3 GI motility

The term gastrointestinal motility refers to the coordinated motor events of the GI musculature in the muscularis externa. The GI muscularis externa generally comprises two layers of muscle — a thicker inner circumferential layer and a thinner outer longitudinal layer. The contraction of the circular wall tissue partially or fully occludes the GI tract and increases the pressure in the lumen. Longitudinal contraction, on the other hand, dilates the lumen and shortens the GI tract (Sarna, 1993). Many of these contractions are local events and their effects depend on the status of the regions adjacent to the point of contraction. The contractions in the nearby regions can occur in a synchronised and controlled fashion which can give rise to propulsion and segmentation as illustrated in Figure 1.2 (Kunze and Furness, 1999).

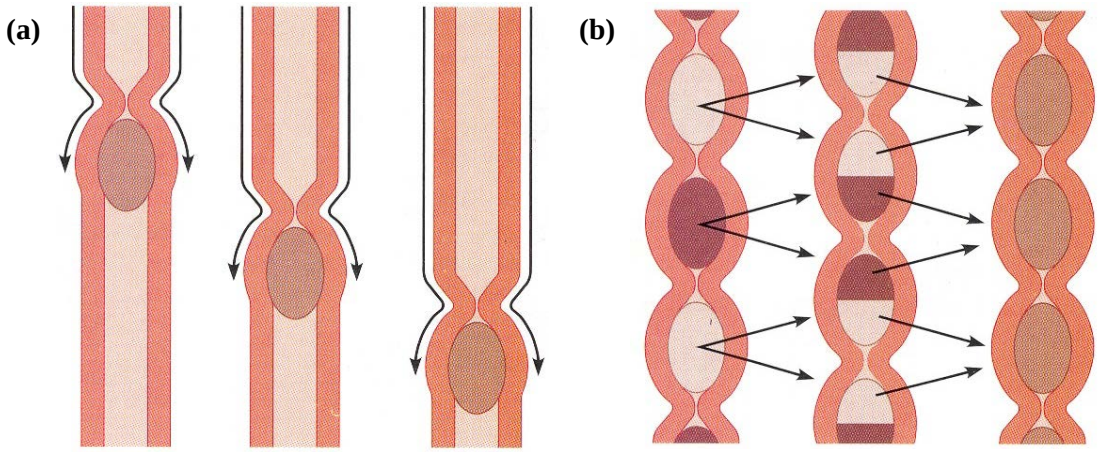

Figure 1.2 Gastrointestinal motility generates propulsion and segmentation. (a) In propulsion, contraction occurs along GI tract sequentially and food bolus is propelled aborally. (b) In segmentation, lumen occludes at isolated point of GI tract. Bolus are divided and mixed with digestive juice. (Source: Marieb, 2004)

During propulsion, a sequence of contractions, called peristalsis, can start from the proximal part of the GI tract and continue in the aboral direction. The peristaltic wave drives the luminal contents to the distal part of the GI tract (Weems, 1981; Sarna, 1999).

Segmentation often occurs in the small bowel and colon. In these GI organs, a contraction can occur at an isolated point with relaxed intestinal wall in the neighbouring regions. As a result, the lumen, together with the food materials in that section, is segmented (Weisbrodt, 1981; Bassotti *et al.*, 1995). Repeated segmentations cause forward and backward movements of luminal contents and facilitate blending of chyme with digestive juice in small intestine. Segmentation also enhances circulation of the mixture in the intestine which results in increased contact with the intestinal wall and improved absorption of nutrients and fluids (Sarna and Otterson, 1989; Geibel, 2005).

1.3 GI smooth muscle mechanics

Within the walls of the GI tract, GI smooth muscle is the actuating component capable of changing its material properties. Smooth muscle mechanical properties can be broadly categorised into passive tension and active force mechanics.

1.3.1 Passive tension mechanics

The passive or resting mechanical properties of smooth muscle demonstrate its resistance to deformation due to external forces. Smooth muscle passive tension influences GI organ distensibility and motility (Kindt and Tack, 2006; Zhao *et al.*, 2011a).

Stress-strain relations, viscoelasticity, and residual stresses in GI smooth muscle have been studied to define its passive properties (Gregersen and Kassab, 1996). The stiffness or elastic modulus of GI smooth muscle can be interpreted from the gradient of its axial stress-strain graph which varies according to the direction of deformation, and indicate that the passive mechanical properties are anisotropic (Zhao *et al.*, 2005). In the case of mammalian gastric smooth muscle tissue, the stiffness in longitudinal direction is higher than that of circumferential direction (Zhao *et al.*, 2008a). It is plausible that the longitudinal tissue stiffness is crucial in preventing the organ from being over-extended under the weight of the food substances while compliance in circumferential direction allows stomach circumferential contraction (important for propulsion and mixing) to take place with less resistance. In both direction, muscle stiffness increases with extension under finite strain (Stavropoulou *et al.*, 2009).

In addition, GI smooth muscle is viscoelastic as its passive mechanical properties are history-dependent and affected by the rate of deformation (Price *et al.*, 1979). Stress relaxation, creep and hysteresis have been demonstrated in various experiments performed on mammalian GI smooth muscle (Storkholm *et al.*, 2007; Comelekoglu and Ozturk, 2008; Liao *et al.*, 2009b).

Furthermore, GI smooth muscle is pre-stressed when it constitutes part of an intact organ. The residual stress exists even when the organ is not subjected to external load (Gregersen *et al.*, 2000). Opening angle experiments have been conducted to measure the residual stress and strain as well as define the zero-stress configuration of GI smooth muscle (Zhao *et al.*, 2007).

Overall, the GI smooth muscle passive mechanics is anisotropic, nonlinear and viscoelastic, and the tissue is pre-stressed in-vivo.

1.3.2 Active force mechanics

The active force is produced spontaneously by GI smooth muscle when stimulated. In GI organs, coordinated smooth muscle contraction generates rhythmic peristaltic waves and different motility patterns which are phasic in nature (Goyal and Chaudhury, 2008; Huizinga and Lammers, 2009). GI smooth muscle activation also generates sustained muscle tone which adds stiffness to the GI organ wall tissue (Gregersen and Christensen, 2000).

The self-actuating phasic and tonic contractions can be quantified in-vivo or in freshly extracted GI tissue in-vitro (Gregersen *et al.*, 2007; Zhao *et al.*, 2008b). GI smooth muscle contraction has been analysed under isometric and isotonic loading conditions. In these studies, the maximum contractile force is determined at pre-

defined muscle length, while shortening velocity is measured under a prescribed load (Meiss, 1971). The dynamic stiffness of contracted GI smooth muscle has also been investigated through perturbing the tissue with small amplitude length perturbations at different frequencies (Comelekoglu and Ozturk, 2008).

1.3.3 Investigating GI smooth muscle cell and sub-cellular mechanics

Advances in biophysics, engineering and nanotechnology permit the pursuit of mechanics at the cellular and sub-cellular levels (Lim *et al.*, 2006a; Vaziri and Gopinath, 2008). By employing a micropipette aspiration technique, the viscoelastic properties of Wistar rat colonic smooth muscle were investigated (Liao *et al.*, 2006b). Force transducers were used to study the cross-bridge mechanics in toad gastric SMC (Warshaw and Fay, 1983a; Harris and Warshaw, 1990, 1991). These investigators noted that, in comparison to the relaxed SMC, the contractile stress and cell stiffness of active myocyte were increased by ten- and hundred-fold, respectively. These studies illustrate that GI SMC contributes to the passive and active mechanics of GI wall tissue.

Other reports suggest that intra-cellular constituents also influence the mechanics of GI smooth muscle. Guinea pig taenia coli SMC contraction was abated when they were treated with an actin filament inhibitor, cytochalasin B (Obara and Yabu, 1994). Smooth muscle myosin isoform expression was found to be positively correlated with the shortening velocity of SMCs extracted at various parts of rabbit stomach (Eddinger and Meer, 2001). The result suggests that the smooth muscle mechanical properties are optimised by quantity of myosin variants to generate appropriate contractile force at different gastric regions.

From the above studies, it is apparent that GI motility is influenced by smooth muscle passive tension and active force at different spatial scales: tissue, cellular and sub-cellular. However, the picture is less clear in terms of how these mechanical properties vary in face of changing physiological requirements.

1.4 Response of GI smooth muscle to mechanical stimuli and its modulation

While the GI organs are performing their physiological roles, the wall tissues are subjected to constant deformations that arising from several sources (Gayer and Basson, 2009). For instance, the tissue layers are compressed by the weight of chyme in the lumen while being stretched to accommodate the volume of food. The mucosa experiences movement of a viscous bolus and the resulting shear stress is transmitted to the other tissue layers such as the muscularis externa. GI motility imposes additional pressure on the wall tissue. In the case of segmentation, contractile activities in neighbouring region exert tensile and compressive force on the resting smooth muscle. Rhythmic loading also exists in the form of phasic contraction which ranges from three to twenty times per minute in various part of the GI tract. Collectively, these physiological events are translated into mechanical stimuli experienced by the GI smooth muscle tissue and SMC (Figure 1.3).

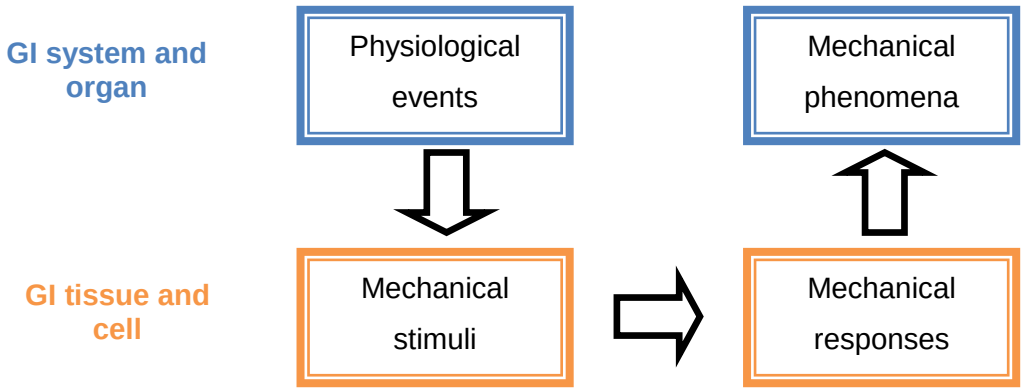

Figure 1.3 Physiological events in GI system or organ generates mechanical stimuli at which GI tissue or cell response to. Mechano-response of tissue or cell influences mechanical phenomena of system and organ. Blue boxes: events and responses in GI system or organ level; Orange boxes: events and responses in GI tissue or cell level.

Several studies have shown that biophysical cues can induce mechanical responses from smooth muscle cells and tissues extracted from other mammalian organ systems. As a case in point, the cyclic loading direction can progressively alter the orientations of adhering vascular SMCs (Liu *et al.*, 2008). The frequency of cyclic loading can also alter the static and dynamic stiffness of airway smooth muscle tissues (Du *et al.*, 2007). The active and passive mechanics of the tracheal and detrusor smooth muscles are modifiable through deformation and stimulation (Wang *et al.*, 2001; Speich *et al.*, 2007). Although GI SMC mechanical signal transduction and response to physical perturbation have not been well-studied, the muscle cells are probably mechano-sensitive and elicit similar mechanical responses.

The mechanical response of individual GI SMC can be aggregated to produce observable macroscopic mechanical phenomena in the GI tract. Table 1.2 summarises selected experimental results performed on GI organs when they are mechanically stimulated. It is interesting to note that the magnitude of mechanical response varies with the intensity of mechanical stimulus. This correlation gives

support to the notion that GI smooth muscle can react to physical perturbation and adjust its response for the purpose of effective and efficient GI motility.

Table 1.2 Response of gastrointestinal organs and tissues under mechanical stimuli for different physiological events. Unless otherwise stated, all the experiments were performed on whole organ.

Species	Organs in alimentary canal	Mechanical stimuli	Modulation of mechanical responses and phenomena	Related physiological events	References
Human, in-vivo	Oeso-phagus	Shear stress exerted by bolus on oesophagus wall.[1]	Viscosity of bolus correlates positively with axial force and contraction duration in oesophageal peristalsis.	Swallowing of food.	Gravesen *et al.* (2011)
Rat, ex-vivo	Stomach	Distension pressure due to volume of fluid.[2]	Frequency of antral contraction shows a decreasing trend with increasing volume of fluid.	Accommodation of food for mixing, physical digestion and propulsion.	Lentle *et al.* (2010)

Species	Organs in alimentary canal	Mechanical stimuli	Modulation of mechanical responses and phenomena	Related physiological events	References
Wistar rats, ex-vivo	Jejunum and ileum sections	Longitudinal stretching of intestine.[3]	Both phasic and tonic active stresses decreases with elevating longitudinal lengthening up to 20% strain.	Lengthening of intestine due to propulsion of bolus.	Zhao *et al.* (2008b)
Human, in-vivo	Colon	Balloon distension pressure.[4]	Circumferential distension provokes a fresh wave of contraction in the intestine if peristalsis is previously initiated.	Propulsion of food and waste substances.	Hardcastle and Mann (1970)

[1] Measurements were obtained from three different points of oesophagus proximal of lower oesophageal sphincter.
[2] Profiles of the whole stomach were recorded through time-series imaging. Contractile frequency was deduced from the images.
[3] The intestinal sections were tied at two ends and inflated. Their lengths were adjusted by micro-manipulators while pressure recorder was used to measure the contraction.
[4] Measurements were obtained from three different points of transverse colon.

1.5 GI diseases and dysmotility

Pathophysiological conditions induce biophysical changes in cells, tissues and their microenvironment, impair proper functioning of organs and systems, and threaten homeostasis (Ingber, 2003c; Suresh *et al.*, 2005; Lee and Lim, 2007). Gastrointestinal

disorders lead to morphological and mechanical changes to the digestive tract wall tissues. Extensive work has been done on comparing the phenotypes of healthy and diseased GI tissues (Liao *et al.*, 2009a). Selected results are shown in Table 1.3.

Table 1.3 Gastrointestinal smooth muscle remodelling in different physiological conditions.

Diseases	Species	Organs in alimentary canal	Muscle layer thickness	Circum-ferential stiffness	Longi-tudinal stiffness	References
Type I diabetes	Human, in-vivo	Oeso-phagus	Increased by 7% at 5mm radius.[1]	Increment [2]	Increment [2]	Frøkjaer *et al.* (2007)
Type II diabetes	Rat, in-vitro	Stomach	Unknown	Increment [3]	Increment [3]	Liao *et al.* (2006c)
Intestinal obstruction	Guinea-pig, in-vitro	Small intestine	Increased by 108%. [4]	Increased by 73% at 70 kPa stress. [5]	Unknown	Storkholm *et al.* (2007)
Ulcerative colitis	Mouse, in-vitro	Colon	Increased by 23%. [6]	Increment [7]	Increment [7]	Yang *et al.* (2009)

[1] Muscle layer thickness is dependent of distension radius.
[2] Oesophagus was expanded by bag distension technique and resulting muscle deformation was observed through ultrasound imaging. Change in muscle stiffness in patient and control subjects was deduced by comparing circumferential and longitudinal deformations due to identical bag distension protocol.
[3] Muscle stiffness is dependent of stretch ratio. Increment of muscle stiffness in diabetic rats over non-diabetic subjects was deduced by the left shift of pressure-stretch ratio curves.
[4] The circumferential muscle thickness was recorded at a location proximal of obstruction site after two weeks of blockage. Microphotographs of hematoxylin and eosin–stained intestinal sections were used to estimate the thickness of muscle layer. In general, muscle thickness is dependent of distension pressure, duration of blockage and location of small intestine relative to site of obstruction.
[5] The stiffness was recorded at a location proximal of obstruction site after two weeks of blockage. In general, muscle thickness is dependent of distension pressure, duration of blockage and location of small intestine relative to site of obstruction.

[6] The circumferential muscle thickness was estimated from images of colon segments.
[7] Muscle stiffness is dependent of strain. Increment of muscle stiffness in diseased mouse over healthy subjects was deduced by the left shift of stress-strain curves.

The change of smooth muscle layer thickness is usually accompanied by structural changes in the mucosa and submucosa layers (Liao *et al.*, 2009a). As a result of impaired GI tissue passive mechanics, GI smooth muscle contraction, its response to physical cues and eventually GI motility are affected. This notion is supported by several studies as listed in Table 1.4.

Table 1.4 Gastrointestinal dysmotility under mechanical stimuli in pathological conditions.

Diseases	Species	Organs in alimentary canal	Mechanical stimuli	Changes in motility	References
Systemic sclerosis	Human, in-vivo	Oesophagus	Distension pressure	Amplitude and velocity of peristaltic contraction reduced by 38% and 71% respectively.[1]	Gregersen *et al.* (2011)
Type I diabetes	Human, in-vivo	Oesophagus	Distension pressure	Increased frequency of contraction by 105%.[2]	Frøkjaer *et al.* (2007)
Functional dyspepsia	Human, in-vivo	Stomach	Liquid ingestion	Postprandial stomach expansion reduced by 11%.[3]	Bredenoord *et al.* (2003)

Diseases	Species	Organs in alimentary canal	Mechanical stimuli	Changes in motility	References
Chronic obstruction	Guinea pig, in-vitro	Small intestine	Bolus-induced shear force and distension	Motility pressure amplitude and frequency increased by 129% and 60% respectively at the proximal segment near to the obstruction site. [4]	Storkholm *et al.* (2008)
Systemic sclerosis	Human, in-vivo	Duodenum	Distension pressure	Contraction pressure amplitude lowered by 15%. [5]	Pedersen *et al.* (2003)

[1] The values were provided at distension pressure of 5 kPa.
[2] The value was reported at the first minute of mechanical stimulation.
[3] Stomach expansion volume was estimated using gamma camera images.
[4] The values were provided with bolus size being 2 ml.
[5] Contraction pressure amplitudes were measured using bag distension technique in both healthy and diseased subjects. The reported value occurred when the bag was expanded to 80 ml.

GI dysmotility can have a severe impact on the health of the GI tract, particularly through affecting the residential environment of the bacteria population which assist in vitamin production, protect the host alimentary tract from pathogens, and regulate the response of host immune system (Bures *et al.*, 2010; Kamada *et al.*, 2013). In some cases, impaired motility can cause pseudo-obstructions in the GI tract which may result in bacteria overgrowth (Rana and Bhardwaj, 2008).

The bacteria compete with the host for nutrients and release toxic substances, poisoning the intestinal tissue. It has been shown that in mice, bacteria located near the ileocecal valve can spread to the liver and blood stream within 24 hours after obstruction and infect the circulatory system (Deitch *et al.*, 1990).

Pathogens can also induce inflammation in the small bowel by weakening the barrier function of the mucosal layer. This is achieved by altering the tight junction proteins which regulate the passage of materials into the intercellular space (Mengheri, 2008). Crohn's disease, a type of inflammatory bowel disease, can cause blockage, rupture or fistulisation to other parts of the GI tract (MacNaughton, 2006). Affected individuals reported pain, diarrhoea and weight loss (Sands, 2004).

An intestinal inflammatory response can also alter the tissue physiology. Experiments conducted on rats showed that the density of interstitial cells of Cajal is reduced and their contacts with SMC are disrupted in the inflamed intestine (Won *et al.*, 2006). The excitability of myenteric neurons in the enteric nerves is undesirably affected (Sharkey and Kroese, 2001). Contractility of SMC is weakened during inflammation (Ohama *et al.*, 2007). Therefore, the motor functions of small intestine, as well as its motility, are further disrupted.

Overall, GI tissue health and motility are closely related. Diseased tissue leads to impaired motility which can cause further deterioration of the well-being of the GI tract.

1.6 Computational modelling of GI smooth muscle mechanics

As mentioned in previous sections, a large quantity of experimental data has been generated from smooth muscle studies in relation to GI physiology, its response to mechanical stimuli and diseases. To control variability and produce statistically significant results, experimental designs usually centre on one or a few biological species populations under prescribed conditions. These laboratory studies are in-depth but they often record truncated episodes of biological processes in terms of spatial scales, durations and levels of organisation (Southern *et al.*, 2008). Overall, such limitations restrict the use of experimental techniques in establishing a holistic

view connecting different aspects of smooth muscle mechanics in wide range of scenarios and scales, and in providing integrated explanations of underlying biological processes.

Mathematical models go hand-in-hand with experimental techniques in biomechanical studies. Multi-scale modelling can consolidate biological events with different physical aspects, temporal and spatial scales. Computational models have been built previously to understand the biomechanics of mammalian GI smooth muscle. For instance, Zhao and colleagues (2005) used an exponential model to quantify the stress-strain relations of mucosa and muscle layers in rabbit stomach. Multi-scale models are also useful for investigating and quantifying the effect of dysfunctional proteins on tissue biomechanics and eventually the physiology of organs. As a case in point, Gao *et al.* (2009) developed a duodenal wall tissue mechanics model for investigating the contribution of smooth muscle and extra-cellular proteins in systemic sclerosis. Currently, there is no existing model that explores the modulation of mechanical response of mammalian GI tissue under mechanical stimulation.

1.7 Scope of Thesis

The fundamental hypothesis of this work is that *"mechanical functions of GI tract are intrinsically dependent on the mechanical properties of its constituents and their regulation of response towards physical and chemical factors. Alterations to any of these factors will naturally change GI smooth muscle cell and tissue mechanics, and consequently physiology of GI tract."*

The smooth muscle in the GI muscularis externa layer is the essential component for motility as explained in the earlier sections. Therefore, the main focus of this thesis is on investigating both the active and passive mechanics of GI smooth muscle as well

as their regulation under the influence of mechanical stimuli. In particular, the integrative actions of mechanical properties and modulating mechanisms are mathematically modelled to understand their cooperation and their influence on one another.

Specifically, the computational studies are conducted with the following objectives:

Objective 1: To understand the structure and mechanical properties of GI smooth muscle and its constituents;

Objective 2: To build a constitutive model to simulate the GI smooth muscle viscoelastic phenomena;

Objective 3: To construct a constitutive model to quantify the active mechanics of GI smooth muscle and investigate its interaction with passive mechanics;

Objective 4: To develop a constitutive model to explore the regulation of GI smooth muscle mechanical response under mechanical stimulation;

Objective 5: To examine the implication of GI smooth muscle mechanical properties and mechano-response modulation in relation to GI tract physiology and pathophysiology.

There are numerous publications dedicated to explain the structure and mechanical properties of smooth muscle. Therefore, Objective 1 will be accomplished by literature research. In Objectives 2, 3 and 4, three constitutive models will be built to describe different aspects of smooth muscle mechanics. We envision that these models can be used as independent model or together in the same computational study. Objective 5 will be achieved by relating the simulation results to the reported phenomena in healthy GI tract, such as gastric reservoir function and gastric emptying, and the

diseased one in the case of intestinal obstruction, from clinical and basic scientific studies. No experimental data will be generated in the thesis.

1.8 Thesis overview

The method of investigation follows the principle of structure-property-function. The smooth muscle ultra-structure, its passive and active mechanical phenomena will be examined in Chapter 2 of the thesis (Objective 1). The investigation will be conducted through modelling and past mathematical models are critically assessed in Chapter 3 (Objective 1). The derivation of a novel nonlinear viscoelastic model and its application in describing the passive mechanical states of GI smooth muscle will be illustrated in Chapters 4 (Objective 2). An enhanced smooth muscle active mechanics model which can quantify the muscle contraction under both the isometric and isotonic loading conditions will be shown in Chapter 5 (Objective 3). A length-adaptive model which explores the adjustment of GI smooth muscle's mechanical response under physical deformation will be explained in Chapter 6 (Objective 4). The possible roles of smooth muscle mechanical phenomena in assisting or hindering the GI functions in both the healthy and diseased states will be discussed in Chapter 7 (Objective 5). Limitation of the models, future work and possible clinical applications will be explained in Chapter 8.

Chapter 2 GI smooth muscle physiology

2.1 Overview

Examining the anatomy, histology and morphology of GI smooth muscle cells and tissues is a prerequisite to investigate the biomechanics of GI motility. Smooth muscle geometry and structure intrinsically affects its mechanical properties and defines its physiological roles in the alimentary canal. Therefore, the constituents of GI smooth muscle, its architecture, organisation and contribution to smooth muscle biomechanical properties are presented in this chapter.

The constituents of GI smooth muscle tissue, its passive and active mechanical properties are well-studied. Conversely, the majority of mammalian SMC physiological knowledge originates from morphological and biomechanical experiments conducted on airway and vascular smooth muscles. Hence, discussions on GI SMC are largely supplemented by SMC studies in other organs. Length adaptation has recently been found to occur in airway, arterial and detrusor smooth muscles. The phenomenon is introduced in the later part of the chapter, even though it has not yet been investigated in mammalian GI smooth muscle to date.

2.2 Structure of smooth muscle cells and tissue

2.2.1 Ultra-structure of smooth muscle cell

The smooth muscle cell is the smallest viable contractile unit in GI wall tissue. The ultra-structure of a generic SMC is illustrated in Figure 2.1. Each SMC is bounded by a layer of membrane or sarcolemma and numerous invaginations, called caveolae,

are found on the membrane surface (Gabella, 1994; Gosens *et al.*, 2008). The caveolae increase the surface-to-volume ratio of the SMC and enhance the exchange of ions with the extracellular space through numerous ion channels. Dense bands or dense plaques are interposed among the caveolae on the intracellular side of the membrane (Figures 2.1 and 2.2). Contractile filaments are attached to the cell membrane at the dense bands (Kuo and Seow, 2004).

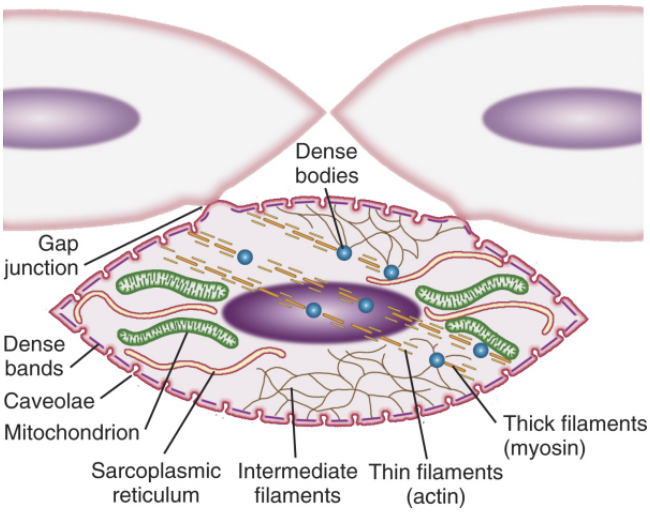

Figure 2.1 Schematic of SMC ultra-structure. (Source: Andrews and Blackshaw, 2006)

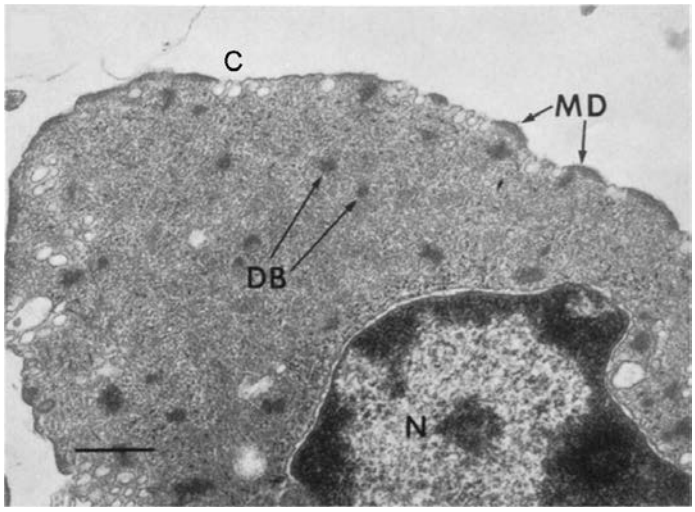

Figure 2.2 Electronic micrograph of transverse section of SMC isolated from toad stomach. C: caveolae; MD: plasma membrane densities or dense bands; DB: dense bodies; N: nucleus. Dense bands are interposed among the caveolae on the cell surface. Scale bar: 0.5 μm. (Source: Kargacin and Fay, 1987)

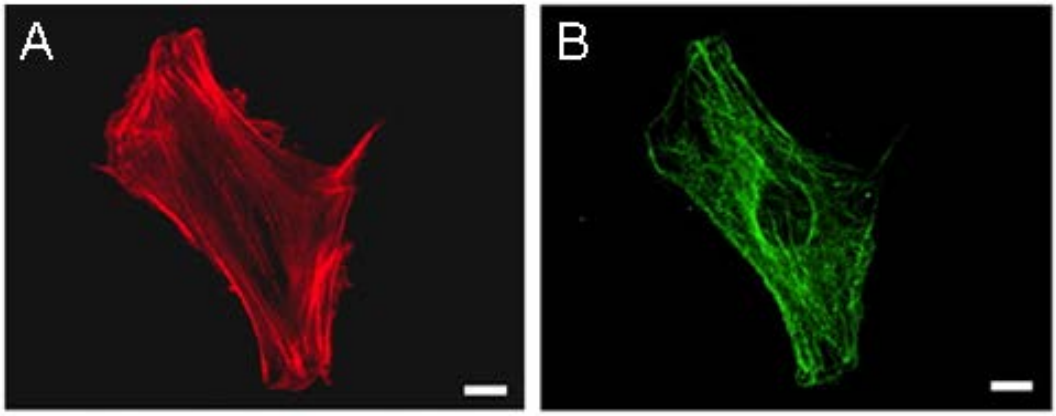

Figure 2.3 Confocal fluorescent image of isolated rat aortic SMC with actin and microtubule staining. (A) Actin filaments align with the long axis of SMC while microtubules do not. (B) A hollow region is created near the cell centre among microtubules suggesting that they circumvent the nucleus. (Source: Nagayama and Matsumoto, 2008)

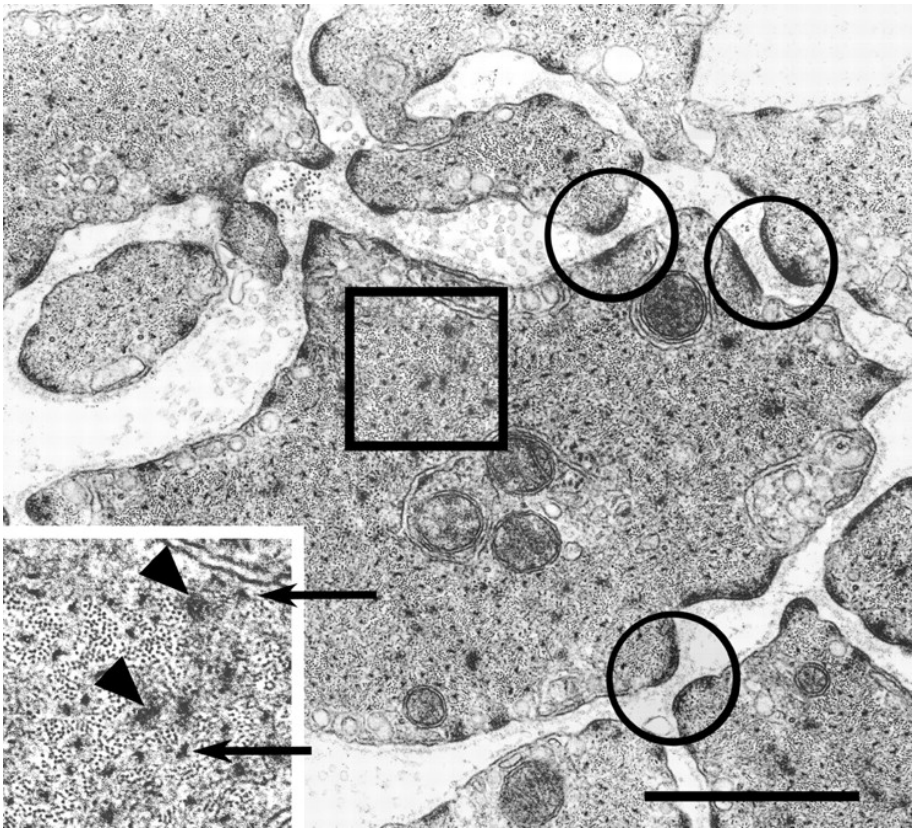

Figure 2.4 Electronic micrograph of transverse section of swine tracheal SMC bundle. Neighbouring SMCs are mechanically connected through intermediate junctions linking opposite dense bands as shown in circles. The inset shows the magnified image of the region bounded by a square. Arrowheads indicate dense bodies while arrows point to myosin filaments surrounded by actin filaments. Scale bar: 1 μm. (Source: Kuo and Seow, 2004)

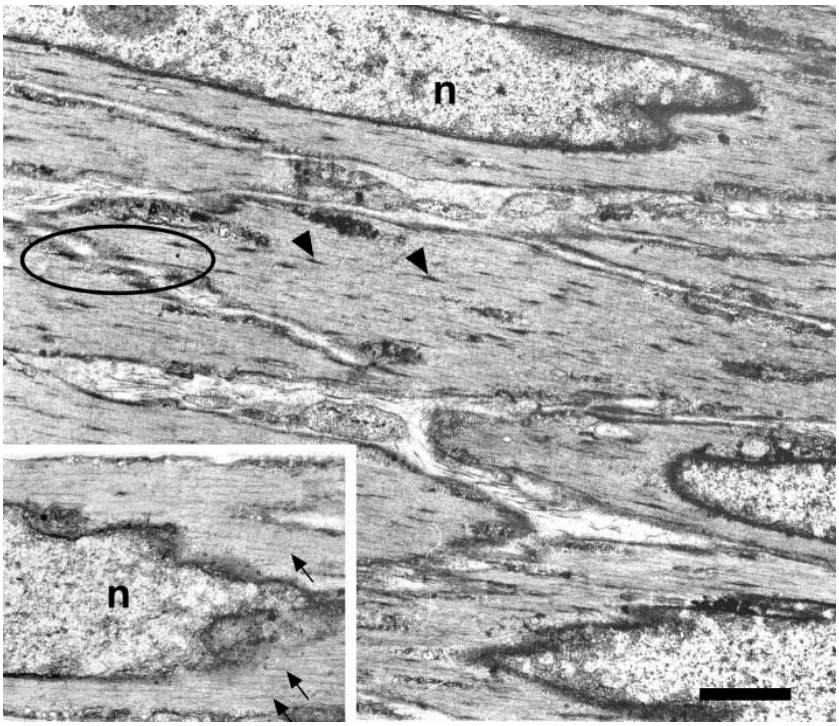

Figure 2.5 Electronic microscopic image of longitudinal section of swine tracheal SMC bundle. Neighbouring SMCs are mechanically connected through intermediate junction linking opposite dense bands as shown in the oval. The contractile filaments and dense bodies (arrowhead) align with the SMC long axis. In the inset, the myosin filaments (arrows) near nucleus are shown. Scale bar: 1 μm. (Source: Kuo and Seow, 2004)

Cytoskeletal filaments support the structure of the SMC and contribute to its passive mechanical properties. Actin filaments and microtubules provide the SMC with its stiffness and viscoelastic characteristics (Laudadio *et al.*, 2005; Nagayama and Matsumoto, 2008; Hemmer *et al.*, 2009). Their architectures and organisations are shown in Figure 2.3. Vimentin and desmin are the major components of SMC intermediate filament network which is dynamic and responsive to contractile stimulation (Tang, 2008). In airway SMC, vimentin filaments join the nucleus to the sarcolemma at desmosomes while desmin is found near the boundary of myocyte and in dense bodies (Paulin and Li, 2004; Tang, 2008). The intermediate filament synemin is also found in SMC but its role is not well characterised (Herrmann *et al.*, 2007; Tang, 2008).

Actin and myosin filaments form the contractile apparatus which make SMC contraction possible. The contractile units are oriented to the long axis of SMC when the cell is extended, and deviate from the axis with an angle of approximately 20 ° when the myocyte is shortened (Small, 1977) (Figures 2.4 and 2.5). Actin filaments attach to the nucleus as well as dense bodies distributed in the sarcoplasm (Kuo and Seow, 2004; Herrera *et al.*, 2005). The average distance between adjacent dense bodies is approximately 2.2 μm in toad SMC and this can be considered as the length of the smooth muscle contractile apparatus (Fay *et al.*, 1983; Herrera *et al.*, 2005).

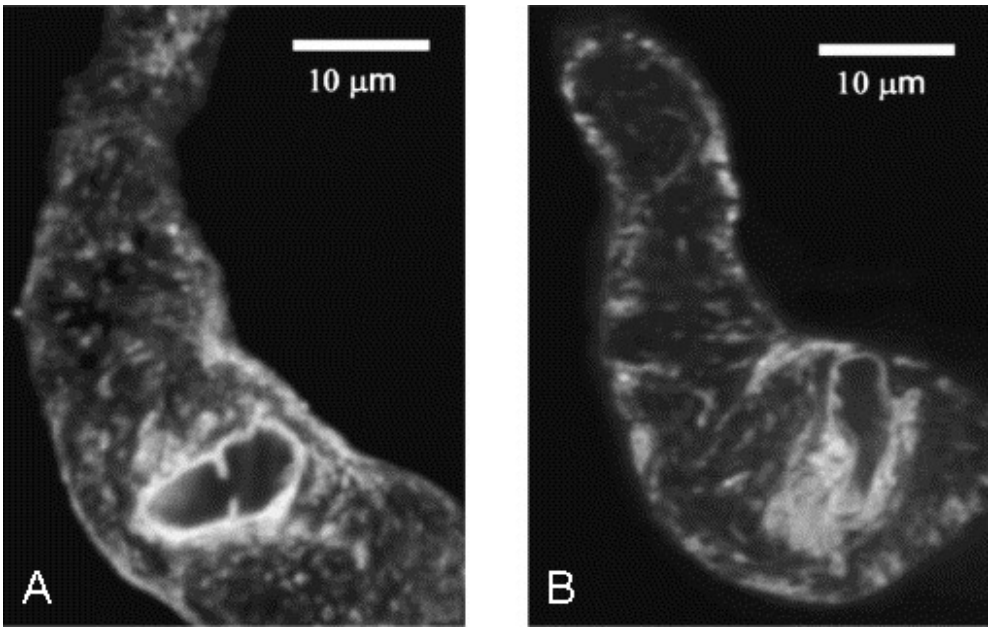

Figure 2.6 Confocal fluorescent images of uterine SMC isolated from pregnant rat. The distribution of SR was deduced by labelling (A) SERCA pumps or (B) ryanodine receptors with fluorescently tagged thapsigargin or ryanodine respectively. Both images suggest that the SR distributes around the nucleus and near the peripheral of SMC. (Source: Shmygol and Wray, 2004)

Within sarcoplasm, an extensive sarcoplasmic reticulum (SR) serves as a store for calcium ions (Ca^{2+}) (Leung *et al.*, 2008). During contraction, release of stored Ca^{2+} from the SR is mainly regulated by ryanodine receptors and inositol 1,4,5-trisphosphate-gated Ca^{2+} channels (Wray and Burdyga, 2010). Ca^{2+} is sequestered

back into the SR by sarco/endoplasmic reticulum Ca^{2+}-ATPase (SERCA) and a $3Na^{+}$-$1Ca^{2+}$ antiporter to lower the myoplasmic [Ca^{2+}] and facilitate SMC relaxation (Watras, 2008). The distribution of SR in freshly isolated uterine SMC is illustrated in Figure 2.6.

Intracellular components found in other mammalian cells also exist within SMC. Mitochondria produce adenosine triphosphate (ATP) to satisfy energy demands for muscle contraction and other cellular functions (Figure 2.7). Golgi apparatus are responsible for protein synthesis and modification. Both organelles are also capable of modulating intracellular [Ca^{2+}] and Ca^{2+} signalling (McCarron *et al.*, 2006).

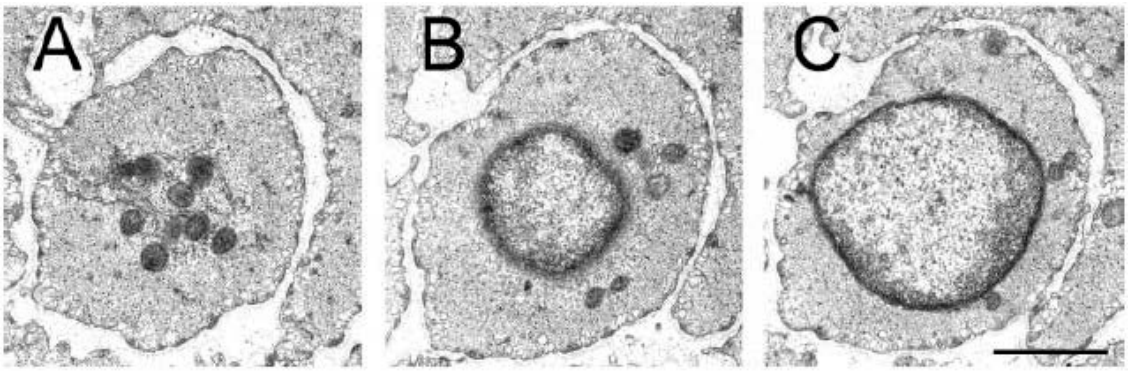

Figure 2.7 A series of swine tracheal SMC transverse sections captured by electronic microscope. (A) Mitochondria and organelles are at the central region of SMC near nuclear pole. (B) Transverse section of nucleus tip. (C) Full transverse cross-section of nucleus. Scale bar: 1 μm. (Source: Kuo and Seow, 2004)

2.2.2 Intercellular connection and extracellular matrix

In the GI muscularis externa, the circumferential and longitudinal muscle layers are constructed into separate syncytia. Within each layer, SMCs are connected mechanically by adherens (intermediate) junctions (Figures 2.4 and 2.5). Bundles of SMCs are joined together by a dense extracellular stroma of collagen filaments (Kuo and Seow, 2004; Andrews and Blackshaw, 2010). The myocytes communicate with one another through low-resistance gap junctions (Figures 2.1 and 2.8) that allow

diffusion of low-molecular-weight compounds and propagation of electrical signals (Watras, 2004). The electrical and mechanical linkages facilitate cooperation among SMCs and enable them to operate as a single unit.

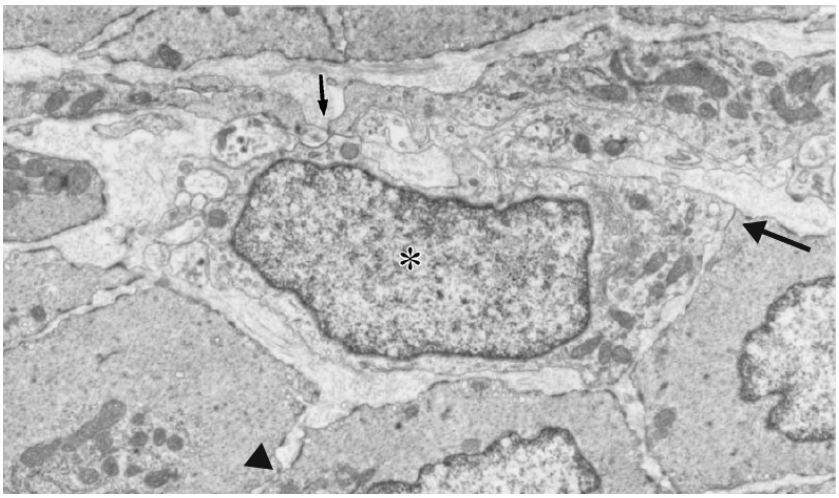

Figure 2.8 Electron microscopic image of rat small intestinal interstitial cells of Cajal (ICC) surrounded by SMC. ICC is indicated by an asterisk. Gap junctions are formed between ICCs (thin arrow), between SMCs (arrow head), and between an ICC and a SMC (thick arrow). Magnification: 9500x. (Source: Hanani *et al.*, 2005)

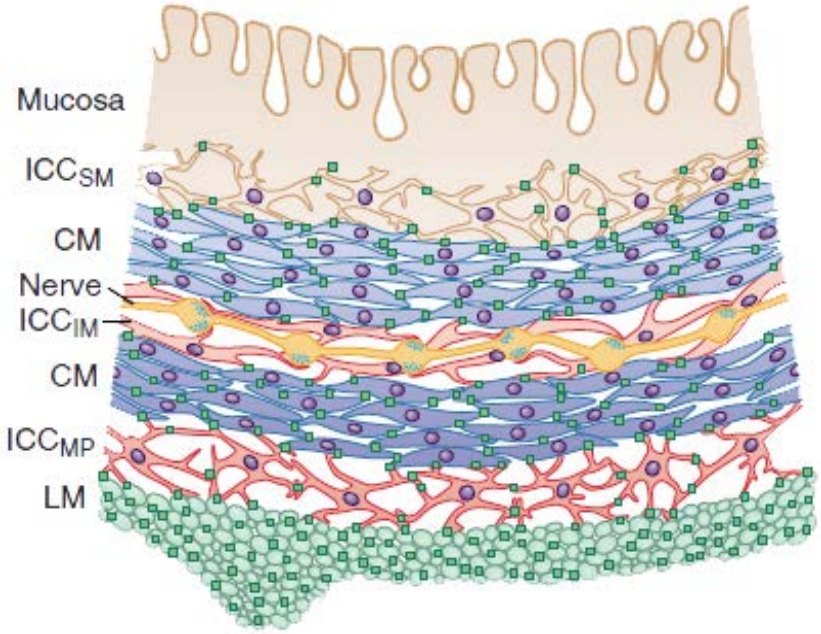

Figure 2.9 Schematic of ICC distribution in colonic wall tissue. ICC$_{SM}$: ICC in submucosa; CM: circumferential muscle; ICC$_{IM}$: intra-muscle ICC; ICC$_{MP}$: ICC in myenteric plexus; LM: longitudinal muscle. (Source: Cook *et al.*, 2010)

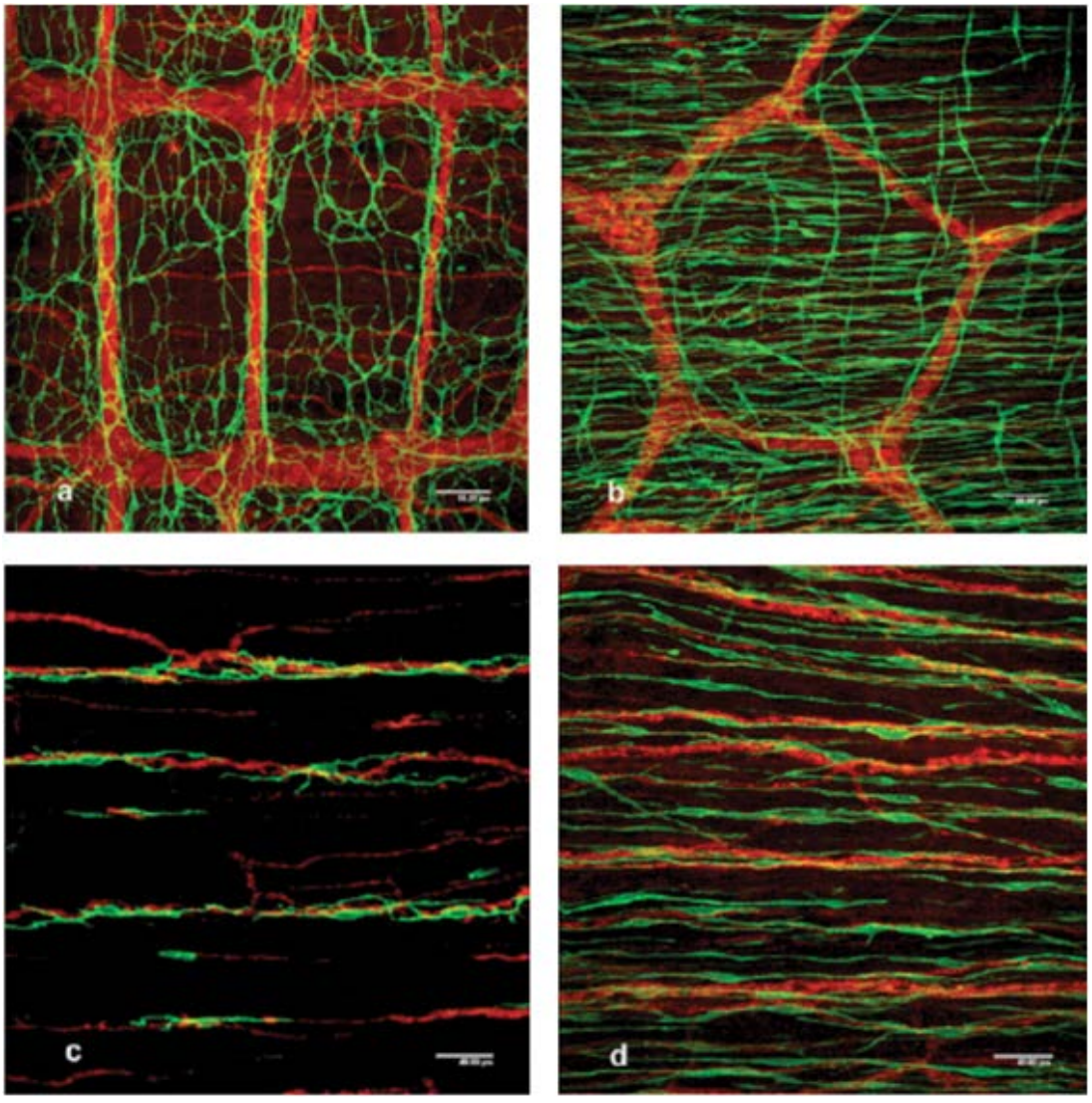

Figure 2.10 Confocal microscopic images of ICC networks and nerves. (a) ICC network in myenteric plexus of guinea-pig small intestine. (b) ICC networks surrounding the myenteric plexus of the guinea-pig colon. ICCs in circumferential muscle are orientated horizontally while those of longitudinal muscle align vertically. (c and d) ICC networks in circumferential muscle layer of guinea-pig (c) small intestine and (d) gastric corpus. Scale bars: 80 μm for a and b, 40 μm for c and d. ICC and nerves are indicated by green fluorescence and red fluorescence, respectively (Source: Komuro, 2006)

In addition to SMC, interstitial cells of Cajal (ICC) can be found within the GI circumferential smooth muscle layer (ICC-IM) as well as in the myenteric layer (ICC-MP), which is sandwiched between the circumferential and longitudinal muscle layers as shown in Figures 2.9 to 2.10. ICCs are also found in the longitudinal muscle layer though at a lower density (Komuro, 2006). ICC are mainly responsible for the inherent

electrical activities, termed slow waves, found in GI smooth muscles (Sanders *et al.*, 2006). ICC spontaneously generate the pacemaking slow waves which are conducted to SMC via the gap junctions, leading to periodic alterations of the SMC membrane potential (Farrugia, 2008). In this way, the slow wave frequency, which can vary from three cycles per minute in stomach to 7 – 12 cycles/min in small intestine, regulates the SMC contractile frequency while its amplitude determines strength of SMC contraction in the GI tract (Hasler, 2006; Koch, 2010).

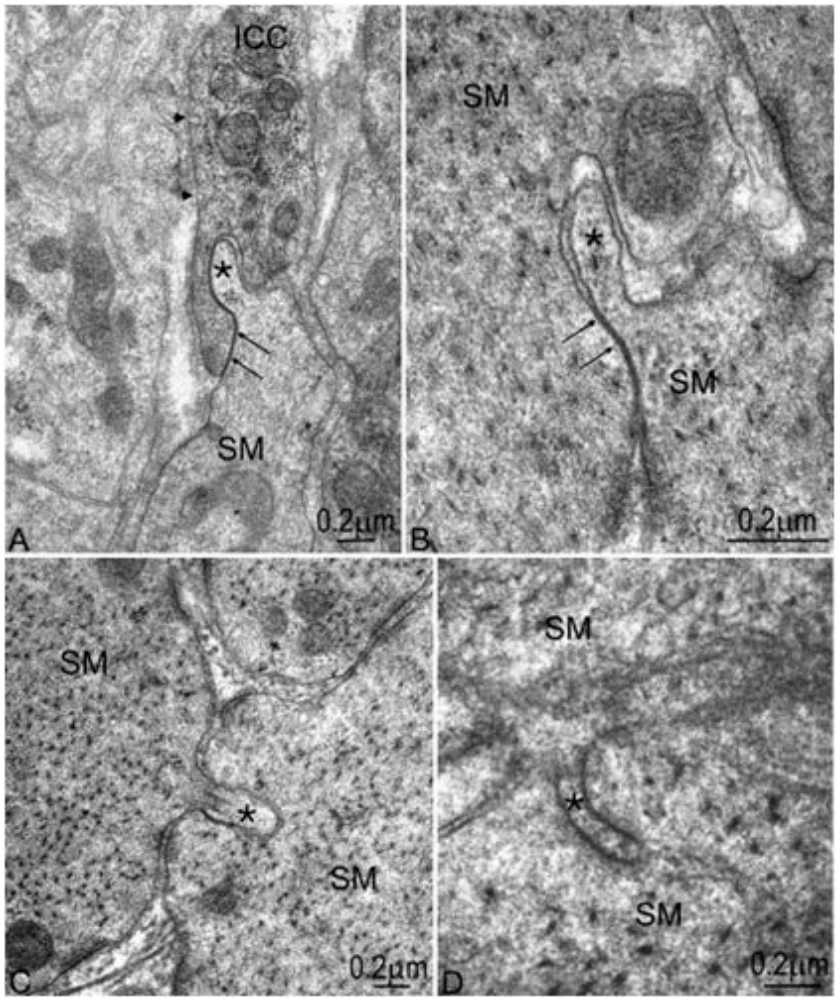

Figure 2.11 Electrical microscopic images of peg-and-socket junctions in human ileum tissue. Peg-and-socket junctions connecting (A) SMC and ICC or (B to D) coupling pairs of SMC. In A and B, gap junctions (arrows) are found near the peg-and-socket junctions. Asterisk: peg-and-socket junction; SM: SMC; arrowhead: caveolae. (Source: Huizinga *et al.*, 2010)

ICC can be electrically connected to the SMC through the gap junctions, as shown in Figure 2.8, and regulate their contractions. Alternative low-resistant channels, termed peg-and-socket junctions (PSJ), have also been hypothesised to provide the ICC-SMC connection (Jimenez, 2011). In the region of ileum undergoing segmentation, the quantity of PSJ is much higher than that in the non-segmented section (Thuneberg and Peters, 2001). The observation suggests that PSJ formation is stretch-induced and the mechanism assists ICC to function as a stretch-sensor (Huizinga *et al.*, 2010). In addition to ICC-SMC coupling, PSJ are also found between pairs of SMC in human ileum as shown in Figure 2.11.

Collagen and elastin support extracellular matrix (ECM) structure which surrounds the myocytes in smooth muscle tissue. Collagen provides structural strength while elastin is mainly responsible for tissue elasticity (Fung, 1993). These extracellular filament proteins often enhance ECM architecture and tissue stiffness by cross-linking. The turnover of ECM proteins is regulated by matrix metalloproteinases and their tissue inhibitors (Black *et al.*, 2003).

2.3 GI smooth muscle viscoelasticity

2.3.1 Viscoelastic features of GI smooth muscle

A viscoelastic material has a non-linear history-dependent stress-strain relationship (Lakes, 1999). A number of special features such as stress relaxation, creep and hysteresis set it apart from its elastic counterpart which has a one-to-one stress-strain function. Fung (1993) suggested that biomechanical tissues contain viscoelastic features. Their mechanical properties, including those of GI smooth muscles, are revealed by exploring their response under isometric, isotonic, isokinetic and step

loading conditions. Under isotonic loading, a constant stress or force is applied to the material. In isometric conditions, the material is kept at constant length. An isokinetic loading is applied when the material is deformed in constant velocity or strain rate. GI smooth muscle can also be deformed in discrete fashion when it is extended or shortened in short duration, kept at the new length before another deformation is applied.

Stress relaxation

When a step strain is applied to a viscoelastic body and the strain is kept constant, the stress withstood by the body diminishes with time. This phenomenon is called stress relaxation.

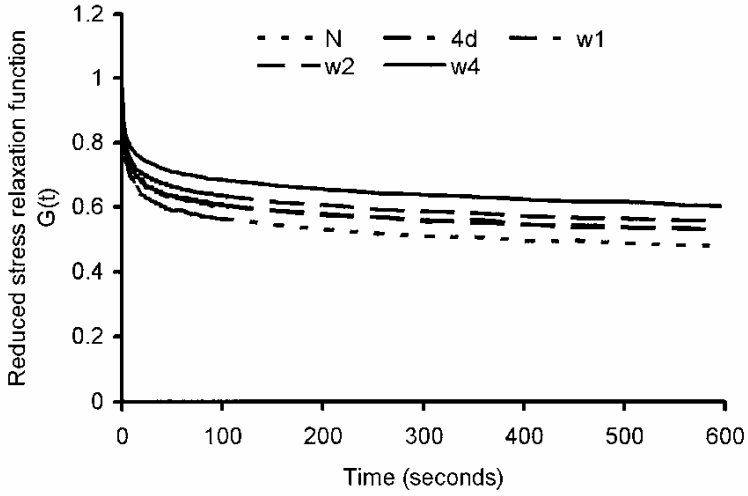

Figure 2.12 Average stress relaxation of duodenal section harvested from healthy rats and diabetic rats with different disease durations. Healthy duodenum appears to be most compliant (lowest curve) with stiffness increases with disease duration. N: healthy; 4d: 4 day; w1: 1 week; w2: 2 weeks; w4: 4 weeks. (Source: Zhao *et al.*, 2003)

Stress relaxation tests were previously performed on small intestinal segments extracted from healthy and diabetic rats at different disease states (Zhao *et al.*, 2003). Three sections of rat small bowel were harvested from duodenum, jejunum and ileum

for each rat. Each section was stretched longitudinally to 40% strain at a rate of 5% s^{-1} before it was kept in an isometric conformation. It was observed that the healthy intestine was more compliant than the diseased samples in terms of fastest force decay and lowest steady-state stress (Figure 2.12). The longitudinal stiffness was also positively correlated with disease duration. Similar experiments have also been performed on guinea pig taenia coli (Price *et al.*, 1979).

Creep and opening angle experiment

When a sudden stress acts on a viscoelastic body and the stress is maintained, the body continues to deform over time. Such a mechanical response is termed creep.

Although simple isotonic experiments on GI smooth muscles have not been reported in the literature, an opening angle technique has been applied by investigators to obtain creep properties of GI tissue. The rationale for using the opening angle technique is based on the observation that intact GI tissue sustains residual stress when no external force acts on it (Gregersen *et al.*, 2000). Cutting the organ can remove the residential stress in the tissue and allow it to deform isotonically without constraint (Figure 2.13). Opening angle experiments were performed to examine the circumferential viscoelastic properties of rat small intestine (Smith, J. B. *et al.*, 2005). Intact thin circular rings were obtained from different intestinal sections before a slit was cut at the circumference of each ring. The rings opened up rapidly at the beginning but the angle increment decayed exponentially as illustrated in Figure 2.14. The duodenum was found to have the largest opening angle, suggesting that it sustained the strongest circumferential residual stress, followed by the ileum and jejunum. To investigate the viscoelastic properties of diseased GI tissues, opening angles of jejunal smooth muscle from healthy guinea pigs and those with intestinal

obstruction were compared (Zhao *et al.*, 2010). The obstructed intestine had a larger opening angle and hence a higher residual stress than the healthy sample.

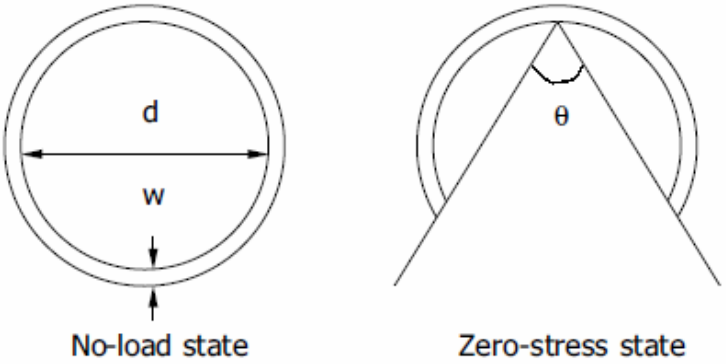

Figure 2.13 Illustration of opening angle experiment. Left: intact intestinal section at no load state which contains circumferential residual stress; Right: open intestinal section at zero-stress state which is free from residual stress. (Source: Smith, J. B. *et al.*, 2005)

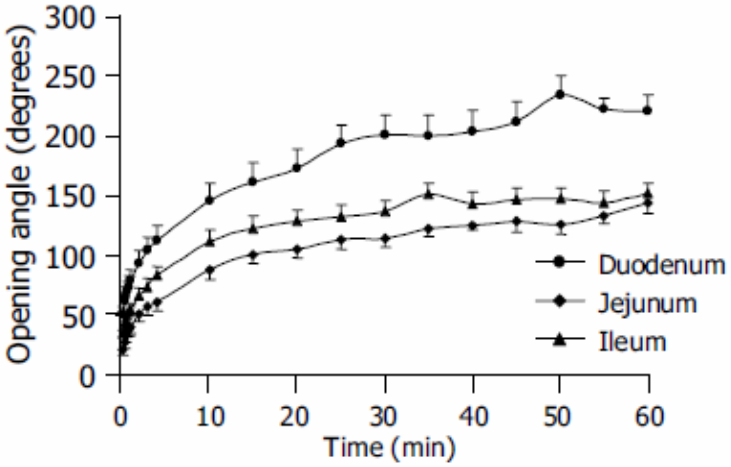

Figure 2.14 Circumferential creep properties of different intestinal sections from rat were elicited by opening angle experiment. (Source: Smith, J. B. *et al.*, 2005)

Cyclic loading

Cyclic loading is performed on viscoelastic materials for different purposes. For one, periodic extension-retraction is often implemented to determine the stress-strain relationship for GI tissues. Loading velocity, or strain rate, affects the gradients and the areas enclosed by the loading and unloading graphs. The slope of a loading or

unloading graph reflects the elastic modulus at the prescribed strain rate. In stress-strain axes, the region demarcated by a lengthening-shortening loop represents the energy loss during the loading cycle which is termed hysteresis (Figure 2.15). Periodic loading on guinea-pig taenia coli tissue has been performed at different strain rates (Price *et al.*, 1979). It was observed that quicker stretch and retraction correlates positively with greater elastic modulus, peak stress and hysteresis.

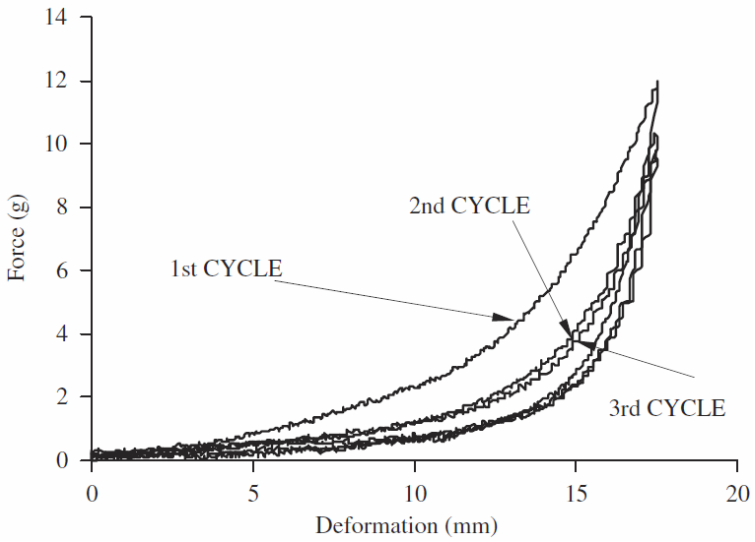

Figure 2.15 Cyclic loading of porcine stomach tissue. Note the decreasing peak stress due to strain softening in 2nd and 3rd cycles. The area bounded by the loading and unloading curves of the same cycle is hysteresis. (Source: Zhao *et al.*, 2008a)

Pre-stretching tissues through cyclic loading helps to obtain repeatable observations in biomechanical experiments (Fung, 1993). During the preconditioning procedure, it is typical that the stress-strain or force-extension curve shifts to the right with reducing peak stress and hysteresis. The phenomenon is also termed strain softening or tissue softening in smooth muscle and cardiac muscle mechanics (Kirton *et al.*, 2004; Speich *et al.*, 2007; Liao *et al.*, 2009b). The number of preconditioning cycles needed depends on the tissue mechanical properties and the procedure is completed when the stress-strain graph of present cycle is sufficiently closed to the previous one. In an

experiment performed on porcine gastric smooth muscle tissue, the samples were stretched with three loading-unloading cycles (Zhao *et al.*, 2008a). The graph of third cycle was used as the experimental result as it was close to the second cycle (Figure 2.15). In other studies, a rabbit oesophagus section was inflated for five times while a guinea-pig jejunum section was preconditioned for ten cycles before actual experiments were performed (Gregersen *et al.*, 1998; Stavropoulou *et al.*, 2009).

Finally, small amplitude cyclic loading can be applied to elicit dynamic mechanical properties and obtain the frequency response of GI tissue. Guinea pig taenia coli tissue stiffness and phase response as well as their variations in wide range of frequency were studied through sinusoidal oscillation (Comelekoglu and Ozturk, 2008). The phase response, which is the gain or lag angle between strain (length) and stress (force), correlates with internal friction and the viscosity of tissue (Fung, 1993).

Step loading

Changing force or length at a constant rate requires the use of a programmable manipulator and feedback control circuit. When such a system is unavailable, researchers manually prescribe a series of length or force changes to deform the tissues and determine their stress-strain relationship (Herlihy and Murphy, 1973; Speich *et al.*, 2007).

A rapid change of extension or stretching force is followed by an equilibration period before another new deformation is imposed (Figure 2.16). The isometric or isotonic equilibration period ranges from one to several minutes with longer times translating to a stress-strain relation that is closer to steady-state. Balloon distension, in which the pressure can be prescribed, was used to study the compliance of rat small bowels which had been surgically shortened (Dou *et al.*, 2002). The circumferential stiffness

of duodenal and ileal sections extracted a week after operation was shown to be higher than that of control samples. The treated samples also had increased wall thickness. The results suggested that resection-provoked tissue remodelling induced changes on bowel morphological and biomechanical properties.

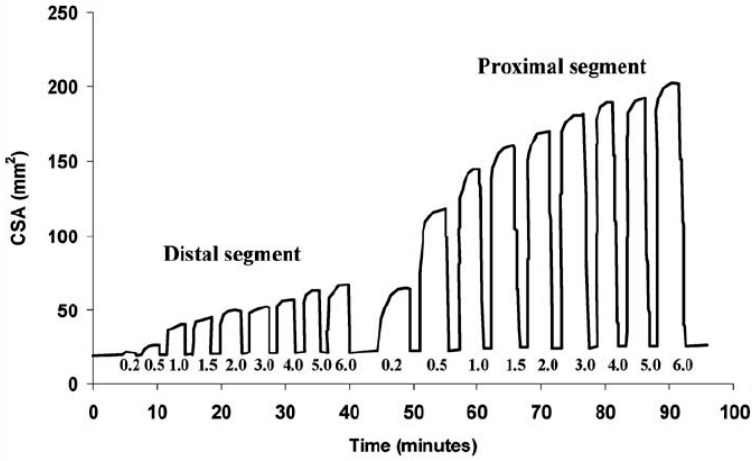

Figure 2.16 Pressure-induced step distension of guinea pig distal and proximal intestinal segment. (Source: Storkholm *et al.*, 2007)

2.3.2 Contribution of intracellular and extracellular components to smooth muscle viscoelasticity

Cytoskeletal proteins as well as extracellular collagen and elastin contribute to smooth muscle viscoelasticity.

The contribution of actin filaments and microtubules to the passive mechanical properties of isolated rat arterial SMC has been previously examined (Nagayama and Matsumoto, 2008). To elucidate the mechanical significance of these cytoskeletal proteins, drug treatment technique is applied to the SMC culture. The SMC were treated with either cytochalasin D (actin polymerisation inhibitor) or colchicines (microtubule polymerisation inhibitor). SMC with abated actin showed increased compliance and hysteresis, suggesting the contribution of actin to SMC stiffness and

viscoelasticity (Figure 2.17a and b). Subtracting microtubules from the SMC reduced the elastic modulus at large stretch (more than 5% strain, Figure 2.17c and d). Another study aimed to quantify the stress relaxation behaviour of vascular SMC treated with cytochalasin D under an indentation load (Hemmer *et al.*, 2009). The result showed that actin-deficient SMC had a more rapid relaxation rate and lower steady-state compressed stress compared to the control sample.

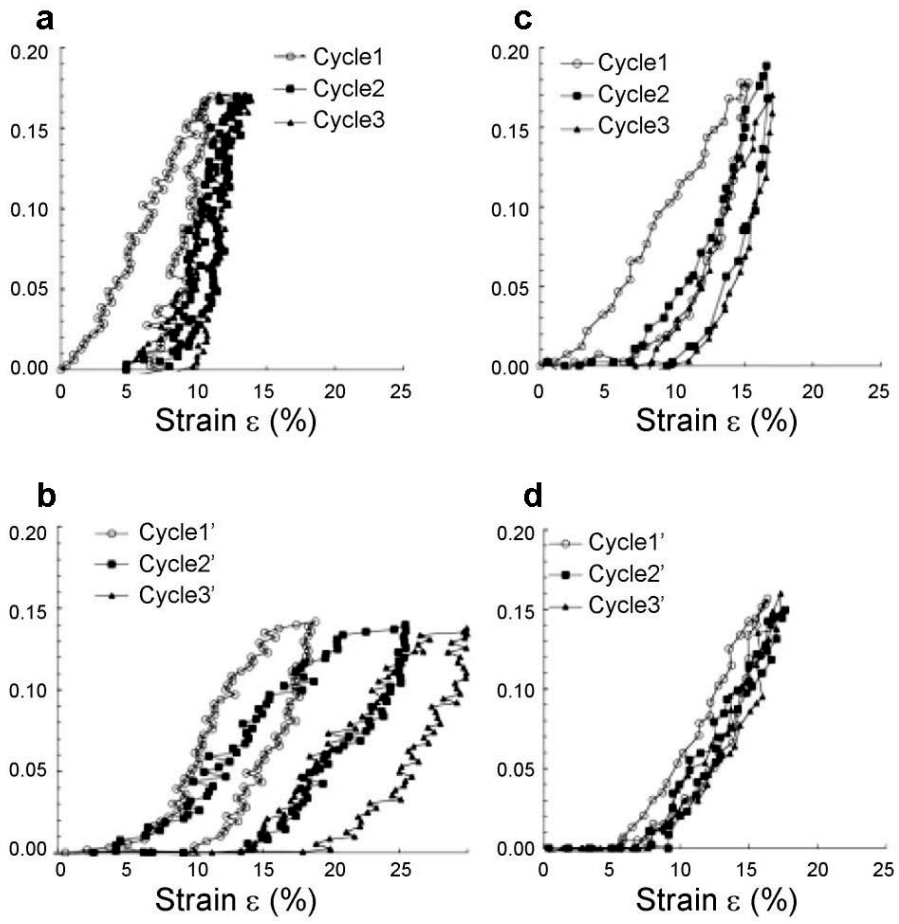

Figure 2.17 Tensile loading of isolated rat arterial smooth muscle cell. Left: (a) Before and (b) after treatment of actin inhibitor. Right: (c) Before and (d) after treatment of microtubule inhibitor. Tension is measured in μN as presented on the y-axis of each graph. (Source: Nagayama and Matsumoto, 2008)

The Type III intermediate filaments vimentin and desmin are found in distinct proportions in a variety of SMCs. Desmin is the major intermediate filament

constituent in GI and airway SMCs while vimentin is expressed in larger quantity in vascular SMC (Gabbiani *et al.*, 1981). The rheological properties of vimentin and desmin meshes have been studied in-vitro (Schopferer *et al.*, 2009). As unconnected filaments congregated and started cross-linking, their storage moduli increased rapidly before tapering off at the formation of mature networks. Both vimentin and desmin had similar strength under low salt conditions but desmin's storage modulus declined and its loss modulus elevated with an increasing salt concentration. In another experiment, disruption of SMC intermediate filament network in human airway SMC using acrylamide caused a 10% drop in the elastic modulus but a 15% increment of the frictional modulus (Stamenovic *et al.*, 2002). The above results suggest that intermediate filament rheology and hence SMC viscoelasticity are influenced by distinct protein phenotype contents, intracellular ionic conditions and filament network formation.

Collagen has the highest tensile strength among the ECM proteins with reported Young's modulus ranges from 10^8 to 10^{10} Pa (Fung, 1993; Eppell *et al.*, 2006; Buehler, 2008). Mechanical properties of isolated collagen fibrils were previously studied and shown to be viscoelastic (Shen *et al.*, 2011). A positive correlation was established between collagen content in guinea pig small bowel sections and their elastic modulus at 70 kPa distension stress (Storkholm *et al.*, 1998). In a GI disease study, excessive collagen deposition was detected in the tissues of systemic sclerosis patients (Sallam *et al.*, 2006; Manetti *et al.*, 2007). A related but separate in-vivo mechanical investigation showed that the small intestine is less compliant in systemic sclerosis patients compared to control subjects (Pedersen *et al.*, 2003). Collectively, these experimental results suggest collagen plays a significant role in tissue stiffening and affects GI tissue viscoelasticity.

Elastin is a thousand times more compliant compared to collagen (Fung, 1993). It allows smooth muscle tissue to restore to its original configuration after deformation (Aitken and Bagli, 2009). Elastin-deficient mice die from hypertension during the developmental stage (Wagenseil *et al.*, 2010). The result suggests the role of elastin in efficient vasodilation and vasoconstriction for blood pressure regulation in vascular SMC. Increased elastin deposition in urinary bladder wall tissue, which also contains smooth muscle and collagen, elevates bladder's compliance and filling capacity (Wognum *et al.*, 2009). The role of elastin in GI smooth muscle is relatively unexplored. A distension experiment was conducted recently on the duodenum of systemic sclerosis patients. Modelling of result suggested that the contribution of elastin to the stiffness of diseased tissue is 30% less than that of control samples (Gao *et al.*, 2009). As the intestinal tissue is stiffer in those patients, the study implicates a positive correlation between the quantity of elastin and GI tissue compliance.

Both the intracellular and extracellular filaments do not exist in isolation. They are often inter-connected to form higher order structures to support the smooth muscle architecture. The tertiary structures often carry more desirable mechanical properties than their constituents. For instance, actin-binding proteins bundle individual actin filaments to form stress fibres in vascular SMC (Deguchi *et al.*, 2006). The tertiary structure is a thousand fold stronger than an isolated actin filament with enhanced compliance, as illustrated by the tensile strength and the elastic modulus respectively in Table 2.1. The in-vitro geometric and mechanical properties of other filaments and fibres are also tabulated.

Table 2.1 In-vitro geometric and mechanical measurements of isolated cytoskeletal and extracellular filaments found in smooth muscle. d: filament diameter; L_p persistence length; E: elastic modulus; F_{max}: tensile strength; E_{max}: elastic modulus corresponding to F_{max}; ε_{max}: strain corresponding to F_{max}.

Filament types	d (nm)	L_p (m)	E (MPa)	F_{max} (nN)	E_{max} (MPa)	ε_{max} (%)	References
Actin filaments	5 –10	10 – 20	2600	0.4	–	0.9	Gittes *et al.* (1993)
Stress fibres	200 – 500	–	1.45	380	100	275	Deguchi *et al.* (2006)
Microtubules	12/25[a]	5000	1200	–	–	–	Gittes *et al.* (1993)
Intermediate filaments	10	1	6.4	14	80	220	Fudge *et al.* (2003)
Collagen fibres	–	–	1000	–	50 – 100	–	Fung (1993)
Elastins	–	–	0.6	–	-	–	Fung (1993)

[a] Inner/outer diameters are reported.

2.4 Active force generation in GI smooth muscle

2.4.1 Sliding filament theory and the crossbridge cycle

Smooth muscle contraction provides additional stiffness to the muscle. Contraction of smooth muscle can be initiated by hormones, pharmaceutical compounds, neurotransmitters from nerve plexuses and electrical signals from pacemaker cells such as ICC (Watras, 2008). In all cases, intracellular [Ca^{2+}] is raised through an influx of Ca^{2+} from the extracellular space or a release of Ca^{2+} ions from the SR (Leung *et al.*, 2008). Sufficient Ca^{2+} ions are then available to bind to calmodulin which subsequently activates myosin light chain kinase (MLCK) (Dillon *et al.*, 1981).

Activated MLCK phosphorylates the myosin light chain (MLC_{20}) on the thick filament such that it can attach to the actin (thin) filament binding site and form the crossbridge.

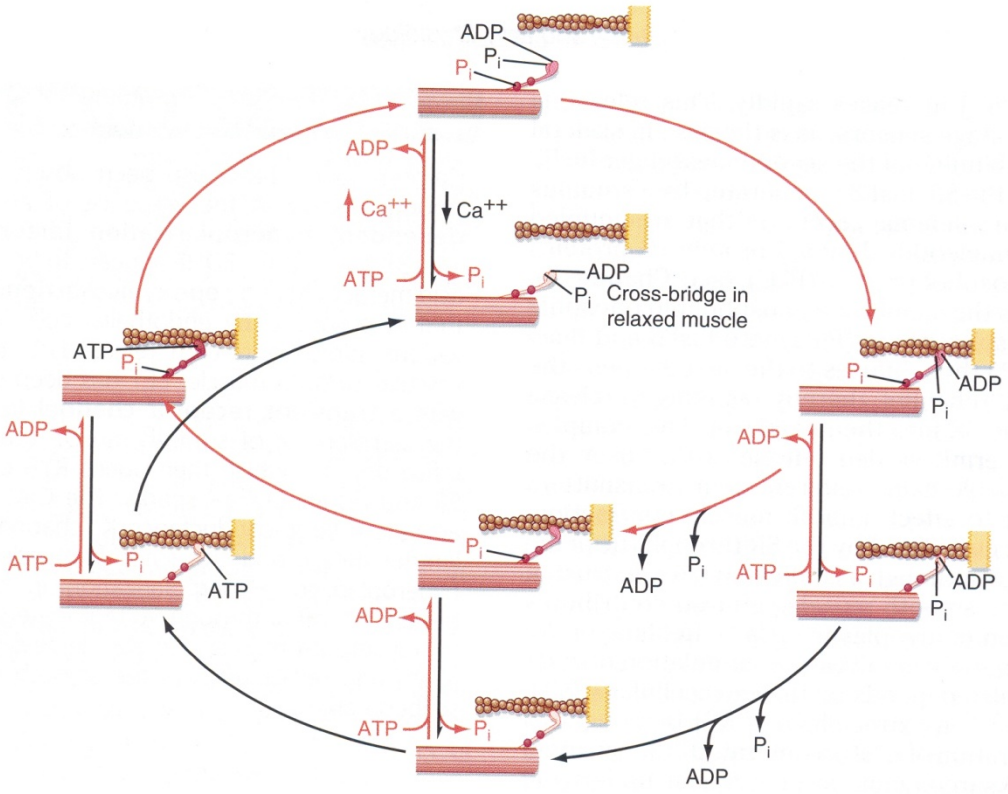

Figure 2.18 Cross-bridge cycles of smooth muscle contraction. Fast and slow cycles are indicated by red and black curved arrows, respectively. Myosin phosphorylation by MLCK (vertical red arrow) is necessary for crossbridge formation. Dephosphorylation of myosin by MLCP (vertical black arrow) slows the cycling rate. (Source: Watras, 2008)

As illustrated by the cycle with red curved arrows in Figure 2.18, the actin-myosin attachment marks the start of crossbridge cycle. The myosin lever arm swings to propel thin filament towards the centre of thick filament and shorten distance between adjacent dense bodies (Figure 2.19). Force is generated and a void is created on myosin due to release of adenosine diphosphate (ADP) and a phosphate ion. The void is quickly filled up with an ATP molecule which causes the myosin arm detaches from the actin binding site. ATP also provides energy for myosin lever arm to restore

to its initial pre-swinging position and this completes the fast cycling process. Repetition of crossbridge cycle creates the observable phenomenon in sliding filament theory (A. F. Huxley and Niedergerke, 1954; H. Huxley and Hanson, 1954).

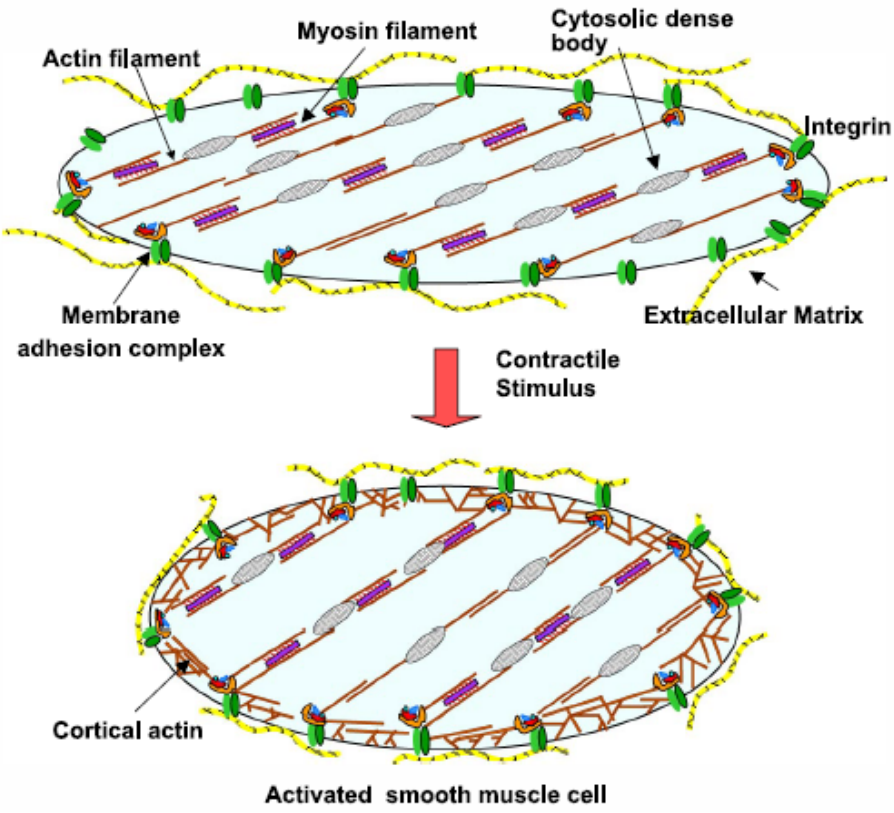

Figure 2.19 Illustration of contracting smooth muscle cell. Note the reduced distance between dense bodies after activation. (Source: Gunst and Zhang, 2008)

In smooth muscle, a slow cycling process can occur concurrently with this fast cycling when whereby a proportion of attached cross-bridges are dephosphorylated by myosin light chain phosphatase (MLCP) (Figure 2.18, cycle with black curved arrows). The dephosphorylated cross-bridges are then transformed to latch bridges (Murphy and Rembold, 2005). Without the phosphate ions, myosin heads detach from actin binding sites at a slower rate and delay the cycling process. Furthermore, dephosphorylated myosin cannot reattach to actin and form new crossbridge. It is believed that the latch bridge cycling process consumes less ATP and provides an

energy-efficient means for maintaining long term smooth muscle tonic contractions (Dillon *et al.*, 1981).

2.4.2 Mechanics of active GI smooth muscle

Spontaneous contraction

The contractions of stomach, small and large intestines are self-actuating and rhythmic in nature. In frog and toad stomachs, the contraction waveform and frequency correlate with the intracellular [Ca^{2+}] transient (Prosser, 1995). The circular and longitudinal muscle layers also act in an antagonistic fashion (Tasaka and Farrar, 1969).

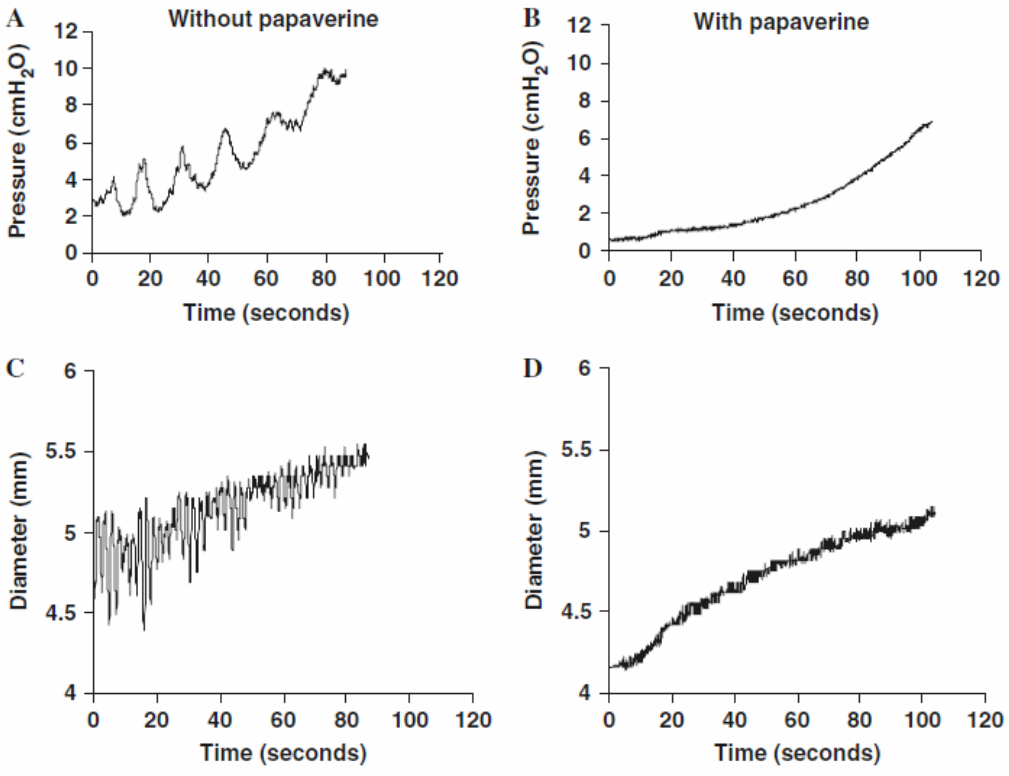

Figure 2.20 In-vitro pressure and diameter measurements of rat jejunal section during ramp distension. (A & C) Peristaltic (phasic and tonic) pressure and diameter were measured in rat jejunal section in-vitro. (B & D) Passive pressure and diameter data were recorded after suppressing contraction with papaverine. Pressure and diameter of the ileal section were obtained in similar manner. (Source: Zhao *et al.*, 2008b)

The GI peristaltic force was previously analysed in both the small and large intestines. Spontaneous contractile forces in the taenia coli were recorded from freshly extracted guinea pig colon sections (Price *et al.*, 1977). As the minimum force was coincidental with tissue passive tension, the maximum contractile force was deduced by calculating the difference between peak and trough of force waveform. In another study, passive, phasic and tonic tensions in rat intestinal sections were examined (Zhao *et al.*, 2008b). Phasic contraction is characterised by rapid rise and decay of contractile stress within tens of seconds, while tonic active tension is sustained for minutes or hours. As shown in Figure 2.20, the peristaltic force waveform was first noted before administering the calcium antagonist papaverine to elicit the passive tension. The phasic and tonic tensions were subsequently computed by subtracting the maximum and minimum peristaltic forces from passive tension respectively. The resulting stress-strain curves are illustrated in Figure 2.21.

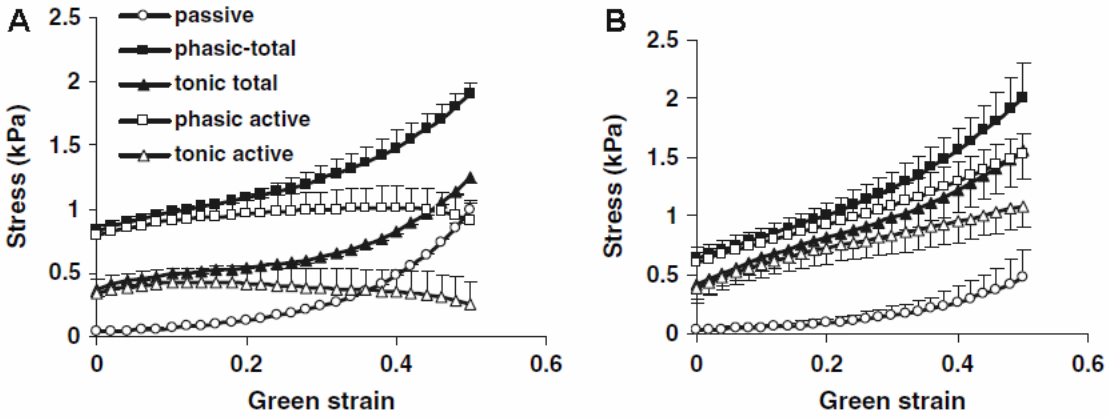

Figure 2.21 Circumferential stress-strain curves of rat small intestinal sections. A: jejunal section B: ileal section. The measurements obtained in Figure 2.20 were separated into passive, tonic active and phasic active stresses. Phasic-total stress is the sum of phasic active and passive stresses while tonic-total stress is the sum of tonic active and passive stresses. (Source: Zhao *et al.*, 2008b)

Isometric contraction and isotonic shortening

Electrical pulses and KCl buffers are commonly applied to stimulate GI tissue contraction in in-vitro isometric and isotonic experiments (Meiss, 1971; Speich *et al.*, 2007). To elucidate the relation between isometric contractile force and tissue deformation, GI tissues are stretched or shortened to prescribed lengths before applying a contractile stimulus. Experiments conducted on cat small intestinal and guinea-pig colonic tissues showed that maximum active tension occurs at an optimum length (Meiss, 1971; Cooke and Fay, 1972). Away from the optimum length on both sides, contractile force descends monotonically as shown in Figure 2.22. A similar length-tension relation was also obtained in isolated active toad stomach SMC by applying step length changes (Harris and Warshaw, 1991). The investigators in this study suggested that the variation of tension force to cell length is contributed by inter-filament lateral spacing, filament overlapping region and the mechanical resistance of intracellular components such as cytoskeleton.

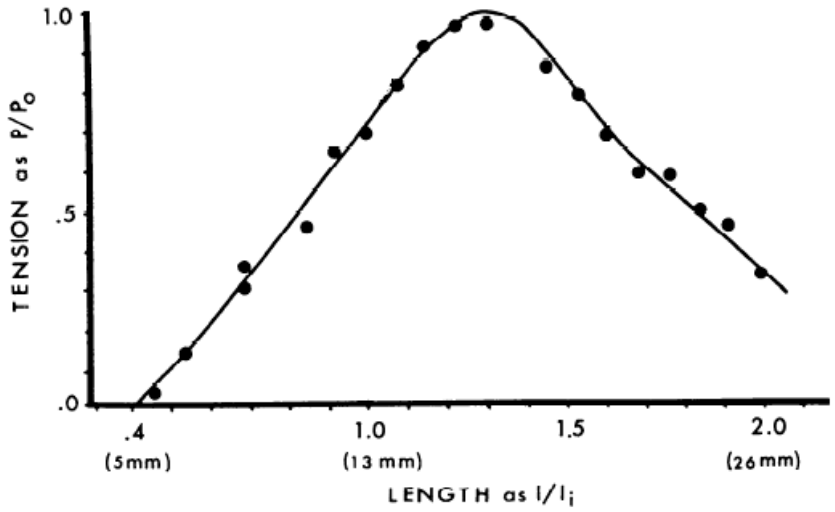

Figure 2.22 Normalised active tension versus length graph of cat duodenal tissue. l_i is denoted as the initial length at which the resting tension developed. l/l_i is the normalised length. The peak stress (P_0) occurs at the optimum length, about 1.3 times of initial length. P/P_0 is the normalised active tension. Active tension decreases beyond optimum length and a bell-shape curve is formed. (Source: Meiss, 1971)

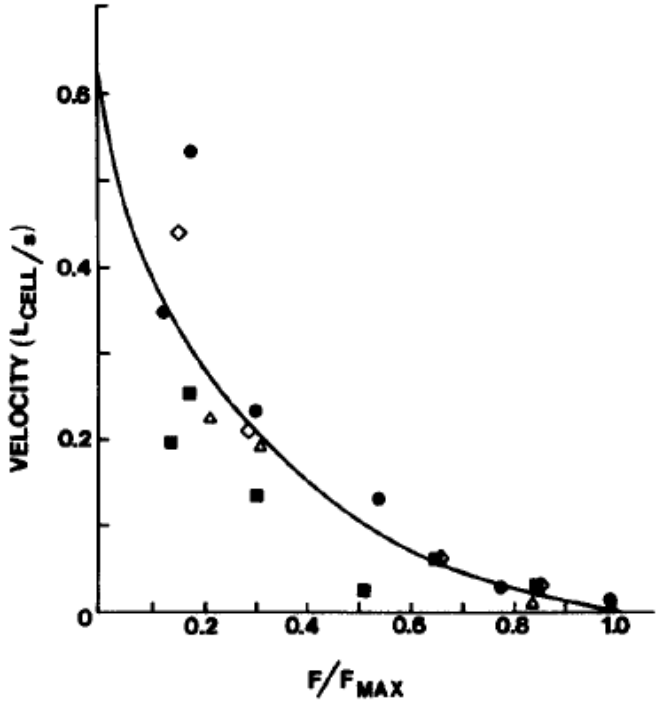

Figure 2.23 Hyperbolic force-velocity relation of isolated toad gastric SMC. The data was obtained from four different cells as indicated by different symbols. Velocity and contractile force (F) are normalised with cell length (L_{CELL}) and maximum isometric force (F_{MAX}). (Source: Warshaw, 1987)

Quick-release or isotonic experiments aim to discover the change in GI smooth muscle shortening velocity and contractile force at different loads. Measurements taken from tetanised toad gastric SMC (Figure 2.23) and activated cat small intestinal strips indicated that the force-velocity relation is hyperbolic (Meiss, 1971; Warshaw, 1987). A similar relation was retrieved in an in-vivo human duodenum study conducted using an infusion balloon with volume control and pressure measurement (Gregersen *et al.*, 2007). In all cases, the data could be fitted to Hill's equation (Equation 3.25) which was derived for activated frog skeletal muscle (Hill, 1938). Warsaw *et al.* (1988) also noted that the Hill's equation parameters obtained from smooth muscle tissues are similar to those obtained from isolated SMC. Overall, the body of evidence supports the notion that the hyperbolic tension-velocity phenomenon

found in smooth muscle tissue is representation of the collective mechanical properties of individual GI SMC.

2.5 Smooth muscle length adaptation

In a smooth muscle, the optimum length, at which maximum active force is generated, can be shifted according to cell or tissue length alteration as illustrated in Figures 2.24a and c (Harris and Warshaw, 1991; Speich *et al.*, 2009). Furthermore, smooth muscle passive stiffness is also capable of adjusting to the new deformation (Figure 2.24b and d) (Speich *et al.*, 2007). The ability of smooth muscle to generate the same level of maximum active force and modulate its passive tension over a broad range of lengths is termed length adaptation (Bai *et al.*, 2004).

The phenomenon of length adaptation has been well-studied in bronchial and tracheal smooth muscles to elucidate the excessive constriction of the airways in asthma (Wang *et al.*, 2005; Chitano *et al.*, 2007). The effective range of smooth muscle lengths was measured in canine tracheal smooth muscle (Pratusevich *et al.*, 1995). The maximum active force differed by merely 4% over a three-fold length alteration. The active and passive force recovery as well as change in optimum length can occur rapidly, within an hour, or gradually in a day depending on the availability, type and frequency of stimulation. In rabbit tracheal smooth muscle, active and passive tension restoration took a day after equilibration at a new length without additional stimulation (Wang *et al.*, 2001). The process was shortened to within an hour when electric current was applied at five-minute intervals. To simulate airway narrowing in-vitro, continuous submaximal stimulation by carbachol, a contractile agonist, was applied to porcine bronchial smooth muscle and it was proven to be successful in evoking length adaptation (McParland *et al.*, 2005). It is worthy to note that the shifting of optimum

length can occur in striated muscles but the adaptation takes much longer to be completed (Bai *et al.*, 2004).

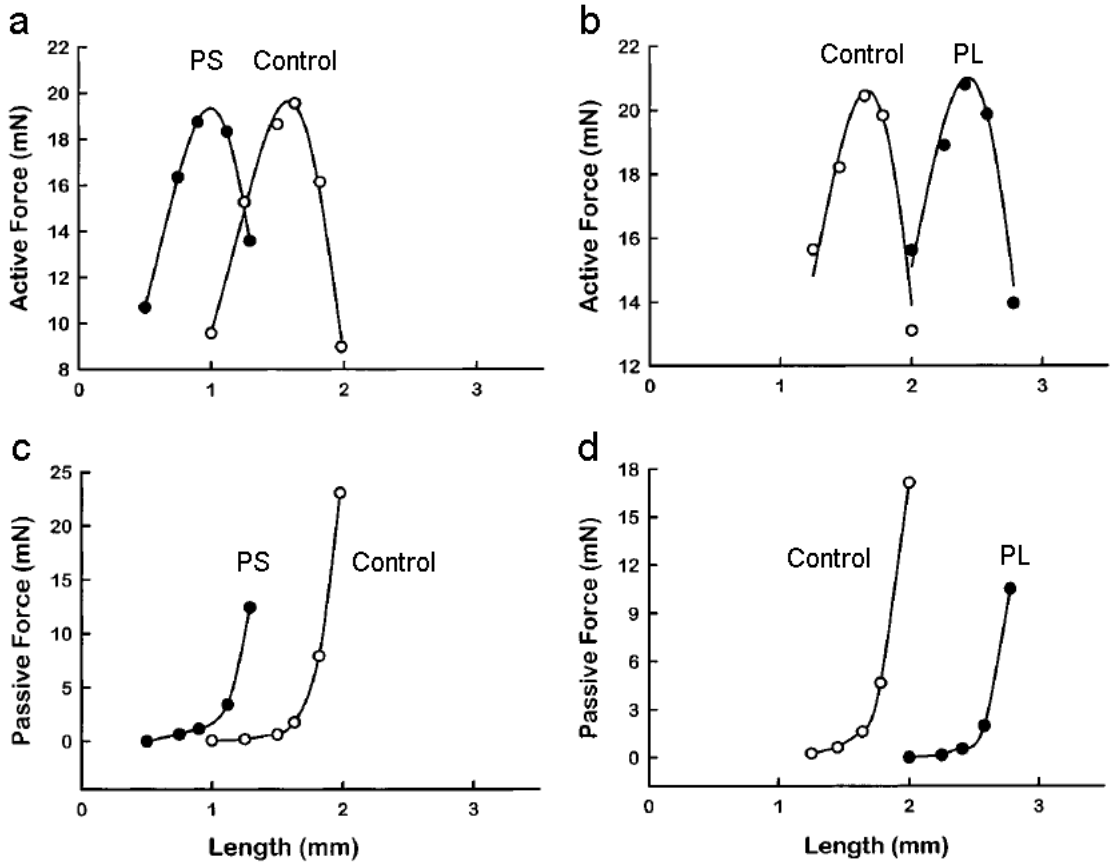

Figure 2.24 Force-length graphs of rabbit tracheal smooth muscle tissue after length adaptation. (A) Isometric active force and (B) passive tension of tissues with (filled circles) or without (empty circles) isometric shortening for 24 hours. (C) Isometric active force and (D) passive tension with (filled circles) or without (empty circles) isometric lengthening for 24 hours. (Source: Wang *et al.*, 2001)

Smooth muscle length adaptation is influenced by subcellular structural modifications. It is postulated that smooth muscle contractile apparatus reassemble with additional serial units when the myocyte is extended and vice versa (Figure 2.25) (Seow *et al.*, 2000). The model is supported by evidence showing greater post-adaptation active smooth muscle stiffness at shorter length than that at longer length (Gunst and Wu, 2001). Smooth muscle shortening velocity, thick filament density and muscle power output increase with tissue length while isometric force remains constant (Kuo *et al.*,

2003). Contraction-induced cytoskeleton dynamics was implicated to influence active force redevelopment during length adaptation (Wang *et al.*, 2005). Recent experiments performed on rabbit arteries showed that length adaptation of active tension is eradicated when actin polymerisation was inhibited (Bednarek *et al.*, 2011). However, such inhibition does not hinder passive tension restoration in ovine airway smooth muscle after prolonged shortening (Bosse *et al.*, 2009). As such, the change in SMC ultra-structure which influences length adaptation of passive tension remains elusive.

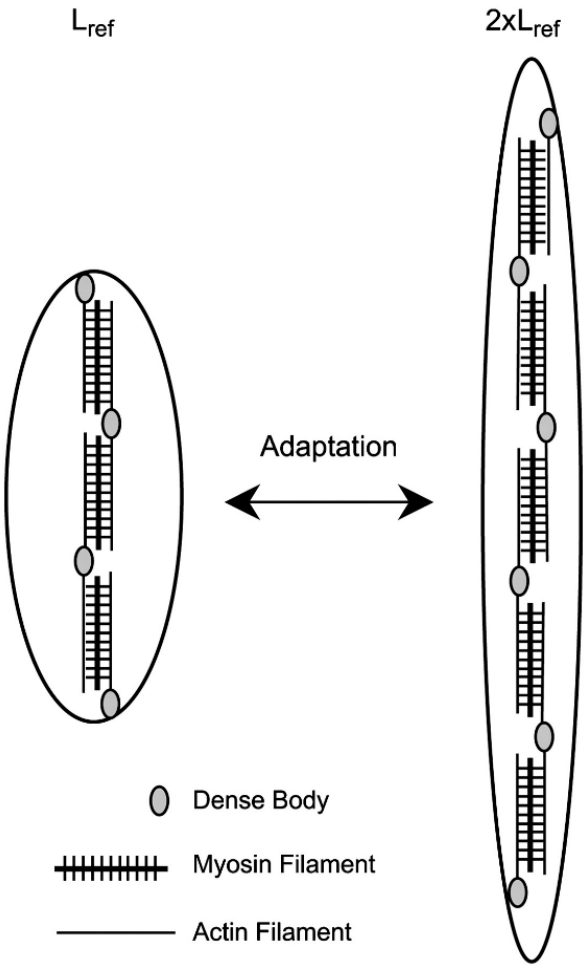

Figure 2.25 Rearrangement of contractile units in SMC under length adaptation. When a SMC is extended from reference length (L_{ref}) to $2L_{ref}$, additional serial contractile units are assembled during length adaptation. Removal of serial contractile units occurs when the cell is shortened. (Source: Bosse *et al.*, 2008)

Length adaptation has been adopted by other investigators to explain the function and remodelling of several types of smooth muscle and related organs. Rabbit detrusor smooth muscle passive stiffness and active tension can adapt to new tissue length after full muscle activation (Almasri *et al.*, 2010b). The result suggests the capability of urinary bladder to maintain physiological function in both empty and filled conditions. The passive and active length-tension graphs of rabbit arterial smooth muscle were also found to be non-static (Seow, 2000). The data demonstrates mechanical recovery of vascular wall tissue under distension caused by varying blood pressure. In isolated toad gastric SMC, similar length-tension relations were observed even though the cells were lengthened or compressed by 40% (Harris and Warshaw, 1991). Although length adaptation has not been explicitly studied in mammalian GI smooth muscle, the above evidence converges to support the likelihood of its existence which is worthy of further investigation.

2.6 Summary

The constituents of smooth muscle, their corresponding physiological roles and major physical phenomena have been reviewed in this chapter.

The smooth muscle passive tension and viscoelasticity is mainly contributed by the intra-SMC cytoskeletal filaments and the extracellular filaments such as collagen and elastin. The interactions between these structural components give rise to important viscoelastic phenomena such as stress relaxation, creep, as well as increasing stiffness, strain softening and hysteresis during cyclic loading.

The smooth muscle contractile force is generated as a result of intracellular cross bridge cycling and filament sliding. The active stress is the aggregate of phasic and tonic contractions in GI smooth muscle. The contractile wave follows closely with

$[Ca^{2+}]_i$ in isometric configuration while the isotonic load-velocity relation obeys the Hill's equation.

The contractile apparatus and cytoskeletal network can adapt to smooth muscle deformation. The structural adaptability leads to dynamic passive and active mechanical properties which is unique in smooth muscle. The ability to generate maximum contractile stress and restoration of smooth muscle passive mechanics to resting configuration over a long range of strain are attributed to the length adaptation phenomenon.

Computational models have been developed to simulate these biomechanical phenomena and these predicate models are detailed in the next chapter.

Chapter 3 Mathematical models of smooth muscle mechanics

3.1 Overview

To describe smooth muscle mechanics, models were initially built to characterise either the spontaneous contractions or passive mechanical responses due to externally applied stresses or strains (Figure 3.1). Subsequently, mathematical descriptions have been derived to integrate both active and passive components in smooth muscles. Recently, mathematical models have been developed to describe smooth muscle length adaptation. A majority of these models has been derived to explain the mechanical phenomena of airway and vascular smooth muscles.

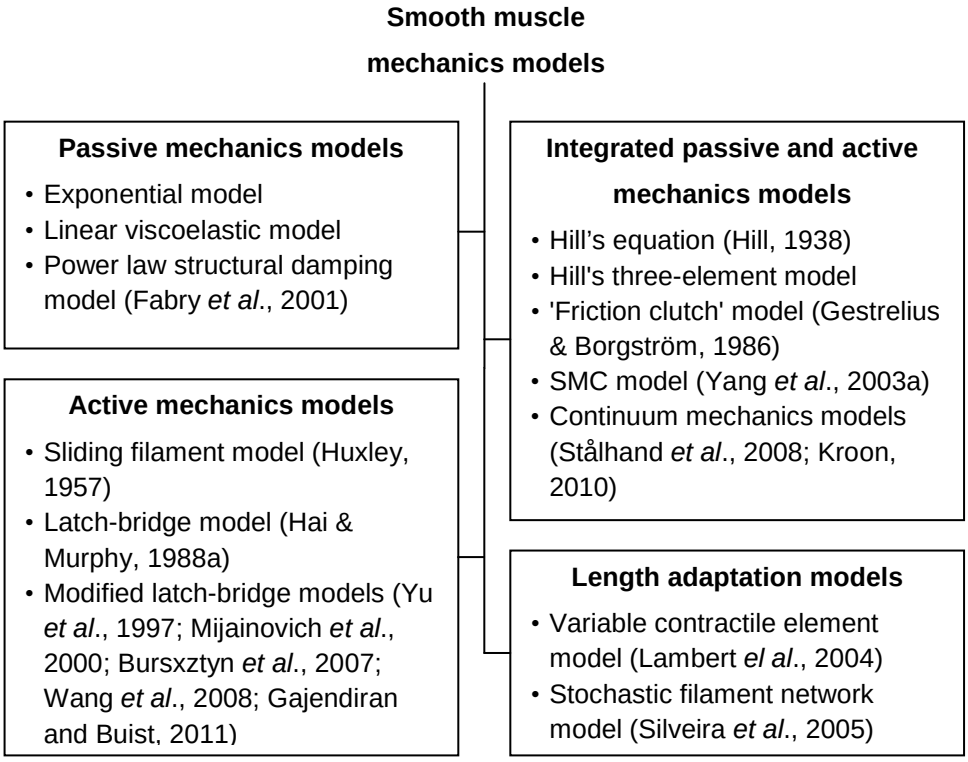

Figure 3.1 An overview of smooth muscle mechanics models.

A selection of these models and their mechanisms are detailed in this chapter. Their strengths and limitations in explaining observed biomechanical phenomena are critically assessed.

3.2 Passive mechanics models

This category of models describes the nonlinear, viscoelastic and dynamic non-contractile properties of smooth muscle cells and tissues.

3.2.1 Exponential models

GI smooth muscle is highly extensible. Experimental data shows that viable porcine gastric muscle strips can be lengthened to 1.8 times its initial length in one-dimension (Zhao *et al.*, 2008a). The measured stress increases slowly for the initial 20% strain before rising rapidly as illustrated in Figure 3.2. A similar phenomenon has been observed in a cylindrical rat ileum section whose radius can be expanded beyond 150% strain without damage (Jorgensen *et al.*, 2001).

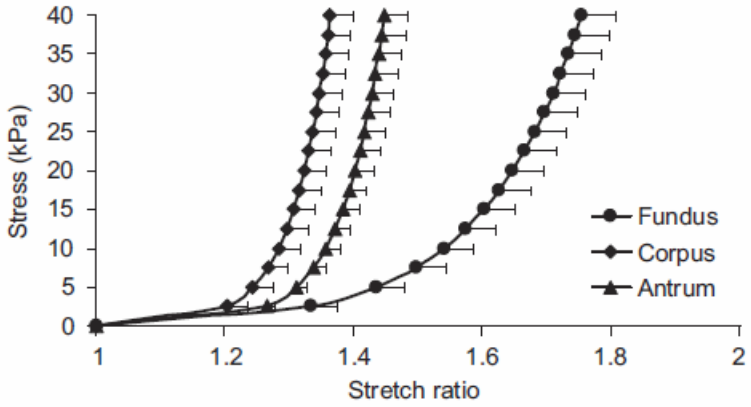

Figure 3.2 Porcine stomach muscle strips extracted from fundus, corpus and antrum under stretching in the longitudinal direction. (Source: Zhao *et al.*, 2008a)

Yin and Fung (1971) characterised the stress-strain relation of mammalian ureteral segments, which contains smooth muscle, using an exponential function,

$$\sigma = \beta[\exp(\alpha\varepsilon) - 1] \tag{3.1}$$

where σ and ε are the Lagrangian stress and strain while α and β are model constants.

Equation (3.1) has been adopted to delineate the passive mechanical properties of mammalian stomach and oesophagus (Zhao *et al.*, 2005; Zhao *et al.*, 2008a; Liao *et al.*, 2009b). The tissue elastic modulus (E) is derived by differentiating Equation (3.1) with respect to ε,

$$E = \frac{d\sigma}{d\varepsilon} = \alpha\beta\exp(\alpha\varepsilon). \tag{3.2}$$

Substituting Equation (3.1) into (3.2),

$$E = \frac{d\sigma}{d\varepsilon} = \alpha(\sigma + \beta). \tag{3.3}$$

Equation (3.3) shows that the tissue elastic modulus varies linearly with the Lagrangian stress. The mathematical result has been validated experimentally in GI smooth muscle, cardiac muscle and other mammalian soft tissues (Fung, 1967; Pinto and Fung, 1973; Zhao *et al.*, 2005).

Application of exponential model on GI tissues

We have collected GI tissues stress-strain data from various published sources and fitted them with the exponential model. For instance, we applied the model to describe the duodenum tissue stress-strain data obtained by Gregersen *et al.* (2007), shown in Figure 3.3. In all cases, the data are well-described by the exponential model as the R^2 values are close to unity. The results are shown in Table 3.1.

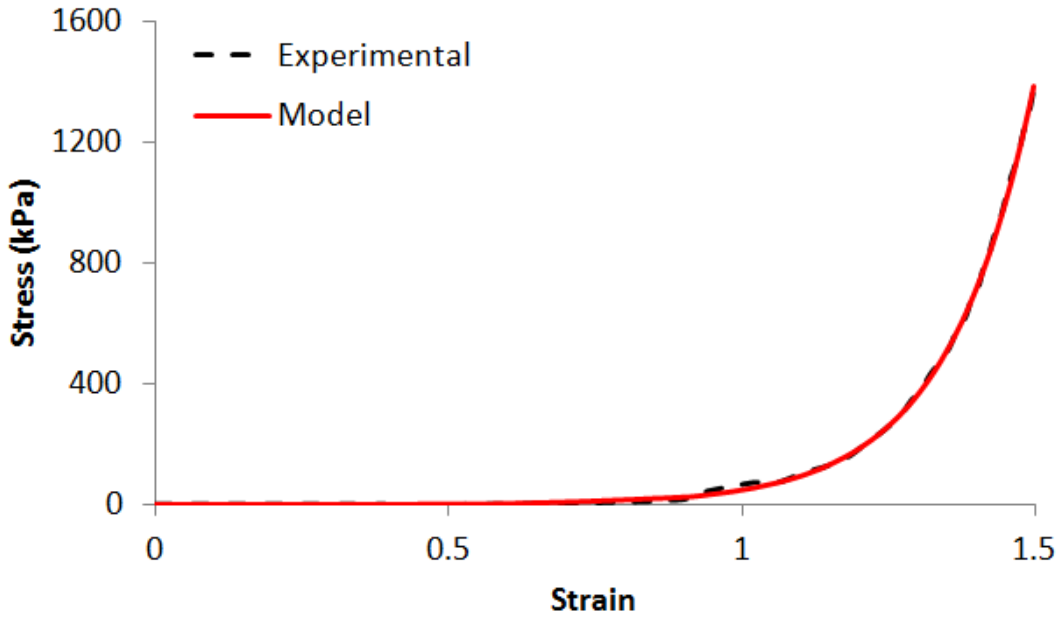

Figure 3.3 Application of exponential model on human duodenum tissue stress-strain data. Experimental data has been provided by Gregersen *et al.* (2007).

Table 3.1 Modelling GI tissue passive stress-strain relation using exponential model. Exponential model constants (α and β) for GI tissues are obtained by fitting published experimental data to Equation (3.1) through nonlinear optimisation. The goodness of fit is represented by R^2 values.

Species and physiological conditions	Organ sections	α	β (kPa)	R^2	References
Healthy porcine, in-vitro	Stomach fundus muscle layer measured in circumferential direction	6.66	0.364	1.00	Zhao *et al.* (2008a)
Healthy porcine, in-vitro	Stomach fundus muscle layer measured in longitudinal direction	6.42	0.850	1.00	Zhao *et al.* (2008a)
Healthy porcine, in-vitro	Stomach corpus muscle layer measured in circumferential direction	15.1	0.141	1.00	Zhao *et al.* (2008a)

Species and physiological conditions	Organ sections	α	β (kPa)	R^2	References
Healthy porcine, in-vitro	Stomach corpus muscle layer measured in longitudinal direction	17.2	0.207	1.00	Zhao *et al.* (2008a)
Healthy porcine, in-vitro	Stomach antrum muscle layer measured in circumferential direction	14.7	0.0714	0.998	Zhao *et al.* (2008a)
Healthy porcine, in-vitro	Stomach antrum muscle layer measured in longitudinal direction	15.3	0.113	0.998	Zhao *et al.* (2008a)
Healthy cat, in-vitro	Duodenal circumferential muscle	9.70	0.239	0.994	Meiss (1971)
Healthy rabbit, in-vitro	Duodenal circumferential muscle	4.30	0.582	0.997	Elbrond (1991)
Healthy human, in-vivo	Intact duodenum measured in circumferential direction	6.76	0.152	1.00	Gregersen *et al.* (2007)
Systemic sclerosis patient (5 year disease duration), in-vivo	Intact duodenum measured in circumferential direction	7.52	25.9	0.999	Gregersen *et al.* (2007)
Systemic sclerosis patient (14 year disease duration), in-vivo	Intact duodenum measured in circumferential direction	13.4	4.49	0.996	Gregersen *et al.* (2007)

Assessment of the exponential model

The exponential model provides an accurate description of the nonlinear stress-strain relation of GI smooth muscle. However, in GI tissue the stress-strain relation is history-dependent. Mechanical factors such as stretching velocity, hysteresis and strain softening affect GI tissue material properties (Price *et al.*, 1979; Zhao *et al.*, 2005; Liao *et al.*, 2009b). These factors restrict the application of the exponential model to describing the stress-rain relation of well-preconditioned GI smooth muscle tissue at a steady-state.

3.2.2 Linear viscoelastic models

Linear viscoelastic models are used to describe the dynamic mechanical properties of soft tissues and cells. A linear viscoelastic model consists of one or more fundamental elements with two basic types: a linear spring and a linear dashpot (Fung, 1993). The linear spring simulates the elastic properties of a Hookean solid such that stress increases proportionally with strain. The linear dashpot possesses the attributes of a viscous Newtonian fluid where stress varies linearly with strain rate. The elastic and viscous components are connected in series and/or in parallel to produce a variety of models. For linear viscoelastic models, their constitutive equations relating stress (σ), strain (ε) and their time-derivative terms can be expressed in the general form (Flügge, 1967)

$$\sigma + p_1 \frac{d\sigma}{dt} + p_2 \frac{d^2\sigma}{dt^2} + \cdots + p_m \frac{d^m\sigma}{dt^m} = q_0\varepsilon + q_1 \frac{d\varepsilon}{dt} + q_2 \frac{d^2\varepsilon}{dt^2} + \cdots + q_n \frac{d^n\varepsilon}{dt^n} \qquad (3.4)$$

where $m, n \geq 0, m, n \in Z$. p_i, with $1 \leq i \leq m$, and q_j, with $0 \leq j \leq n$, are coefficients of the i^{th} time-derivative of σ and the j^{th} time-derivative of ε respectively. Derivations and

characteristics of selected linear viscoelastic models, such as the Maxwell model, the Kelvin body and the standard linear solid (SLS), are discussed in Appendix A.

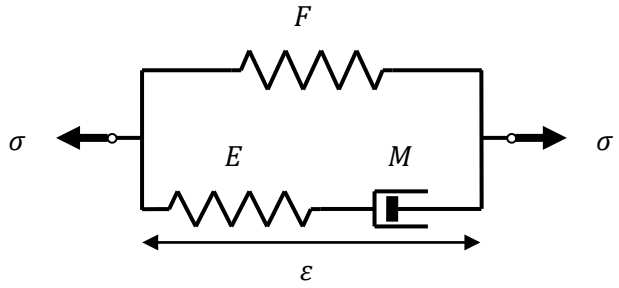

Figure 3.4 Illustration of the standard linear solid model. F and E are the elastic moduli of parallel and series springs while M is the coefficient of viscosity of linear dashpot. σ and ε are the applied stress and strain respectively.

The SLS model is widely employed in biomechanics research. It is constructed by connecting a linear spring in parallel with a Maxwell element, which consists of a linear spring and a linear dashpot joined in series, as shown in Figure 3.4. An alternative configuration, also commonly referred to as a SLS, consists of a linear spring connected in series with a Kelvin element, which contains a linear spring and a linear dashpot connected in parallel. The alternative configuration is discussed in Appendix A.

The SLS constitutive equation, in accordance to the configuration presented in Figure 3.4, is

$$\frac{d\sigma}{dt} + \frac{E}{M}\sigma = (E + F)\frac{d\varepsilon}{dt} + \frac{EF}{M}\varepsilon \tag{3.5}$$

where F and E are the elastic moduli of the parallel and series springs while M is the coefficient of viscosity of the linear dashpot. σ and ε are the applied stress and strain, respectively.

Application of SLS model on GI tissues

The SLS model has been applied to simulate creep responses of neutrophils, endothelial cells, fibroblasts and chondrocytes in micropipette experiments (reviewed by Lim *et al.*, 2006b). SLS has also been used in SMC and GI tissue mechanical modelling. We collected SLS parameters from several publications and listed the results in Table 3.2. In the case of the rat small intestinal ring section, the standard errors of SLS parameters (SE) have not been provided and thus was estimated using the error propagation method provided by Meyer (1975).

Table 3.2 Modelling in-vitro SMC and GI tissues experimental results using SLS. SLS parameters (mean ± SE) are reported according to Equation (3.5). Note the units and table footnote.

Species and organs	Experiments	F	E	M	References
Rat duodenum ring section [a]	Creep (opening angle)	1.05 ± 0.03	2.57 ± 0.17	716 ± 78 s	Smith *et al.* (2005)
Rat jejunum ring section [a]	Creep (opening angle)	1.02 ± 0.02	3.60 ± 0.26	617 ± 52 s	Smith *et al.* (2005)
Rat ileum ring section [a]	Creep (opening angle)	0.995 ± 0.013	2.56 ± 0.16	440 ± 37 s	Smith *et al.* (2005)
Rat colonic SMC	Creep (micropipette aspiration)	20.0 ± 2.87 Pa	7.23 ± 9.84 Pa	25.4 ± 6.16 Pa s	Liao *et al.* (2006b)

Species and organs	Experiments	F	E	M	References
Rat arterial SMC (Passages 5 to 6)	Stress relaxation	3.90 ± 1.31 kPa	5.09 ± 1.93 kPa	1491 ± 806 kPa s	Nagayama *et al.* (2007)
Rat arterial SMC (Passages 17 to 19)	Stress relaxation	4.18 ± 1.50 kPa	6.36 ± 2.73 kPa	1458 ± 428 kPa s	Nagayama *et al.* (2007)

[a] SLS parameters are presented as normalised values and the values are computed from the mean ± SE of empirical parameters using the method outlined by Meyer (1975).

Assessment of linear viscoelastic models

As presented in Table 3.2, the SLS is capable of reproducing stress relaxation and creep in SMCs and GI tissues. However, its ability to describe other nonlinear viscoelastic properties, for example, the cyclic stretching of stomach tissue at finite strain, are limited (Zhao *et al.*, 2005). Constructing models with additional springs and dashpots, such as a Generalised Maxwell model or a Kelvin Chain model, as well as solving the hereditary integral of the constitutive equation are alternate methods to extend the applicability of the model. However, these approaches significantly increase complexity of the description (Flügge, 1967; Argyris *et al.*, 1991).

Overall, regardless of the number of relaxation modes, the linear viscoelastic model is linear by design. A possible refinement is to identify a strain measure and use it in conjunction with a relaxation spectrum.

3.2.3 Power-law structural damping model (Fabry *et al.*, 2001)

GI tissue is periodically stretched, compressed and sheared by neighbouring tissues during motility (Gayer and Basson, 2009). The effects of this repetitive application of

physical forces on cell morphology, growth, differentiation and stiffness through mechano-transduction have been examined in GI mucosa but not in gut smooth muscle (Basson, 2003). However, experiments performed on non-GI SMC have ascertained that dynamic forces influence their cell biology (Lim *et al.*, 2010; Janmey and Miller, 2011). The results support the notion that small amplitude oscillations and modelling of the phenomenon are needed to properly understand GI SMC physiology.

Small amplitude periodic stretching has been well-studied in mammalian airway SMC. Optical magnetic twisting cytometry and atomic force microscopy techniques can induce oscillatory forces on adherent SMC (Fabry *et al.*, 2003; Laudadio *et al.*, 2005; Smith, B. A. *et al.*, 2005). The complex elastic modulus (G^*) obtained can be decomposed into an elastic storage modulus (G') and a loss modulus (G'') in the form

$$G^* = G' + jG'' \tag{3.6}$$

where $j = \sqrt{-1}$.

The SMC storage modulus has been found to be following a weak power law and is linearly correlated with perturbing frequency up to 1000 Hz (Figure 3.5a). Similarly, the frictional modulus varies linearly with the driving frequency up to 10 Hz (Figure 3.5b). To describe the SMC complex elastic modulus, Fabry and colleagues (2001) used an empirical power-law structural damping model,

$$G^* = G_0\left(\frac{\omega}{\Phi_0}\right)^{\alpha}(1 + j\bar{\eta})\Gamma(1-\alpha)\cos\frac{\pi\alpha}{2} + j\omega\mu \tag{3.7}$$

where G_0 and Φ_0 are scaling factors for stiffness and frequency respectively. $\omega = 2\pi f$ is the radian frequency and $\bar{\eta} = \tan(\alpha - 1)\pi/2$ is the structural damping coefficient.

$\Gamma(\cdot)$ denotes the gamma function, and G' and G'' can be computed from the real and imaginary part of Equation (3.7).

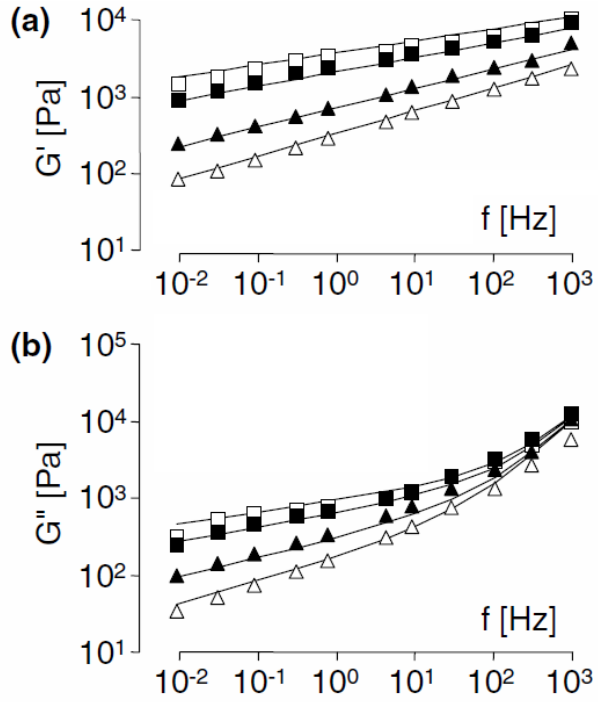

Figure 3.5 Storage and loss moduli of human airway SMC obtained from optical magnetic twisting cytometry. (a) G' and (b) G'' indicate storage and loss moduli, respectively. SMC is either untreated (■) or administered with one of the three drugs: contractile agonist histamine (□), relaxation agonist DBcAMP (▲) and actin polymerisation inhibitor cytochalasin D (△). (Source: Fabry *et al.*, 2001)

In Equation (3.7), α is the power-law exponent which ranges from zero to unity. When it is close to zero, the SMC behaves approximately like an elastic solid, and near one the cell mechanical properties are similar to those of a viscous fluid (Bursac *et al.*, 2005; Laudadio *et al.*, 2005). μ is a Newtonian viscosity term. Both α and μ are assumed to be frequency-independent and related to both cytoskeletal and contractile disruptions.

Application of the power-law structural damping model to SMC

The power-law structural damping model has been employed by several investigators to elucidate the mechanical response of SMC to small amplitude oscillations. We standardised the model parameters (α and μ) from several published studies for ease of comparison. The results are listed in Table 3.3.

Table 3.3 Modelling mammalian SMC passive mechanics using power-law structural damping model. Model parameters (mean ± SE) are obtained from SMC with or without drug treatment. Cytochalasin D inhibits actin polymerization; genistein hinders actin branching while jasplakinolide facilitates it; latrunculin binds to globular actin to jeopardise polymerisation; histamine and 5-HT are contractile agonists while DBcAMP lowers intracellular [Ca^{2+}] for SMC relaxation. Results and parameters are reported according to Equation (3.7).

Species and organs	Experiments [d]	Drug treatments	α	μ (Pa s)	References
Rat tracheal SMC	OMTC	None	0.20 ± 0.0066 [a]	0.259 ± 0.022 [b]	Laudadio *et al.* (2005)
Rat tracheal SMC	OMTC	Cytochalasin D	0.21 ± 0.0070 [a]	0.258 ± 0.018 [b]	Laudadio *et al.* (2005)
Rat tracheal SMC	OMTC	Jasplakinolide	0.20 ± 0.0066 [a]	0.515 ± 0.038 [b]	Laudadio *et al.* (2005)
Rat tracheal SMC	OMTC	Latrunculin A	0.27 ± 0.0075 [a]	0.239 ± 0.014 [b]	Laudadio *et al.* (2005)
Rat tracheal SMC	OMTC	Genistein	0.22 ± 0.0068 [a]	0.425 ± 0.029 [b]	Laudadio *et al.* (2005)
Rat tracheal SMC	OMTC	DBcAMP	0.26 ± 0.0074 [a]	0.344 ± 0.020 [b]	Laudadio *et al.* (2005)
Rat tracheal SMC	OMTC	5-HT	0.18 ± 0.0066 [a]	0.482 ± 0.038 [b]	Laudadio *et al.* (2005)

Species and organs	Experiments [d]	Drug treatments	α	μ (Pa s)	References
Rat tracheal SMC	AFM	None	0.120 ± 0.005	5.1 ± 0.4	Smith *et al.* (2005)
Rat tracheal SMC	AFM	Cytochalasin D	0.160 ± 0.009	7.2 ± 0.6	Smith *et al.* (2005)
Rat tracheal SMC	AFM	5-HT	0.055 ± 0.005	21 ± 2	Smith *et al.* (2005)
Human airway SMC	OMTC	None	0.204 ± 0.001 [a,c]	0.680 ± 0.023 [b,c]	Fabry *et al.* (2003)
Human airway SMC	OMTC	Cytochalasin D	0.329 ± 0.002 [a,c]	0.401 ± 0.010 [b,c]	Fabry *et al.* (2003)
Human airway SMC	OMTC	DBcAMP	0.277 ± 0.001 [a,c]	0.741 ± 0.017 [b,c]	Fabry *et al.* (2003)
Human airway SMC	OMTC	Histamine	0.166 ± 0.002 [a,c]	0.911 ± 0.033 [b,c]	Fabry *et al.* (2003)

[a] A conversion formulation of $\alpha = x - 1$ is used.
[b] A geometric scaling factor of 6.8 um is multiplied to experimental results for the value of μ.
[c] Standard errors are calculated from 95% confident intervals.
[d] In-vitro experiments were performed. OMTC: optical magnetic twisting cytometry; AFM: atomic force microscopy.

Assessment of power-law structural damping model

The power-law structural damping model can demonstrate the mathematical relations between the storage and loss moduli against loading frequency. It can be used to describe small amplitude dynamic loading phenomena, observed in SMC and other cell types. Recently, the model has also been applied to explain transient loading behaviour such as cell creep (Lenormand *et al.*, 2004; Desprat *et al.*, 2005; Zhou *et al.*, 2010). Currently, there is no evidence showing that the power-law structural model

can be used to describe other viscoelastic phenomena such as stress relaxation and finite deformations.

3.2.4 Other passive force models

Other smooth muscle passive force models include the fractional derivative models and the adjustable passive stiffness (APS) model. The proponents of fractional derivative models suggest that the applied stress (σ) on a viscoelastic material is a fractional time-derivative of strain (ε) such that $\sigma = d^{\alpha}\varepsilon/dt^{\alpha}$ where $0 < \alpha < 1$. The model has been used to study viscoelasticity of aortic valve cusp and artery (Doehring *et al.*, 2005; Craiem and Armentano, 2007). Speich and colleagues (2006; 2007) developed a linear viscoelastic model with additional cross-linking elastic components whose stiffness is reduced after rapid extension and is restored after muscle activation. The APS model has been applied to simulate strain-softening behaviour and its recovery in rabbit detrusor tissue which contains smooth muscle.

3.3 Active mechanics models

Modelling of active force generation in smooth muscle has been greatly influenced by Huxley's sliding filament theory as well as Hai and Murphy's latch-bridge formalism. Investigators have sought to include new experimental findings into the classical models for improved explanations and mathematical descriptions of contractile function.

3.3.1 Sliding filament model (Huxley, 1957)

The sliding filament phenomenon was observed and deduced by A. F. Huxley & Niedergerke (1954) from interference microscopic images of frog muscle fibres and H. Huxley & Hanson (1954) from phase contrast microscopic images of rabbit psoas

muscles independently. They noticed the extension of actin filaments from the I-band to the A-band in stimulated muscle and hypothesised that the actin filaments slides over the myosin filaments during muscle contraction.

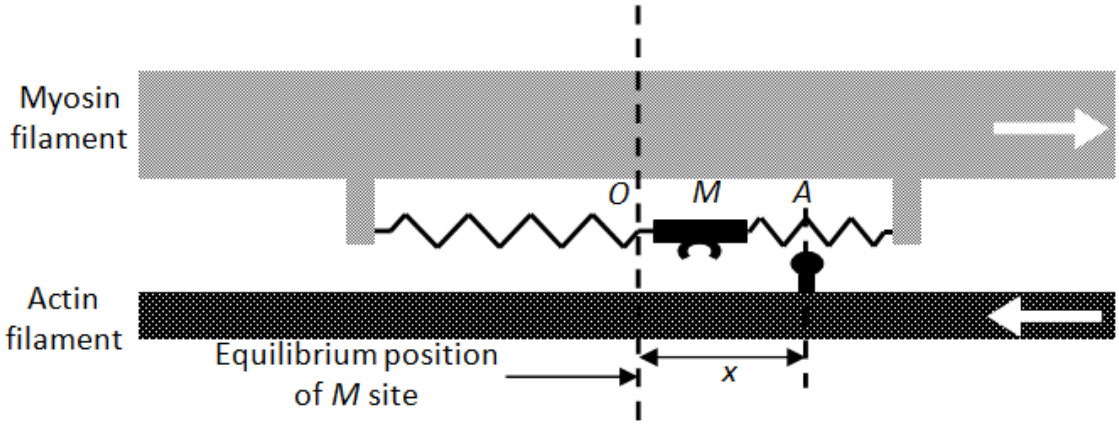

Figure 3.6 Illustration of sliding filament model. The swinging myosin light chain is represented by a catch element supported by a pair of linear springs attached to the think filament. Catch element position, *M*, oscillates about Position *O* with the range of movement limited by the springs. The actin binding site at Position *A* is presented as a protruding knob fixed on thin filament. Displacement of *A* from *O*, *x*, decreases as actin filament slides past myosin filament. (Adapted from Huxley, 1957)

A. F. Huxley (1957) later formalised the theory mathematically using a knob-and-catch model as shown in Figure 3.6 (refer to figure caption for model description). The actin-myosin cross-bridge formation and detachment are regulated by rate constants f and g correspondingly, as shown in the following reactions (Huxley, 1957; Watras, 2008):

$$A + M \xrightarrow{f} AM \tag{3.8}$$

$$AM + ATP \xrightarrow{g} A \cdot ATP + M \tag{3.9}$$

$$A \cdot ATP \rightarrow A + ADP + P_i. \tag{3.10}$$

It was postulated that the actomyosin association and dissociation rate constants, f and g, vary with x, which indicates a displacement of *A* from *O* (x is positive for right side of *O*) such that

$$x < 0: \qquad f = 0 \text{ and } g = g_2 \tag{3.11}$$

$$0 < x < h: \qquad f = f_1 x/h \text{ and } g = g_1 x/h \tag{3.12}$$

$$x > h: \qquad f = 0 \text{ and } g = g_1 x/h \tag{3.13}$$

where distance h is the limit beyond which myosin cannot bind to actin. f_1, g_1 and g_2 determine the increment of f and g relative to the displacement of actin binding site. The possibility of attachment is higher within $0 < x < h$, thus $f_1 > g_1$ in Equation (3.12). The chance for cross-bridge disassembly is far greater, that is, $g_2 > g_1$, if the actin site travels beyond Position *O*.

The myosin and actin elements are not bound initially. *M* was assumed to oscillate about *O* due to thermal agitation. During muscle shortening, *A* travels towards *O* and attaches to *M* if it is within displacement h from *O*. When a cross-bridge is established, tension on the elastic spring is transferred to thin filament that helps to shorten the muscle further as long as it is on the right side of *O*. Although the possibility of cross-bridge disassembly exists throughout the muscle shortening, it rises considerably when *A* translates beyond *O*. This sequence of events occurs independently at other myosin and actin sites along the filaments to sustain muscle shortening.

Assessment of sliding filament model

The Huxley's sliding filament model incorporates both spatial and mechano-chemical variables to explain striated muscle contraction. However, it excludes the contribution of passive forces which resist muscle shortening. Huxley also did not address the relation between muscle length and isometric force, which is the contractile force generated by the muscle while its length is kept constant. Although the sliding filament model was originally designed to explain striated muscle actomyosin interaction, it has been implemented in a number of smooth muscle biophysical models with modifications as shown in the following sections.

3.3.2 Latch-bridge model (Hai and Murphy, 1988b)

In addition to the formation of cross-bridges, actin and myosin can assemble to establish a latch-bridge in smooth muscle. A latch-bridge is formed when an attached cross-bridge is dephosphorylated by MLCP, which leads to slow detachment of the myosin head from the actin binding site and delays the cycling process.

Hai and Murphy (1988b) developed a four-state chemical kinetic model which describes the formation of cross-bridges and latch-bridges in smooth muscle. The model consists of four species which include free unphosphorylated myosin (M), unbound phosphorylated myosin (M_p), attached cross-bridges (AM_p) and unphosphorylated latch-bridges (AM). Transitions between states are regulated by seven rate constants as illustrated in Figure 3.7.

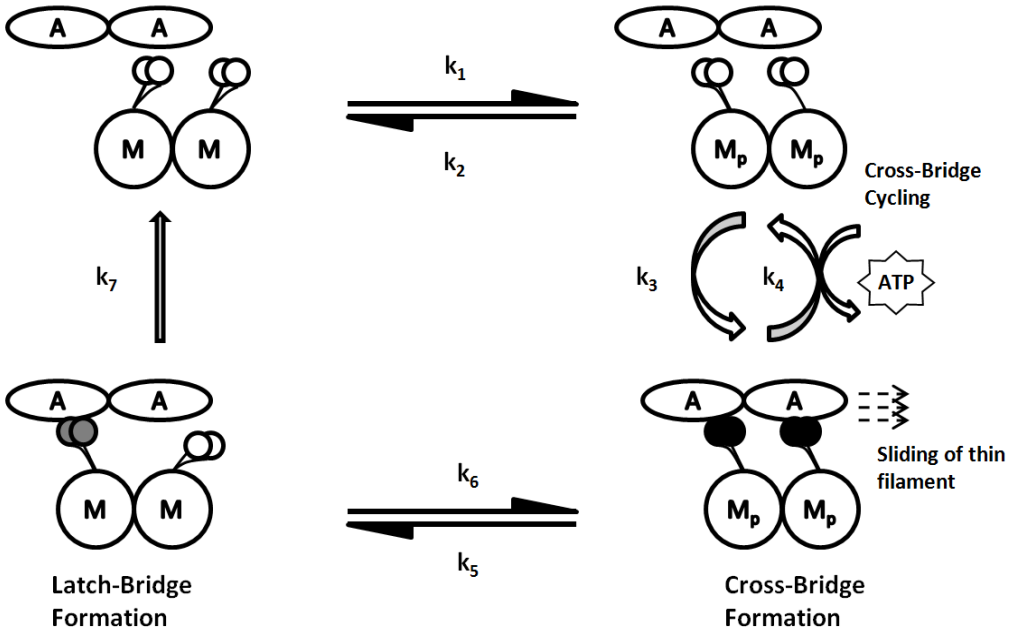

Figure 3.7 Hai and Murphy latch-bridge model for smooth muscle contraction. Fast cross-bridge cycle is governed by k_3 and k_4 while slow latch-bridge cycle is regulated by k_1, k_3, k_5 and k_7. Note that myosin phosphorylation is necessary for the formation of cross-bridges (AM_p) and latch-bridges (AM). A: actin binding site; M: unphosphorylated myosin; M_p: phosphorylated myosin. k_1 to k_7 are rate constants. (Source: Gajendiran and Buist, 2011)

A set of four linear ordinary differential equations can be derived from the model:

$$\frac{d[M]}{dt} = -k_1[M] + k_2[M_p] + k_7[AM] \tag{3.14}$$

$$\frac{d[M_p]}{dt} = k_4[AM_p] + k_1[M] - (k_2 + k_3)[M_p] \tag{3.15}$$

$$\frac{d[AM_p]}{dt} = k_3[M_p] + k_6[AM] - (k_4 + k_5)[AM_p] \tag{3.16}$$

$$\frac{d[AM]}{dt} = k_5[AM_p] - (k_6 + k_7)[AM] \tag{3.17}$$

In the original model, first-order chemical kinetics were assumed for all reactions, with the rate constants, except k_1 and k_6, remain unaltered during the course of

contraction. The myosin phosphorylation and dephosphorylation rates were hypothesised to be identical regardless of actin attachment, hence

$$k_1 = k_6 \tag{3.18}$$

$$k_2 = k_5. \tag{3.19}$$

Hai and Murphy (1988b) suggested a cross-bridge association-dissociation ratio of 4:1 which limits the maximum number of cross-bridges in steady-state to 80% of available myosin. Therefore,

$$k_3/k_4 = 4. \tag{3.20}$$

The model consists of two loops with different cycling speeds: a fast cycling cross-bridge loop which initiates filament sliding and muscle contractile force generation, and a slow dissociating latch-bridge loop which maintains muscle stiffness with an abated cycling rate and lower energy consumption (Huxley, 1957; Dillon *et al.*, 1981). Therefore, the rate of cross-bridge dissociation is far greater than that of the latch-bridges, such that

$$k_4 \gg k_7. \tag{3.21}$$

The model has been used to describe isometric contractions in swine carotid arterial smooth muscle and bovine tracheal smooth muscle (Kamm and Stull, 1985; Singer and Murphy, 1987). In the model, $k_1$and k_6 are time-dependent step functions which model the [Ca^{2+}] transient due to MLCK activation after stimulation. The authors assumed that both cross-bridges and latch-bridges contribute uniformly to contractile stress whose magnitude is proportional to [$AM + AM_p$].

Assessment of the latch-bridge model

A spatial description of smooth muscle cross-bridge cycle is lacking in the Hai and Murphy model. Therefore, it cannot simulate isotonic contractions or shortening velocity. Nevertheless, it introduces the concept of a latch-bridge and provides a comprehensive mathematical explanation of latch-bridge formation in smooth muscle contraction.

3.3.3 Modifications of the Hai and Murphy model

Greater availability of experimental data on smooth muscle physiology has lead to enhancements of the Hai and Murphy latch-bridge model. The modifications can be classified into two main categories: adoption of sliding filament theory, and improved representations of Ca^{2+}-driven MLC_{20} phosphorylation and dephosphorylation dynamics.

Adopting sliding filament theory

In a separate work, Hai and Murphy (1988a) inserted Huxley's formalism (Section 3.2.1) into their latch-bridge model. The original four species were condensed to two, namely attached myosin ($\widetilde{AM} = AM + AM_p$) and unattached myosin ($\widetilde{M} = M + M_p$). The rationale is that the net transaction between phosphorylated and dephosphorylated states is close to zero in steady-state due to a fast reaction speed. The simplification also facilitates the implementation of Huxley's formulation as follows [c.f. Equations (3.8) to (3.10)]:

$$A + \widetilde{M} \xrightarrow{f} \widetilde{AM} \tag{3.22}$$

$$\widetilde{AM} \xrightarrow{g} A + \widetilde{M}. \quad (3.23)$$

Similar to Huxley's model, the rate constants f and g are regulated by f_1, g_1 and g_2 according to Equations (3.11) to (3.13). However, instead of constant values, f_1, g_1 and g_2 are dependent on the latch-bridge model rate constants k_1 to k_7. The modified latch-bridge model can simulate the force-velocity relation of swine carotid arterial smooth muscle at distinct phosphorylation states, even though the result derivates from the hyperbola predicted by Hill's equation (Hill, 1938; Dillon and Murphy, 1982). However, the model should be credited as a smooth muscle equivalent to Huxley's model of striated muscle contraction.

Yu *et al* (1997) developed a non-isometric latch-bridge model which consisted of a contractile element and a passive serial element. The contractile element was driven by the four-state latch-bridge model with Huxley's formalism [Equations (3.22) and (3.23)] which produces active force while the passive element was modelled as a linear spring. The model was able to illustrate the availability of myosin as a result of changing muscle length which caused altered active force magnitudes in vascular and airway smooth muscles. Mijainovich *et al* (2000) adopted a similar approach to investigate the effect of cyclic length fluctuations on myosin binding in airway smooth muscle. Their model elucidated the features of hysteresis and elastic modulus in relation to myosin bond length.

Improved descriptions of myosin light chain phosphorylation and dephosphorylation dynamics

Influx of Ca^{2+} from extracellular space and the SR increases cytosolic [Ca^{2+}] upon stimulation of smooth muscle. Sufficient Ca^{2+} is then available to bind with calmodulin

(CaM) which in turn activates MLCK (Dillon *et al.*, 1981). MLCK phosphorylates MLC_{20} on the thick filament such that it can attach to the actin (thin) filament binding site and form a cross-bridge. In the latch-bridge model, the sequence of events is condensed to reactions driven by rate constants k_1 and k_6 (Figure 3.7). Investigators have sought to present a more detailed description of the aforementioned Ca^{2+}-driven MLC_{20} phosphorylation process.

In a uterine SMC excitation-contraction model, Bursxztyn *et al* (2007) suggested the MLCK reaction is rapid when intracellular calcium concentration ($[Ca^{2+}]_i$) increases but tapers off at high $[Ca^{2+}]_i$. Therefore, k_1 can be modelled by a sigmoid function driven by $[Ca^{2+}]_i$ as follows:

$$k_1(t) = \frac{\{[\mathrm{Ca}^{2+}]_\mathrm{i}(t)\}^n}{\left\{[\mathrm{Ca}^{2+}]_{\mathrm{i,1/2MLCK}}(t)\right\}^n + \{[\mathrm{Ca}^{2+}]_\mathrm{i}(t)\}^n} \tag{3.24}$$

where $[\mathrm{Ca}^{2+}]_{\mathrm{i,1/2MLCK}}$ is the $[Ca^{2+}]_i$ when half of MLCK is activated. $n = 8.7613$ is the Hill coefficient of MLCK activation.

Wang *et al* (2008) stimulated arterial and airway smooth muscle contractions by prescribing the contractile agonist 5-HT. The smooth muscles were also treated with caffeine so that their ryanodine receptors would be persistently open to allow modulation of $[Ca^{2+}]_i$. Both MLC_{20} phosphorylation and dephosphorylation processes were modelled from the experimental results. k_1 followed a sigmoidal function similar to Equation (3.24) with $n = 4$. The value was chosen as four Ca^{2+} ions are needed to form a catalytic calcium-calmodulin complex (Ca-CaM), which can activate MLCK for MLC_{20} phosphorylation (see Figure 3.8). k_2 is dependent on both $[Ca^{2+}]_i$ and an

agonist concentration. The model was later adopted for uterine smooth muscle analysis (Maggio *et al.*, 2012).

Recently, Gajendiran and Buist (2011) presented a biophysical model which explains the Ca^{2+}-dependent contraction of isolated GI SMC. The modified latch-bridge model has a separate module which describes the $[Ca^{2+}]_i$-dependent MLC_{20} phosphorylation process in detail (Figure 3.8). The model is capable of simulating rhythmic phasic contractions in GI SMC driven by an intracellular calcium signal. It would be interesting to see if a model of comparable detail describing the MLC_{20} dephosphorylation process can be developed for investigating GI SMC contraction.

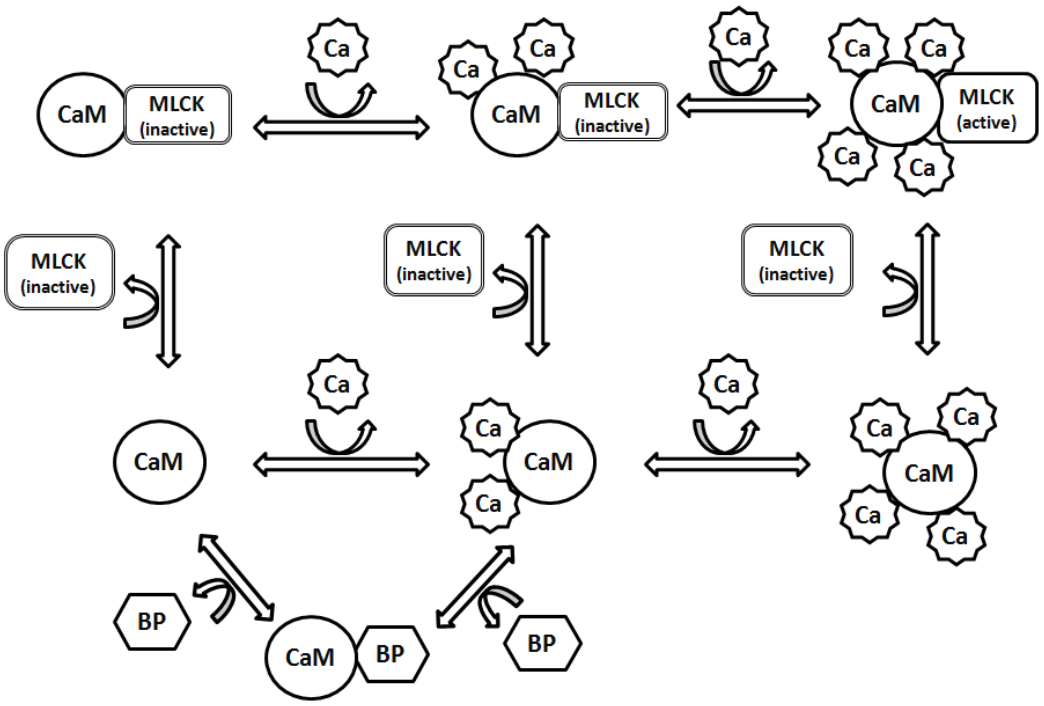

Figure 3.8 Illustration of GI SMC MLC_{20} phosphorylation in the Gajendiran and Buist (2011) model. The above reactions are formulated as a MLC_{20} phosphorylation module which supplements k_1 in the latch-bridge model. MLCK is activated only when four Ca^{2+} ions and CaM are bind to it (top right corner). CaM: calmodulin; MLCK: myosin light chain kinase; Ca: calcium ion; BP: binding protein. (Source: Gajendiran and Buist, 2011)

3.4 Integrated passive and active mechanics models

The task of merging both the passive and active smooth muscle mechanical properties into a single mathematical model is non-trivial. Two major approaches are popular among investigators, namely the Hill's model approach and the continuum mechanics approach.

3.4.1 Hill's equation and three-element model (Hill, 1938)

Hill's equation

Hill (1938) measured the energy released from a frog sartorius muscle undergoing isotonic shortening. He found that at a given temperature, the muscle contractile force (P) and shortening velocity (v) are related by

$$(P + a)(v + b) = (P_0 + a)b \tag{3.25}$$

where P_0 is the maximum isometric active force, a is the sum of activation or maintenance heat and energy generated from muscle shortening per unit of shortening distance, and b is the absolute energy release rate.

Application of Hill's equation to GI tissues

Equation (3.25) can be normalised with the sample initial cross-sectional area (A) and length (l) and relates contractile stress (σ) and strain rate ($\dot{\varepsilon}$) as shown below

$$\left(\frac{P + a}{A}\right)\left(\frac{v + b}{l}\right) = \left(\frac{P_0 + a}{A}\right)\frac{b}{l} \tag{3.26}$$

$$(\sigma + \tilde{a})\left(\dot{\varepsilon} + \tilde{b}\right) = (\sigma_0 + \tilde{a})\tilde{b} \tag{3.27}$$

where σ_0 is the maximum isometric active stress while $\tilde{a}$ and $\tilde{b}$ are the normalised Hill's equation parameters. We standardised the Hill's equation parameters from several different studies to the form shown in Equation (3.27). The corresponding standard errors were also calculated from the standard derivation or estimated from the experimental results. The normalised parameters for GI SMC and smooth muscle tissues are shown in Table 3.4.

Table 3.4 Modelling GI SMC and smooth muscle tissues isotonic shortening with Hill's equation. Hill's equation parameters (mean ± SE) are reported according to Equation (3.27). σ_0 is the maximum isometric active stress while $\tilde{a}$ and $\tilde{b}$ are the normalised Hill's equation parameters.

Species and organs	σ_0 (kPa)	$\tilde{a}/\sigma_0$	$\tilde{b}$ (s^{-1})	References
Toad gastric SMC	101 ± 44 [a]	0.394 ± 0.104	0.211 ± 0.049	Warshaw (1987)
Guinea-pig stomach circumferential muscle tissue [b]	319 ± 8	0.107 ± 0.008	0.056 ± 0.002	Moriya and Miyazaki (1982, 1985)
Guinea-pig stomach longitudinal muscle tissue [b]	188 ± 8	0.292 ± 0.025	0.056 ± 0.003	Moriya and Miyazaki (1982, 1985)
Cat duodenal circumferential muscle tissue [c]	42.2	0.146	0.035	Meiss (1971)
Canine colonic circumferential muscle tissue	259 ± 33	0.275 ± 0.040	0.0049 ± 0.0005	Gerthoffer *et al.* (1991)
Guinea-pig taenia coli tissue [c]	216	0.11	0.056	Mashima *et al.* (1979)

Species and organs	σ_0 (kPa)	$\tilde{a}/\sigma_0$	$\tilde{b}$ (s^{-1})	References
Skinned guinea-pig taenia coli tissue	108 ± 17	0.110 ± 0.013	0.015 ± 0.001	Arner (1982)
Rabbit taenia coli tissue	87.3 ± 10.8	0.331 ± 0.051	0.010 ± 0.001	Gordon and Siegman (1971)

[a] Mean and SE are calculated from maximum isometric active force and cell cross-sectional area. SE is computed by the method outlined by Meyer (1975).
[b] SE are computed from sample standard derivation (SD) and sample size (n) such that $SE = SD/\sqrt{n}$.
[c] Only mean values have been reported by the authors.

Hill's three-element model

Hill (1938) further suggested that an activated muscle's properties could be characterised by an 'undamped elastic element', and a 'damped element' which is governed by Equation (3.25), connected in series, while the mechanics of resting muscle is dominated by the elastic element. Subsequent models of muscle mechanics have been influenced by Hill's hypothesis. One of these frameworks is the Hill's three-element model shown in Figure 3.9 (Fung, 1993).

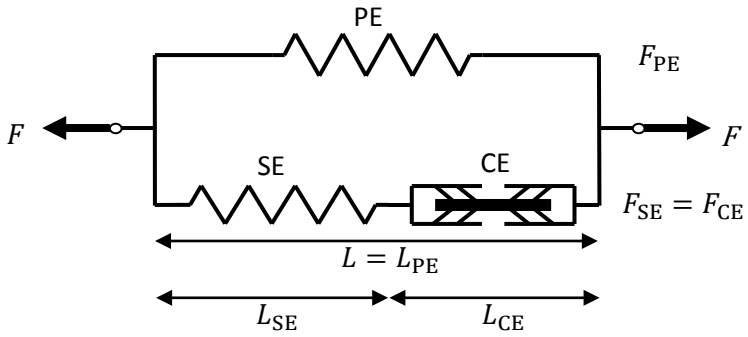

Figure 3.9 Hill's three-element model. PE, SE and CE indicate the parallel elastic, serial elastic and contractile elements respectively. F and L denote force and length.

Hill's model for muscle mechanics includes a contractile element (CE) and an elastic element (SE) connected in series, with another elastic element arranged in parallel

(PE) with the contractile-elastic series element. It was assumed that both SE and PE are passive while CE can generate active force spontaneously based on actin-myosin interactions. The arrangement of the elements closely resembles the biological structure of a striated muscle sarcomere (Fung, 1993). The governing equations of the three-element model relate the forces (F) and lengths (L) of different elements in the following manner:

$$F = F_{PE} + F_{SE} \tag{3.28}$$

$$F_{SE} = F_{CE} \tag{3.29}$$

$$L_{PE} = L_{SE} + L_{CE} \tag{3.30}$$

$$L = L_{PE} \tag{3.31}$$

In isotonic shortening, F is constant. From Equations (3.28) and (3.29), any change in F_{PE} is compensated by a corresponding adjustment of F_{SE} or F_{CE} and vice-versa. Conversely, L and L_{PE} are unchanged during isometric contraction. An alteration in L_{CE} is absorbed by a change in L_{SE} as shown by Equation (3.30).

Assessment of Hill's three-element model

The simplicity of Hill's model has drawn several comments from researchers. Specific to the single contractile-elastic connection in the model, Fung (1993) opined that the assumption of identical sarcomeres in a muscle tissue is not entirely valid. It is impossible to determine the correct proportions of strain allocated to the contractile element and serial elastic element. He suggested that the passive elastic elements should be replaced with viscoelastic ones to improve the resting muscle properties.

Nonetheless, the Hill's model is able to integrate the contractile component with the other non-contractile (passive) components found in muscle tissues. Although it was originally developed for striated muscle, it has been adopted by researchers in the field of smooth muscle mechanics with modifications as illustrated in the next section.

3.4.2 'Friction-clutch' model (Gestrelius and Borgström, 1986)

Hill's model provides a mathematical framework which has inspired the development of several smooth muscle biophysical models. Their structures and mechanisms are now introduced.

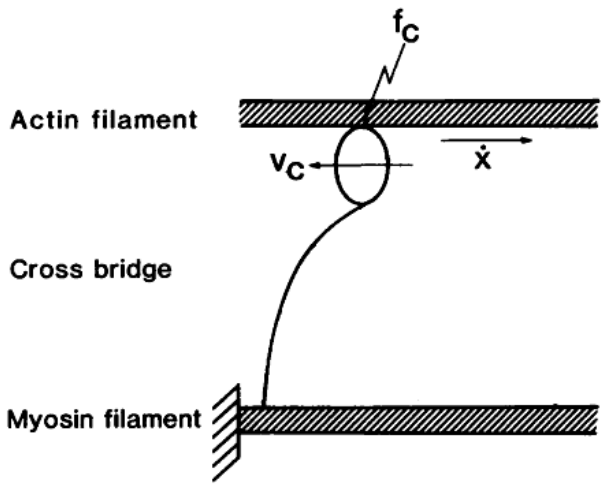

Figure 3.10 Illustration of 'friction clutch' mechanism. f_c: frictional interaction between myosin head and actin filament; v_c: mean velocity of cross-bridge; $\dot{x}$: smooth muscle shortening velocity. (Source: Gestrelius and Borgström, 1986)

Gestrelius and Borgström (1986) pioneered the use of a 'friction clutch' mechanism which accounts for the interaction or friction (f_c) between the myosin head and actin filament in a smooth muscle (Figure 3.10). Assuming that the attached cross-bridges move with a velocity v_c while the muscle shortens at a velocity $\dot{x}$, the active force of contractile component (F_{cc}) is

$$F_{cc} = n_c f_c(v_c + \dot{x}) \tag{3.32}$$

where n_c is the fraction of available cross-bridges during maximum contraction at an optimum muscle length.

The authors suggested that the 'friction clutch' mechanism represents the mean cross-bridge function which can be substituted into the mathematical description illustrated in Huxley's sliding filament model [Equations (3.8) to (3.13)]. Furthermore, the novel mechanism provides an initial explanation of the effect of slow latch-bridge cycling on smooth muscle contraction before the development of latch-bridge model (Hai and Murphy, 1988b). It can also demonstrate the maintenance of an isometric contractile force by compensating the decrement of v_c, which represents slow cycling rate, with a stronger actomyosin interaction f_c (Equation (3.32)).

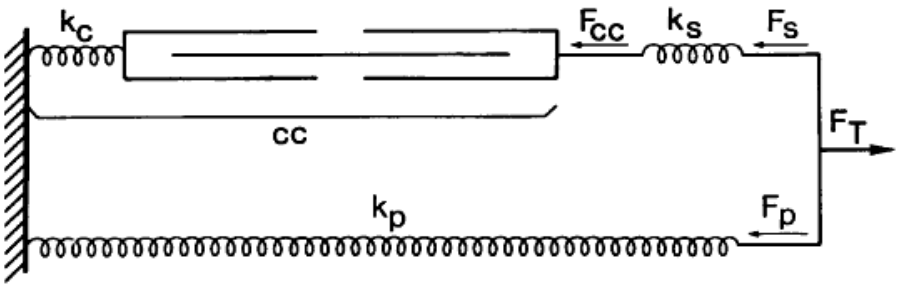

Figure 3.11 Configuration of Gestrelius and Borgström (1986) smooth muscle model. CC is the contractile component; k_c, k_s and k_p are the elastic moduli of cross-bridge, serial elastic component and parallel elastic component correspondingly; F_{cc}, F_s and F_p are the forces from contractile component, serial elastic component and parallel elastic component respectively; F_T is the aggregate smooth muscle force. (Source: Gestrelius and Borgström, 1986)

The overall configuration of Gestrelius and Borgström model is similar to that of Hill's framework (Figure 3.11). The contractile component consists of the 'friction clutch' serially connected to a linear spring, which describes the elasticity of attached cross-

bridges. Exponential models (see Equation (3.1)) have been employed to simulate the force-length relations in the parallel and serial elastic components.

Assessment of 'Friction-clutch' model

The model can reproduce several contractile phenomena in portal veins such as quick release experiments and cyclic loading at a finite strain. It can replicate the force-length relation found in periodic stretching of smooth muscle under Ca^{2+}-free conditions, even though the hysteresis loop is lacking. Nevertheless, the Gestrelius and Borgström model can be regarded as one of the earlier biophysical models that can demonstrate both passive and active smooth muscle mechanics.

3.4.3 Smooth muscle cell model (Yang *et al.*, 2003b)

Yang and co-workers (2003b) addressed the electrical-chemical-mechanical coupling of a stimulated SMC with their integrative model. The model is primarily divided into an electrochemical subsystem and a chemo-mechanical subsystem. The second subsystem contains a contractile kinetic model which computes the $[Ca^{2+}]_i$-dependent proportion of attached cross-bridges (AM_p) and latch-bridges (AM) using the Hai and Murphy framework (

Figure 3.7). However, the rate constant k_1 ($= k_6$) is dependent on [Ca-CaM].

The cell mechanics model, which is another component in the chemo-mechanical subsystem, resembles Hill's framework with a few modifications (Figure 3.12). The CE encompasses the force contributions from AM_p and AM elastic extensions, and AM_p-dependent contractile force generation. It is interesting to note that the computation of active force generated by AM_p in Yang's model incorporates the 'friction clutch' concept (see Equation (3.32)). Strain-dependent exponential factors are multiplied to

AM and AM_p force contributions. The exponential factors help to account for the change of force due to displacement from the optimum length at which the maximum overlap between actin and myosin filaments occurs. A Kelvin model (see Appendix A), which consists of an exponential elastic element arranged in parallel to a dashpot, is serially joined to the active force component for describing the nonlinear viscoelastic force. The parallel elastic component is also characterised by an exponential force-length function.

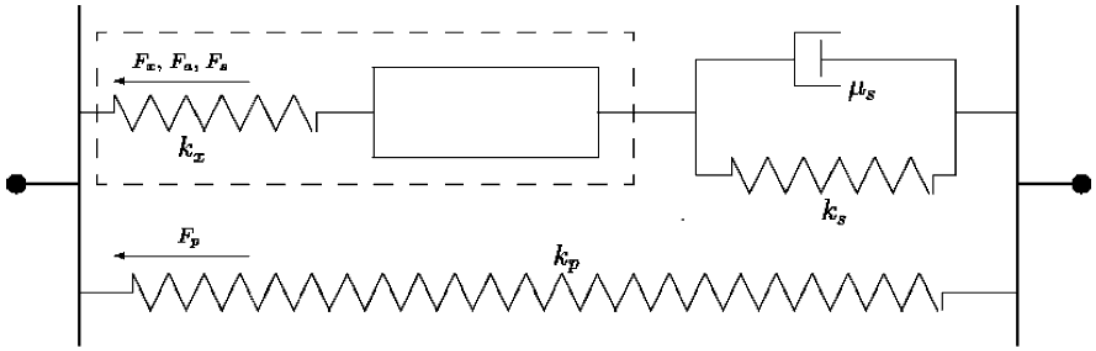

Figure 3.12 Structure of cell mechanics component in Yang *et al.* (2003b) SMC model. F, k and μ represent force, stiffness and coefficient of viscosity correspondingly. Subscripts x, a, s and p refer to cross-bridge elastic component, active force generation component, serial viscoelastic component and parallel elastic component respectively. (Source: Yang *et al.*, 2003b).

The model has been tested against results from length-force and force-velocity experiments performed on toad stomach SMC (Warshaw, 1987; Harris and Warshaw, 1991). The simulations agree with the experimental results, and Hill's equation in the case of force-velocity measurements. The SMC model has been integrated into a vascular wall tissue model which is used to investigate the vessel pressure-diameter relationship (Yang *et al.*, 2003a). The multi-scale model provides a biophysical platform to investigate the effect of Ca^{2+} transients on SMC contraction in relation to macroscopic vasomotor phenomena.

Assessment of the smooth muscle cell model

Yang's SMC model is the most comprehensive to date in characterising the electrical, chemical and mechanical properties as well as their inter-connections in activated SMC. With increased availability of SMC experimental data, the model can be improved with additional details to simulate other newly-discovered biophysical phenomena such as length adaptation.

3.4.4 Continuum mechanics models

Continuum mechanics is an alternative approach for developing mathematical models for smooth muscle mechanics. The models developed through the continuum methodology in accordance with frame invariance, and the degree of isotropy that the material is supposed to possess. In addition, upon successful derivation of one-dimensional continuum model, it can be scaled up to a planar or a three-dimensional description.

To simulate chemo-mechanical active force generation, investigators usually couple their models with the Hai and Murphy's latch-bridge framework (Hai and Murphy, 1988b). For instance, Stålhand *et al* (2008) derived a mechano-chemical finite strain model with a parallel configuration of an elastic element and a contractile element. The parallel elastic element denotes the cell stiffness while the contractile element computes the contractile force from a $[Ca^{2+}]$-dependent latch-bridge model. With this approach, the authors derived the strain energy function which is dependent on the chemical kinetics. The model has been further enhanced to a three-dimensional framework to study uniaxial extension of arterial smooth muscle (Stålhand *et al.*, 2011).

Kroon (2010) followed a similar approach and established a theoretical framework for smooth muscle mechanics by connecting a SLS model to an active element in parallel. The SLS component exhibits smooth muscle viscoelasticity while the active component is driven by cross-bridge cycling. The continuum model is able to demonstrate isometric contraction in swine carotid arterial smooth muscle and isotonic shortening in skinned guinea-pig taenia coli tissue (Arner, 1982; Kamm *et al.*, 1989). It has been modified to investigate the effect of myosin filament orientations on contractile stress during uniaxial stretching (Kroon, 2011). The author concluded that there is a limited difference in muscle stress whether the myosin filaments are heterogeneously oriented or preferentially aligned to stretching direction.

3.5 Length adaptation models

Despite the short history of length adaptation, several mathematical models have been suggested to describe this smooth muscle phenomenon. The length adaptation models are simplistic in nature but they adhere to the available experimental evidence.

3.5.1 Variable contractile element model (Lambert *et al.*, 2004)

Lambert *et al* (2004) proposed a smooth muscle model that has a contractile element within which N $(= N_s \times N_p)$ contractile units are contained. N_s contractile units are joined end-to-end to form a chain while N_p chains are connected in parallel in the contractile element. Each contractile unit can generate an active force which is proportional to the overlap of actin and myosin elements. It was assumed that greatest active force is generated by a maximum overlap, which occurs when the smooth muscle is fully adapted to a new length.

The model is able to demonstrate the maintenance of maximum contractile force when the smooth muscle is deformed to a new length (Seow *et al.*, 2000). The variation in thick and thin filaments overlapping is compensated by the change of N_s and N_p in the model. Such parallel-to-series reconfiguration of contractile units has been observed in porcine and canine tracheal smooth muscles (Kuo *et al.*, 2003). The model can also illustrate the growth of compliance, shortening velocity and power as muscle length increases (Pratusevich *et al.*, 1995; Kuo *et al.*, 2003).

Assessment of variable contractile element model

The previous model is able to demonstrate structural and mechanical properties relating to length adaptation. However, the mechanism through which these properties are redeveloped after a length alteration in smooth muscle is unexplained. Actin polymerisation dynamics has been postulated to be involved in length adaptation but this has been excluded from the model (Bednarek *et al.*, 2011).

3.5.2 Stochastic filament network model (Silveira *et al.*, 2005)

The stochastic model contains numerous links which are connected between nodes in a regular grid (Figure 3.13). The links symbolise stress fibres and contractile filaments while the nodes represent the dense plaques that are found in SMC. The authors suggested the connected grid can be taken as a filament network in a section of SMC, in a whole SMC or in a smooth muscle consisting of many connected SMC working as a syncytium.

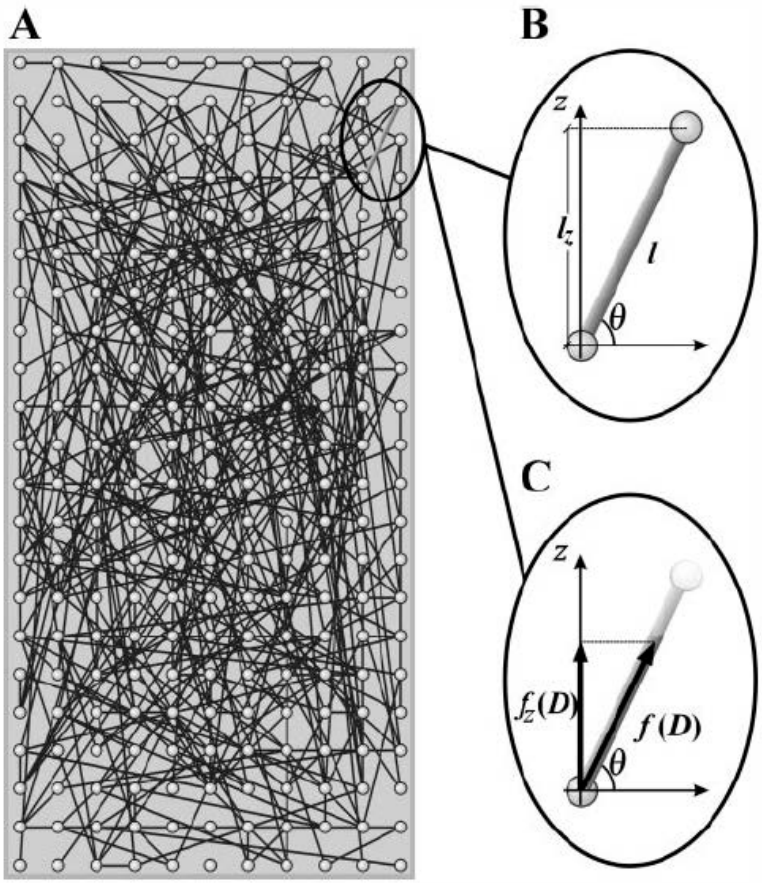

Figure 3.13 Schematic of stochastic filament network model.(A) Nodes are arranged in regular lattice and represent smooth muscle dense plaques. Links of variable lengths are connected to the nodes and symbolise stress fibres or contractile filaments. B and C: Link length, l, and contractile force, $f(D)$, are resolved in the longitudinal (z) direction and the resulting magnitudes are l_z and $f_z(D)$ respectively. D is the ratio of current link length to optimal link length. Maximum contractile force occurs when $D = 1$. θ is the angle between l or $f(D)$with the transverse direction. (Source: Silveira *et al.*, 2005)

The model can simulate molecular processes including filament polymerisation, rupture and deformation. The filament formation probability is directly proportional to the availability of unconnected contractile units and the activation state, but inversely related to the distance between nodes. The filament breakage probability decays over time after a change in the muscle activation state, which suggests that the filament network is increasingly robust over time. Filament lengthening and shortening vary with the contractile force.

Assessment of stochastic filament network model

The main contribution of the model is its capability in illustrating the dynamics of active force recovery under stimulation after a length change, in addition to the shift of the force-length curve during length adaptation (Wang *et al.*, 2001). The model allows link formation of different lengths in two-dimensional space, which is more realistic than the one-dimensional configuration of uniform contractile units used in the Lambert *et al.* (2004) model. However, the stochastic filament network model does not separate the contribution of passive tension components, such as cytoskeleton, from that of the active contractile elements.

3.6 Concluding remarks

Previous efforts in constructing smooth muscle mechanics model have centred on first constructing and then integrating the passive and active components. However, the current models are limited in terms of their ability in demonstrating major mechanical phenomena. The rigid model structures also hinder them from including new experimental observation such as length adaptation.

The challenge is to build a generalised model framework which can accommodate different nonlinear stress-strain relations observed in resting and contracted smooth muscle cells and tissues. The new model should also be able to describe the dynamic nature of smooth muscle mechanical properties.

Chapter 4 Nonlinear Viscoelastic Solid

4.1 Overview

GI smooth muscle material properties are closely related to physiology and pathophysiology of the alimentary canal. Essential digestive processes, such as mixing and transportation, are closely related to GI motility which is generated by the GI smooth muscle. Alteration of GI smooth muscle stiffness is also linked with several GI diseases (Table 1.3). Furthermore, the stress-strain relation of GI smooth muscle is highly nonlinear (Figure 3.2). The physiological working range of GI smooth muscle is beyond the quasi-linear region which is near zero strain. Overall, quantifying the nonlinear viscoelasticity of GI smooth muscle is important to understand the GI tissue physiology and pathophysiology.

Various mathematical models have been suggested by investigators to describe the passive mechanical properties of smooth muscle. Empirical expressions, such as the exponential and power-law structural damping models, have been created to describe a subset of viscoelastic phenomena but they cannot simulate any feature outside of their domains. Linear viscoelastic models are by far the most versatile. The constitutive equations of these models, derived by either relating stress and strain and their higher order time derivatives or integrating over the relaxation spectrum multiplied by a strain measure, can be ascertained in a relatively straight forward manner and solved to describe different stress or strain perturbation scenarios. Complications arise when numerous components are needed to properly represent the desired material properties (Lakes, 1999). These shortcomings motivate the

development of a novel mathematical model to describe smooth muscle viscoelasticity.

Among the linear viscoelastic models, the SLS model (Figure 3.4), also known as the Zener model, has been widely employed because of its simplicity and its ability to replicate many linear viscoelastic phenomena (Nagayama *et al.*, 2007). However, its ability to describe the nonlinear viscoelastic phenomena that are often observed in biological tissues is limited. Previous studies have postulated the idea of including nonlinear elastic components into the SLS framework to better describe material nonlinearities. For instance, investigators were able to model some of the biomechanical properties of smooth muscle and cardiac muscle by replacing the serial or parallel linear spring in the SLS with a nonlinear one (Sonnenblick, 1964; Yin and Fung, 1971). The proponents of the power law models have also proposed that the fluid component may also be non-Newtonian in such materials (Tsai *et al.*, 1993; Fabry *et al.*, 2001). Overall, these modifications were applied only on the elastic components while there is no published attempt to implement non-linear dashpot in the SLS.

To allow for the inclusion of such complexities while maintaining the compactness of the SLS framework, the stress-strain relationships of the individual SLS model components have been generalised here. The resulting formulation is termed the nonlinear viscoelastic solid model (NVS) and provides significant flexibility in terms of representing nonlinear viscoelastic behaviour, while keeping conceptual and computational complexity to a minimum.

The mathematical derivation of NVS is introduced in the next section. A tri-linear NVS model is then developed to show that the SLS is a special case of NVS.

Subsequently, various NVS variants which possess a mixture of linear and nonlinear components are illustrated with their constitutive equations. They are then applied to describe the nonlinear viscoelastic properties of GI smooth muscle. Finally, the NVS formalism is extended to accept piecewise constitutive relations. The development enables it to properly describe muscle compression.

4.2 Model development

4.2.1 NVS constitutive equation

The SLS model consists of two springs, whose contributions to stress (σ) are linear functions of strain (ε), and a dashpot, whose contribution to stress is a linear function of the strain rate ($\dot{\varepsilon}$). Here, a generalisation of these components is proposed whereby the linearity constraint is removed allowing the substitution of nonlinear stress-strain and stress-strain rate relations as illustrated in Figure 4.1.

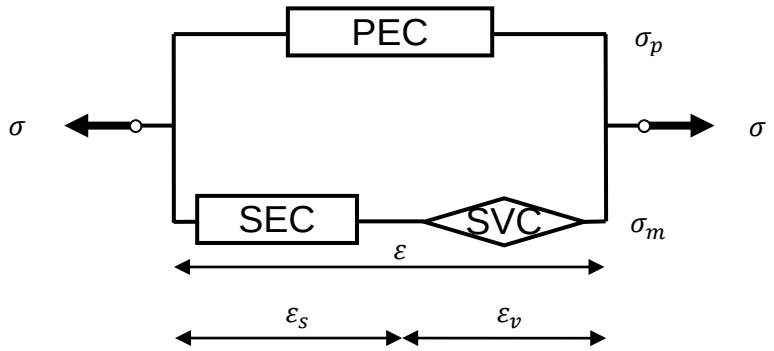

Figure 4.1 Illustration of NVS. The model consists of a parallel elastic component (PEC), a series elastic component (SEC) and a series viscous component (SVC). The configuration is identical to that of the SLS model when linear springs are used for the PEC and SEC, and a linear dashpot is used for the SVC. The SEC and SVC are serially connected and termed a Maxwell element. σ and ε represent stress and strain while subscripts p, s, v and m indicate the quantities belonging to the PEC, the SEC, the SVC and the Maxwell element.

The parallel and serial springs are termed the parallel elastic component (PEC) with subscript p, and serial elastic component (SEC) with subscript s, respectively, while

the dashpot is termed the serial viscous component (SVC) with subscript v as shown in Figure 4.1.The general stress-strain relationships for these three components can be written as

$$\sigma_p = f(\varepsilon_p) = f_p \tag{4.1}$$

$$\sigma_s = f(\varepsilon_s) = f_s \tag{4.2}$$

$$\sigma_v = f(\dot{\varepsilon}_v) = f_v. \tag{4.3}$$

The combination of the SEC and SVC in series forms what is commonly known as a Maxwell element and is denoted here by the *m* subscript. The following constraints apply to the system,

$$\sigma = \sigma_p + \sigma_m \tag{4.4}$$

$$\sigma_m = \sigma_s = \sigma_v \tag{4.5}$$

$$\varepsilon_m = \varepsilon_s + \varepsilon_v \tag{4.6}$$

$$\varepsilon = \varepsilon_p = \varepsilon_m. \tag{4.7}$$

Equations (4.1) to (4.7) can be used to derive a governing equation for the generalised system using the procedure outlined below. Differentiating Equations (4.1) and (4.2) with respect to time gives

$$\dot{\sigma}_p = \frac{d}{dt}(\sigma_p) = \frac{df_p}{d\varepsilon_p}\frac{d\varepsilon_p}{dt} = \frac{df_p}{d\varepsilon_p}\dot{\varepsilon}_p \tag{4.8}$$

$$\dot{\sigma}_s = \frac{d}{dt}(\sigma_s) = \frac{df_s}{d\varepsilon_s}\frac{d\varepsilon_s}{dt} = \frac{df_s}{d\varepsilon_s}\dot{\varepsilon}_s. \tag{4.9}$$

Next, differentiating Equation (4.6) with respect to time and substituting into Equation (4.9) gives

$$\dot{\varepsilon}_m = \dot{\varepsilon}_s + \dot{\varepsilon}_v = \frac{\dot{\sigma}_s}{\left(\frac{df_s}{d\varepsilon_s}\right)} + \dot{\varepsilon}_v. \tag{4.10}$$

Rearranging Equation (4.10) and using Equation (4.7) then gives

$$\frac{df_s}{d\varepsilon_s}\dot{\varepsilon} = \dot{\sigma}_s + \frac{df_s}{d\varepsilon_s}\dot{\varepsilon}_v. \tag{4.11}$$

Differentiating Equation (4.4) with respect to time and using Equation (4.5) gives

$$\dot{\sigma} = \dot{\sigma}_p + \dot{\sigma}_m = \dot{\sigma}_p + \dot{\sigma}_s. \tag{4.12}$$

Substituting the right hand side of Equation (4.12) with Equation (4.8) and rearranging gives

$$\dot{\sigma}_s = \dot{\sigma} - \frac{df_p}{d\varepsilon_p}\dot{\varepsilon}_p. \tag{4.13}$$

Next, substituting Equation (4.13) into (4.11) and rearranging gives

$$\dot{\sigma} = \frac{df_s}{d\varepsilon_s}\dot{\varepsilon} + \frac{df_p}{d\varepsilon_p}\dot{\varepsilon}_p - \frac{df_s}{d\varepsilon_s}\dot{\varepsilon}_v. \tag{4.14}$$

From Equation (4.7),

$$\dot{\sigma} = \frac{df_s}{d\varepsilon_s}\dot{\varepsilon} + \frac{df_p}{d\varepsilon_p}\dot{\varepsilon} - \frac{df_s}{d\varepsilon_s}\dot{\varepsilon}_v \tag{4.15}$$

$$= \left(\frac{df_s}{d\varepsilon_s} + \frac{df_p}{d\varepsilon_p}\right)\dot{\varepsilon} - \frac{df_s}{d\varepsilon_s}\dot{\varepsilon}_v \tag{4.16}$$

$$= \frac{df_p}{d\varepsilon_p}\dot{\varepsilon} + \frac{df_s}{d\varepsilon_s}(\dot{\varepsilon} - \dot{\varepsilon}_v) \tag{4.17}$$

which is the governing equation for the NVS model. An alternate rearrangement can provide a more compact form

$$\dot{\sigma} = \frac{df_p}{d\varepsilon_p}\dot{\varepsilon} + \frac{df_s}{d\varepsilon_s}\dot{\varepsilon}_s. \tag{4.18}$$

However, the form in Equation (4.16) appears to be the most amenable to practical application where the functions in Equations (4.1)-(4.3) are provided. From Equation (4.7), $\varepsilon = \varepsilon_p$, meaning that the evaluation of the derivative of f_p is trivial. To evaluate the derivative of f_s, Equations (4.4) & (4.5) can be employed to give $\sigma_s = \sigma - \sigma_p$, which can be used to describe f_s in terms of σ and ε. To evaluate $\dot{\varepsilon}_v$, one can use Equations (4.3)-(4.5) with Equation (4.16) to get

$$\dot{\varepsilon}_v = f_v^{-1} = g(\sigma_v) = g\big(\sigma - \sigma_p\big). \tag{4.19}$$

However, this adds the restriction that f_v must be invertible. The equivalent derivation for the alternate three parameter solid configuration that is also commonly termed the SLS is provided in Appendix B for completeness (Flügge, 1967).

Viscoelastic materials possess behavioural features that include stress relaxation, creep and hysteresis (Fung, 1993; Lakes, 1999). These are commonly quantified using models such as the SLS or a power-law (Nagayama *et al.*, 2007; Liu and Qi,

2010). Here, the mathematical expressions describing these major features are developed using the NVS model.

4.2.2 Response of NVS under various loading conditions

Isokinetic loading

Sawtooth loading describes a series of isokinetic segments whereby a sample is extended and then shortened with a constant strain rate. This type of loading is sometimes used as a way to precondition a viscoelastic material before an experiment (Fung, 1993). The applied strain rate, k, and resulting strain for one isokinetic segment can be described as

$$\dot{\varepsilon}(t) = k, t \geq 0 \tag{4.20}$$

$$\varepsilon(t) = kt, t \geq 0. \tag{4.21}$$

Substituting Equations (4.19) & (4.20) into Equation (4.16) gives the isokinetic governing equation.

$$\dot{\sigma} = \left(\frac{df_s}{d\varepsilon_s} + \frac{df_p}{d\varepsilon_p}\right)k - \frac{df_s}{d\varepsilon_s}g(\sigma - \sigma_p). \tag{4.22}$$

When $k > 0$, the sample is being extended. Conversely, $k < 0$ can be used to describe the shortening phase.

Isometric loading

Stress relaxation occurs when the stress in a viscoelastic material diminishes while it is held in an isometric configuration. Such a situation is often described by an instantaneous step change in strain at the initial time, followed by an extended period

of constant strain. Here it is assumed that the NVS is deformed in the following manner:

$$\varepsilon(t) = \varepsilon_0 H(t) \tag{4.23}$$

where $H(t)$ is the Heaviside step function and ε_0 is the magnitude of the applied strain. As a result,

$$\dot{\varepsilon}(t) = 0, t \neq 0. \tag{4.24}$$

The step transition at $t = 0$ causes the PEC and SEC to deform instantaneously, while the SVC adapts slowly (Fung, 1993). The initial instantaneous stress is therefore given by

$$\sigma_0 = \sigma_p(\varepsilon_0) + \sigma_s(\varepsilon_0) = \sigma_{p0} + \sigma_{s0} \tag{4.25}$$

where the 0 subscripts indicate the stress and strain quantities at the initial time after the step. Substituting Equations (4.19) & (4.24) into Equation (4.16) produces an expression for the stress relaxation response of the NVS given the initial condition provided by Equation (4.25),

$$\dot{\sigma} + \frac{df_s}{d\varepsilon_s} g\left(\sigma - \sigma_{p0}\right) = 0. \tag{4.26}$$

Isotonic loading

Creep is observed when a viscoelastic material continues to extend under a constant applied stress. A step increment in stress of magnitude σ_0 at time $t = 0$ can be written as

$$\sigma(t) = \sigma_0 H(t). \tag{4.27}$$

For $t \neq 0$, the stress rate is then given by

$$\dot{\sigma}(t) = 0, t \neq 0. \tag{4.28}$$

The initial strain and stress are again related by Equation (4.25). Substituting Equations (4.19) & (4.28) into Equation (4.16) gives an expression for the rate of change of strain during an isotonic extension with the initial condition in Equation (4.25),

$$\dot{\varepsilon} = \frac{df_s}{d\varepsilon_s} g(\sigma_0 - \sigma_p) \Big/ \left(\frac{df_s}{d\varepsilon_s} + \frac{df_p}{d\varepsilon_p} \right). \tag{4.29}$$

4.3 NVS model variants

4.3.1 NVS with linear components

With reference to NVS configuration in Figure 4.1, it can be shown that if linear functions are chosen for the three components then the model can be readily simplified to the original SLS governing equation. In this case the following constitutive equations are appropriate, where $F, E, M \in R^+$.

$$\sigma_p = F\varepsilon_p = f_p \tag{4.30}$$

$$\sigma_s = E\varepsilon_s = f_s \tag{4.31}$$

$$\sigma_v = M\dot{\varepsilon}_v = f_v. \tag{4.32}$$

Derivatives of σ_p and σ_s with respect to the relevant strains can be obtained from Equations (4.30) & (4.31) as

$$\frac{d\sigma_p}{d\varepsilon_p} = \frac{df_p}{d\varepsilon_p} = F \tag{4.33}$$

$$\frac{d\sigma_s}{d\varepsilon_s} = \frac{df_s}{d\varepsilon_s} = E. \tag{4.34}$$

Rearranging Equation (4.32) and using the results from Equations (4.4) & (4.5) gives

$$\dot{\varepsilon}_v = \frac{\sigma_v}{M} = \frac{\sigma - \sigma_p}{M}. \tag{4.35}$$

Substituting Equations (4.7) & (4.30) into Equation (4.35) produces

$$\dot{\varepsilon}_v = \frac{\sigma - F\varepsilon_p}{M} = \frac{\sigma - F\varepsilon}{M}. \tag{4.36}$$

Substituting Equations (4.33), (4.34) & (4.36) into Equation (4.16) and rearranging gives

$$\dot{\sigma} + \frac{E}{M}\sigma = (E + F)\dot{\varepsilon} + \frac{EF}{M}\varepsilon. \tag{4.37}$$

Equation (4.37) is the governing equation of NVS with three linear elements and is also identical to the SLS governing equation, shown previously in Equation (3.5). The result shows that the SLS is a special case of the NVS model.

4.3.2 NVS with exponential components

The versatility of the NVS allows a variety of nonlinear components to be included in its framework. To illustrate this point, a NVS variant with exponential elastic and

viscous components is introduced in this section. Similar derivation steps can be applied to develop other NVS models with different components.

The rationale for selecting exponential components is twofold. Firstly, exponential functions haven been previously adopted by other investigators to describe the uniaxial stress-strain relations of cardiac, ureteral and striated muscle tissues (Yin and Fung, 1971; Fung, 1993; Kirton *et al.*, 2004). Stomach tissues, which undergo large uniaxial extensions, also experience an exponential increase in their elastic moduli (Zhao *et al.*, 2008a). Secondly, experiments performed on human neutrophils showed that cytoplasmic viscosity varies with shear rate in a power law manner (Tsai *et al.*, 1993). The results suggested that the cytoplasm is non-Newtonian with a nonlinear shear stress-shear rate relation. Although the evidence is not directly related to viscoelastic effect, the notion implies that a nonlinear viscous component, such as exponential SVC, is appropriate for describing cell and tissue viscoelasticity.

If it is assumed that the stress in each of the three components of the NVS model varies exponentially with strain or strain rate, the following constitutive equations can be applied

$$\sigma_p = \beta\left[\exp\left(\alpha\varepsilon_p\right) - 1\right] = f_p \tag{4.38}$$

$$\sigma_s = \delta[\exp(\gamma\varepsilon_s) - 1] = f_s \tag{4.39}$$

$$\sigma_v = \mu[\exp(\lambda\dot{\varepsilon}_v) - 1] = f_v \tag{4.40}$$

where $\alpha, \beta, \gamma, \delta, \lambda, \mu \in R^+$. Differentiating Equation (4.38) and applying Equation (4.7) gives

$$\frac{d\sigma_p}{d\varepsilon_p} = \frac{df_p}{d\varepsilon_p} = \alpha\beta \exp\left(\alpha\varepsilon_p\right) = \alpha\beta \exp(\alpha\varepsilon). \tag{4.41}$$

Similarly, differentiating Equation (4.39) gives

$$\frac{d\sigma_s}{d\varepsilon_s} = \frac{df_s}{d\varepsilon_s} = \gamma\delta \exp(\gamma\varepsilon_s). \tag{4.42}$$

Multiplying Equation (4.39) by γ and rearranging gives

$$\gamma\delta \exp(\gamma\varepsilon_s) = \gamma(\delta + \sigma_s). \tag{4.43}$$

Substituting Equation (4.43) into Equation (4.42) eliminates ε_s,

$$\frac{df_s}{d\varepsilon_s} = \gamma(\delta + \sigma_s). \tag{4.44}$$

Inserting Equations (4.4), (4.5), (4.7) & (4.38) into Equation (4.44) gives

$$\frac{df_s}{d\varepsilon_s} = \gamma\{\delta + \sigma - \beta[\exp(\alpha\varepsilon) - 1]\}. \tag{4.45}$$

To obtain $\dot{\varepsilon}_v$, f_v from Equation (4.40) can be inverted to produce

$$\dot{\varepsilon}_v = {f_v}^{-1} = \frac{1}{\lambda} \ln\left(1 + \frac{\sigma_v}{\mu}\right). \tag{4.46}$$

Then, using Equations (4.4), (4.5), (4.7) & (4.38) and rearranging gives

$$\dot{\varepsilon}_v = \frac{1}{\lambda} \ln\left(1 + \frac{\sigma - \beta[\exp(\alpha\varepsilon) - 1]}{\mu}\right). \tag{4.47}$$

Substituting Equations (4.41), (4.45) & (4.47) into Equation (4.17) gives the governing equation for the tri-exponential NVS model.

$$\dot{\sigma} = \alpha\beta \exp(\alpha\varepsilon)\dot{\varepsilon} + \gamma\{\delta + \sigma - \beta[\exp(\alpha\varepsilon) - 1]\} \times \left[\dot{\varepsilon} - \frac{1}{\lambda} \ln\left(1 + \frac{\sigma - \beta[\exp(\alpha\varepsilon) - 1]}{\mu}\right)\right]. \quad (4.48)$$

4.3.3 Other NVS model variants

In addition to all-linear (SLS) and all-exponential models, NVS can accommodate sets of heterogeneous components. Therefore, models with one or two exponential components can be developed by replacing the linear parts in SLS (Equations (4.30) to (4.32)) with exponential ones (Equations (4.38) to (4.40)), respectively. The governing equations of these models can be derived by following the procedure illustrated in Sections 4.3.1 and 4.3.2. Table 4.1 lists the constitutive equations of NVS models with different PEC-SEC-SVC combinations.

Table 4.1 Constitutive equations of NVS model variants.

Models (PEC-SEC-SVC) [a]	Equations	
lin-lin-lin	$\dot{\sigma} = F\dot{\varepsilon} + E\left(\dot{\varepsilon} - \frac{\sigma - F\varepsilon}{M}\right)$	(4.49)
exp-lin-lin	$\dot{\sigma} = \alpha\beta \exp(\alpha\varepsilon)\dot{\varepsilon} + E\left\{\dot{\varepsilon} - \frac{\sigma - \beta[\exp(\alpha\varepsilon) - 1]}{M}\right\}$	(4.50)
lin-exp-lin	$\dot{\sigma} = F\dot{\varepsilon} + \gamma(\delta + \sigma - F\varepsilon)\left(\dot{\varepsilon} - \frac{\sigma - F\varepsilon}{M}\right)$	(4.51)
lin-lin-exp	$\dot{\sigma} = F\dot{\varepsilon} + E\left[\dot{\varepsilon} - \frac{1}{\lambda} \ln\left(1 + \frac{\sigma - F\varepsilon}{\mu}\right)\right]$	(4.52)

Models (PEC-SEC-SVC) [a]	Equations	
lin-lin-pow	$\dot{\sigma} = F\dot{\varepsilon} + E\left[\dot{\varepsilon} - \left(\frac{\sigma - F\varepsilon}{b}\right)^{\frac{1}{a}}\right]$	(4.53)
exp-exp-lin	$\dot{\sigma} = \alpha\beta\,\exp(\alpha\varepsilon)\dot{\varepsilon} + \gamma\{\delta + \sigma - \beta[\exp(\alpha\varepsilon) - 1]\} \times \left[\dot{\varepsilon} - \frac{\sigma - \beta[\exp(\alpha\varepsilon) - 1]}{M}\right]$	(4.54)
exp-lin-exp	$\dot{\sigma} = \alpha\beta\,\exp(\alpha\varepsilon)\dot{\varepsilon} + E\left[\dot{\varepsilon} - \frac{1}{\lambda}\ln\left(1 + \frac{\sigma - \beta[\exp(\alpha\varepsilon) - 1]}{\mu}\right)\right]$	(4.55)
lin-exp-exp	$\dot{\sigma} = F\dot{\varepsilon} + \gamma(\delta + \sigma - F\varepsilon)\left[\dot{\varepsilon} - \frac{1}{\lambda}\ln\left(1 + \frac{\sigma - F\varepsilon}{\mu}\right)\right]$	(4.56)
exp-lin-pow	$\dot{\sigma} = \alpha\beta\,\exp(\alpha\varepsilon)\dot{\varepsilon} + E\left(\dot{\varepsilon} - \left\{\frac{\sigma - \beta[\exp(\alpha\varepsilon) - 1]}{b}\right\}^{\frac{1}{a}}\right)$	(4.57)
lin-exp-pow	$\dot{\sigma} = F\dot{\varepsilon} + \gamma(\delta + \sigma - F\varepsilon)\left[\dot{\varepsilon} - \left(\frac{\sigma - F\varepsilon}{b}\right)^{\frac{1}{a}}\right]$	(4.58)
exp-exp-pow	$\dot{\sigma} = \alpha\beta\,\exp(\alpha\varepsilon)\dot{\varepsilon} + \gamma\{\delta + \sigma - \beta[\exp(\alpha\varepsilon) - 1]\} \times \left(\dot{\varepsilon} - \left\{\frac{\sigma - \beta[\exp(\alpha\varepsilon) - 1]}{b}\right\}^{\frac{1}{a}}\right)$	(4.59)
exp-exp-exp	$\dot{\sigma} = \alpha\beta\,\exp(\alpha\varepsilon)\dot{\varepsilon} + \gamma\{\delta + \sigma - \beta[\exp(\alpha\varepsilon) - 1]\} \times \left[\dot{\varepsilon} - \frac{1}{\lambda}\ln\left(1 + \frac{\sigma - \beta[\exp(\alpha\varepsilon) - 1]}{\mu}\right)\right]$	(4.60)

[a] lin: linear component; exp: exponential component; pow: power-law component.

Experiments performed on human neutrophils have shown that cytoplasmic viscosity varies with shear rate in a power law manner (Tsai *et al.*, 1993). Thus, it is plausible that the SVC could be modelled with a power function such that

$$\sigma_v = b(\dot{\varepsilon}_v)^a. \tag{4.61}$$

The governing equations of NVS models with power-law SVC, namely the *lin-lin-pow*, *exp-lin-pow*, *lin-exp-pow* and *exp-exp-pow* models, are also included in Table 4.1

4.4 Modelling GI tissue viscoelasticity

4.4.1 Cyclic stretching of porcine gastric tissue

Zhao and co-workers (2008a) harvested five porcine stomachs and investigated their viscoelastic properties. From three different locations, namely the fundus, the corpus and the antrum, they excised tissue strips parallel to the longitudinal or the circumferential direction of the stomach. Each tissue strip underwent three loading-unloading cycles with amplitude 0.532 (engineering strain) at an average strain rate of 0.0161 s^{-1} in a non-activated state. Figure 4.2 (black broken lines) shows the result for fundus tissue being stretched in the circumferential direction of the stomach.

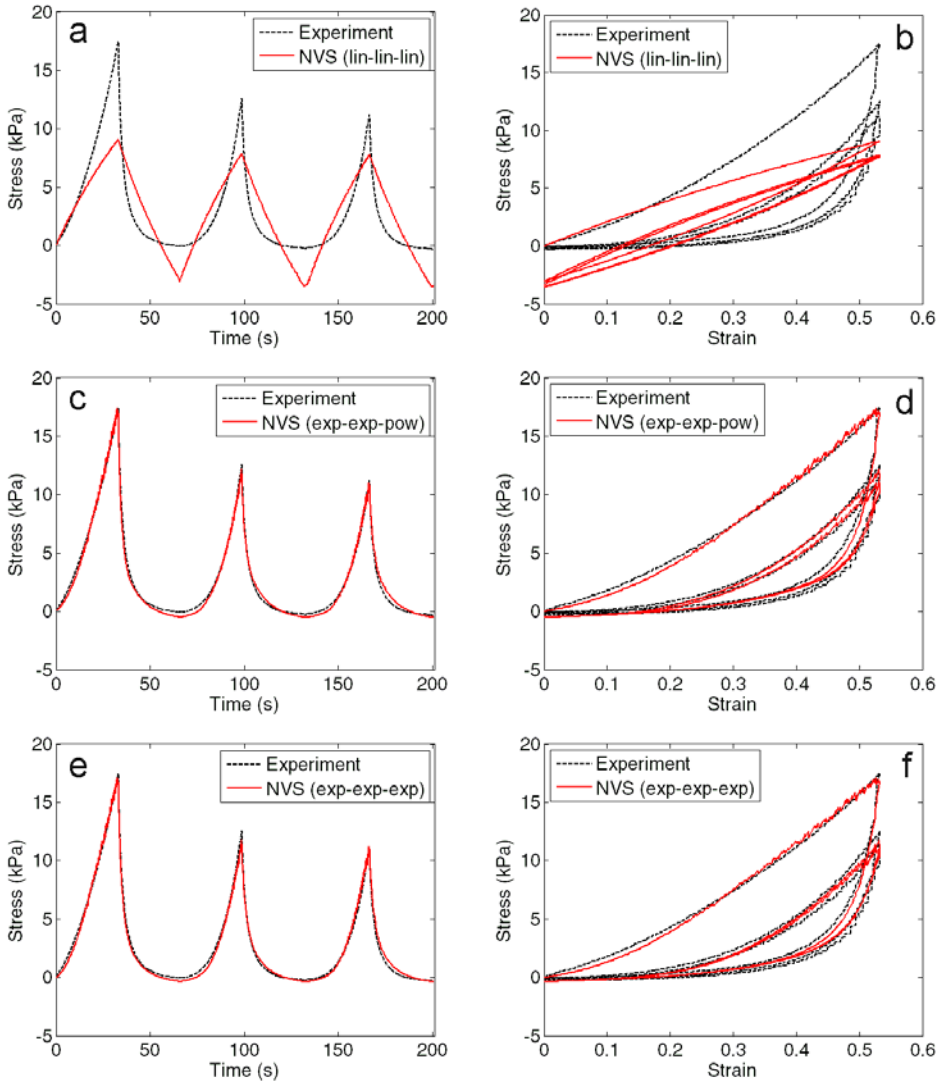

Figure 4.2 Modelling the cyclic extension of porcine fundus tissue using NVS. The tissue strip was excised parallel to the circumferential direction of the stomach and stretched along the same direction. (a, c & e) Stress-strain and (b, d & f) stress-time graphs are presented. Experimental (Experiment) and model (NVS) data are represented by black broken and red solid lines, respectively. (a & b) The *lin-lin-lin* model parameters are $F = 7.65$ kPa; $E = 14.5$ kPa; $M = 512$ kPa s ($R^2 = 0.679$). (c & d) The *exp-exp-pow* model parameters are $\alpha = 5.64$; $\beta = 0.258$ kPa; $\gamma = 19.9$; $\delta = 0.496$ kPa; $a = 3.95$; $b = 2.14 \times 10^8$ kPa s^a ($R^2 = 0.993$). (e & f) The *exp-exp-exp* model parameters are $\alpha = 5.59$; $\beta = 0.222$ kPa; $\gamma = 17.3$; $\delta = 0.367$ kPa; $\lambda = 234$ s; $\mu = 0.443$ kPa ($R^2 = 0.993$). The average strain rate for each cycle is 0.0161 s^{-1}. Experimental data is provided by Zhao *et al.* (2008a).

As illustrated in Figure 4.2a (black broken line), the stress-strain graph has a nonlinear curvature with non-overlapping loading and unloading portions. The peak stress decreases from the first to subsequent periods, suggesting strain-softening of

stomach tissue. The corresponding hysteresis, illustrated by area enclosed by each loading-unloading cycle, also indicates decreasing energy dissipation in later cycles. In Figure 4.2b (black broken line), the stress-time graph rises in an increasing rate to peak stress before returning to minimum stress in a convex manner, producing a sharp peak and a wide trough in each period.

To find the most appropriate NVS model to describe the stomach tissue viscoelasticity, twelve NVS model variants, each with between three and six parameters, were derived (Table 4.1). The model parameters were determined by minimising the distance between the experimental data and the simulation using MATLAB® (The MathWorks, Inc, Massachusetts, U.S.A.) searching algorithm, *fminsearch*. The optimised models were compared by computing the R^2 values such that

$$R^2 = 1 - \frac{\sum\left(y_{\mathrm{exp},i} - y_{\mathrm{sim},i}\right)^2}{\sum\left(y_{\mathrm{exp},i} - \bar{y}_{\mathrm{sim}}\right)^2} \tag{4.62}$$

where $y_{\mathrm{exp},i}$ is the ith experimental data value with $i = 1,2,\cdots,n$, $y_{\mathrm{sim},i}$ is the corresponding simulated value from NVS model, and $\bar{y}_{\mathrm{sim}}$ is the average simulated value.

As shown by the R^2 values in Table 4.2, the tri-linear model is least capable of representing the stomach tissue viscoelasticity ($R^2 = 0.679$). The SLS cannot trace the curvatures of both stress-time and stress-strain experimental curves (Figures 4a and 4b). Replacing any one of the linear components in the SLS with exponential one can improve the result. Installing the exponential SEC ($R^2 = 0.929$) is the most

effective way, followed by inserting the exponential PEC ($R^2 = 0.769$), the power-law SVC ($R^2 = 0.694$) or the exponential dashpot ($R^2 = 0.680$).

Table 4.2 Optimised parameters of NVS models in simulating the intact porcine fundus tissue cyclic stretching in circumferential direction. Experimental data are provided by Zhao *et al.* (2008a).

Models (PEC-SEC-SVC) [a]	Equations	Optimised parameters	R^2
lin-lin-lin	(4.49)	$F = 7.65$ kPa; $E = 14.5$ kPa; $M = 512$ kPa s	0.679
exp-lin-lin	(4.50)	$\alpha = 6.81$; $\beta = 0.310$ kPa; $E = 82.3$ kPa; $M = 92.3$ kPa s	0.769
lin-exp-lin	(4.51)	$F = 5.71$ kPa; $\gamma = 8.07$; $\delta = 1.42$ kPa; $M = 768$ kPa s	0.929
lin-lin-exp	(4.52)	$F = 7.62$ kPa; $E = 14.6$ kPa; $\lambda = 6.38$ s; $\mu = 77.8$ kPa	0.680
lin-lin-pow	(4.53)	$F = 9.03$ kPa; $E = 18.6$ kPa; $a = 9.65$; $b = 1.14 \times 10^{20}$ kPa s[a]	0.694
exp-exp-lin	(4.54)	$\alpha = 6.46$; $\beta = 0.210$ kPa; $\gamma = 10.7$; $\delta = 0.789$ kPa; $M = 613$ kPa s	0.947
exp-lin-exp	(4.55)	$\alpha = 10.8$; $\beta = 0.0322$ kPa; $E = 20.2$ kPa; $\lambda = 144$ s; $\mu = 0.314$ kPa	0.753
lin-exp-exp	(4.56)	$F = 3.19$ kPa; $\gamma = 12.9$; $\delta = 0.568$ kPa; $\lambda = 249$ s; $\mu = 0.608$ kPa	0.989

Models (PEC-SEC-SVC) [a]	Equations	Optimised parameters	R^2
exp-lin-pow	(4.57)	$\alpha = 6.57$; $\beta = 0.344$ kPa; $E = 77.8$ kPa; $a = 7.30 \times 10^{-3}$; $b = 1.62$ kPa s^a	0.772
lin-exp-pow	(4.58)	$F = 4.96$ kPa; $\gamma = 2.00 \times 10^3$; $\delta = 8.73$ kPa; $a = 1.67$; $b = 1.52 \times 10^3$ kPa s^a	0.956
exp-exp-pow	(4.59)	$\alpha = 5.64$; $\beta = 0.258$ kPa; $\gamma = 19.9$; $\delta = 0.496$ kPa; $a = 3.95$; $b = 2.14 \times 10^8$ kPa s^a	0.993
exp-exp-exp	(4.60)	$\alpha = 5.59$; $\beta = 0.222$ kPa; $\gamma = 17.3$; $\delta = 0.367$ kPa; $\lambda = 234$ s; $\mu = 0.443$ kPa	0.993

[a] lin: linear component; exp: exponential component; pow: power-law component.

Replacing another linear component with a nonlinear one in *lin-exp-lin* ($R^2 = 0.929$) can enhance the NVS model as illustrated by the R^2 values of *exp-exp-lin* ($R^2 = 0.947$), *lin-exp-pow* ($R^2 = 0.956$) and *lin-exp-exp* ($R^2 = 0.989$). Similar improvements can be observed in the case of *lin-lin-exp* ($R^2 = 0.680$) when it is compared with *exp-lin-exp* ($R^2 = 0.753$) and *lin-exp-exp* ($R^2 = 0.989$). The result is also positive for swapping linear element for exponential part in *lin-lin-pow* ($R^2 = 0.694$) as both *exp-lin-pow* ($R^2 = 0.772$) and *lin-exp-pow* ($R^2 = 0.956$) provide better descriptions of the mechanical phenomenon. However, the result is mixed for *exp-lin-lin* ($R^2 = 0.769$). Substituting the linear SEC with an exponential spring can produce better result (*exp-exp-lin*, $R^2 = 0.947$) but not replacing the linear dashpot with exponential one (*exp-lin-*

exp, $R^2 = 0.753$). Exchanging the linear dashpot in *exp-lin-lin* with power-law SVC also enhances the capability of the model ($R^2 = 0.772$).

Both the tri-exponential and *exp-exp-pow* models can produce good description of porcine fundus tissue viscoelasticity ($R^2 = 0.993$ for both models). The *exp-exp-pow* model (Figures 4.2c & d) can simulate the maximum stress for each cycle more accurately than the *exp-exp-exp* counterpart (Figures 4.2e & f). Conversely, the tri-exponential model can follow the stress-time profile more closely especially at the transitions from one cycle to another.

Any model with a linear SEC can be enhanced by replacing it with an exponential spring. For example, *lin-exp-lin* ($R^2 = 0.929$) is a more suitable model than *lin-lin-lin* ($R^2 = 0.679$). Similarly, substituting exponential PEC in any model that carries linear spring, such as modifying *lin-lin-pow* ($R^2 = 0.694$) to become *exp-lin-pow* ($R^2 = 0.772$), can improve the description. An exponential SVC can improve all the models that carries linear dashpot except that *exp-lin-exp* ($R^2 = 0.753$) does not perform better than *exp-lin-lin* ($R^2 = 0.769$). Power-law SVC makes all models with linear dashpot more fitting.

Overall, both the *exp-exp-exp* model and the *exp-exp-pow* model provide quality description of fundus tissue viscoelasticity ($R^2 = 0.993$). However, the optimisation process for *exp-exp-exp* is quicker and more efficient than that of *exp-exp-pow*. Therefore, the exp-exp-exp model is selected and being used in the work shown in the following sections.

4.4.2 Stress relaxation and creep response of rat jejunum tissue

To investigate if the tri-exponential NVS is capable of reproducing other viscoelastic phenomena, the model was used to simulate the stress relaxation and creep responses of rat jejunum tissue.

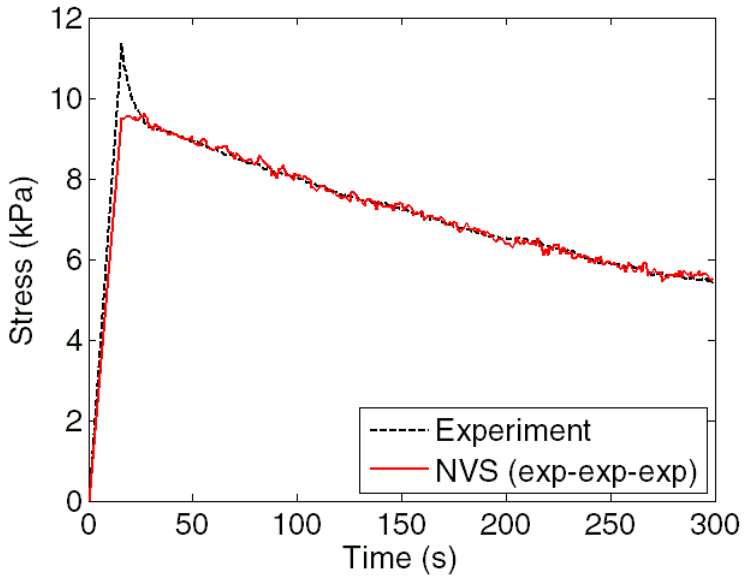

Figure 4.3 The tri-exponential NVS model can simulate the stress relaxation of rat jejunum. Experimental (Experiment) and tri-exponential (NVS) model data are represented by black broken and red solid lines, respectively. Model parameters are $\alpha = 6.66 \times 10^{-3}$; $\beta = 624$ kPa; $\gamma = 0.132$; $\delta = 59.1$ kPa; $\lambda = 1.99$ s; $\mu = 103$ kPa ($R^2 = 0.980$). A strain of 0.815 ± 0.009 was applied throughout the experiment. Experimental data has been provided by Zhao *et al.* (2003).

Zhao and colleagues (2003) obtained the jejunum from ten adult male Wistar rats and studied their passive mechanical properties. The calcium antagonist, papaverine, was administered to each rat to eliminate GI contractile activity. Each jejunal segment, six centimetres in length, was submerged in Ca^{2+}-free Kerbs organ bath and tied at two end of the mechanical testing machine. For stress relaxation, an average strain of 81.5% was maintained for 300 seconds. A step stress of 10.2 kPa was applied isotonically on the tissue for the creep experiment. Figures 4.3 and 4.4 (black broken lines) show the results for stress relaxation and creep of the rat jejunal segment.

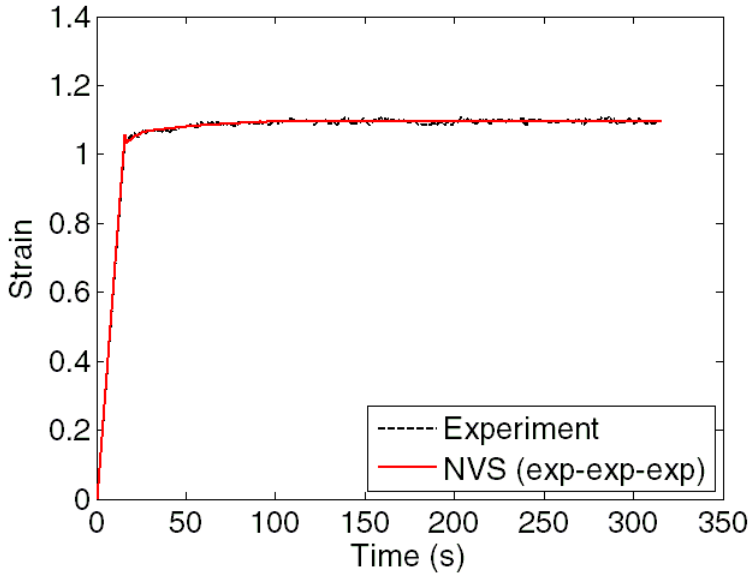

Figure 4.4 The tri-exponential NVS model can simulate the creep phenomenon of rat jejunum. Experimental (Experiment) and tri-exponential (NVS) model data are represented by black broken and red solid lines, respectively. Model parameters are $\alpha = 2.84$; $\beta = 0.471$ kPa; $\gamma = 4.82 \times 10^{-4}$; $\delta = 2.46 \times 10^{3}$ kPa; $\lambda = 219$ s; $\mu = 0.0417$ kPa ($R^2 = 0.993$). An isotonic tension of 10.2 ± 0.1 kPa was applied throughout the experiment. Experimental data has been provided by Zhao *et al.* (2003).

Figure 4.3 shows both the experimental stress relaxation result (black broken line) and corresponding simulation data (red solid line) produced by tri-exponential NVS. The NVS is unable to replicate the peak stress which immediately occurred after the application of step strain but it can follow the profile of diminishing stress from 40 s onwards. The experimental stress relaxation curve is composed of minimum two relaxation elements: a quick relaxation from the peak stress to 40 s and a slow relaxation afterwards. It shows that the combination of exponential SEC and exponential SVC cannot describe two-stage relaxation phenomenon. Other than alternative nonlinear SEC-SVC combinations, a configuration similar to the Generalised Maxwell model structure, which consists of a PEC connected to two or more SEC-SVC elements in parallel, can be considered (Flügge, 1967).

The tri-exponential NVS model was also adapted to model the rat jejunal creep data and the result is shown in Figure 4.4. The tri-exponential NVS strain replicated the experimental data as it continued to rise, at decreasing rates, over time in response to the initial stress step before reaching a steady state.

4.5 Modelling compressive deformation of muscle

Non-isometric smooth muscle activation shortens the tissue if the contractile force is stronger than the applied load. Microscopically, it has been suggested that the intra-SMC actins and microtubules provide the mechanical resistance against compressive deformation (Hemmer *et al.*, 2009). Therefore, it is important to consider the compressive stress-strain relation and viscoelasticity of smooth muscle when studying the overall mechanics of smooth muscle. However, as smooth muscle compressive mechanical data is rare, the skeletal muscle data is referenced in this work.

Several experimental reports have showed that the compressive viscoelastic profiles are comparable to those in extension in mammalian skeletal muscles. A rapid isometric compression produces negative stress relaxation, which consists of a quick decent in stress followed by a recovery at a decreasing rate, as shown in Figure 4.5a (Bosboom *et al.*, 2001; Van Loocke *et al.*, 2008). The cyclic stretching in negative strain regime produces stress-time profile which has sharp valleys and round peaks as illustrated in Figure 4.5c (Van Loocke *et al.*, 2009). Both profiles are similar to those found in positive strain with vertical reflections along the horizontal axis (Figures 4.2 & 4.3). In addition, several studies have reported that the compressive stress-strain relation of mammalian skeletal muscle is nonlinear with the magnitude of stress increasing rapidly at finite compression (Van Loocke *et al.*, 2006; Stollberger *et al.*, 2007).

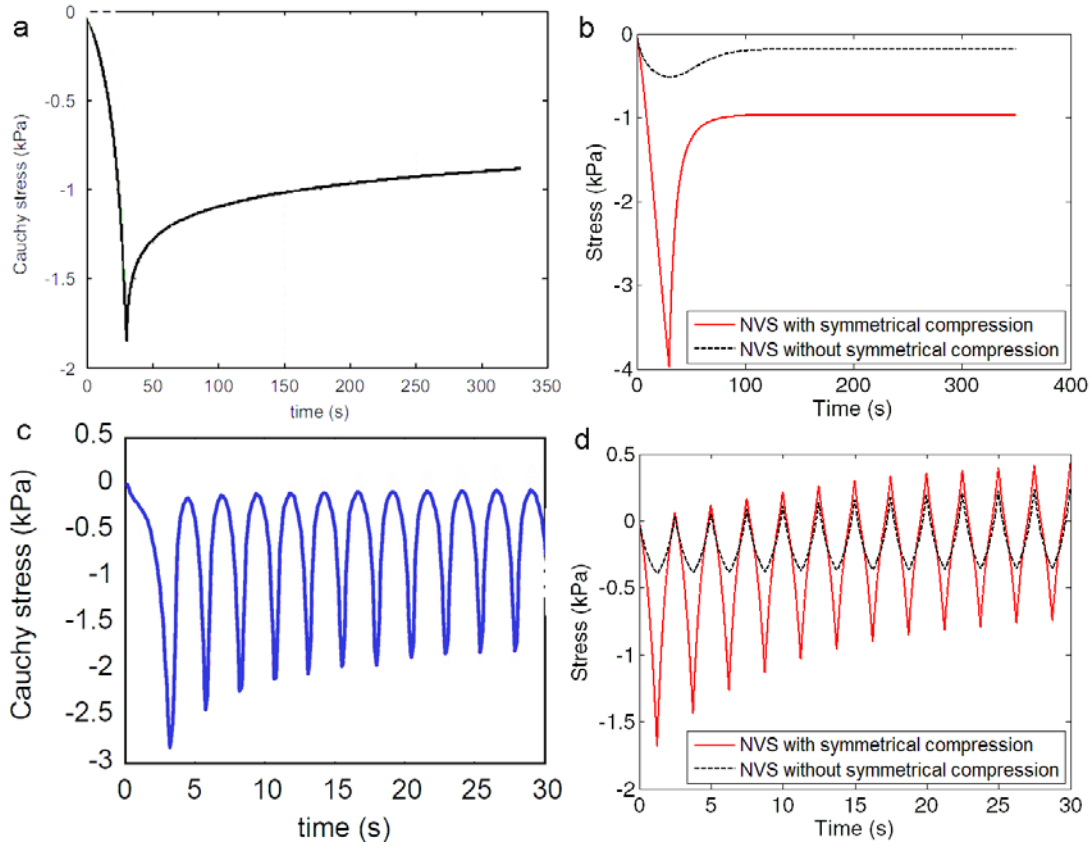

Figure 4.5 Stress relaxation and cyclic loading in skeletal muscle compression. (a) Stress relaxation of a fresh porcine gluteus muscle tissue after step compression of 30% at a strain rate of 0.01 s^{-1} (Source: Van Loocke *et al.*, 2008). (b) Stress relaxation of tri-exponential NVS models with (red solid line) and without (black broken line) symmetrical compression. The magnitude and velocity of compression are identical to those in (a). (c) Cyclic compression of a fresh porcine gluteus muscle tissue at an amplitude of 10% strain and strain rate of 0.1 s^{-1} (Source: Van Loocke *et al.*, 2009). (d) Cyclic compression of tri-exponential NVS models with (red solid line) and without (black broken line) symmetrical compression. The amplitude and velocity of compression are identical to those in (c). Refer to Equations (4.67) and (4.60) for the tri-exponential NVS models with and without symmetrical compression. For both models, the parameters are $\alpha = 5.59$, $\beta = 0.222$ kPa, $\gamma = 17.3$, $\delta = 0.367$ kPa, $\lambda = 234$ s and $\mu = 0.443$ kPa. The parameters were obtained from the optimised *exp-exp-exp* model (See Table 4.2).

The NVS tri-exponential model has been used to describe with porcine stomach cyclic extension data in Section 4.4. To extend its usage to model compressive deformation, in the absence of experimental data it is postulated that the passive mechanics of compression in smooth muscle is symmetrical to that in stretching. The constitutive

equations of exponential PEC, SEC and SVC in Equations (4.38) to (4.40) can be modified to include additional expressions for negative strain such that

$$\sigma_p = \beta\ \mathrm{sgn}(\varepsilon_p)\left[\exp\left(\alpha\left|\varepsilon_p\right|\right) - 1\right] = f_p \tag{4.63}$$

$$\sigma_s = \delta\ \mathrm{sgn}(\varepsilon_s)[\exp(\gamma|\varepsilon_s|) - 1] = f_s \tag{4.64}$$

$$\sigma_v = \mu\ \mathrm{sgn}(\dot{\varepsilon}_v)[\exp(\lambda|\dot{\varepsilon}_v|) - 1] = f_v. \tag{4.65}$$

where $\mathrm{sgn}(\bullet)$ is the signum function whose definition is

$$\mathrm{sgn}(\bullet) = \begin{cases} -1 \text{ if } \bullet < 0 \\ 0 \text{ if } \bullet = 0 \\ 1 \text{ if } \bullet > 0 \end{cases}. \tag{4.66}$$

Note that in the case of tri-exponential NVS with symmetrical compression, the SEC and SVC are extended or compressed in tandem (that is $\mathrm{sgn}(\varepsilon_s) = \mathrm{sgn}(\sigma_s) = \mathrm{sgn}(\sigma_v) = \mathrm{sgn}(\dot{\varepsilon}_v)$, refer to Appendix C for details). Following a similar procedure to that illustrated in Equations (4.41) – (4.48), the tri-exponential model with symmetrical compression is

$$\begin{aligned} \dot{\sigma} = {} & \alpha\beta\ \exp(\alpha|\varepsilon|)\dot{\varepsilon} + \gamma[\delta + |\sigma - \beta\ \mathrm{sgn}(\varepsilon)[\exp(\alpha|\varepsilon|) - 1]|] \\ & \times \left[\dot{\varepsilon} - \frac{\mathrm{sgn}(\sigma_v)}{\lambda}\ \ln\left\{1 + \frac{|\sigma - \beta\ \mathrm{sgn}(\varepsilon)[\exp(\alpha|\varepsilon|) - 1]|}{\mu}\right\}\right]. \end{aligned} \tag{4.67}$$

The detail derivation of the model is illustrated in Appendix C.

We compared the simulation result generated by the original NVS model (Equation (4.60)) and the one with symmetrical compression (Equation 4.67)) using the

optimised parameters obtained in *exp-exp-exp* model (Table 4.2). A step compression was applied to NVS models with and without symmetrical compression.

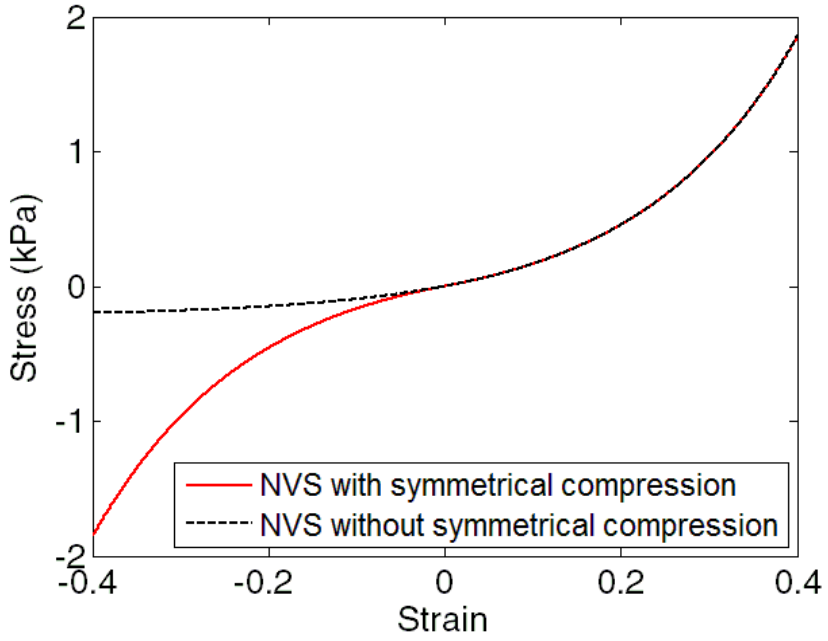

Figure 4.6 Comparison of NVS models with or without symmetric compression. Steady-state stress-strain relation (stress-strain of PEC) of tri-exponential NVS with (red solid line) and without (black broken line) symmetrical compression. Refer to Equations (4.70) and (4.48) for the tri-exponential NVS models with and without symmetrical compression. For both models, the parameters are $\alpha = 5.59$, $\beta = 0.222$ kPa, $\gamma = 17.3$, $\delta = 0.367$ kPa, $\lambda = 234$ s and $\mu = 0.443$ kPa. Note that without symmetrical compression, the maximum compressive stress is restricted to 0.222 kPa.

As shown in Figure 4.5b, the modified NVS produced a stress profile with a sharp valley, which is similar to the result of stress relaxation experiment performed on skeletal muscle (Figure 4.5a). The model with symmetrical compression also presents a stress-time graph with sharp valleys and increasing minimum stress for each cycle when prescribed with cyclic compressive loading (Figure 4.5d). The simulated result resembles the profile of experimental cyclic loading in skeletal muscle as shown in Figure 4.5c. In contrast, the tri-exponential NVS without symmetrical compression produces a stress-time profile with wide valleys in both stress relaxation and cyclic

loading (black broken lines in Figures 4.5b & d). Its maximum compressive stress is also restricted by the exponential function in the PEC (Figure 4.6).

4.6 Discussion

The NVS framework in Figure 4.1 can be separated into two components: the exclusively strain-dependent PEC component, and the time and strain dependent Maxwell element. This is analogous to the resulting tension due to periodic stretching being categorised into steady-state and time-dependent components. The tri-exponential NVS model prescribes that the steady-state tension of porcine stomach tissue is an exponential function of strain. This relation is supported by evidence provided by other investigators as shown previously in Table 3.1.

The exponential stress-strain relation can be explained by the tissue microstructure. Extracellular collagen fibres demonstrate waviness in an unstretched tissue (Wess, 2008). When the tissue is extended, the fibres are straightened and this contributes to the initial gentle rise in tension (Maceri *et al.*, 2010). Continued extension causes the unfolding of the collagen triple helix which requires a larger force than straightening the kinked collagen fibres. Furthermore, the natural lengths of collagen fibres also vary (Gao *et al.*, 2009). An increasing quantity of fibres are recruited to resist tissue stretching at larger strain and this results in a larger stiffness (Pinart *et al.*, 2011). Similarly, a nonlinear positive relation between the elastic modulus and the applied stress has been found in an in-vitro atomic force microscopy experiment on the intracellular actin network (Chaudhuri *et al.*, 2007). Overall, both the intra- and extra-cellular structural materials contribute to the nonlinear stress-strain relation shown in Figure 4.2a. Their contributions are represented by the exponential elastic elements in the NVS model.

The SVC provides a strain rate-dependent resistant force during deformation. We inserted the linear, exponential and power-law SVC, in turn, into NVS to model the cyclic stretching of stomach tissue. Both the *exp-exp-exp* model and the *exp-exp-pow* model perform better than the other variants. The result supports the existence of a nonlinear SVC whose stress varies positively with strain rate.

Recently, Speich *et al*. (2006; 2007) suggested that the strain softening phenomenon observed in rabbit detrusor tissue is related to the abolition of cross-linking proteins during cyclic stretching. They demonstrated their theory by using a modified viscoelastic model incorporated with several cross-linking elastic components (XEC) connected in series as shown in Figure 4.7.

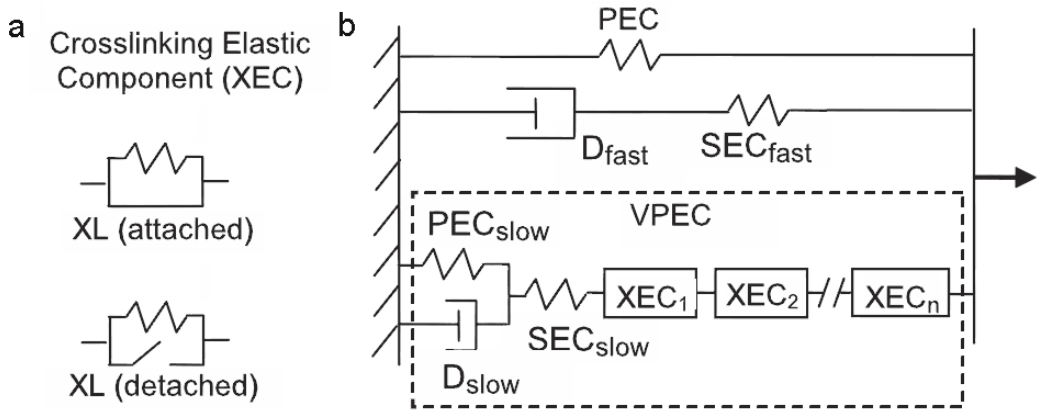

Figure 4.7 Illustration of the adjustable passive stiffness (APS) model. (a) The attached and unattached states of the cross-linking elastic component (XEC) represent the stiffness of intact and broken cross-linking proteins. (b) The configuration of APS model with the parallel elastic element (PEC), the serial elastic component (SEC), the dashpot (D) and the variable passive elastic component (VPEC). The VPEC consists of a serial connection of multiple XEC, the SEC and the Kelvin element which contains the parallel connection of the PEC and the D. Slow components have larger stiffness and viscosity than the fast components. (Source: Speich *et al.*, 2006)

To simulate mechanical damage to the cross-linking proteins, the stiffness of one or more XEC are reduced after each extension cycle. As a result, the model produces decreasing peak stresses which are similar to strain softening. However, the results

from the NVS imply that the physical phenomenon can be largely explained by the exponential or the power-law stress-strain and stress-strain rate relations which describe the aggregate viscoelasticity of constituent structural proteins (Figure 4.2), thus reducing the need for the additional complexity of the XEC approach. However, further experimental investigations are warranted to establish the factors that lead to the observed phenomenon of strain softening found in smooth muscle tissue.

4.7 Summary of NVS

In this Chapter, it has been shown that the SLS model framework can be extended to enable it to describe nonlinear viscoelastic phenomena by generalising the linear stress-strain and stress-strain rate relationships imposed in a conventional SLS. Such a generalisation results in a compact stress-strain relation in the form of the NVS model. Insertion of linear components into the NVS reproduces the familiar SLS governing equations and this is therefore a special case of the NVS.

Upon the insertion of exponential elastic and viscous elements, the tri-exponential NVS model can reproduce the major viscoelastic phenomena in mammalian GI tissues observed under isometric, isotonic and isokinetic conditions. The NVS is also more capable than its linear SLS counterpart in modelling cyclic stretching of porcine gastric tissue. Thus, the tri-exponential NVS provides an appropriate mathematical description of GI tissue viscoelastic and passive mechanical properties.

The NVS was also extended to accept piecewise constitutive relations for its components. The development further extends the usage of NVS in modelling complex uniaxial mechanical behaviour which can be described by piecewise mathematical functions.

Chapter 5 Active Nonlinear Viscoelastic Solid

5.1 Overview

Tensile or compressive stress is recorded when the gastrointestinal smooth muscle is subjected to external deformation. The uniaxial passive mechanical phenomena can be mathematically captured by the NVS. In addition, GI smooth muscle is also capable of self-actuating contraction. This chapter details the development of a compact mathematical model which aggregates both the active and passive mechanics of GI smooth muscle.

GI smooth muscle contraction is the driving force of GI motility. Activation of GI smooth muscle can generate contractile stress and increase stiffness of a myocyte ten-fold (Warshaw and Fay, 1983a; Warshaw *et al.*, 1988; Yamakawa *et al.*, 1990). Combinations of different contractile patterns in the longitudinal, circumferential and, in the case of stomach, oblique layers influence the digestive processes in the GI tract. It has been suggested that tonic contraction is associated with a reservoir function, such as the holding of a bolus at the fundus, while phasic contraction is related to the segmentation and movement of a bolus (Golenhofen and Mandrek, 1991).

In GI smooth muscle, phasic or rhythmic contraction is the product of intrinsic pacemaking electrical activity that originates from the ICC (Sanders *et al.*, 2006). ICC spontaneously generate the pacemaker currents which depolarises surrounding SMC through gap junctions. In the depolarised SMC, the electrical signal induces the release of calcium ions from the SR through the ryanodine receptors and inositol

1,4,5-trisphosphate-gated Ca^{2+} channels. In addition, extra-cellular Ca^{2+} enters the sarcoplasm through sarcolemma-localised ion channels such as T-type and L-type Ca^{2+} channels (Kuo *et al.*, 2011).

The rise of intra-cellular [Ca^{2+}] facilitates the formation of cross-bridges and latch-bridges for SMC contractile activities (Hong *et al.*, 2011). In this Ca^{2+}-dependent mechanism, myosin light chain kinase (MLCK) is activated when it binds with four Ca^{2+} ions and calmodulin. The activated MLCK complex phosphorylates a thick filament myosin head which can then attach to an actin binding site on the thin filament and produces associated cross-bridges. The MLCK-catalysed myosin phosphorylation activity is counter-balanced by the concurrent dephosphorylation of myosin heads facilitated by myosin light chain phosphatase (MLCP) (Kim *et al.*, 2008). As a result, the ratio of active MLCK to MLCP determines the mechanical state of smooth muscle. When the MLCK activity dominates, the formation of cross-bridges and the dephosphorylated latch-bridges gives rise to the observable contractile activities in the GI smooth muscle during the onset of contraction.

The electrical signal reaches a maximum and starts to decay (Watras, 2008). The diminishing activity induces the sequestration of Ca^{2+} ions as the intra-cellular [Ca^{2+}] returns to pre-depolarisation levels. This leads to an accumulation of inactive MLCK and the consequent domination of MLCP activity. The biochemical process induces the detachment of cross-bridges and latch-bridges, and subsequently the relaxation of the SMC. Overall, ICC electrical activity is periodic and its frequency varies from three to twelve cycles per minute in different parts of GI tract (Barrett and Raybould, 2008). The variation of intra-cellular [Ca^{2+}] leads to phasic contraction in GI smooth muscle.

While phasic contraction is characterised by rapid rise and decay of contractile stress within tens of seconds, tonic contraction can last for minutes or hours. GI smooth muscle tonic contraction, or tone, is defined as the physiological and sustained firmness of GI tissue that arises from active contraction (Gregersen and Christensen, 2000). Two types of tone are suggested by Mandrek and Golenhofen (1990), namely tetanic and specific tone. The former originates from the merging of high-frequency phasic contractions, in which the SMC is repeatedly activated before its contractile force returns to the baseline level. The specific tone is merely the sustained contraction at one location, supported by the low energy-turnover and slow-cycling latch-bridges (Himpens *et al.*, 1988).

In addition to activated MLCK and MLCP, smooth muscle deformation has significant effect on the magnitude of its contraction. Lengthening and shortening of smooth muscle can influence the quantity of free myosin heads and actin binding sites available for cross-bridge cycling and consequent active stress generation (Herrera *et al.*, 2005). In non-isometric contraction of smooth muscle, active stress overcomes the compressive mechanical resistance posed by structural filaments such as microtubules in order to produce muscle shortening (Hemmer *et al.*, 2009).

To provide a mathematical description of GI smooth muscle active mechanics, a model framework, termed the active nonlinear viscoelastic solid (ANVS), is developed in this chapter. Both the passive and active mechanical components are incorporated within ANVS, which can describe their independent mechanics as well as their interactions in GI smooth muscle. The model can account for the mechanical phenomena as well as the underlying Ca^{2+}-dependent contraction mechanism observed in both phasic and tonic contraction. It can also reproduce in-vitro experimental results conducted under both isometric and isotonic conditions.

5.2 Model development

5.2.1 ANVS model framework

An active contractile component (ACC) was inserted into the NVS framework introduced in Chapter 4, and the result is an active nonlinear viscoelastic solid (ANVS) model. As per the NVS, the parallel and serial springs are termed the parallel elastic component (PEC) with subscript p, and serial elastic component (SEC) with subscript s, respectively, while the dashpot is termed the serial viscous component (SVC) with subscript v as shown in Figure 5.1. The general stress versus strain (σ vs ε) and stress versus strain rate (σ vs $\dot{\varepsilon}$) relationships for these three components can be written as

$$\sigma_p = f(\varepsilon_p) = f_p \tag{5.1}$$

$$\sigma_s = f(\varepsilon_s) = f_s \tag{5.2}$$

$$\sigma_v = f(\dot{\varepsilon}_v) = f_v. \tag{5.3}$$

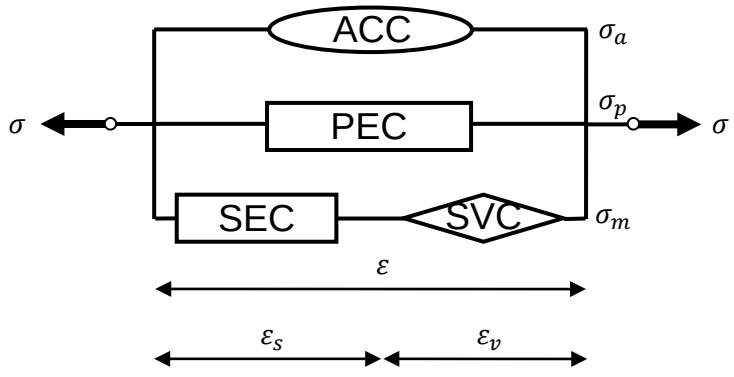

Figure 5.1 Illustration of ANVS. The ANVS model with an active contractile component (ACC), a parallel elastic component (PEC), a series elastic component (SEC) and a series viscous component (SVC). The SEC and SVC are serially connected and termed a Maxwell element. σ and ε represent stress and strain while subscripts a, p, m, s, and v indicate the quantities belonging to the ACC, the PEC, the Maxwell element, the SEC and the SVC, respectively.

The combination of the SEC and SVC in series forms what is commonly known as a Maxwell element and is denoted here by the m subscript. Smooth muscle activation initiates time-dependent (t) cross-bridge cycling which generates the contractile stress and stiffness. The quantity of available cross-bridges is also influenced by the strain (ε_a) experienced by the contractile apparatus. Overall, the active mechanics is represented by the ACC whose stress (σ_a) is dependent on both time and strain such that

$$\sigma_a = g(t)h(\varepsilon_a) = g_a h_a. \tag{5.4}$$

g is an arbitrary time-dependent function while h is a arbitrary strain-dependent function in the ANVS model framework. It has been postulated that the total stress in smooth muscle is the sum of its passive and active stresses (Fung, 1993). Hence, the following constraints apply to the system,

$$\sigma = \sigma_a + \sigma_p + \sigma_m \tag{5.5}$$

$$\sigma_m = \sigma_s = \sigma_v \tag{5.6}$$

$$\varepsilon_m = \varepsilon_s + \varepsilon_v \tag{5.7}$$

$$\varepsilon = \varepsilon_a = \varepsilon_p = \varepsilon_m. \tag{5.8}$$

Differentiating Equations (5.4), (5.5) and (5.8) with respect to time produces

$$\dot{\sigma}_a = \frac{dg_a}{\partial t} h_a + g_a \frac{dh_a}{d\varepsilon_a}\frac{d\varepsilon_a}{dt} = \frac{dg_a}{dt} h_a + g_a \frac{dh_a}{d\varepsilon_a}\dot{\varepsilon}_a \tag{5.9}$$

$$\dot{\sigma} = \dot{\sigma}_a + \dot{\sigma}_p + \dot{\sigma}_m \tag{5.10}$$

$$\dot{\varepsilon} = \dot{\varepsilon}_a = \dot{\varepsilon}_p = \dot{\varepsilon}_m. \tag{5.11}$$

In Figure 5.1, the PEC, SEC and SVC form the NVS model. Considering the aggregate stress and strain in the PEC and the Maxwell elements, the NVS constitutive equation [Equation (4.17)] can be rewritten as

$$\dot{\sigma}_p + \dot{\sigma}_m = \frac{df_p}{d\varepsilon_p}\dot{\varepsilon} + \frac{df_s}{d\varepsilon_s}(\dot{\varepsilon} - \dot{\varepsilon}_v). \tag{5.12}$$

Substituting Equations (5.9), (5.11) and (5.12) into Equation (5.10) and rearranging gives the constitutive equation of ANVS model,

$$\dot{\sigma} = \left(g_a \frac{dh_a}{d\varepsilon_a} + \frac{df_p}{d\varepsilon_p} + \frac{df_s}{d\varepsilon_s}\right)\dot{\varepsilon} + \frac{dg_a}{dt}h_a - \frac{df_s}{d\varepsilon_s}\dot{\varepsilon}_v. \tag{5.13}$$

5.2.2 Configurations of active contractile component

The ACC is the general active mechanical element in the ANVS model framework. When determining the final configuration of ACC, our objective was to use the minimum number of elements and parameters to illustrate the prominent features of active GI smooth muscle. Four possible configurations have been considered as shown in Figure 5.2.

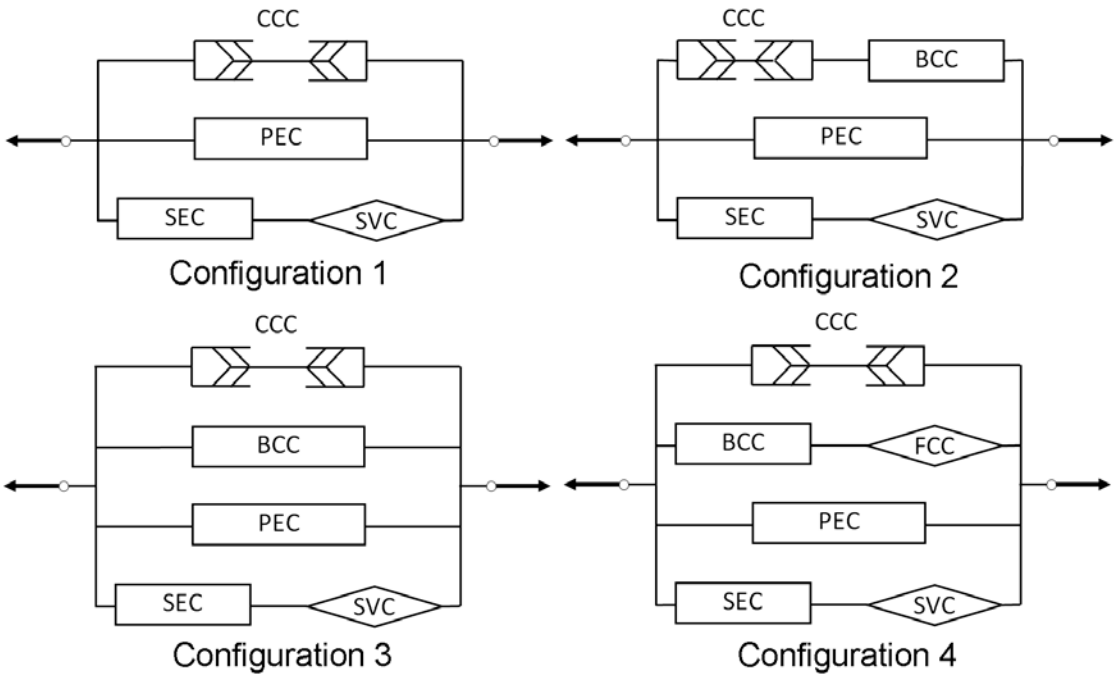

Figure 5.2 Possible configurations of ANVS model. The parallel elastic component (PEC), serial elastic component (SEC) and serial viscous component (SVC) are parts of the NVS model which describes the passive mechanical properties. Additional contractile component (CCC), elastic component (BCC) and frictional component (FCC) are inserted to describe the active mechanical properties.

A simple arrangement is to substitute the ACC with a contractile component (CCC) (Configuration 1). As such, the CCC connects in parallel to NVS and it is able to demonstrate both isometric and isotonic contraction phenomena. However, the resulting model does not possess active stiffness contributed by the attached cross-bridges and latch-bridges. An elastic component (BCC) can be connected to the CCC serially (Configuration 2) and the arrangement has been widely used in Hill's three-element model and other smooth muscle mechanics models as shown in Section 3.4. However, the allocation of strain to CCC and BCC varies among different investigators and there is no consensus that how it should be done (Gestrelius and Borgström, 1986; Fung, 1993; Yang *et al.*, 2003b).

To circumvent the issue, a parallel connection of CCC and BCC (Configuration 3) has been considered. The arrangement has the advantage of separating the contribution

of cross-bridges and latch-bridges to cycling (force generation and shortening) and cross-linking (stiffening) effects in smooth muscle. Experimental studies have shown that the stress due to active stiffness in smooth muscle tissues and cells is 10 to 100 times larger than that of contractile force (Singer *et al.*, 1986). However, a BCC with high stiffness prevents the generation of isometric stress and inhibits the shortening of smooth muscle under isotonic conditions. Therefore, a viscous component (FCC) was inserted in series with the BCC (Configuration 4). Such a configuration with CCC, BCC and FCC, can produce important smooth muscle biomechanical features under isometric and isotonic conditions with stiffness. Overall, Configuration 4 was selected to model GI smooth muscle active mechanics in this thesis.

5.2.3 Constituents of active contractile component

In the ANVS GI smooth muscle mechanics model, the CCC, BCC and FCC represents the different mechanical roles and properties of attached cross-bridges and latch-bridges in smooth muscle contraction.

Cycling cross-bridge component

The cycling cross-bridge component (CCC), with subscript cc, is equivalent to the contractile element found in the Hill's three-element model (Section 3.4.1). As explained in the subsequent sections, the contractile stress (σ_{cc}), generated by the cycling cross-bridges and latch-bridges, is dependent of the overlap between actin and myosin filaments in the contractile apparatus. Consequently, σ_{cc} is a function of time and the contractile apparatus strain (ε_{cc}) such that

$$\sigma_{cc} = g(t)h(\varepsilon_{cc}) = g_{cc}h_{cc}. \tag{5.14}$$

Bound cross-bridge component

In addition to the contractile stress, attached cross-bridges and latch-bridges also stiffen the smooth muscle due to increased protein cross-linking (Warshaw *et al.*, 1988; Speich *et al.*, 2007). The bound cross-bridge component (BCC), with subscript bc, thus represents an elastic element whose tensile stress (σ_{bc}) arises from the strain (ε_{bc}) applied on the binding cross-bridges. Similar to CCC, the stress on BCC is formulated as

$$\sigma_{bc} = g(t)h(\varepsilon_{bc}) = g_{bc}h_{bc}. \tag{5.15}$$

Frictional cross-bridge component

Both the contractile stress and the active stiffness result from the binding of myosin heads to the actin filaments. The attachments increase the resistance for filament sliding and subsequent muscle shortening (Imafuku *et al.*, 1999). The presence of frictional heat production due to the unwinding of thin filaments when the activated muscle is stretched has also been suggested (Jarosch, 2011). These phenomena have been modelled as a 'friction-clutch' element in both the Gestrelius and Borgström (1986), and Yang *et al.* (2003b) models. In the ANVS model, the FCC encapsulates the resistant stress (σ_{fc}) due to sliding friction and protein unfolding at strain rate $\dot{\varepsilon}_{fc}$ and is represented as

$$\sigma_{fc} = g(t)h\left(\dot{\varepsilon}_{fc}\right) = g_{fc}h_{fc}. \tag{5.16}$$

Constitutive equation of ANVS with CCC, BCC and FCC

Figure 5.3 illustrates the ANVS configuration with CCC, BCC and FCC. The BCC and the FCC are connected serially to form a Maxwell cross-bridge element which is denoted by the subscript mc. The stress-strain and stress-strain rate relations of PEC, SEC and SVC have been previously described by Equations (5.1) to (5.3). The following equations, together with Equations (5.6) and (5.7), describe the constraints that apply to the system,

$$\sigma = \sigma_{cc} + \sigma_{mc} + \sigma_p + \sigma_m \tag{5.17}$$

$$\sigma_{mc} = \sigma_{bc} = \sigma_{fc} \tag{5.18}$$

$$\varepsilon_{mc} = \varepsilon_{bc} + \varepsilon_{fc} \tag{5.19}$$

$$\varepsilon = \varepsilon_{cc} = \varepsilon_{mc} = \varepsilon_p = \varepsilon_m. \tag{5.20}$$

To develop the constitutive equation for the system, Equations (5.14) and (5.15) are differentiated with respect to time such that

$$\dot{\sigma}_{cc} = \frac{dg_{cc}}{\partial t} h_{cc} + g_{cc} \frac{dh_{cc}}{d\varepsilon_{cc}} \frac{d\varepsilon_{cc}}{dt} = \frac{dg_{cc}}{dt} h_{cc} + g_{cc} \frac{dh_{cc}}{d\varepsilon_{cc}} \dot{\varepsilon}_{cc} \tag{5.21}$$

$$\dot{\sigma}_{bc} = \frac{dg_{bc}}{\partial t} h_{bc} + g_{bc} \frac{dh_{bc}}{d\varepsilon_{bc}} \frac{d\varepsilon_{bc}}{dt} = \frac{dg_{bc}}{dt} h_{bc} + g_{bc} \frac{dh_{bc}}{d\varepsilon_{bc}} \dot{\varepsilon}_{bc}. \tag{5.22}$$

Aggregating Equations (5.21) and (5.22), and applying the time derivatives of Equations (5.18) to (5.20) obtains

$$\dot{\sigma}_{cc} + \dot{\sigma}_{mc} = \frac{dg_{cc}}{\partial t} h_{cc} + g_{cc} \frac{dh_{cc}}{d\varepsilon_{cc}} \dot{\varepsilon} + \frac{dg_{bc}}{\partial t} h_{bc} + g_{bc} \frac{dh_{bc}}{d\varepsilon_{bc}} \left(\dot{\varepsilon} - \dot{\varepsilon}_{fc}\right). \tag{5.23}$$

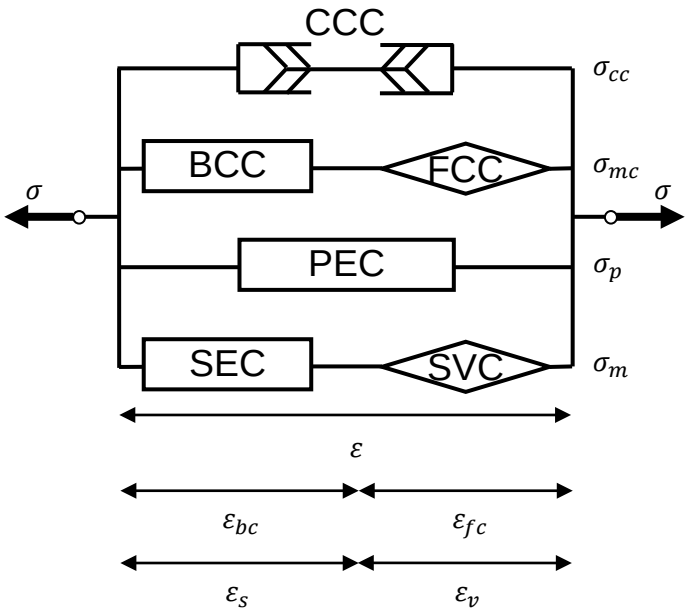

Figure 5.3 An ANVS variant which has an ACC structurally similar to NVS. The ACC consists of a cycling cross-bridge component (CCC), a bound cross-bridge component (BCC) and a frictional cross-bridge component (FCC). The BCC joins the FCC serially to form a Maxwell cross-bridge element, which connects to the CCC in parallel. The passive mechanical components encompass a parallel elastic component (PEC), a series elastic component (SEC) and a series viscous component (SVC). The SEC and SVC are serially connected and termed a Maxwell element. σ and ε represent stress and strain while subscripts cc, bc, fc and mc indicate the quantities belonging to the CCC, BCC, FCC and the Maxwell cross-bridge element, correspondingly. Subscripts p, m, s, and v indicate the quantities belonging to the PEC, the Maxwell element, the SEC and the SVC, respectively.

The constitutive relation of the passive components, PEC, SEC and SVC, is stated in Equation (5.12). Differentiating Equation (5.17) with respect to time and substituting Equations (5.12) and (5.23) gives

$$\dot{\sigma} = \dot{\sigma}_{cc} + \dot{\sigma}_{mc} + \dot{\sigma}_p + \dot{\sigma}_m \tag{5.24}$$

$$\dot{\sigma} = \frac{dg_{cc}}{\partial t} h_{cc} + g_{cc} \frac{dh_{cc}}{d\varepsilon_{cc}} \dot{\varepsilon} + \frac{dg_{bc}}{\partial t} h_{bc} + g_{bc} \frac{dh_{bc}}{d\varepsilon_{bc}} \left(\dot{\varepsilon} - \dot{\varepsilon}_{fc}\right) + \frac{df_p}{d\varepsilon_p} \dot{\varepsilon} + \frac{df_s}{d\varepsilon_s} (\dot{\varepsilon} - \dot{\varepsilon}_v). \tag{5.25}$$

Equation (5.25) is the constitutive equation of the ANVS model with CCC, BCC and FCC arranged in a NVS-like manner.

5.3 Coupling ANVS with strain-dependent and Ca^{2+}-dependent models to simulate GI smooth muscle contraction

5.3.1 Strain-dependent active force generation model

Experiments conducted on cat small intestinal and guinea pig colonic tissues have shown that active stress is maximised at the optimum muscle length (Meiss, 1971; Cooke and Fay, 1972; Price *et al.*, 1977). When the tissues were deformed from their optimum length, the contractile stress subsided (Figures 5.6c and 5.6d). Similar length-tension relations have also been obtained by applying step length changes in isolated active toad stomach SMC (Harris and Warshaw, 1991).

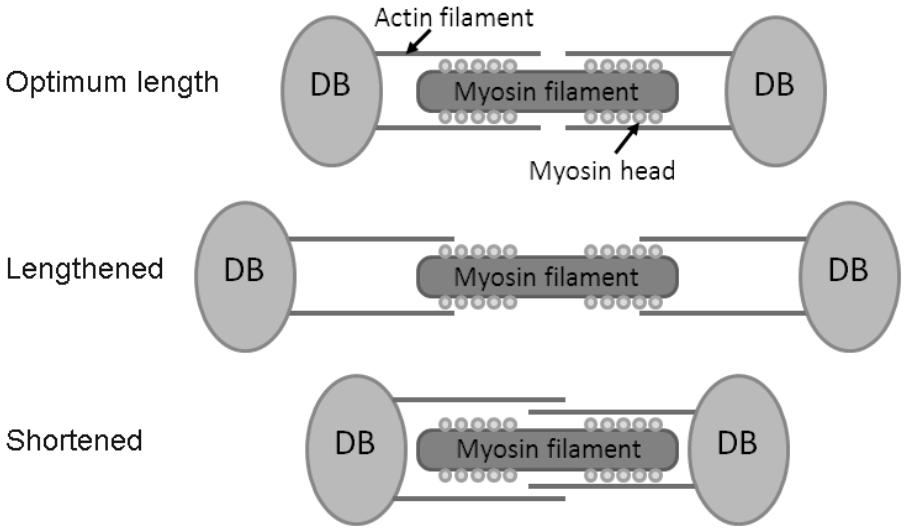

Figure 5.4 Illustration of strain-dependent activation. The number of myosin heads available for actin binding site attachment is highest at the reference strain, $\varepsilon = \varepsilon_{\mathrm{opt}}$ (top row). The number of available myosin heads decreases when the muscle is lengthened, $\varepsilon > \varepsilon_{\mathrm{opt}}$, or shortened, $\varepsilon < \varepsilon_{\mathrm{opt}}$ (middle and bottom rows). DB: dense body.

The alteration of isometric stress with respect to strain can be largely explained by the quantity of free myosin heads and actin binding sites available for attachment, which changes according to the extent of overlap between myosin and actin filaments (Herrera *et al.*, 2005). When the smooth muscle is held at its optimum strain ($\varepsilon_{\mathrm{opt}}$), the myosin and actin filaments are maximally overlapped (Figure 5.4). Consequently, the largest quantity of the myosin heads is available for attachment to the actin binding sites and the strongest contractile stress is attainable. When the smooth muscle is lengthened, the dense bodies, with their attached thin filaments, are pulled apart which decreases the overlapping area and reduces the achievable contractile stress. When the smooth muscle is shortened, the actin filaments bend and interfere with one another's attachment with myosin filaments. This also decreases the maximum achievable contractile stress.

As the quantity of available cross-bridges (n_{ac}) is positively correlated to the maximum achievable contractile stress, the former also varies inversely with the distance between current strain (ε) and $\varepsilon_{\mathrm{opt}}$. Gestrelius and Borgström (1986) have described the relation between n_{ac} and ε in portal vein smooth muscle successfully using the expression

$$n_{ac} = 1 - a_n\left|\varepsilon - \varepsilon_{\mathrm{opt}}\right|^{b_n} \tag{5.26}$$

where a_n and b_n are arbitrary constants.

As n_{ac} ranges from zero (no overlapping or maximum interference) to unity (maximum overlapping), Equation (5.26) is valid only if $\left|\varepsilon - \varepsilon_{\mathrm{opt}}\right| \leq (1/a_n)^{1/b_n}$. Beyond this range, $n_{ac} = 0$. The derivative of n_{ac} with respect to time can be expressed as

$$\frac{dn_{ac}}{dt} = a_n b_n \left|\varepsilon - \varepsilon_{\text{opt}}\right|^{b_n - 1} \dot{\varepsilon}\, \text{sgn}\left(\varepsilon_{\text{opt}} - \varepsilon\right). \tag{5.27}$$

Equations (5.26) and (5.27) have been adopted in the ANVS model for describing the strain-dependent active force generation in GI smooth muscle.

5.3.2 ACC for GI smooth muscle mechanics

To apply the ANVS model to describe GI smooth muscle mechanics, the CCC, BCC and FCC components introduced in Section 5.2 were customised according to the current knowledge and postulations on GI smooth muscle mechanics. The customised components were then inserted into the ANVS model illustrated in Figure 5.3.

Linear cycling cross-bridge component

The MLCK and MLCP activities influence the quantity of phosphorylated myosin, which is ready for cross-bridge formation and cycling. A portion of the attached actomyosin is dephosphorylated and becomes the latch-bridges. Previous reports have indicated that the contractile stress in smooth muscle is positively correlated to the proportions of attached cross-bridges (P_{CB}) and latch-bridges (P_{LB}) (Gestrelius and Borgström, 1986; Hai and Murphy, 1988b; Gajendiran and Buist, 2011). In addition, the actual number of available cross-bridges and latch-bridges are strain-dependent (Section 5.3.1). Overall, the total contractile stress generated in GI smooth muscle, denoted by CCC in ANVS (σ_{cc}), can be expressed as

$$\sigma_{cc} = n_{ac}(P_{CB} + P_{LB})F_{cc}. \tag{5.28}$$

F_{cc} is the maximum active stress that can be generated by the cycling cross-bridges and the latch-bridges, while n_{ac} denotes the quantity of free myosin heads available for cross-linking corresponding to the applied strain (Equation (5.26)).

P_{CB} and P_{LB} can be evaluated from the numbers of cross-bridges, $[AM_p]$, latch-bridges, $[AM]$ and the total available myosin, $[M_{total}]$, in the GI smooth muscle such that

$$P_{CB} = \frac{[AM_p]}{[M_{total}]} \tag{5.29}$$

$$P_{LB} = \frac{[AM]}{[M_{total}]}. \tag{5.30}$$

Substitute Equations (5.29) and (5.30) into Equation (5.28) gives

$$\sigma_{cc} = n_{ac} \frac{[AM_p] + [AM]}{[M_{total}]} F_{cc}. \tag{5.31}$$

Exponential bound cross-bridge component

The stress due to contractile stiffness (σ_{bc}) originates from the actomyosin cross-linking. Both the attached phosphorylated cross-bridges and the bound dephosphorylated latch-bridges are capable of contributing to the active stiffness of smooth muscle (Kamm and Stull, 1986). As the two actomyosin species differ by only a single phosphate ion, they are assumed to possess identical stiffness.

The aggregate smooth muscle active stiffness is also subjected to the influence of current deformation (Section 5.3.1). In addition, Warsaw and Fay (1983a) have reported an exponential stress-strain relation in the serial element of contracted toad

stomach SMC. The mathematical relation has been applied in other smooth muscle models (Yang *et al.*, 2003b). Therefore, the total active stiffness in GI smooth muscle, represented by BCC (σ_{bc}), is written as

$$\sigma_{bc} = n_{ac}(P_{CB} + P_{LB})\delta_{bc}[\exp(\gamma_{bc}\varepsilon_{bc}) - 1]. \quad (5.32)$$

where γ_{bc} is the coefficient of cross-bridge and latch-bridge strain in smooth muscle, δ_{bc} is the maximum active stiffness generated by all the cross-bridges and the latch-bridges in smooth muscle and n_{ac} denotes the quantity of available myosin heads.

Using the definitions of P_{CB} and P_{LB} in Equations (5.29) and (5.30), Equation (5.32) can be written as

$$\sigma_{bc} = n_{ac}\frac{[AM_p] + [AM]}{[M_{total}]}\delta_{bc}[\exp(\gamma_{bc}\varepsilon_{bc}) - 1]. \quad (5.33)$$

Linear frictional cross-bridge component

A source of resistance originates from the chemical bonds between myosin and actin (Gestrelius and Borgström, 1986). This frictional resistance hinders filament sliding as the number of attached cross-bridges and latch-bridges increases. In the case that the smooth muscle is in rigor, filament sliding becomes near impossible as majority of myosin heads are attached (Bose and Bose, 1975).

The frictional stress also varies positively with the velocity of extension and shortening ($\dot{\varepsilon}_{fc}$). Overall, the total stress due to viscous resistance in GI smooth muscle, represented by FCC (σ_{fc}), can be formulated as

$$\sigma_{fc} = n_{ac}(P_{CB} + P_{LB})M_{fc}\dot{\varepsilon}_{fc} \quad (5.34)$$

M_{fc} is the maximum coefficient of friction when all the cross-bridges and latch-bridges are attached, while n_{ac} denotes the quantity of free myosin heads available for cross-linking corresponding to the applied strain (Equation (5.26)).

Applying Equations (5.29) and (5.30) to Equation (5.34) obtains

$$\sigma_{fc} = n_{ac}\frac{[AM_p] + [AM]}{[M_{total}]}M_{fc}\dot{\varepsilon}_{fc}. \tag{5.35}$$

5.3.3 Constitutive equation of ANVS GI smooth muscle mechanics model

To derive the constitutive equation, Equations (5.31) and (5.33) are differentiated with respect to time such that

$$\dot{\sigma}_{cc} = \frac{dn_{ac}}{dt}\frac{[AM_p] + [AM]}{[M_{total}]}F_{cc} + n_{ac}\frac{d}{dt}\left(\frac{[AM_p] + [AM]}{[M_{total}]}\right)F_{cc} \tag{5.36}$$

$$\begin{aligned}\dot{\sigma}_{bc} = {} & \frac{dn_{ac}}{dt}\frac{[AM_p] + [AM]}{[M_{total}]}\delta_{bc}[\exp(\gamma_{bc}\varepsilon_{bc}) - 1] \\ & + n_{ac}\frac{d}{dt}\left(\frac{[AM_p] + [AM]}{[M_{total}]}\right)\delta_{bc}[\exp(\gamma_{bc}\varepsilon_{bc}) - 1] \\ & + n_{ac}\frac{[AM_p] + [AM]}{[M_{total}]}\gamma_{bc}\delta_{bc}\exp(\gamma_{bc}\varepsilon_{bc})\dot{\varepsilon}_{bc}.\end{aligned} \tag{5.37}$$

Rearranging Equation (5.33) gives

$$n_{ac}\frac{[AM_p] + [AM]}{[M_{total}]}\delta_{bc}\exp(\gamma_{bc}\varepsilon_{bc}) = \sigma_{bc} + n_{ac}\frac{[AM_p] + [AM]}{[M_{total}]}\delta_{bc}. \tag{5.38}$$

Applying Equations (5.18) to (5.20), (5.33) and (5.38) into Equation (5.37) illustrates the mechanical properties of the Maxwell cross-bridge element such that

$$\dot{\sigma}_{mc} = \frac{dn_{ac}}{dt}\frac{\sigma_{mc}}{n_{ac}} + \frac{d}{dt}\left(\left[AM_p\right] + [AM]\right)\frac{\sigma_{mc}}{\left[AM_p\right] + [AM]} + \gamma_{bc}\left(\sigma_{mc} + n_{ac}\frac{\left[AM_p\right] + [AM]}{[M_{total}]}\delta_{bc}\right)\left(\dot{\varepsilon} - \dot{\varepsilon}_{fc}\right) \tag{5.39}$$

where $\dot{\varepsilon}_{fc}$ can be expressed by rearranging Equation (5.35).

The NVS tri-exponential model has been validated with porcine stomach cyclic extension data in Chapter 4. The model has been further enhanced to encompass mechanical resistance due to compression. In the ANVS model, the tri-exponential model with symmetrical compression [Equation (4.70)] is employed to describe the mechanical properties of the PEC, SEC and SVC such that

$$\dot{\sigma}_p + \dot{\sigma}_m = \alpha\beta\,\exp(\alpha|\varepsilon|)\dot{\varepsilon} + \gamma(\delta + |\sigma_v|)\left\{\dot{\varepsilon} - \frac{\mathrm{sgn}(\sigma_v)}{\lambda}\,\ln\left[1 + \frac{|\sigma_v|}{\mu}\right]\right\} \tag{5.40}$$

where σ_v is the stress applied to the SVC such that

$$\sigma_v = \sigma - \sigma_{cc} - \sigma_{mc} - \beta\,\mathrm{sgn}(\varepsilon)[\exp(\alpha|\varepsilon|) - 1]. \tag{5.41}$$

The constitutive equation of the ANVS model with linear CCC, exponential BCC and linear FCC (lin-exp-lin ACC) is completed by aggregating Equations (5.36), (5.39) and (5.40) as illustrated by Equation (5.24) such that

$$\begin{aligned}\dot{\sigma} = {} & \frac{dn_{ac}}{dt}\frac{[AM_p]+[AM]}{[M_{total}]}F_{cc} + n_{ac}\frac{d}{dt}\left(\frac{[AM_p]+[AM]}{[M_{total}]}\right)F_{cc} \\ & + \frac{dn_{ac}}{dt}\frac{\sigma_{mc}}{n_{ac}} + \frac{d}{dt}\left([AM_p]+[AM]\right)\frac{\sigma_{mc}}{[AM_p]+[AM]} \\ & + \gamma_{bc}\left(\sigma_{mc} + n_{ac}\frac{[AM_p]+[AM]}{[M_{total}]}\delta_{bc}\right)\left(\dot{\varepsilon} - \dot{\varepsilon}_{fc}\right) \\ & + \alpha\beta\,\exp(\alpha|\varepsilon|)\dot{\varepsilon} \\ & + \gamma(\delta + |\sigma_v|)\left\{\dot{\varepsilon} - \frac{\mathrm{sgn}(\sigma_v)}{\lambda}\,\ln\left[1 + \frac{|\sigma_v|}{\mu}\right]\right\}.\end{aligned} \tag{5.42}$$

5.3.4 Ca^{2+}-dependent active force generation model

In Equation (5.42), the magnitudes of $[AM]/[M_{total}]$ and $[AM_p]/[M_{total}]$ can be evaluated by existing smooth muscle cross-bridge and latch-bridge models mentioned in Chapter 3. In this work, the Gajendiran and Buist (2011) bimodular active force generation model was selected as it provides a detailed description of [Ca^{2+}]-dependent processes for MLCK activation, myosin phosphorylation and generation of contractile stress in smooth muscle. The model description and relevant computations of $[AM]/[M_{total}]$ and $[AM_p]/[M_{total}]$ using [Ca^{2+}] are discussed in Appendix D.

5.4 Simulating phasic contraction of GI smooth muscle

5.4.1 Phasic contraction under isometric conditions

Ca^{2+}-dependent phasic contraction

GI smooth muscle phasic contraction is a prominent feature in GI motility. The contraction is influenced by a Ca^{2+}-dependent mechanism. Therefore, it is important

for the ANVS model to simulate the rhythmic contraction as a result of $[Ca^{2+}]$ transient observed in the experiments.

Ozaki and colleagues (1991a) harvested smooth muscle tissues which remained spontaneously active after being detached from the canine stomach. The contractile force was measured while the profile of $[Ca^{2+}]_i$ were observed concurrently through the usage of Fura-2 which gives off a fluorescent signal when it binds to free Ca^{2+} ions. The investigators discovered a strong association between free Ca^{2+} and active force transients. Intra-cellular $[Ca^{2+}]$ rose before force development and it peaked after one to three seconds. Maximum force was achieved at about 0.25 s after the detection of maximum $[Ca^{2+}]_i$. It was also reported that the force transient had quicker rate of decay than that of the $[Ca^{2+}]_i$.

Both the $[Ca^{2+}]_i$ and force transients can be reproduced by ANVS as shown in Figure 5.5. The rhythmic $[Ca^{2+}]$ waves, which served as an input to the ANVS, have been modelled by Gajendiran and Buist (2011) as follows,

$$[\mathrm{Ca}^{2+}]_i(t) = \begin{cases} [\mathrm{Ca}^{2+}]_{rest}, & t < t_{start} \\ [\mathrm{Ca}^{2+}]_{rest} + \Delta[\mathrm{Ca}^{2+}]\dfrac{t - t_{start}}{t_{peak} - t_{start}}, & t_{start} \le t \le t_{peak} \\ [\mathrm{Ca}^{2+}]_{rest} + \Delta[\mathrm{Ca}^{2+}]\exp\left[-k_{decay}\left(t - t_{peak}\right)\right], & t_{peak} < t \le t_{end} \end{cases} \quad (5.43)$$

where $\Delta[\mathrm{Ca}^{2+}]$ is defined as

$$\Delta[\mathrm{Ca}^{2+}] = [\mathrm{Ca}^{2+}]_{peak} - [\mathrm{Ca}^{2+}]_{rest}. \quad (5.44)$$

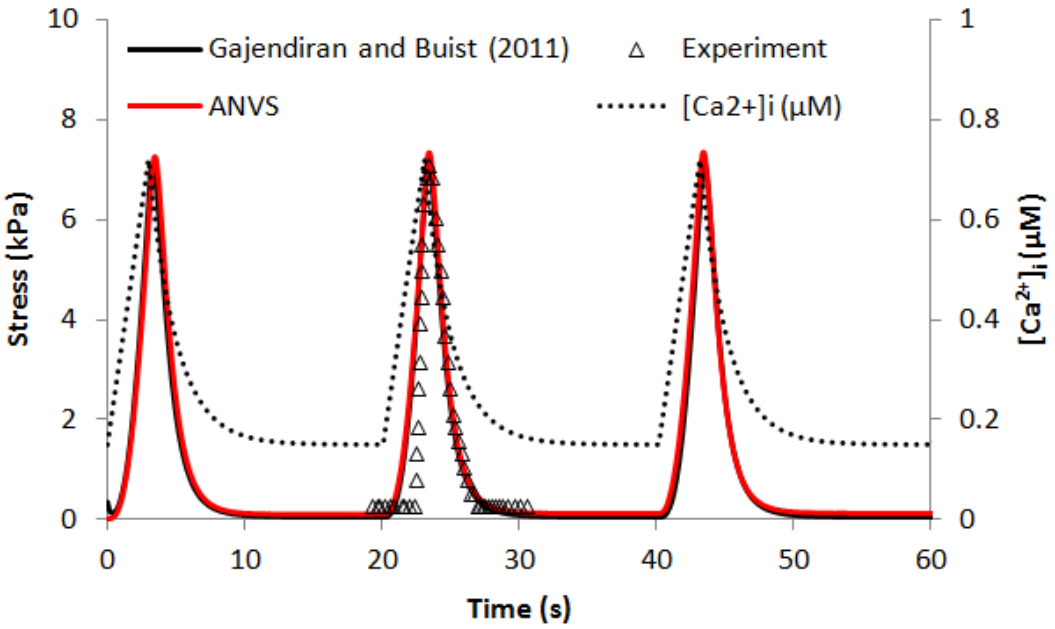

Figure 5.5 Isometric contraction of unstretched GI smooth muscle simulated by ANVS with peak $[Ca^{2+}]_i$ = 0.72 μM. The contractile stress (red solid line) generated by ANVS overlaps with that produced by Gajendiran and Buist (2011) model (black solid line) and it is in phase with the intra-cellular wave (black dotted line). Results from both models adhere closely to the experimental observation from Ozaki *et al*. (1991a) (empty black triangle). The model parameters are stated in Appendices D and E.

$[Ca^{2+}]_{rest}$ was set as 150 nM in ANVS as typical resting $[Ca^{2+}]$ ranges from 80 to 200 nM (Somlyo and Himpens, 1989). The period of $[Ca^{2+}]$ wave, and consequently the force transient, was prescribed to be 20 s, which agrees with the physiological frequency of stomach motility (Corrias and Buist, 2007). Other relevant parameters for Equations (5.43) and (5.44) are listed in Table E.1.

Effect of isometric strain on phasic contraction amplitude

GI smooth muscle phasic contraction is also influenced by mechanical stimuli. The ANVS GI smooth muscle model can be used to predict the effects of applied strain on phasic contraction.

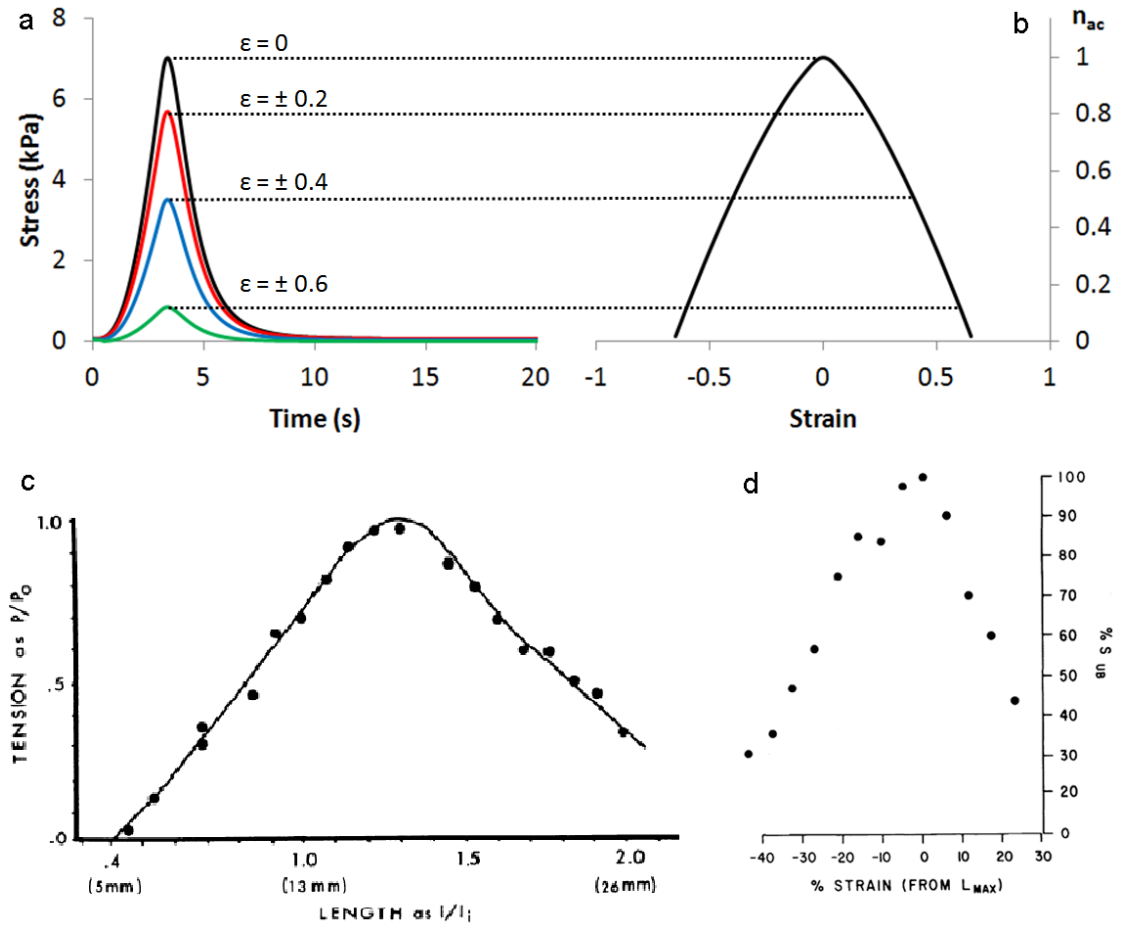

Figure 5.6 Effect of strain on GI smooth muscle contraction. Isometric contraction of GI smooth muscle at different strains as simulated by ANVS with peak $[Ca^{2+}]_i$ = 0.72 μM. The applied strains of smooth muscle [$\varepsilon = 0$ (black), $\varepsilon = \pm 0.2$ (red), $\varepsilon = \pm 0.4$ (blue) and $\varepsilon = \pm 0.6$ (green)] in (a) influence the quantity of available cross-bridge (n_{ac}) in (b) and consequently the peak active stresses. Modelling parameters are stated in Appendices D and E. The simulation results agree with experimental data obtained from (c) cat duodenal circumferential smooth muscle and (d) guinea pig taneia coli smooth muscle (Source: Meiss, 1971; Price *et al.*, 1977).

Different isometric strains were applied to the ANVS model. The resultant peak contractile stress decreases from the level at $\varepsilon = 0$ in either extension or shortening (Figure 5.6a). The phasic contractile waveforms remain unchanged as reported in literature (Zhao *et al.*, 2011b). The maximum active stress was plotted against the applied strain shown in Figure 5.6b. The simulated graph resembled the experimental results obtained from cat duodenal circumferential smooth muscle and guinea pig taneia coli smooth muscle (Figures 5.6c and d).

Effect of isometric strain on spontaneous contraction and viscoelasticity

Price and co-workers (1977) investigated the effect of applied strain on both the passive tension and active force in GI smooth muscle. They conducted biomechanical experiments on guinea pig taneia coli which was contracting spontaneously with a periodic force waveform.

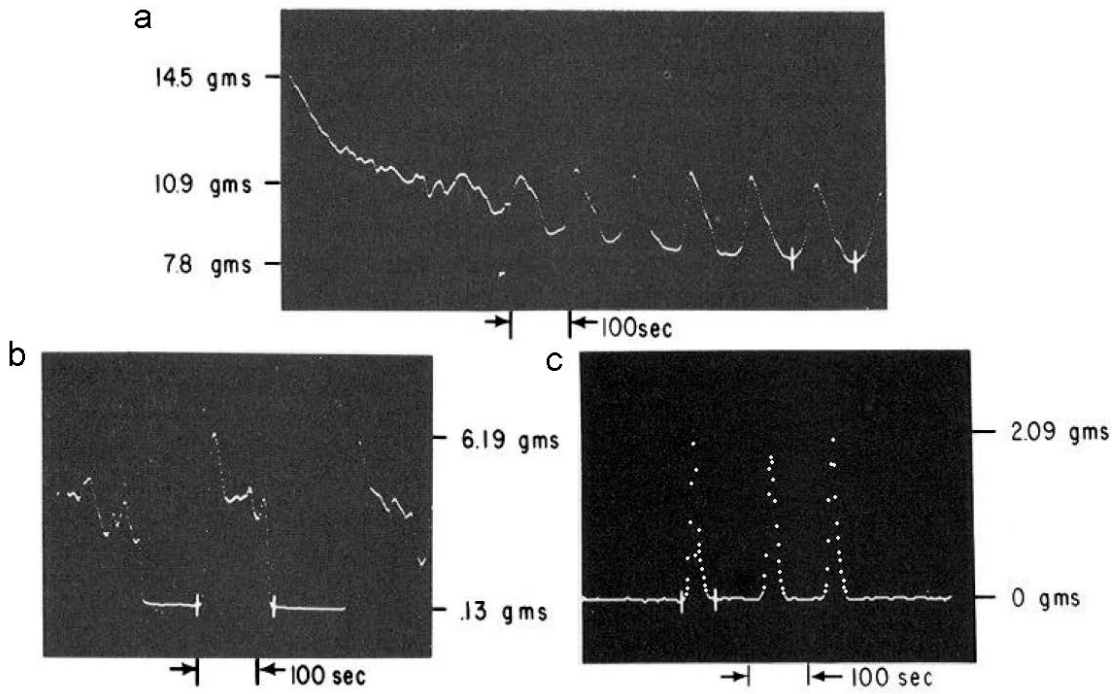

Figure 5.7 Passive and contractile force of guinea pig taneia coli at different isometric strains. Force against time were recorded when the tissue was (a) extended by 28%, (b) extended by 4% and (c) shortened by 36%. In (a), top marker indicates the force at the instant when extension was completed. Middle and bottom markers represent peak contractile force and passive force. In (b) and (c), the top and bottom middle markers denote peak contractile force and passive force (Price *et al.*, 1977).

When the tissue was extended, a sudden increment of baseline passive force was observed which coincided with the modified active force wave (Figure 5.7a). The passive force diminished while the oscillating active force became consistent after 500 s. The magnitude of maximum active force, measured from the baseline force to the peak of active force, was greatest when the tissue was near to its initial strain (Figure 5.7b). The reduction of active force was also observed when the GI tissue was

shortened (Figure 5.7c). For baseline passive force, smallest value was recorded when the taneia coli was shortened and it increased with tissue extension.

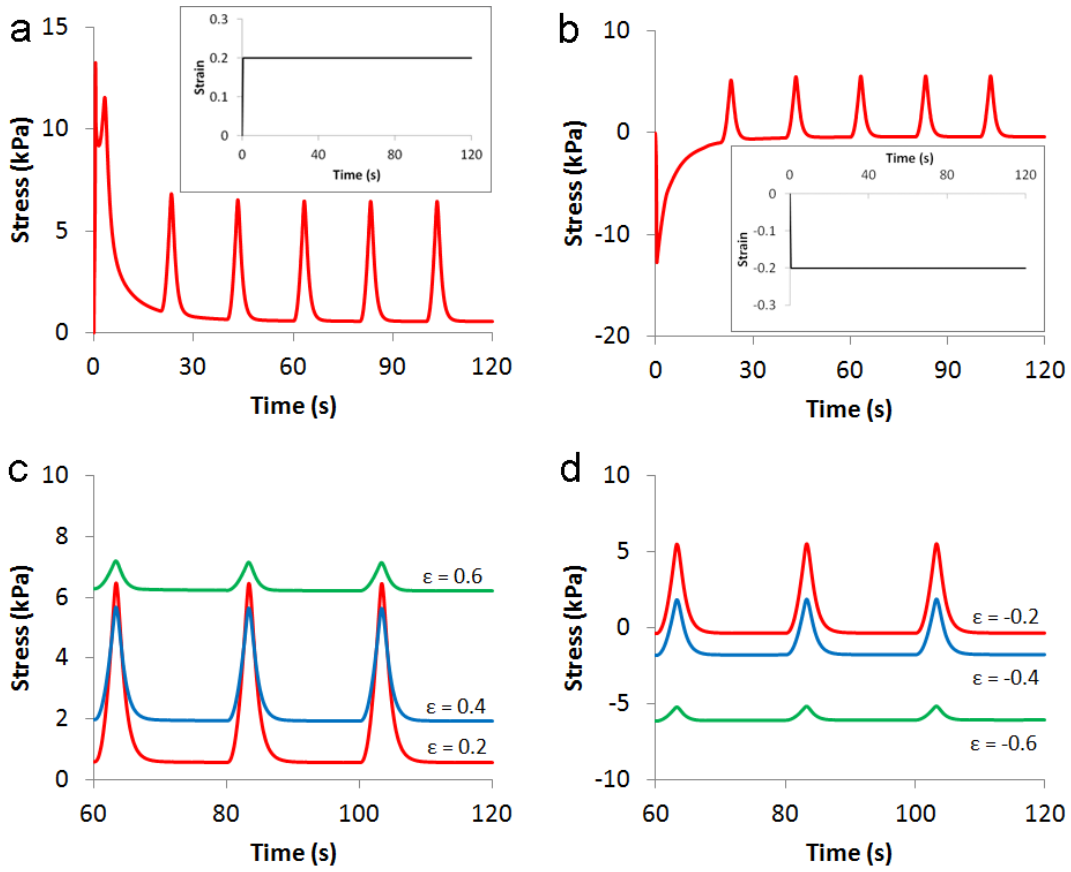

Figure 5.8 Simulating GI smooth muscle phasic contraction in different isometric loading conditions. (a) Total stress, consists of both passive and active stresses, experienced by GI smooth muscle as a result of isometric loading as shown by the inset ($\varepsilon = 0.2$). (b) Similar to (a) but with a step compression as illustrated by the inset ($\varepsilon = -0.2$). (c) Steady-state total stress at $\varepsilon = 0.2$ (red), $\varepsilon = 0.4$ (blue) and $\varepsilon = 0.6$ (green). (d) Steady-state total stress at $\varepsilon = -0.2$ (red), $\varepsilon = -0.4$ (blue) and $\varepsilon = -0.6$ (green). The initial strain step is completed within 0.5 s for all cases. Modelling parameters are stated in Appendices D and E.

The ANVS model was used to simulate the following experimental protocol. A step extension of 20% strain (Figure 5.8a inset) was applied to the model together with the periodic $[Ca^{2+}]_i$ transient as defined by Equations (5.43) and (5.44). A passive stress relaxation phenomenon, with elevated but decreasing baseline stress, was observed when the smooth muscle was suddenly lengthened (Figure 5.8a). The passive tension

and phasic contraction combine for a transformed stress waveform at the onset of step loading. Beyond that, phasic contraction is more apparent as the passive stress reaches a steady-state. The simulated phenomenon resembles to that shown in Figure 5.7a.

It is interesting to predict the effect of a step compression on the biomechanics of GI smooth muscle as experimental data on compressive mechanics is rare. As predicted by the ANVS, a negative stress relaxation occurs together with the phasic contraction give rise to the stress transients as shown in Figure 5.8b.

Overall, both tensile and compressive strains caused the steady-state peak active stress to decrease (Figures 5.8c and d). The steady-state passive (baseline) stress rises as the strain increases. The results generated by ANVS agree with those observed in experiments (Figures 5.7b and c).

Aggregate effect of $[Ca^{2+}]_i$ and isometric strain on phasic contraction

The magnitude of GI smooth muscle isometric contraction is also influenced by the intra-cellular calcium concentration. In another experiment, Ozaki *et al*. (1991b) extracted antral circumferential smooth muscle strips from canine stomach. They observed the $[Ca^{2+}]_i$ fluctuations in the tissue and recorded the contractile force simultaneously (Figure 5.9). The tissue was later treated with 3×10^{-7} M of the excitatory neurotransmitter acetylcholine, which resulted in the increased magnitudes of both $[Ca^{2+}]_i$ and peak contractile force.

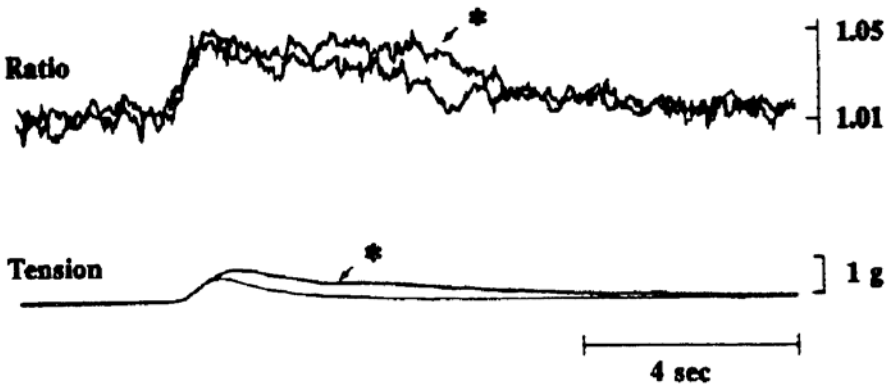

Figure 5.9 $[Ca^{2+}]_i$ and tension development in canine antral circumferential smooth muscle. Fluctuation of $[Ca^{2+}]_i$ (top) and contractile tension (bottom) were recorded concurrently. $[Ca^{2+}]_i$ is expressed in terms of ratio of fluorescent emissions at 400 nm and 500 nm. Asterisks indicate the responses after treatment with $3\,x\,10^{-7}$ M ACh. (Source: Ozaki et al., 1991b)

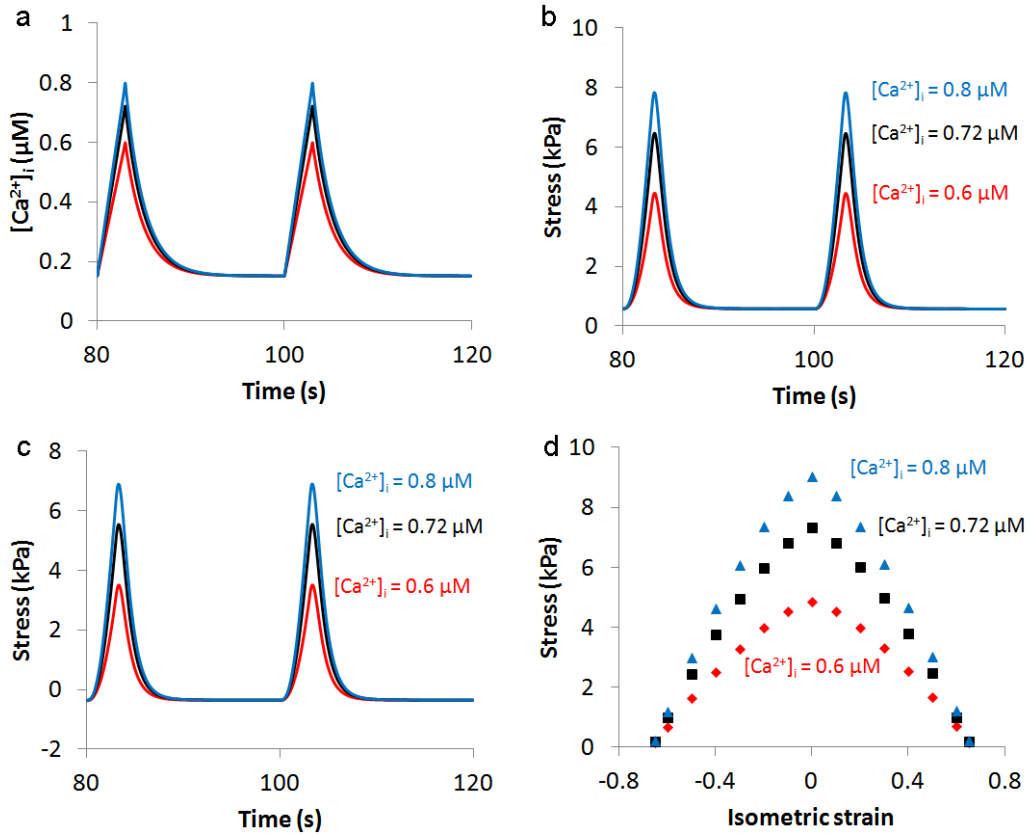

Figure 5.10 Isometric contraction of GI smooth muscle at different $[Ca^{2+}]_i$ as simulated by ANVS. Calcium transients with peak $[Ca^{2+}]_i$ of 0.6 μM (red line), 0.72 μM (black line) and 0.8 μM (blue line) are shown in (a). The resulting steady-state stress transients at strains 0.2 and -0.2 are illustrated in (b) and (c) respectively. The variation of maximum phasic stress with isometric strain at different $[Ca^{2+}]_i$ is summarised in (d). The colour codes in (b), (c) and (d) are identical to those in (a). Modelling parameters are stated in Appendices D and E.

To demonstrate this experimental phenomena in ANVS, $[Ca^{2+}]_i$ transients with three distinct peak values, 0.6 μM, 0.72 μM and 0.8 μM, are prescribed in the model (Figure 5.10a). The three $[Ca^{2+}]$ transient values were previously used by Gajendiren and Buist (2011) to simulate the antral smooth muscle contraction. The ANVS GI smooth muscle model predicted that the magnitude of peak $[Ca^{2+}]_i$ is positively correlated to that of contractile stress. Similar results were also obtained in the cases of isometric tension or compression (Figure 5.10 b and c). Alteration of peak $[Ca^{2+}]_i$ had no effect on the passive stress, as illustrated by the common baseline stress in both figures.

Overall, both the mechanical and chemical stimuli influence the peak contractile stress in GI smooth muscle. The ANVS simulation was repeated for other strains in each of the three $[Ca^{2+}]_i$. The results indicated that the change in peak $[Ca^{2+}]_i$ modifies the envelope of active stress versus applied strain graph (Figure 5.10d). However, the inverse relation between contractile stress and isometric strain is unaltered.

5.4.2 Phasic contraction under isotonic conditions

Isotonic experiments have been conducted by other investigators to evaluate the magnitudes of muscle shortening displacement and velocity corresponding to different applied loads during phasic contraction.

Moriya and Miyazaki (1982) began their investigation on guinea pig corpus circumferential smooth muscle tissue by comparing the resulting phasic contractions under AC field stimulations of different frequencies and durations. They discovered that the circumferential smooth muscle is maximally stimulated at 200 Hz AC, 5 V cm^{-1} for five seconds. The contractile stress reached its peak at the end of electrical excitation before diminishing (Figure 5.9a, empty triangle). They also determined that the rate of tension increment was highest at 1.5 s after stimulation.

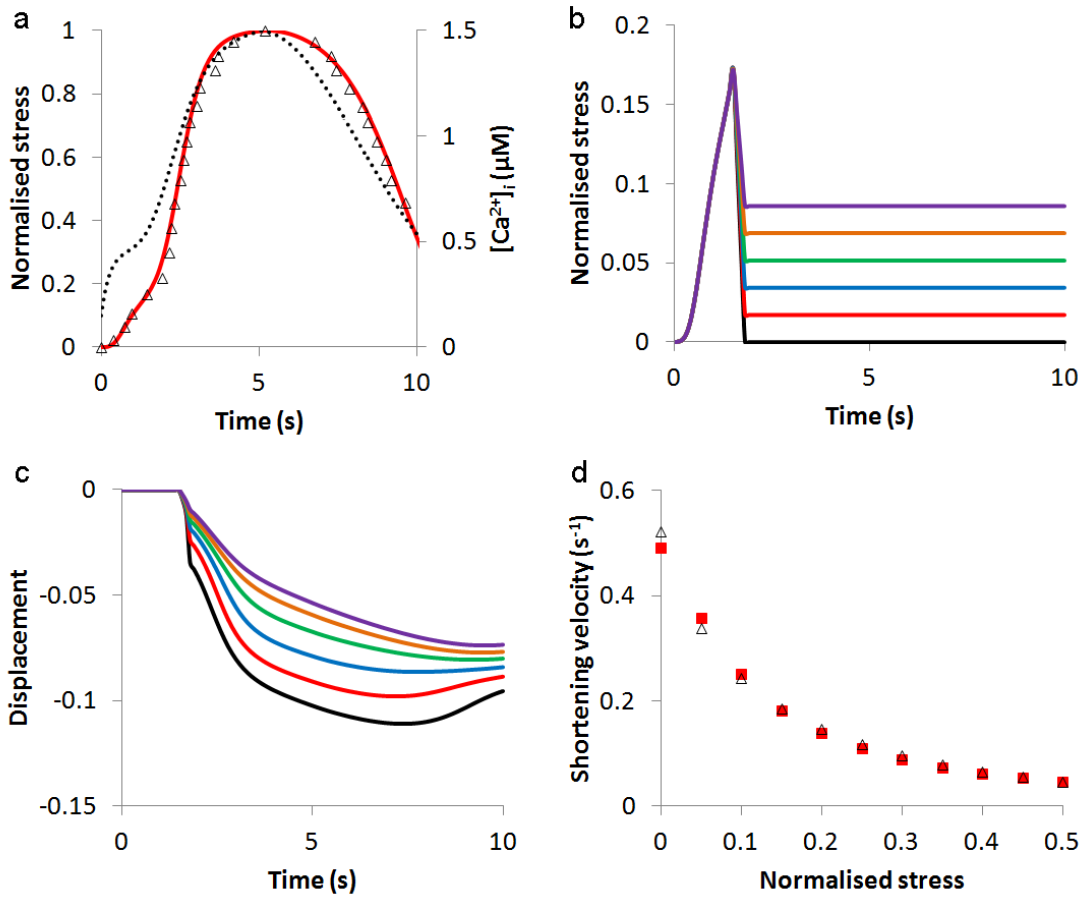

Figure 5.11 Simulating isotonic shortening of guinea pig corpus circumferential smooth muscle during phasic contraction. (a) Simulated $[Ca^{2+}]_i$ (dotted line) and force transients (red line) when the smooth muscle is stimulated with 200 Hz AC, 5 V cm^{-1} for 5 s. Experimental data is denoted by empty triangles. Variations of (b) stress and (c) shortening velocity with time when the tissue is released from isometric position at $t = 1.5$ s. Magnitudes of afterloads are expressed as percentages of isometric stress and indicated by different colour lines: 0% (black), 10% (red), 20% (blue), 30% (green), 40% (orange) and 50% (purple). (d) Velocity-load relation of experimental (empty triangles) and simulation (filled squares) studies. Parameters of Hill's equation are provided in Table 5.1. Experimental data were extracted from literature (Moriya and Miyazaki, 1982). Modelling parameters are stated in Appendices D and E.

To model the force transient, the electrically activated GI smooth muscle $[Ca^{2+}]_i$ was assumed to vary according to the following formulation:

$$[\mathrm{Ca}^{2+}]_i(t)$$

$$= \begin{cases} [\mathrm{Ca}^{2+}]_{rest}, & t < t_{start} \\ [\mathrm{Ca}^{2+}]_{rest} + \Delta[\mathrm{Ca}^{2+}] \times \left(\dfrac{0.8(t - t_{start})^{4.5}}{(t - t_{start})^{4.5} + 59.0} + 0.23\{1 - \exp\left[-3.7(t - t_{start})\right]\} \right), & t_{start} \le t \le t_{peak} \\ [\mathrm{Ca}^{2+}]_{rest} + \Delta[\mathrm{Ca}^{2+}] \exp\left[-0.05\left(t - t_{peak}\right)^2\right], & t_{peak} < t \le t_{end}. \end{cases} \quad (5.45)$$

The parameters for Equation (5.45) are illustrated in Table E.2. As shown in Figure 5.11a, $[Ca^{2+}]_i$ rises before force development which agrees with Figure 5.5. The $[Ca^{2+}]_i$ accumulation is biphasic with a rapid rise in the initial 1.5 s modelled by the exponential function in Equation (5.45), and a subsequent gentler increment until $t = 5.0$ s. In contrast, the force development is initially slow before accelerating after 1.5 s.

In the second part of the study, the investigators aimed to obtain the fastest shortening velocity during phasic contraction (Moriya and Miyazaki, 1985). AC field stimulation (200 Hz, 5 V cm^{-1}, 5 s) was applied to corpus circumferential smooth muscle while it was held isometrically. The muscle was then released with an isotonic afterload, which varied from 0% to 50% of the isometric force, at the instance of highest rate of force development, that is, 1.5 s after stimulation.

The quick-release study was simulated by converting the GI smooth muscle model from an isometric position to isotonic shortening within 0.3 seconds (Figure 5.11b). The resulting displacement was downward sloping before reversing at eight to ten seconds after stimulation (Figure 5.11c). At that instance, the active force was too weak to counter the afterload and compressive resistance. From the simulation study, the largest shortening displacement, recorded from the case of zero afterload, was 11.1%.

Table 5.1 Hill's equation parameters obtained from experimental and simulation studies on guinea pig corpus circumferential smooth muscle. V_{max} is maximum shortening velocity with no afterload; a/P_0 and b are Hill's equation parameters, refer to Section 3.4.1 for details.

Study	V_{max}(s^{-1})	a/P_0	b (s^{-1})
ANVS	0.491	0.109	0.054
Moriya and Miyazaki (1985)	0.576 ± 0.167	0.107 ± 0.036	0.056 ± 0.009

The shortening velocity varies with the isotonic load in a hyperbolic fashion (empty triangle, Figure 5.9d). In fact, Moriya and Miyazaki (1985) found that the force-velocity relation of corpus smooth muscle obeys the Hill's equation (see Equation (3.25)). A similar outcome was obtained from the ANVS model (filled square, Figure 5.11d). The parameters of Hill's equation obtained from both the experimental and simulation studies are given in Table 5.1.

5.5 Simulating tonic contraction of GI smooth muscle

5.5.1 Tonic contraction under isotonic conditions

GI smooth muscle tone provides physical reinforcement to the wall tissue and facilitates the containment of pressure and load during digestion. The role of Ca^{2+}-dependent contraction mechanism in influencing the tonic contraction can be elucidated by the ANVS model.

Gerthoffer and co-workers (1991) isolated circumferential smooth muscle tissue from the canine proximal colon and activated it with a depolarising solution, which contained 60 mM of K^+. The depolarising solution initiated tonic contraction in the colonic smooth muscle. The muscle was stimulated for 10 minutes before being

quickly released to an isotonic load ranging from 5% to 60% of the maximum isometric stress.

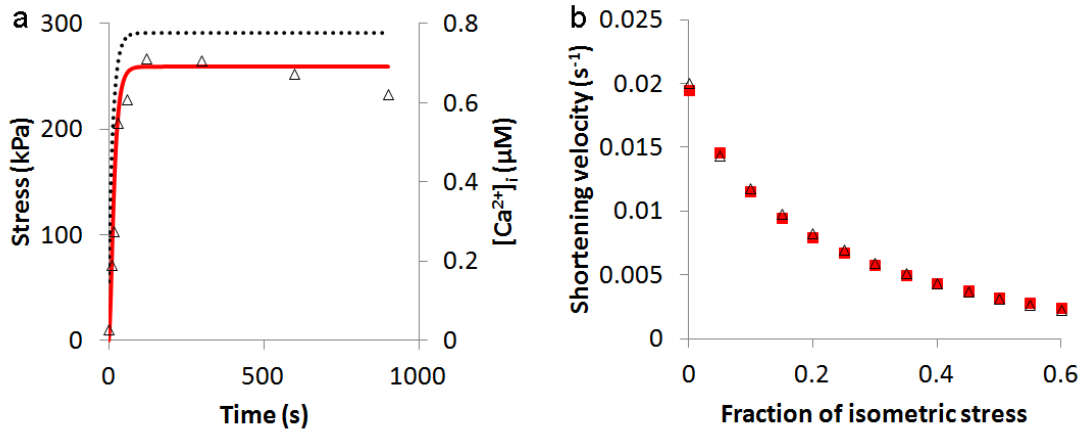

Figure 5.12 Simulating tonic contraction of colonic smooth muscle induced by high [K^+] solution. (a) The [Ca^{2+}]$_i$ (black dotted line) and stress (red filled line) transients are modelled by ANVS. Black empty triangles denote stress values obtained from experiment. (b) The shortening velocities are obtained from releasing the stationary smooth muscle at 600 s after stimulation in both experiment (black empty triangles) and simulation (red filled squares). The isotonic loads are expressed as fractions of isometric stress just before release. Experimental data are extracted from literature (Gerthoffer *et al.*, 1991). Modelling parameters are stated in Appendices D and E.

The investigators recorded the fraction of phosphorylated myosin through immunoblotting before the isotonic release (Table 5.2). The information can be translated to [Ca^{2+}]$_i$ = 0.777 μM using the Gajendiran and Buist (2011) model. To mimic the tonic tension production at the initial stage (Figure 5.12a), the [Ca^{2+}]$_i$ was assumed to increase exponentially such that

$$[\mathrm{Ca}^{2+}]_i(t) = \begin{cases} [\mathrm{Ca}^{2+}]_{rest}, & t < t_{start} \\ [\mathrm{Ca}^{2+}]_{rest} + \Delta[\mathrm{Ca}^{2+}]\{1 - \exp[-k_{rise}(t - t_{start})]\}, & t \geq t_{start} \end{cases}. \quad (5.46)$$

Table 5.2 Hill's equation parameters obtained from experimental and simulation studies on canine proximal colonic circumferential smooth muscle. $V_{\max}$ is maximum shortening velocity with no afterload; a/σ_0 and b are Hill's equation parameters, refer to Section 3.4.1 for details.

Study	σ_0 (kPa)	Fraction of myosin phosphorylation	$V_{\max}$ (s^{-1})	a/σ_0	b (s^{-1})
ANVS	259	0.234	0.019	0.285	0.0049
Gerthoffer *et al.* (1991)	259 ± 33	0.233 ± 0.023	0.020 ± 0.002	0.275 ± 0.040	0.0049 ± 0.0005

The parameters of Equation (5.47) are listed in Table E.3. A series of isotonic releases with different afterloads were simulated at $t = 600$ s. The resulting shortening velocities are shown in Figure 5.12b. The simulation results illustrated an inverse load-velocity hyperbolic relation which follows the Hill's equation. The Hill's equation parameters determined from both the experiment and simulation are stated in Table 5.2.

5.5.2 Tonic contraction and dynamic stiffness

Smooth muscle is stiffened during activation due to increased cross-linking between myosin heads and actin binding sites. As illustrated in Section 3.2.3, a wide range of frequencies have been used to test the dynamic response of smooth muscle. In particular, low frequencies are applicable for testing GI smooth muscle dynamic stiffness as its contraction cycles range from three to twelve cycles per minute, that is, 0.05 to 0.2 Hz. GI smooth muscle can also be subjected to extension and compression at a variety of strain rates. These mechanical perturbations originate from electrical signals or externally applied forces.

Comelekoglu and Ozturk (2008) applied sinusoidal length perturbations on relaxed guinea pig taenia coli tissues as well as contracted ones, which were treated with 60 mM KCl. The tissues were oscillated at 0.5% peak-to-peak strain with frequencies ranging from 0.0007 Hz to 1Hz. The investigators observed sinusoidal force oscillation in both samples (Figure 5.13). The amplitude of force was greater in contracted tissue than the passive tissue. The force amplitude also increased positively with the oscillating frequency.

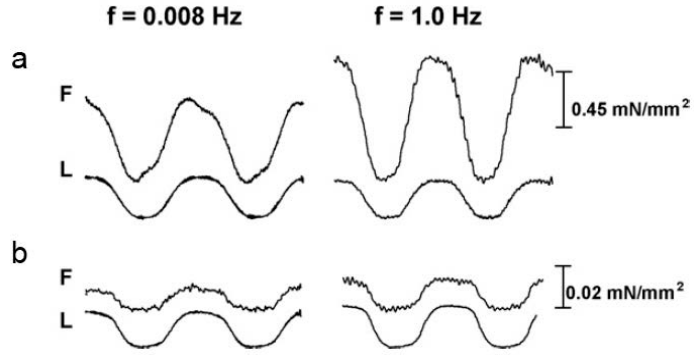

Figure 5.13 Responses of passive and active guinea pig taneia coli tissues under oscillating strains at different frequencies. Sinusoidal length perturbation (L) was applied to the tissue and the force (F) waveform was obtained. The tissue was either (a) activated with 60 mM KCl or (b) remained passive. Two perturbing frequencies at 0.008 Hz and 1.0 Hz are shown. The average stress is 5.03 ± 0.09 mN/mm^2. (Source: Comelekoglu and Ozturk, 2008)

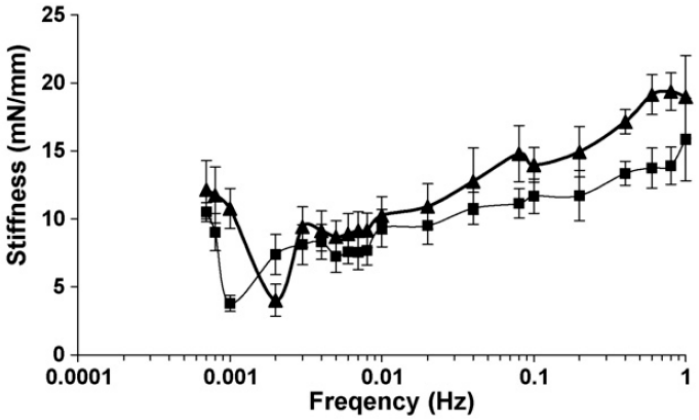

Figure 5.14 Dynamics stiffness of guinea pig taenia coli tissue treated with 60 mM KCl Two methods, sinusoidal (square) and step (triangle) length perturbations, were employed by the investigators in determining the stiffness. (Source: Comelekoglu and Ozturk, 2008)

The stiffness of the tissue was computed by dividing the magnitude of stress to that of strain. The stiffness was shown to be related to oscillating frequency in a power-law manner (Figure 5.14).

The experimental protocol was applied to the ANVS mammalian colonic smooth muscle model to determine its frequency response. Sinusoidal strain functions of amplitude 0.1% strain and frequency 0.01 Hz to 1 Hz were applied to perturb the stimulated smooth muscle model with $[Ca^{2+}]_{peak}$ = 0.300 μM, 0.500 μM and 0.777 μM. The $[Ca^{2+}]_i$ transient was modelled using Equation (5.47). A typical stress-time graph is shown in Figure 5.15a. The steady-state stress waveform was also sinusoidal (Figure 5.15b) which agreed with the experimental observations (Figure 5.13b).

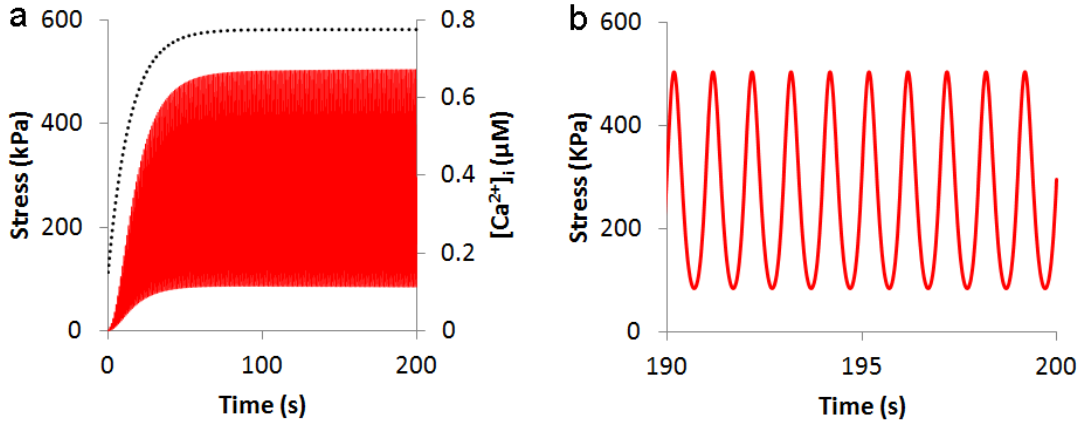

Figure 5.15 Dynamic stress of the colonic smooth muscle under strain perturbation at 1 Hz as simulated by ANVS with maximum $[Ca^{2+}]_i$ = 0.777 μM. (a) The $[Ca^{2+}]_i$ (black dotted line) and stress (red filled line) transients during perturbation are illustrated. (b) A closer examination of stress waveform at steady-state. The peak-to-peak dynamic stress was used in the computation of dynamic stiffness. Modelling parameters are stated in Appendices D and E.

To calculate the active dynamic stiffness, the ratio between the steady-state peak-to-peak stress to the modulus of the strain function was obtained at 200 s after starting of stimulation. In general, the ANVS model showed greater stiffness with higher $[Ca^{2+}]_i$ (Figure 5.16). The result was comparable to the higher dynamic stiffness shown in

contracted taneia coli than relaxed tissue (Figure 5.13). The stiffness of toad stomach SMC has also been reported to be positive correlated with the extra-cellular calcium concentration which in turn affects $[Ca^{2+}]_i$ (Yamakawa *et al.*, 1990).

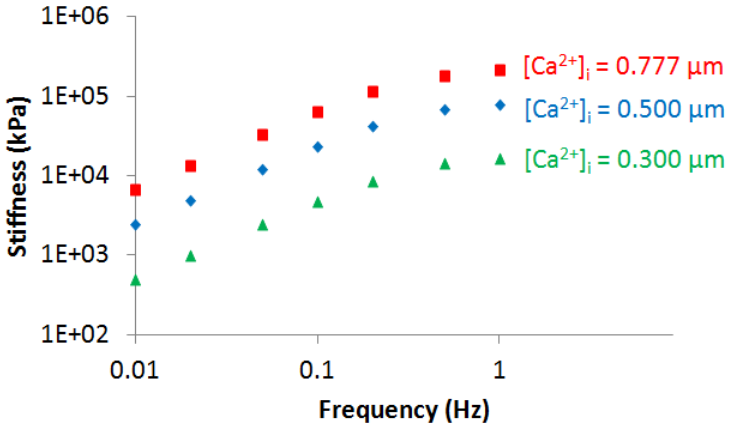

Figure 5.16 Dynamic stiffness of activated mammalian colonic smooth muscle obtained from ANVS simulation. Stiffness of smooth muscle at $[Ca^{2+}]_i$ = 0.300 µM (green), $[Ca^{2+}]_i$ = 0.500 µM (blue) and $[Ca^{2+}]_i$ = 0.777 µM (red) under strain perturbation of amplitude 0.001 and frequency 0.01 Hz to 1 Hz as simulated by ANVS. All three data sets can be fitted by a power-law model $y = ax^n$ such that the exponents are 0.791, 0.783 and 0.781 for $[Ca^{2+}]_i$ at 0.300 µM, 0.500 µM and 0.777 µM, respectively. Modelling parameters are stated in Appendices D and E.

The stiffness magnitude also increased with frequency in a power-law ($y = ax^n$) manner from 0.01 Hz to 1 Hz, which agrees with several experimental observations conducted on airway and colonic smooth muscles (Maksym *et al.*, 2000; Comelekoglu and Ozturk, 2008). The power-law exponents were found to be 0.791, 0.783 and 0.781 for $[Ca^{2+}]_i$ at 0.300 µM, 0.500 µM and 0.777 µM, respectively.

5.6 Discussion

5.6.1 Model structure

The active nonlinear viscoelastic solid is a novel mathematical model that encompasses passive and active mechanical components. The compact model framework is expressed as a single ODE which can be incorporated in a larger scale

model with minimal computational cost. The general ANVS framework also permits flexibility such that different mathematical relations can be applied to define the unique mechanical properties of a material. The structure of ANVS adheres to the notion that the total stress applied to a material, such as smooth muscle, is the aggregate of passive and active stresses (Fung, 1993). Therefore, when the material is not activated, it reverts to the nonlinear viscoelastic solid model.

A piece-wise implementation of NVS has been developed in Chapter 4 and it has been applied to describe smooth muscle viscoelasticity in compression. The implementation makes the study of the influence of compressive mechanical resistance on smooth muscle contraction, which has not been implemented in previous models, possible. Although the symmetrical compression implementation is only validated with skeletal muscle data due to a lack of similar studies in smooth muscle, it improves the quality of the simulation, and facilitates the computational assessment of smooth muscle mechanics over the full range of unilateral (tensile and compressive) deformation in ANVS.

The ANVS model has been used to simulate the mechanical properties of GI smooth muscle. The three ACC components in ANVS model denote the biomechanical roles of attached cross-bridges and latch-bridges in smooth muscle: the generation of active stress due to cross-bridge cycle and actin-myosin filament sliding (CCC), the active stiffness caused by increased protein cross-linking during activation (BCC), and the energy dissipation due to bonding and sliding between myosin heads and actin binding sites (FCC). Although these roles have been discussed in the literature and selected ones have been applied in past models, ANVS is the first model that encompasses all of them in separate elements. Elastic and viscous elements are employed to represent the cross-bridge stiffness and viscosity, so that the active

components can combine seamlessly with the NVS to provide a homogeneous structure.

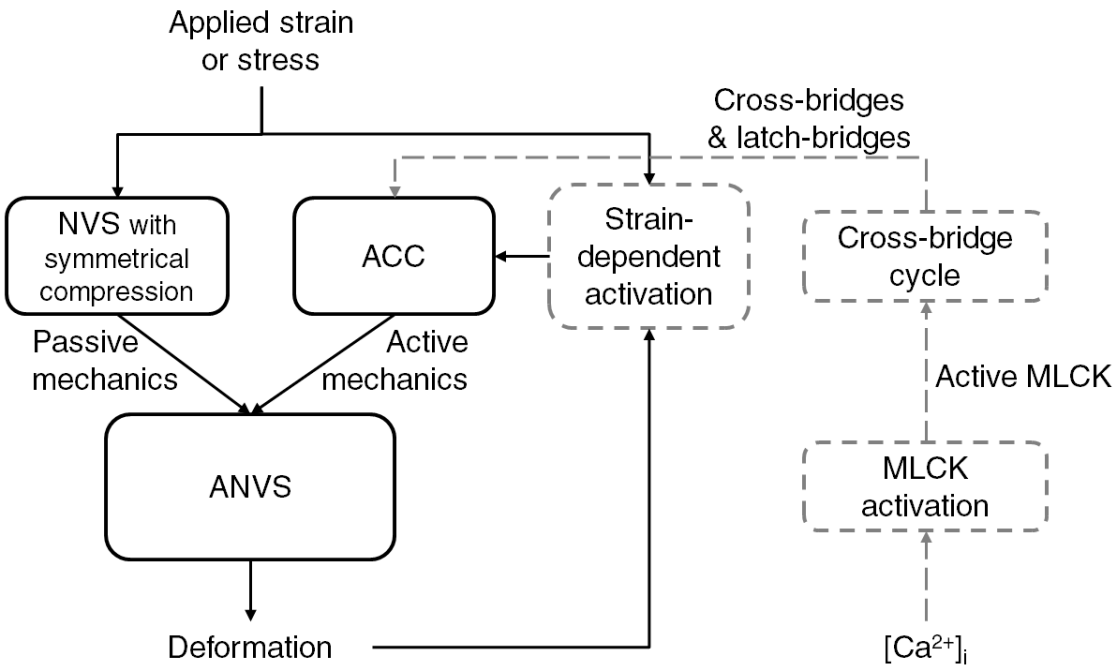

Figure 5.17 Overview of the ANVS model. The ANVS comprises both NVS and the ACC which take in the applied stress or strain, and quantity of cross-bridges and latch-bridges as inputs. The ANVS is supported by components developed by other investigators (grey rectangles with broken boundary). These components are strain-dependent activation component (Gestrelius and Borgström, 1986), as well as cross-bridge cycle and MLCK activation components (Gajendiran and Buist, 2011).

As a stand-alone mechanics model, the ANVS receives inputs in the forms of the applied stress or strain, and the quantity of attached cross-bridges and latch-bridges to simulate the resulting deformation (Figure 5.13). The inclusion of smooth muscle cross-bridge models, such as the Gajendiran and Buist (2011) model, enables ANVS to demonstrate $[Ca^{2+}]_i$-dependent smooth muscle contraction (grey boxes and broken line in Figure 5.13). The coupling also allows the ANVS to demonstrate the mechanical response of smooth muscle under the influence of both mechanical (stress and strain) and biochemical ($[Ca^{2+}]_i$) stimuli.

5.6.2 Simulation of GI smooth muscle mechanics

Phasic contraction

Waves of contractile force are generated by the smooth muscle in the GI wall tissue in the form of phasic contractions. These contractions are closely coordinated in both space and time, which leads to effective digestive processes such as segmentation and propulsion of a bolus. As such, close control of GI contraction through the manipulation of intra-cellular calcium concentration is necessary. The magnitudes and waveforms of $[Ca^{2+}]_i$ are highly correlated with the activated GI smooth muscle force transients which suggests a Ca^{2+}-dependent mechanism dominates the phasic contractile process (Figure 5.5). This mechanism has been theorised and modelled by several investigators (Hai and Murphy, 1988b; Yang *et al.*, 2003b; Bursztyn *et al.*, 2007). Experimental observations have also indicated that the fraction of phosphorylated myosin is correlated with the force development. Overall, the evidence suggests the role of Ca^{2+}-dependent mechanism in determining the quantity of fast cycling phosphorylated cross-bridges, which are responsible for phasic contraction.

The ANVS model can illustrate the interaction of active and passive mechanics in GI smooth muscle. However, the model is unable to demonstrate the temporary disappearance of spontaneous contraction after sudden stretching reported by Price and colleagues (1977) (Figure 5.8a versus Figure 5.7a). The limitation suggests the possible involvement of mechano-sensitive ion channels and mechanical feedback mechanism which is not considered in ANVS (Farrugia *et al.*, 1999).

A $[Ca^{2+}]_i$ transient has been generated from the observed force transient in phasic contraction using the Gajendiran and Buist (2011) model (Figure 5.11a). The deduced

$[Ca^{2+}]_i$ graph is biphasic. A rapid intra-cellular accumulation of Ca^{2+} ions takes place within the first second of electrical stimulation, accompanied by a gentle rate of force development. Subsequently, as the rate of $[Ca^{2+}]_i$ decelerates, the force production quickens. The simulation result indicates a minimum threshold of $[Ca^{2+}]_i$, at approximately 0.5 μM, above which a strong contractile force is produced. Similar observations have been reported by Ozaki *et al*. (1991b) who induced phasic contraction in mammalian smooth muscle. The initial accumulation of Ca^{2+} ions is thought to be necessary for the activation of MLCK which affects the rate of phosphorylation of myosin and consequent formation of cross-bridges. Furthermore, both the simulated and experimental shortening velocities recorded at 1.5 s after stimulation varies with the isotonic loads in a hyperbolic manner in agreement with Hill's equation (Figure 5.11d). The result affirms the close relation between $[Ca^{2+}]_i$ and mechanical properties of GI smooth muscle during phasic contraction.

Tonic contraction

GI smooth muscle tonic contraction provides the extra stiffness to GI wall tissues additional to its passive tension and material properties. A sustained tonic stiffness is essential for maintaining the shape of hollow GI organs which are filled with food contents during digestion. Although the smooth muscle tonic contraction also originates from attached cross-bridges and latch-bridges, the regulation mechanism is reported to be different from that of phasic contraction. Both $[Ca^{2+}]$-dependent and $[Ca^{2+}]$-independent (such as protein kinase C) signalling pathways are reported to be involved in tonic contraction (Horowitz *et al.*, 1996b).

The $[Ca^{2+}]_i$ transient for colonic smooth muscle tonic contraction has been recreated using the force profiles obtained by Gerthoffer *et al.* (1991). In these simulations,

$[Ca^{2+}]_i$ increases monotonically with a steady-state concentration of 0.777 μM. The $[Ca^{2+}]_i$ graph precedes and resembles to the force transient as in phasic contraction. Both the experimental and simulation results show hyperbolic force-velocity relations are obtained after ten minutes of tonic contraction. The result from ANVS supports the notion that $[Ca^{2+}]$-dependent mechanism is involved in tonic contraction. Several investigators have reported initial biphasic phosphorylated myosin transients during tonic tension development (Gerthoffer and Murphy, 1983; Kamm and Stull, 1985; Rembold and Murphy, 1988). As the rate of myosin phosphorylation relates positively with MLCK activation, which is influenced by magnitude of $[Ca^{2+}]_i$, the indirect evidence implies that the initial $[Ca^{2+}]_i$ is possibly biphasic (Hai and Murphy, 1988b). We have attempted to introduce biphasic $[Ca^{2+}]_i$ waveform into ANVS but with a biphasic input it was unable to reproduce monotonic tonic stress transients. The discrepancy can be possibly explained by the involvement of $[Ca^{2+}]$-independent mechanisms in tonic contraction, or other $[Ca^{2+}]$-dependent signalling pathways, such as CaMKII (Kim *et al.*, 2008).

The stiffness of colonic smooth muscle was simulated using length perturbations within the frequency range of 0.01 to 1 Hz. The stiffness-frequency relation agrees with the power-law structural damping model suggested by Fabry *et al*. (2001). The ANVS also illustrates different stiffness at distinct $[Ca^{2+}]_i$ levels. Shue and Brozovich (1999) measured the stiffness of isolated rabbit vascular SMC of different intra-cellular calcium concentrations by submerging them in pCa 4 activating solution for different durations. They observed an increment in stiffness as the duration was extended. The ANVS simulation result agrees with the experimental observation and illustrates the role of $[Ca^{2+}]$-dependent mechanism in determining compliance of GI wall tissue stiffness in tonic contraction.

5.7 Summary of ANVS

The development of ANVS, which can describe smooth muscle active mechanics, has been detailed in this chapter. The model is an extension of the NVS framework which provides the contribution of passive mechanics in ANVS. Important considerations in ANVS include the active stress, stiffness and viscous force supplied by the quantity of attached actomyosin, strain-dependent activation due to altering overlap between thick and thin filaments, and passive mechanics of compression.

By coupling with other smooth muscle cross-bridge cycle model, the ANVS can illustrate GI smooth muscle phasic and tonic contractions in which $[Ca^{2+}]$-dependent mechanisms are involved. The mechano-response of the coupled model is in line with the experimental findings. ANVS provides a useful avenue to improve our understanding of GI motility.

Chapter 6 Length-adaptive Active Nonlinear Viscoelastic Solid

6.1 Overview

Length adaptation is a mechanical phenomenon in which smooth muscle cells and tissues can adjust their mechanical properties as a result of a geometric change. It is closely related to the physiology of GI tract, which is tasked to operate at different mechanical states due to the distinct quantity and quality of ingested food material (Kraichely and Farrugia, 2007). For instance, aboral peristalsis in oesophagus persists even though the geometry, volume and weight of food contents are not identical; effective gastric reservoir and emptying functions occur for meals of different sizes; contractility of the small bowel is adapted to the intra-luminal pressure that builds up during segmentation; propulsion of material continues in large intestine even though the water content of waste differ. Collectively, it is plausible that length adaptation and other mechanical adaptive mechanisms enable the GI wall tissue to regulate its viscoelastic and contractile properties to fulfil the physiological roles of GI tract

For mammalian hollow organ systems other than the GI tract, their constituent smooth muscle mechanical properties are known to be adjustable according to the applied deformation. Canine tracheal smooth muscle can generate maximum contractile stress over a three-fold length range (Pratusevich *et al.*, 1995). Alterations of the active and passive force-length relations can occur within a day if rabbit tracheal smooth muscle is held at an altered length without other stimuli (Wang *et al.*, 2001). The modification process can be reduced to an hour by stimulating the smooth muscle

with electric field or submerging it in an activating bath solution (Naghshin *et al.*, 2003). Similar phenomena have been observed in rabbit detrusor and arterial smooth muscles (Speich *et al.*, 2009; Bednarek *et al.*, 2011). The empirical evidence suggests that the malleability of smooth muscle mechanical properties is conserved across different organ systems. The term length adaptation has been coined to describe the recovery of active stress and decay of passive stress over a wide range of muscle lengths (Bai *et al.*, 2004).

These experimental findings in smooth muscle tissue have also been shown to be scalable to the organ level. After demonstrating length adaptation in isolated rabbit detrusor tissue, Speich *et al.* (2012) illustrated volume adaptation in the distended mouse bladder. They measured the contractile pressure before and after filling the organ with additional fluid. The active pressure of the expanded bladder was weakened initially before being restored to the pre-inflation level. The result suggests that the physiology of other hollow organs may be similarly influenced by a smooth muscle length adaptation mechanism. Harris and Warsaw (1991) observed that isolated *Bufo marinus* gastric SMC can still exert maximum contractile stress at 40% extension. Using the same argument, it can be inferred that length adaption has a prominent role in the physiology of stomach.

The underlying mechanism of length adaptation remains elusive. Length adaptation can be initiated through inducing phasic contractions in smooth muscle (Almasri *et al.*, 2010a). This suggests the involvement of Ca^{2+}-dependent cross-bridge cycling. However, this is unlikely as the level of myosin light chain phosphorylation is unaltered during the adaptation process (Bednarek *et al.*, 2011). Blockage of Ca^{2+} influx has also been shown to have a negligible influence on length adaptation, but abolishing actin polymerisation can inhibit the adaptive process. Overall, the evidence indicates

the possible involvement of a Ca^{2+}-independent mechanism, such as protein kinase C signalling pathway, in smooth muscle length adaptation (Horowitz *et al.*, 1996a).

The existence of length adaptation in mammalian GI smooth muscle remains a hypothesis. Despite this, it appears that length adaptation is conserved across species and hollow organs, and therefore here the ANVS is extended to include length-adaptive active and passive mechanics. The improved model, termed Length-adaptive Active Nonlinear Viscoelastic Solid (LANVS), is then used to demonstrate observed experimental phenomena relating to length adaptation such as shifting of passive and active force-length relations, as well as the dynamics of active force recovery and passive force decay in a deformed smooth muscle tissue.

6.2 Model development

The phenomenon of length adaptation was first observed and investigated in toad stomach SMC and canine tracheal smooth muscle active contractions (Harris and Warshaw, 1991; Pratusevich *et al.*, 1995). Later, investigators discovered that smooth muscle passive mechanical properties were also influenced by alteration of muscle length (Wang *et al.*, 2001; Naghshin *et al.*, 2003). As such, the active force adaptation is introduced followed by its passive force counterpart.

6.2.1 Active force and length adaptation

Smooth muscle active stress is influenced by the portion of overlapping filaments, which changes according to the strain applied to the smooth muscle (Section 5.3.1). However, recent studies have shown that smooth muscle has the ability to re-attain its active contractile properties after prolonged deformation. This implies that the filament overlap is restored through length adaptation.

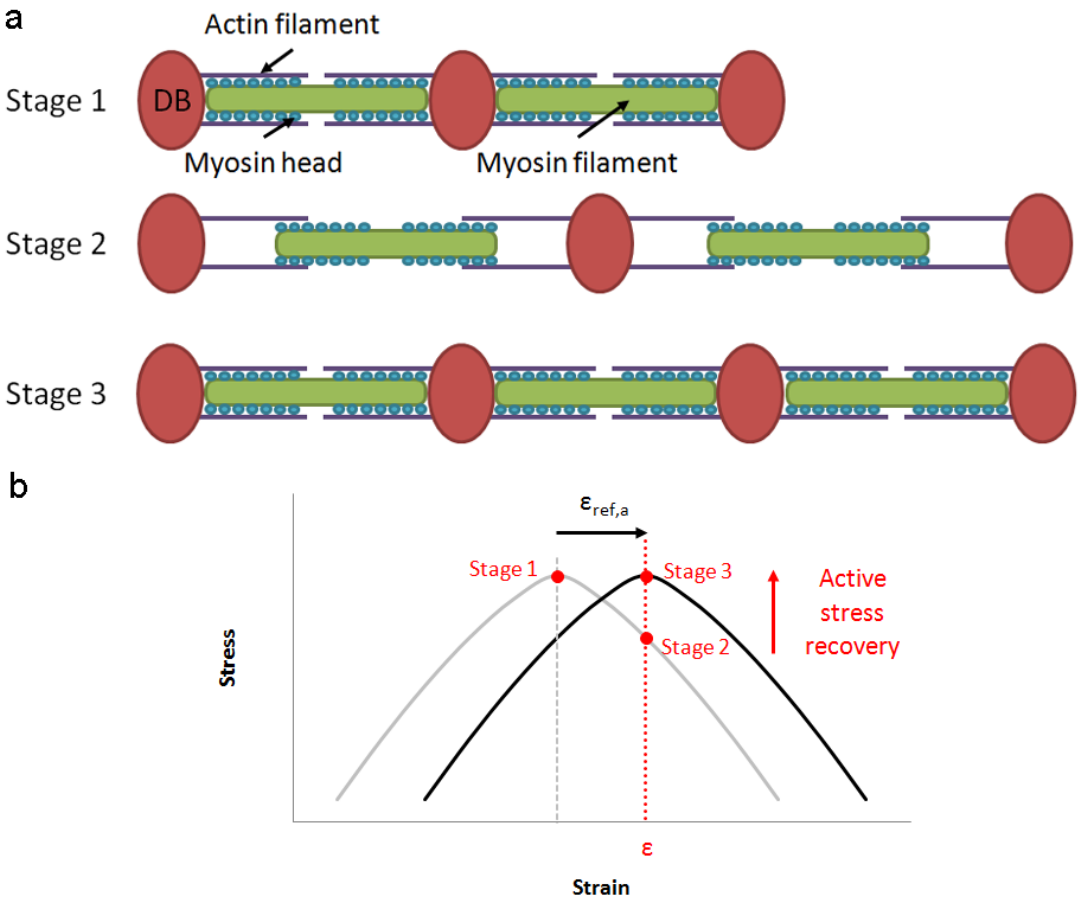

Figure 6.1 Dynamic of smooth muscle active mechanics influenced by length adaptation. (a) Illustration of contractile unit rearrangement during length adaptation. Maximum active stress is generated at pre-extension phase (Stage 1). Lengthening causes a decrement of active stress due to reduced overlap between myosin and actin filaments (Stage 2). Serial addition of contractile units allows restoration of both the overlap and active stress (Stage 3). DB: dense body. (b) Active stress regeneration in Stage 1 to Stage 3 is shown by movement and translation of active stress-strain graph. Extension of smooth muscle to strain ε causes a dip in active stress (movement along grey graph from Stage 1 to Stage 2). Rearrangement of the contractile units is represented by translation of the graph towards right (from grey to black). The translation leads to a recovery of active stress from Stage 2 to Stage 3. The horizontal shifting of active stress-strain is quantified by the movement of active stress reference strain ($\varepsilon_{ref,a}$) in LANVS.

Modification to the intra-cellular structure allows SMC to adjust its mechanical properties in response to a new deformation (Bosse *et al.*, 2008; Seow and Fredberg, 2010). Reassembly of the contractile units can be inferred from the observed variability of actin and myosin filament contents during smooth muscle readjustment to a new length (Kuo *et al.*, 2001; Herrera *et al.*, 2004). In the case of smooth muscle

lengthening, the process leads to a serial addition of contractile units and, consequently, an extension of the contractile element (Fig 6.1a). Conversely, a serial-to-parallel reconfiguration of contractile apparatus occurs when the smooth muscle is shortened from its initial length (Seow *et al.*, 2000). The force-velocity properties and isometric contraction profiles evaluated from the reference and length adapted smooth muscles are also in support of this postulation (Herrera *et al.*, 2005).

At this juncture, it is important to clarify that the term optimum strain originates from biomechanical studies on striated muscle, whose active stress versus strain graph and optimum strain are relatively stable (Bai *et al.*, 2004). However, as the smooth muscle's optimum strain, that is, the strain at which the maximum contractile stress occurs, is adjustable due to contractile element reassembly, the entity is renamed here as the active stress reference strain ($\varepsilon_{\mathrm{ref,a}}$).

The position of $\varepsilon_{\mathrm{ref,a}}$ represents the location of active stress-strain relation in relative to the current strain, ε (Figure 6.1b). It also signifies the SMC's adaptive state and contractile apparatus configuration in relation to the present deformation. As the smooth muscle grows accustomed to the new length, $\varepsilon_{\mathrm{ref,a}}$ moves towards ε. This movement leads to the recovery of maximum active stress. Experimental results have revealed that the active force recovers in an exponential manner (Pratusevich *et al.*, 1995; Wang *et al.*, 2001; Naghshin *et al.*, 2003; Chin *et al.*, 2012). Therefore, the rate at which $\varepsilon_{\mathrm{ref,a}}$ approaches ε, can be represented by

$$\frac{d\varepsilon_{\mathrm{ref,a}}}{dt} = \frac{\varepsilon - \varepsilon_{\mathrm{ref,a}}}{\tau_{\mathrm{a}}} \tag{6.1}$$

where τ_{a} corresponds to the active stress reference strain time constant.

The re-attainment of actin-myosin overlap through length adaptation leads to the restoration of available free myosin heads and actin binding sites ($\bar{n}_{ac}$). To incorporate the effect of length adaptation in the computation of $\bar{n}_{ac}$, Equations (5.26) and (5.27) are therefore rewritten as

$$\bar{n}_{ac} = 1 - a_n\left|\varepsilon - \varepsilon_{\mathrm{ref,a}}\right|^{b_n} \tag{6.2}$$

$$\frac{d\bar{n}_{ac}}{dt} = -a_n b_n\left|\varepsilon - \varepsilon_{\mathrm{ref,a}}\right|^{b_n-1}\left(\dot{\varepsilon} - \dot{\varepsilon}_{\mathrm{ref,a}}\right)\mathrm{sgn}\left(\varepsilon - \varepsilon_{\mathrm{ref,a}}\right) \tag{6.3}$$

where a_n and b_n are arbitrary constants.

In the ANVS model, the GI smooth muscle active mechanical properties are governed by a linear CCC, exponential BCC and linear FCC with subscripts cc, bc and fc, respectively (Figure 5.3). The stress generated or stored in each component is influenced by smooth muscle deformation, which can be adjusted through the rearrangement of the contractile units. As such, Equations (5.35), (5.36) and (5.39) are restated such that

$$\dot{\sigma}_{fc} = \bar{n}_{ac}\frac{\left[AM_p\right] + [AM]}{[M_{total}]}M_{fc}\dot{\varepsilon}_{fc} \tag{6.4}$$

$$\dot{\sigma}_{cc} = \frac{d\bar{n}_{ac}}{dt}\frac{\left[AM_p\right] + [AM]}{[M_{total}]}F_{cc} + \bar{n}_{ac}\frac{d}{dt}\left(\frac{\left[AM_p\right] + [AM]}{[M_{total}]}\right)F_{cc} \tag{6.5}$$

$$\begin{aligned}\dot{\sigma}_{mc} = \frac{d\bar{n}_{ac}}{dt}\frac{\sigma_{mc}}{\bar{n}_{ac}} + \frac{d}{dt}\left(\left[AM_p\right] + [AM]\right)\frac{\sigma_{mc}}{\left[AM_p\right] + [AM]} \\ + \gamma_{bc}\left(\sigma_{mc} + \bar{n}_{ac}\frac{\left[AM_p\right] + [AM]}{[M_{total}]}\delta_{bc}\right)\left(\dot{\bar{\varepsilon}} - \dot{\varepsilon}_{fc}\right).\end{aligned} \tag{6.6}$$

Variable $\dot{\varepsilon}$ is the time-derivative of difference between the passive stress reference strain and the current stain, which is introduced in more detail in the next section.

6.2.2 Passive force and length adaptation

The smooth muscle cytoskeleton is a mechano-responsive intra-cellular structure. For instance, applying an oscillatory shear stress to the surface of a SMC causes actin remodelling and reorganisation (Deng *et al.*, 2004). Adjusting the tonic contraction of smooth muscle also affects the mechanical properties of cytoskeleton induced by external strain (Deng *et al.*, 2005). When a uniaxial strain is applied to a SMC periodically, the myocyte re-orientates its long axis to be perpendicular to the deformation direction while the intra-cellular stress fibres realign to the longitudinal axis of the SMC (Smith *et al.*, 2000; Liu *et al.*, 2008). In addition, a reduction of cell stiffness and recovery has been observed in human bladder SMC when the cell was extended by 10% and then released to its initial length within four seconds (Chen *et al.*, 2010). The fluidisation-resolidification phenomenon was accompanied by a reduction and subsequent restoration of intracellular F-actin. Furthermore, after reducing the tensile force applied to a tracheal smooth muscle, it has been observed that the intermediate filaments are re-straightened to maintain the muscle stiffness (Zhang *et al.*, 2010). In summary, the above evidence suggests that SMC have the ability to remodel their cytoskeletal structure according to the applied deformation.

These studies indicate that smooth muscle passive mechanics is also dynamic and mechano-sensitive. A possible connection between smooth muscle cytoskeletal remodelling and its adjustable passive mechanics is proposed here. When the SMC is extended, the filament proteins, which form the structural network of SMC, are stretched (Figure 6.2a, green filament). The rise of tensile stress in some filaments

aggregates to increase the smooth muscle passive stress. Concurrently, reassembly of filaments and their organisations are initiated during length adaptation. The rearrangement facilitates a reduction of individual filament extension, and leads to a subsequent decay of passive stress.

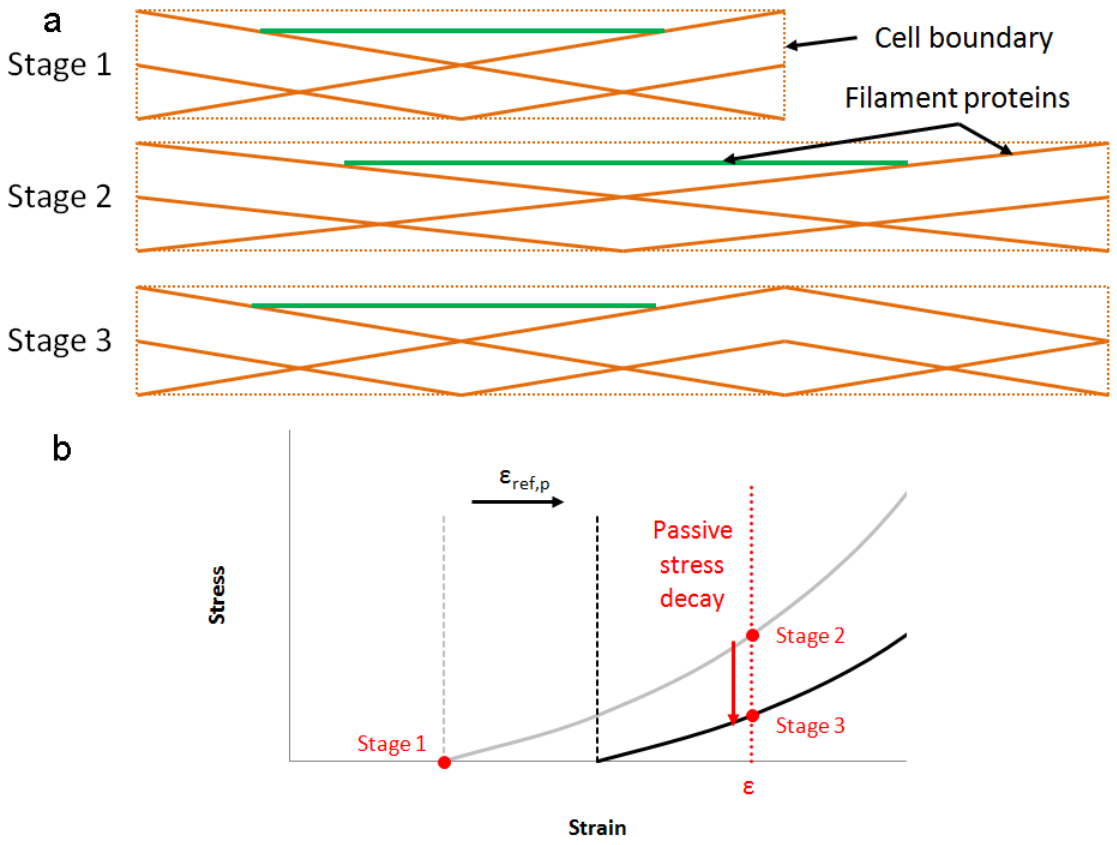

Figure 6.2 Dynamic of smooth muscle passive mechanics influenced by length adaptation. (a) Illustration of intra-cellular filament reorganisation during length adaptation. Minimum passive stress is generated at pre-extension phase (Stage 1). Lengthening causes an increment of passive stress due to filament stretching (Stage 2, green filament). Re-polymerisation of filament subunits leads to some filaments return to their initial lengths and passive stress reduction (Stage 3, green filament). (b) Variation of passive stress in Stage 1 to Stage 3 is shown by movement and translation of passive stress-strain graph. Extension of smooth muscle causes a rise in passive stress (movement along grey graph from Stage 1 to Stage 2). Reorganisation of the filaments is represented by translation of the graph towards right from grey to black. The translation leads to a decay of passive stress from Stage 2 to Stage 3 at strain ε. The horizontal shifting of passive stress-strain graph is quantified by the movement of passive stress reference strain ($\varepsilon_{ref,p}$) in LANVS.

In LANVS, a passive stress reference strain ($\varepsilon_{\mathrm{ref,p}}$) is defined to indicate the position at which the passive stress is zero (see Figure 6.2b). The passive stress reference strain is dynamic and associated with the smooth muscle filament configuration. The initial position of $\varepsilon_{\mathrm{ref,p}}$ is marked by the light grey vertical axis while the corresponding passive stress-strain relation is represented by the light grey graph. When the smooth muscle is extended to strain ε (red axis), the passive stress increases (red filled circles, Stage 1 to Stage 2). The difference between $\varepsilon_{\mathrm{ref,p}}$ and ε indicates the actual strain experienced by the filament structure. It is postulated that SMC aims to minimise the strain or stress applied on the filament structure, that is, $\varepsilon = \varepsilon_{\mathrm{ref,p}}$ (See Section 6.5.2). Therefore, the disparity between $\varepsilon_{\mathrm{ref,p}}$ and ε also suggests the current adaptive state of filament architecture with respect to the deformation. Reassembly of filament structure leads to a horizontal shift of the stress-strain graph and $\varepsilon_{\mathrm{ref,p}}$ towards ε (black filled graph and broken vertical axis), which results in a decay in passive stress (red filled circles, Stage 2 to Stage 3).

As experimental results have revealed that the passive force diminishes in an exponential manner (Pratusevich *et al.*, 1995; Wang *et al.*, 2001; Naghshin *et al.*, 2003; Chin *et al.*, 2012), the rate at which $\varepsilon_{\mathrm{ref,p}}$ approaches ε is represented as

$$\frac{d\varepsilon_{\mathrm{ref,p}}}{dt} = \frac{\varepsilon - \varepsilon_{\mathrm{ref,p}}}{\tau_{\mathrm{p}}} \tag{6.7}$$

where τ_{p} corresponds to the passive stress reference strain time constant.

To model the effect of length adaptation on the mammalian GI tissue viscoelasticity, the tri-exponential NVS model with symmetric compression from Equation (4.70) is modified such that

$$\dot{\sigma}_p + \dot{\sigma}_m = \alpha\beta \exp(\alpha|\bar{\varepsilon}|)\dot{\bar{\varepsilon}} + \gamma(\delta + |\sigma_v|)\left\{\dot{\bar{\varepsilon}} - \frac{\operatorname{sgn}(\sigma_v)}{\lambda} \ln\left[1 + \frac{|\sigma_v|}{\mu}\right]\right\} \tag{6.8}$$

$$\sigma_v = \sigma - \sigma_{cc} - \sigma_{mc} - \beta \operatorname{sgn}(\bar{\varepsilon})[\exp(\alpha|\bar{\varepsilon}|) - 1] \tag{6.9}$$

Variable $\bar{\varepsilon}$ is the difference between the current strain and the passive stress reference strain. The variables $\bar{\varepsilon}$, ε, $\varepsilon_{\mathrm{ref,p}}$ and their time-derivatives are related by the equations

$$\bar{\varepsilon} = \varepsilon - \varepsilon_{\mathrm{ref,p}} \tag{6.10}$$

$$\dot{\bar{\varepsilon}} = \frac{d\bar{\varepsilon}}{dt} = \frac{d\varepsilon}{dt} - \frac{d\varepsilon_{\mathrm{ref,p}}}{dt}. \tag{6.11}$$

Overall, the constitutive equation of the LANVS, which can demonstrate smooth muscle viscoelasticity, an active contractile response, and length adaptation is completed by aggregating Equations (6.5), (6.6) and (6.8) in the same manner as Equation (5.24), that is,

$$\dot{\sigma} = \dot{\sigma}_{cc} + \dot{\sigma}_{mc} + \dot{\sigma}_p + \dot{\sigma}_m. \tag{6.12}$$

$$\begin{aligned}\dot{\sigma} = {} & \frac{d\bar{n}_{ac}}{dt}\frac{[AM_p]+[AM]}{[M_{total}]}F_{cc} + \bar{n}_{ac}\frac{d}{dt}\left(\frac{[AM_p]+[AM]}{[M_{total}]}\right)F_{cc} \\ & + \frac{d\bar{n}_{ac}}{dt}\frac{\sigma_{mc}}{\bar{n}_{ac}} + \frac{d}{dt}\left([AM_p]+[AM]\right)\frac{\sigma_{mc}}{[AM_p]+[AM]} \\ & + \gamma_{bc}\left(\sigma_{mc} + \bar{n}_{ac}\frac{[AM_p]+[AM]}{[M_{total}]}\delta_{bc}\right)\left(\dot{\bar{\varepsilon}} - \dot{\varepsilon}_{fc}\right) \\ & + \alpha\beta\,\exp(\alpha|\bar{\varepsilon}|)\dot{\bar{\varepsilon}} \\ & + \gamma(\delta + |\sigma_v|)\left\{\dot{\bar{\varepsilon}} - \frac{\mathrm{sgn}(\sigma_v)}{\lambda}\ln\left[1 + \frac{|\sigma_v|}{\mu}\right]\right\}.\end{aligned} \tag{6.13}$$

6.3 Simulating the adaptation of smooth muscle mechanics after a prolonged passive deformation

The LANVS model can be verified by simulating the smooth muscle length adaptation experimental protocols and comparing the computational results with experimental outcomes. The length adaptation phenomena observed in chronic passive deformation is illustrated by LANVS in this section. The dynamics of smooth muscle length adaptation under electric field stimulation is demonstrated by the model in Section 6.4.

The adaptability of the mechanical properties of mammalian smooth muscle has been investigated and quantified by Wang and colleagues (2001). In their experiments, rabbit tracheal smooth muscle tissues were harvested and the samples were divided into three groups, namely the control group, passively shortened (PS) group and the passively lengthened (PL) group. In the control group, each tissue was straightened with minimum tension and was submerged in a bath filled with a physiological saline solution. The PS and PL samples were pre-shortened and pre-lengthened in tissue

baths, respectively. All tracheal tissues were refrigerated at 4 °C for 24 hours before commencing the experiment.

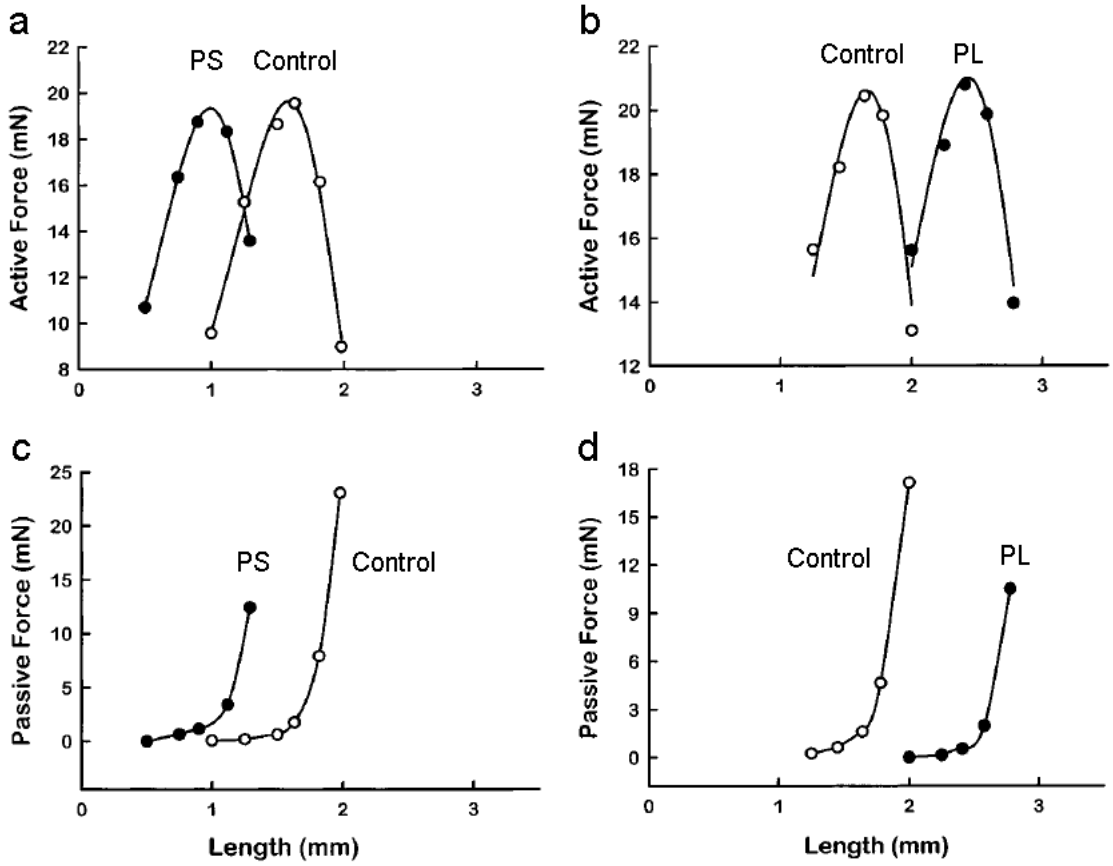

Figure 6.3 Length adaptation experimental results obtained from rabbit tracheal smooth muscle with or without applying chronic passive deformation. Top row shows the active force-length relations of (a) PS (filled circle) versus control (empty circle) groups, and (b) PL (filled circle) versus control (empty circle) groups. Bottom row shows the passive force-length relations of (a) PS (filled circle) versus control (empty circle) groups, and (b) PL (filled circle) versus control (empty circle) groups. The graphs are adopted from Figure 1 of Wang *et al.* (2001).

The experiments were performed in a 37 °C tissue bath in which each sample was first equilibrated at its initial length. The tissue was then stretched in a step-and-hold fashion every five minutes to record its active and passive length-tension properties. Electrical field stimulation was applied to generate contractile response from the tracheal samples. The investigators observed that the control, PS and PL could

generate similar active force-length relations (Figure 6.3a & b), indicating a shift of the active mechanical properties. Similarly, all groups could produce consistent passive force-length relations (Figure 6.3c & d) developed at different initial lengths.

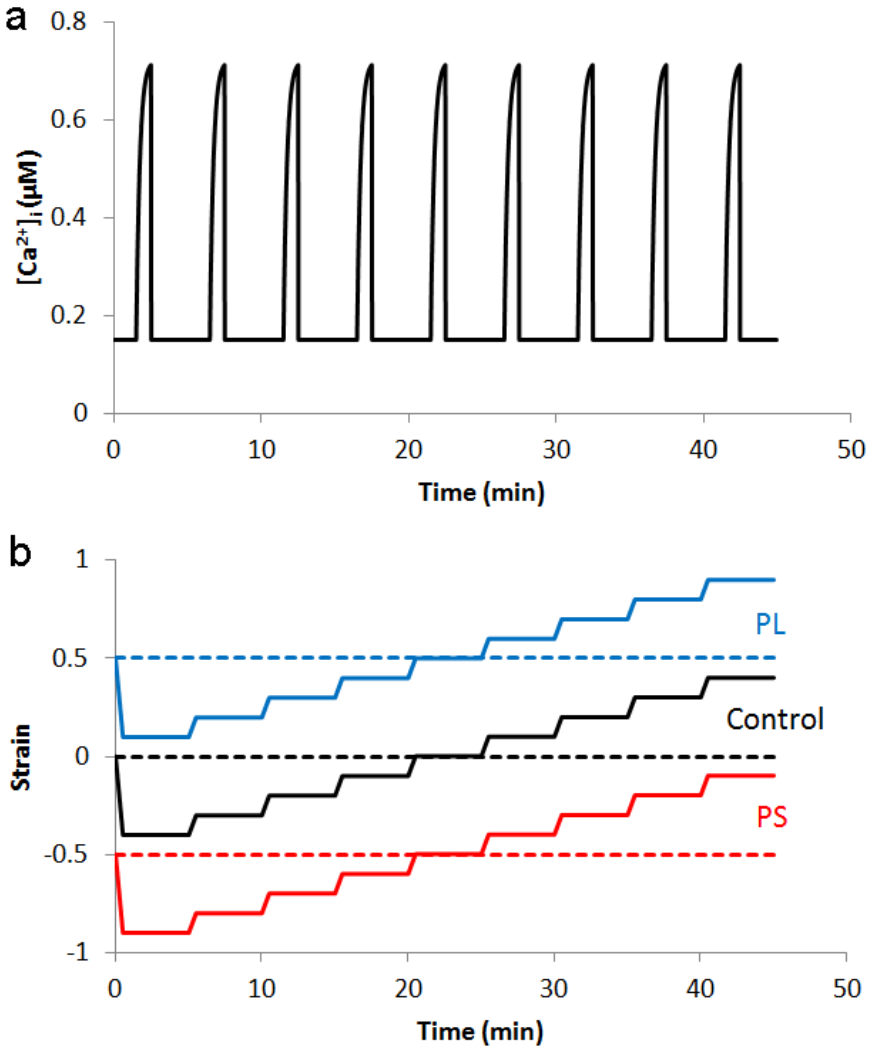

Figure 6.4 Simulating the adaptation of smooth muscle mechanics after a prolonged passive deformation. (a) Simulated variation of GI smooth muscle $[Ca^{2+}]_i$ due to electric field stimulation in five-minute intervals. (b) Simulated strain perturbations are (solid lines) applied to passively lengthened (PL, blue), control (Control, black) and passively shortened (PS, red) GI smooth muscle and simulated by LANVS. The positions of active stress reference strain and passive stress reference strain are identical and invariant within each sample (broken lines). Refer to Tables E.4 to E.6, E.8 and E.9 for the parameter values.

To simulate this experimental protocol being applied on GI tissue in LANVS, it was assumed that the active stress reference strains of the control, PS and PL tissues were 0.0, -0.5 and 0.5, respectively (Figure 6.4b). The active stress reference strains were assumed to be invariant during the experiment. A step stretch of 10% strain was applied every five minutes. The concurrent electric field stimulation performed in the experiment started at 60 seconds (t_{delay}) after completing each extension step and the excitation was assumed to last for 60 seconds (t_{peak}). The electrical excitation leads to an increment of $[Ca^{2+}]_i$ from resting level ($[\mathrm{Ca}^{2+}]_{rest}$) to peak level ($[\mathrm{Ca}^{2+}]_{peak}$) which was modelled by a monotonic exponential function (Figure 6.4a)

$$[\mathrm{Ca}^{2+}]_i(t) = \quad (6.14)$$

6.14)

where $\Delta[\mathrm{Ca}^{2+}]$ is defined as

$$\Delta[\mathrm{Ca}^{2+}] = [\mathrm{Ca}^{2+}]_{peak} - [\mathrm{Ca}^{2+}]_{rest}. \quad (6.15)$$

Parameter values of Equations (6.14) and (6.15) are presented in listed in Table E.4.

The active stress-strain graph of mammalian GI smooth muscle after being passively shortened for 24 hours was simulated using LANVS model. The translation of $\varepsilon_{\mathrm{ref,a}}$ from 0 to -0.5 allows the GI smooth mechanical model to generate maximum contractile stress at reduced length (Figure 6.5a). There is no alteration in the shape of the stress-strain graph. Similar results are computed using LANVS model for passively lengthened GI smooth muscle in which both the $\varepsilon_{\mathrm{ref,a}}$ axis and stress-strain graph translate to the right (Figure 6.5b). The experimental results performed on rabbit tracheal smooth muscle (Figures 6.3a and 6.3b) show similar phenomena

which support the simulation results. It is interesting to note that similar translation of active force-length relation has been observed in biomechanical experiments performed on toad gastric SMC (Harris and Warshaw, 1991).

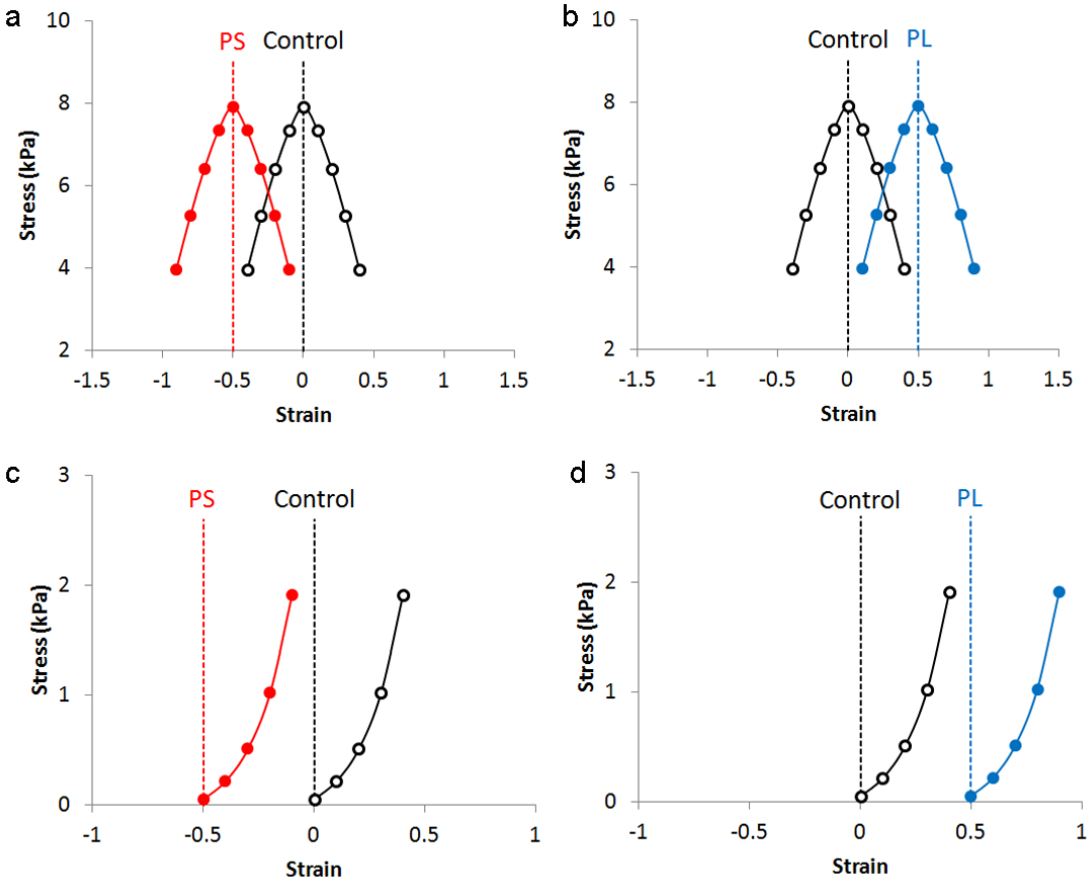

Figure 6.5 Simulation of GI smooth muscle steady-state active and passive length-force relations under the influence of length adaptation. Top row shows the active force-length relations of (a) PS (red filled circle) versus control (black empty circle) groups, and (b) PL (blue filled circle) versus control (black empty circle) groups. Bottom row shows the passive force-length relations of (a) PS (red filled circle) versus control (black empty circle) groups, and (b) PL (blue filled circle) versus control (black empty circle) groups.

The LANVS can also be used to predict the passive mechanical properties of GI smooth muscle undergoing PS treatment. A leftward movement of passive stress reference strain is accompanied by a comparable shift of passive stress-strain graph without any change in its slope (Figure 6.5c). Conversely, the LANVS predicts a

translation of $\varepsilon_{\mathrm{ref,p}}$ axis and stress-strain graph towards the right for GI smooth muscle in the PL group (Figure 6.5d). The experimental data recorded from rabbit tracheal smooth muscle also give support to the LANVS simulation results (Figure 6.3c and 6.3d).

6.4 Simulating the dynamics of smooth muscle length adaptation

6.4.1 Time constants for length adaptation

To model the dynamics of smooth muscle length adaptation, it is paramount to quantify the rates of active force recovery and passive force decay. However, as length adaptation experiments on mammalian GI smooth muscle have not been conducted previously, it is postulated that the GI smooth muscle length adaptation dynamics and the underlying mechanism are similar to that found in mammalian tracheal smooth muscle.

In another experiment, Wang *et al.* (2001) investigated the active force restoration and passive force decline in smooth muscle tissue which was separated from rabbit trachea. The tissue was shortened to 20% of its *in situ* length initially before being re-stretched in steps of 20% strain at five-minute intervals. Concurrently, electrical field stimulation of 60 Hz AC was applied to the smooth muscle at the same interval. The active force and passive force of the smooth muscle were measured after each extension, and both increased initially. The maximum active force was recorded near to the in situ length of the tissue, beyond that it started to decrease while the passive force continued to rise. The smooth muscle extension was halted at the decreasing portion of the active force-length graph while the electrical stimulation continued to be

applied. While the tissue remained under an isometric loading condition, the investigators observed a recovery of active force to its maximum (Figures 6.6a and 6.6b), and a simultaneous decay of passive force (Figures 6.6c and 6.6d) in 35 minutes.

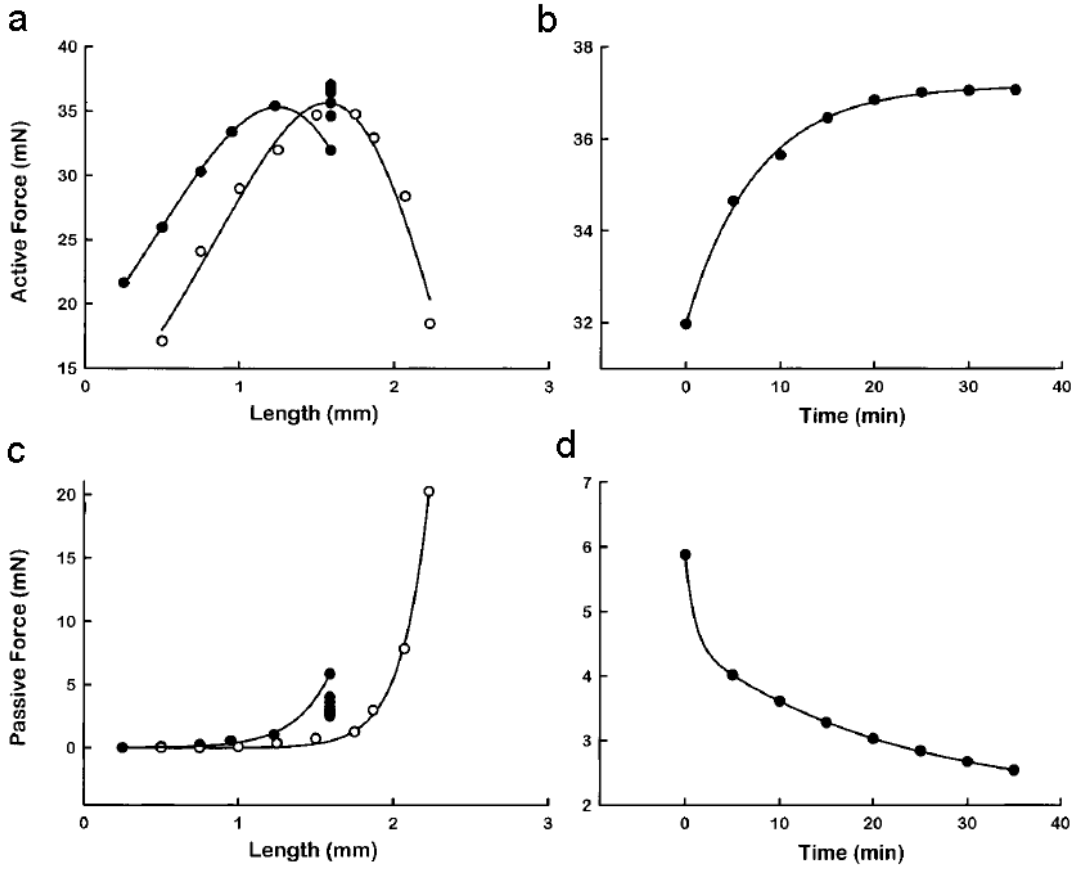

Figure 6.6 Active force recovery and passive force decay observed in passively shortened rabbit tracheal smooth muscle during electrical field stimulation. (a) The passively shortened smooth muscle was extended in step fashion until the decreasing portion of the active force-length graph before being held isometrically (filled circle). Active force was obtained by applying electrical field stimulation at five-minute intervals. Active force-length relation of control group is presented for comparison (empty circle). (b) Active force recovery was observed during the isometric phase. (c) The corresponding passive force readings during the extension and isometric phases. Passive force-length relation of control group is presented for comparison (empty circle). (d) Passive force decay was observed during the isometric phase. The graphs are adopted from Figures 3 and 5 of Wang *et al.* (2001).

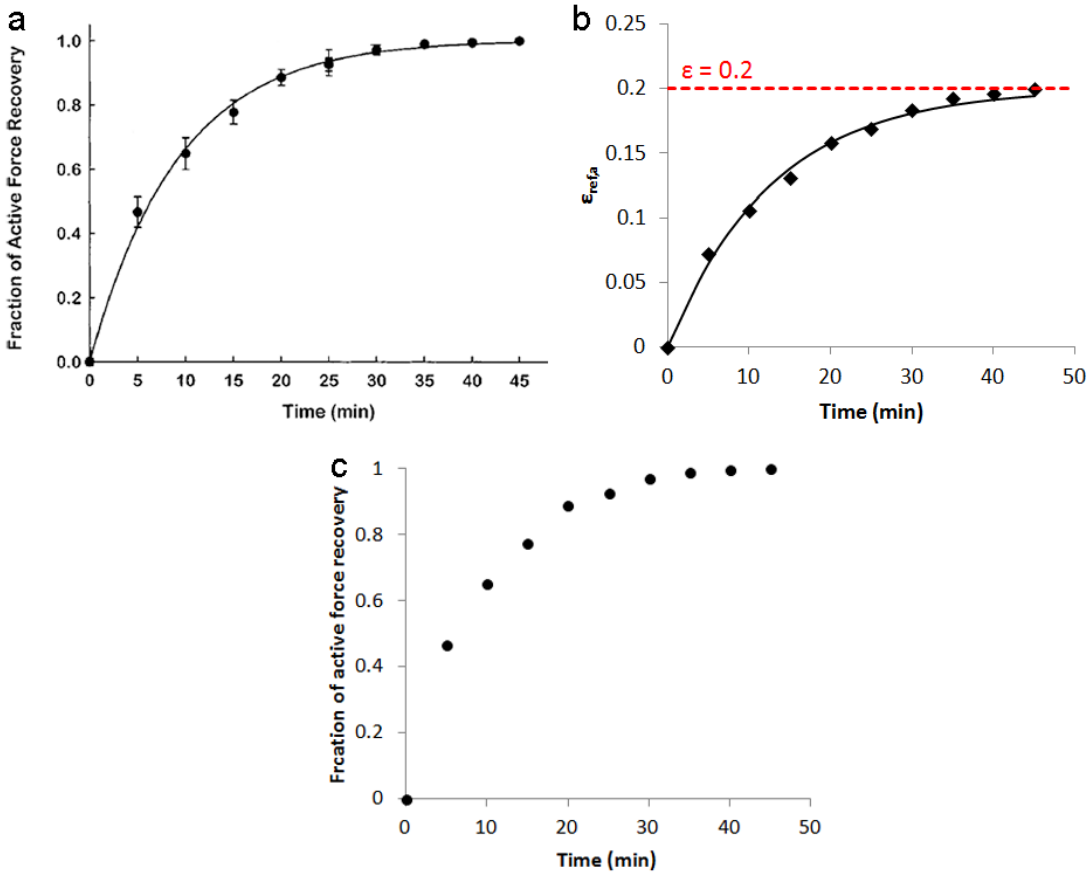

Figure 6.7 Experimental and simulated active force recovery in smooth muscle. (a) Fraction of rabbit tracheal smooth muscle active force recovery as observed by Wang *et al.* (2001) (Fig. 4). The force restoration was modelled by the investigators using an exponential model $y = a[1 - \exp(-bx)]$ with $b = 0.11 \pm 0.04$ min^{-1}. (b) The active stress reference strain ($\varepsilon_{\mathrm{ref,a}}$) was computed from (a) assuming that $\varepsilon_{\mathrm{ref,a}} = 0$ before length adaptation and it moves towards the current strain of smooth muscle ($\varepsilon = 0.2$). The movement of $\varepsilon_{\mathrm{ref,a}}$ is modelled by another exponential function $\varepsilon_{\mathrm{ref,a}} = \varepsilon[1 - \exp(-t/\tau_{\mathrm{a}})]$ with $\varepsilon = 0.2$ and $\tau_{\mathrm{a}} = 12.8$ min ($R^2 = 0.994$). τ_{a} is the active stress reference strain time constant. (c) Active stress recovery obtained from LANVS simulation with the τ_{a} value obtained in (b).

In LANVS, the rate of adaptive change for active mechanics is regulated by the time constant τ_{a}. To obtain this value, the active stress reference strain is first computed from the simulated GI active stress-strain graph and the tracheal smooth muscle active force recovery data (Figures 5.6b and 6.7a). The resulting $\varepsilon_{\mathrm{ref,a}}$ against time relation is shown to be exponential with τ_{a} being 12.8 min (Figure 6.7b). When the active stress reference strain time constant being inserted into the ANVS, it produced

an exponential active stress recovery resembling to the experimental observation (Figure 6.7c).

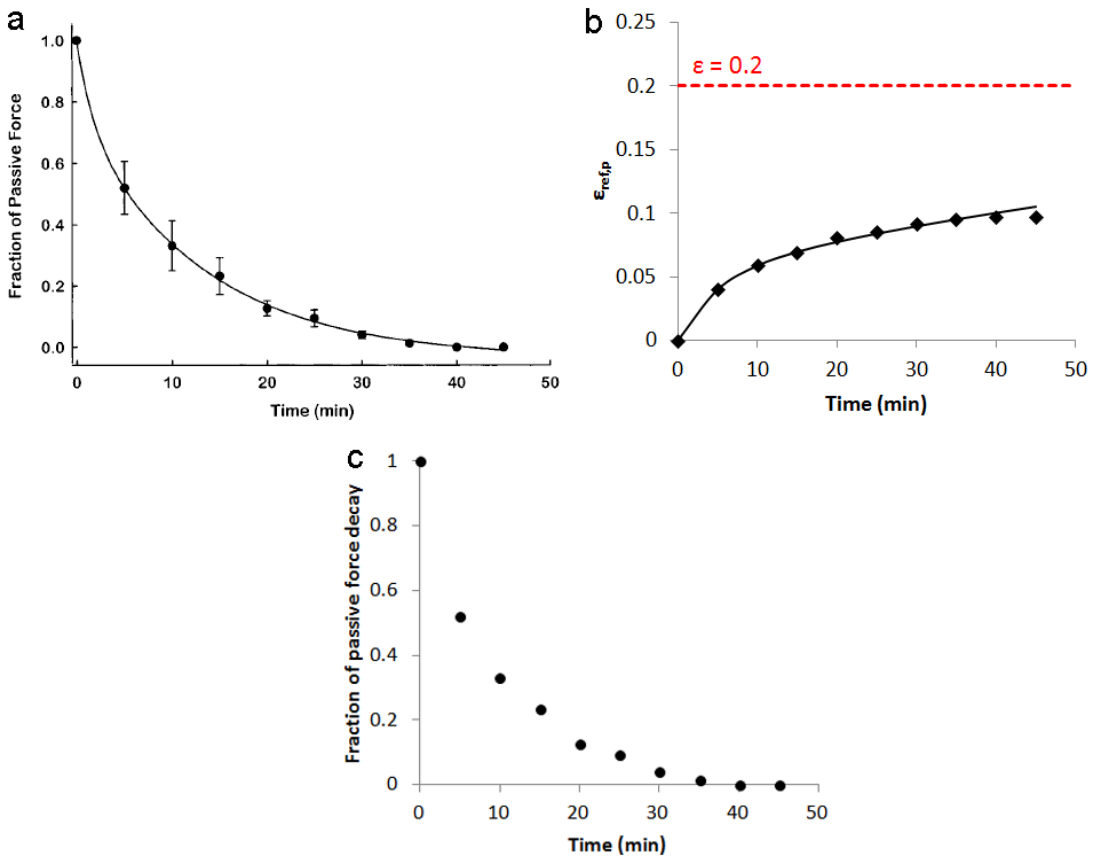

Figure 6.8 Experimental and simulated passive force decay in smooth muscle. (a) Fraction of rabbit tracheal smooth muscle passive force decay observed by Wang *et al.* (2001) (Fig. 6). The force decay was modelled by the investigators using a bi-exponential model $y = a\exp(-bx) + c\exp(-dx)$ with $b = 0.43 \pm 0.36$ min^{-1} and $d = 0.07 \pm 0.05$ min^{-1}. (b) The passive stress reference strain ($\varepsilon_{ref,p}$) was computed from (a) assuming that $\varepsilon_{ref,p} = 0$ before length adaptation and it moves towards the current strain of smooth muscle ($\varepsilon = 0.2$). The movement of $\varepsilon_{ref,p}$ is modelled by another bi-exponential function $\varepsilon_{ref,p} = a[1 - \exp(-t/\tau_{p1})] + (\varepsilon - a)[1 - \exp(-t/\tau_{p2})]$ with $a = 0.0517$, $\tau_{p1} = 4.95$ min and $\tau_{p2} = 101$ min ($R^2 = 0.998$). τ_{p2} is selected to be the passive stress reference strain time constant. (c) Passive stress decay obtained from LANVS simulation with the τ_{p2} value obtained in (b).

To obtain the value of τ_p which determines the rate of adaptive change for LANVS passive mechanics, the passive stress reference strain was similarly computed from the simulated GI passive stress-strain graph and the passive force recovery data

(Figures 4.7 and 6.8a). As the empirical passive force decay was modelled by a bi-exponential function, the mathematical function was applied to model the relation of $\varepsilon_{\mathrm{ref,p}}$ against time (Figure 6.8b). Therefore, two time constants, 4.95 min and 101 min, were obtained.

Wang and co-workers (2001) suggested that part of the passive force decay was influenced by stress relaxation. Experimental results obtained from canine ureteral segments, rat jejunum tissue and porcine oesophagus sections have also showed that the applied stress decreases by 40% or more within five minutes after step-and-hold stretches (Yin and Fung, 1971; Zhao *et al.*, 2003; Yang *et al.*, 2006). Therefore, the faster time constant could possibly be attributed to stress relaxation while the second time constant may be attributed to length adaptation.

When the passive stress reference strain time constant being inserted into the ANVS, it produced an exponential passive stress decay resembling to the experimental observation (Figure 6.8c).

6.4.2 Length adaptation and active mechanics

To verify that the LANVS can reproduce the recovery of active mechanics observed in experiments, the protocol mentioned in Section 6.4.1 was simulated by introducing both biochemical and biomechanical perturbations into the model.

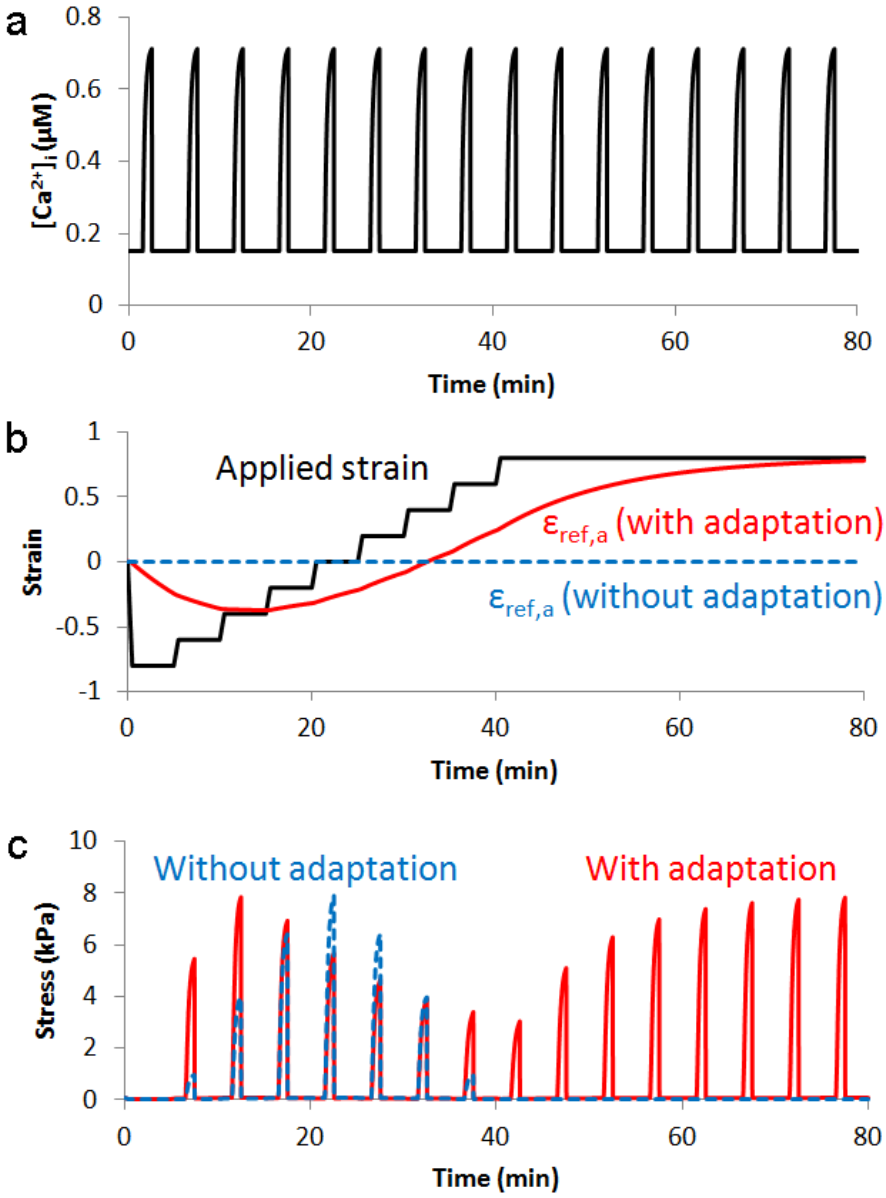

Figure 6.9 Effect of length adaptation on GI smooth muscle active stress is studied using LANVS. (a) Smooth muscle is activated by electrical field stimulation in five-minute interval which leads to periodic intra-cellular Ca^{2+} wave. (b) The stimulation is coupled with tissue deformation (black solid line). The active stress reference strain ($\varepsilon_{\mathrm{ref,a}}$) is unvaried without length adaptation (blue broken line) while it changes with the applied strain when the active stress length adaptation component is enabled (red solid line). (c) The resulting active stress wave with (blue) and without (red) length adaptation is illustrated. Refer to Tables E.4 to E.6, and E.8 to E.11 for parameter values.

The electric field stimulation performed in the experiments was assumed to last for 60 seconds every five minutes. The excitation leads to a regular $[Ca^{2+}]_i$ wave which was

modelled by a monotonic increasing exponential function as shown in Equations (6.14) and (6.15) (Figure 6.9a). Concurrently, the simulated GI tissue was shortened by 80% before being re-lengthened by 20% in every five minutes (Figure 6.9b, black solid line). Each ramp compression or extension was assumed to complete within 30 seconds while the electrical stimulation was applied 60 seconds after each length change as per the experimental protocol. The tissue was held at an isometric configuration when it was extended to 180% of its initial length at which it was allowed to adapt to the deformation under continued electrical stimulation.

The contribution of the LANVS length adaptation components (Equations (6.1) and (6.7)) can be illustrated by comparing the simulation results generated with and without enabling length adaptation. As illustrated in Figure 6.9b, the active stress reference strain remains invariant in the absence of length adaptation (blue broken line). The increment of active stress is attributed to the movement of the applied strain towards $\varepsilon_{\mathrm{ref,a}}$. The peak active stress occurs at the initial strain after which the active stress declines (Figure 6.9c, blue broken line). No active stress is recorded at the final isometric position.

After enabling the length adaptation component, the active stress reference strain (red solid line, Figure 6.9b) tends to follow the applied strain (black solid line). The distance between $\varepsilon_{\mathrm{ref,a}}$ and applied strain influences the rate of change of $\varepsilon_{\mathrm{ref,a}}$ and the magnitude of active stress. The movement of $\varepsilon_{\mathrm{ref,a}}$ is more rapid when it is further from the applied strain as illustrated by the gradient of the graph in Figure 6.9b. The magnitude of the active stress magnitude increases as $\varepsilon_{\mathrm{ref,a}}$ approaches the applied strain. The response of $\varepsilon_{\mathrm{ref,a}}$ to the applied strain also leads to a shift in the peak stress. The first peak stress occurs when the graphs of $\varepsilon_{\mathrm{ref,a}}$ and applied strain

intersect at approximately $\varepsilon = -0.4$ (Figure 6.9c). The rise of $\varepsilon_{\mathrm{ref,a}}$ after 40 minutes also reduces the gap with the applied strain, which causes isometric active stress recovery.

The LANVS simulation predicts restoration of active stress in GI smooth muscle during the final isometric phase (Figure 6.10a) which resembles the experimental results (Figure 6.6a, filled circle). Furthermore, the simulation study also shows that the active force recovery follows an exponential trend (Figure 6.10b) as observed experimentally (Figure 6.6b). The active force recovery rate is found to be 0.110 min^{-1} which is similar to that obtained by Wang *et al.* (2001) in rabbit tracheal smooth muscle (Figures 6.6b and 6.7a).

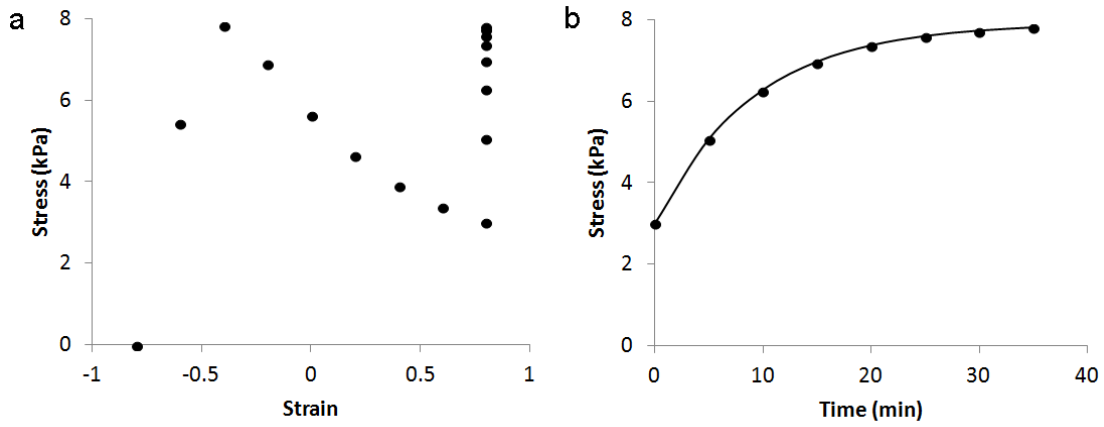

Figure 6.10 Simulation of active stress recovery in passively shortened mammalian GI smooth muscle during electrical field stimulation. (a) The passively shortened smooth muscle was extended in step fashion until the decreasing portion of the active force-length graph before being held isometrically. Active stress recovery was observed during the isometric phase. (b) The recovery transient is modelled by an exponential function $y = a + b[1 - \exp(-cx)]$ with $a = 3.01$ kPa, $b = 4.89$ kPa and $c = 0.110$ min^{-1} ($R^2 = 1$).

6.4.3 Length adaptation and passive mechanics

Similar to its active stress counterpart, the passive stress reference strain remains at the initial strain in the absence of length adaptation (Figure 6.11a, blue broken line).

The initial 80% strain shortening step (Figure 6.11a, black solid line) leads to a sudden surge of compressive stress before it plateaus at -20 kPa (Figure 6.11b, blue broken line). The stress relaxation phenomenon is displayed in each subsequent lengthening step such that the passive stress reaches a steady-state five minutes after each extension. When the GI tissue was held isometrically at 80% tensile strain, a constant steady-state stress of 20 kPa was predicted.

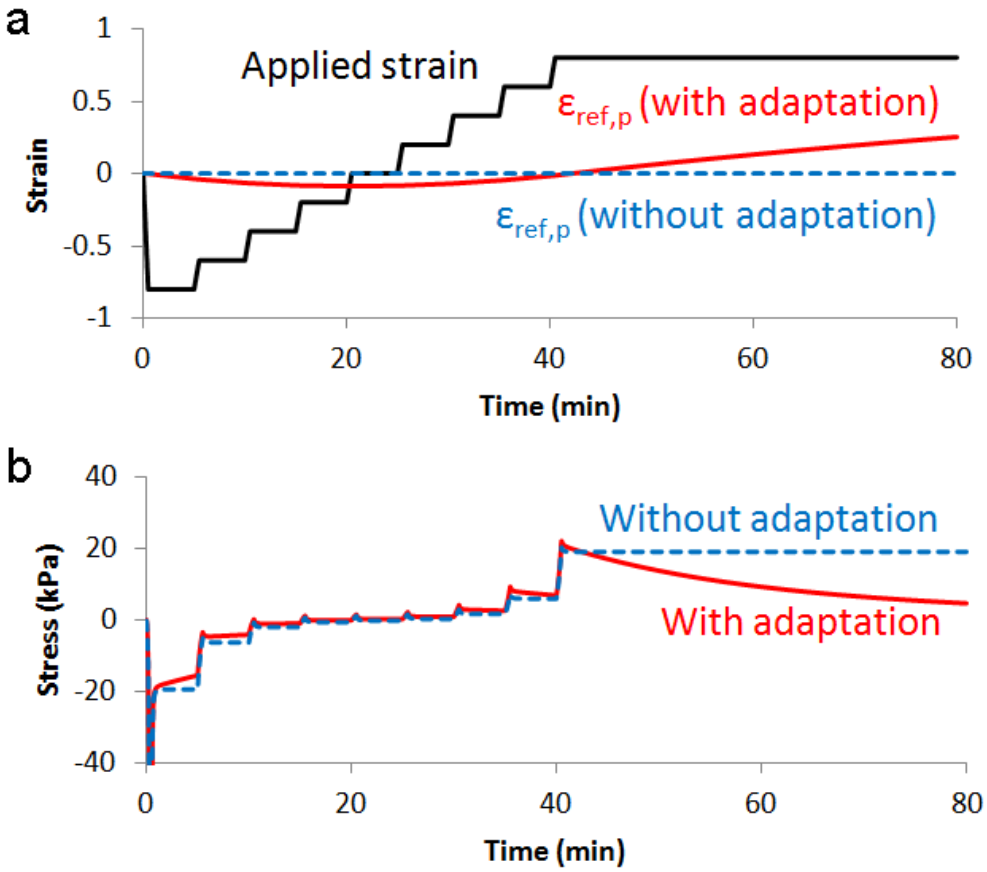

Figure 6.11 Effect of length adaptation on GI smooth muscle passive stress is studied using LANVS. (a) The length of the tissue is first compressed then re-stretched to 1.8 times of its initial length in steps of 20% strain (black solid line). The passive stress reference strain ($\varepsilon_{ref,p}$) is unvaried without length adaptation (blue broken line) while it changes with the applied strain when the passive stress length adaptation component is enabled (red solid line). (b) The resulting passive stress transient with (red) and without (blue) length adaptation is illustrated. Note that the maximum compressive stress of 132 kPa (without adaptation) and 130 kPa (with adaptation) are recorded at 0.5 min which is not shown in the graph. Refer to Tables E.4 to E.6, and E.8 to E.11 for parameter values.

When the passive stress length adaptation component in the LANVS is enabled, the passive stress reference strain (Figure 6.11a, red solid line) moves towards the applied strain (black solid line). The distance between $\varepsilon_{\mathrm{ref,p}}$ and the applied strain influence the speed of $\varepsilon_{\mathrm{ref,p}}$ alteration, and the consequent magnitude of passive stress. Less rapid $\varepsilon_{\mathrm{ref,p}}$ movement and little reduction of passive stress magnitude occurs when $\varepsilon_{\mathrm{ref,p}}$ is near to the applied strain at the 20 minute time point. The response of $\varepsilon_{\mathrm{ref,p}}$ to the applied strain leads to a continuous adjustment of the steady-state passive stress. The rise of $\varepsilon_{\mathrm{ref,p}}$ after 40 minutes reduces its gap with the applied strain, which leads to perpetual decrement of passive stress towards zero (Figure 6.11b, red solid line).

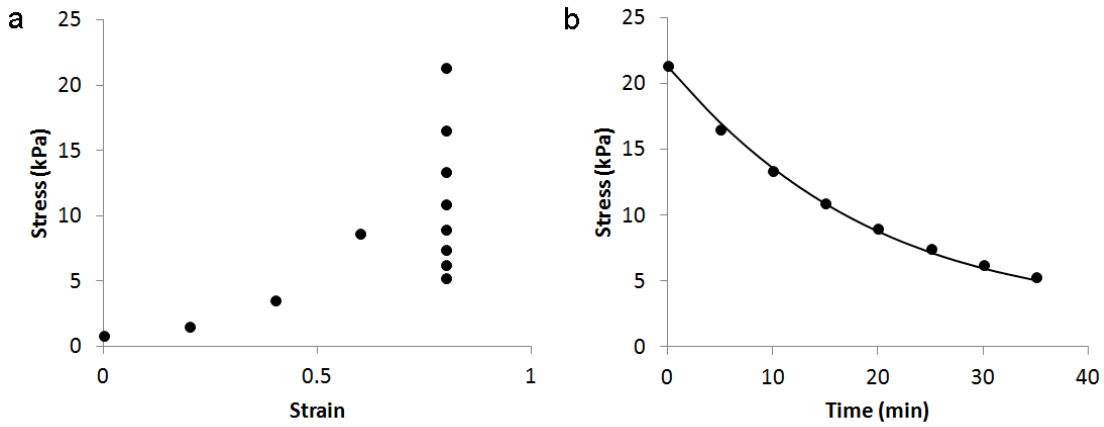

Figure 6.12 Simulation of passive stress decay in passively shortened mammalian GI smooth muscle during electrical field stimulation. (a) The passively shortened smooth muscle was extended in step fashion before being held isometrically at 80% strain. Passive stress decrement was observed during the isometric phase. (b) The decay transient is modelled by a bi-exponential function $y = a + b\exp(-cx) + d\exp(-ex)$ with $a = 2.54$ kPa, $b = -25.0$ kPa, $c = 0.0851$ min^{-1}, $d = 43.8$ kPa and $e = 0.0700$ min^{-1} ($R^2 = 0.999$).

The LANVS simulation predicts a diminishing passive stress during the final isometric phase (Figure 6.12a) which resembles the experimental results (Figure 6.6c, filled circle). In addition, the simulation study shows that the passive stress decay can be modelled by a bi-exponential function (Figure 6.12b) as observed experimentally

(Figure 6.6d). The passive force decay rates were computed to be 0.0851 min^{-1} and 0.0700 min^{-1}. These values are both within the one standard error variability of mean experimental passive force decay rates which were found to be 0.43 ± 0.36 min^{-1} and 0.07 ± 0.05 min^{-1} (Figure 6.8a).

6.5 Discussion

The biomechanical properties of smooth muscle were previously thought to be stable, which is the case for striated muscle. However, recent experimental results have illustrated that smooth muscle can adjust to changing geometric constraints and physical deformations by altering its passive and active mechanics. The notion is integrated with existing knowledge on smooth muscle viscoelasticity and contractile properties in the novel LANVS model which presents our current understanding of smooth muscle mechanics. The mathematical model can be used to demonstrate the postulated dynamics of length adaptation in GI smooth muscle.

6.5.1 Model structure

Previous smooth muscle length adaptation models emphasise either the active stress adaptive mechanism, such as the serial-to-parallel rearrangement of contractile apparatus, or the aggregate influence due to filament network reconfiguration, without differentiating the contributions to passive and active mechanics (Lambert *et al.*, 2004; Ali *et al.*, 2005; Silveira and Fredberg, 2005). With the incorporation of the passive (NVS) and active (ACC) mechanical components, the LANVS model can describe the effects of length adaptation on smooth muscle viscoelasticity and active contraction. The independent operation of NVS and the ACC also allows descriptions of different length-adaptive mechanisms for smooth muscle passive and active mechanics.

In fact, experimentalists have suggested different length-adaptive mechanisms for active and passive mechanics previously. The recovery of active stress is postulated to be the result of altered contractile elements, while the decay of passive stress is proposed to be related to cytoskeletal reorganisation (Seow and Fredberg, 2010). The rate of contractile force restoration has also shown to be faster than that of passive tension decay in mammalian tracheal smooth muscle (Wang *et al.*, 2001). Overall, the experimental evidence lends support to the LANVS structure which segregates the passive viscoelastic and contractile components.

The active and passive mechanical components are connected in parallel in the LANVS framework such that their mechanics are aggregated to reflect the overall smooth muscle mechanical properties under length adaptation. The parallel configuration in the model also allows independent enhancement of the length-adaptive NVS and ACC components when additional experimental results emerge. It also facilitates testing of new hypothesis as the NVS and ACC can be disabled separately.

The LANVS is also capable of illustrating the individual exponential time courses of passive stress decay and active stress recovery in smooth muscle, which has not been demonstrated in other models. The simulation results have been verified with experimental data such that both the rates of passive and active stress restoration agree with those reported in rabbit tracheal smooth muscle.

6.5.2 Implication of smooth muscle deformation-adaptation cycle

The malleability of smooth muscle can be described by a deformation-adaptation cycle which is illustrated in LANVS.

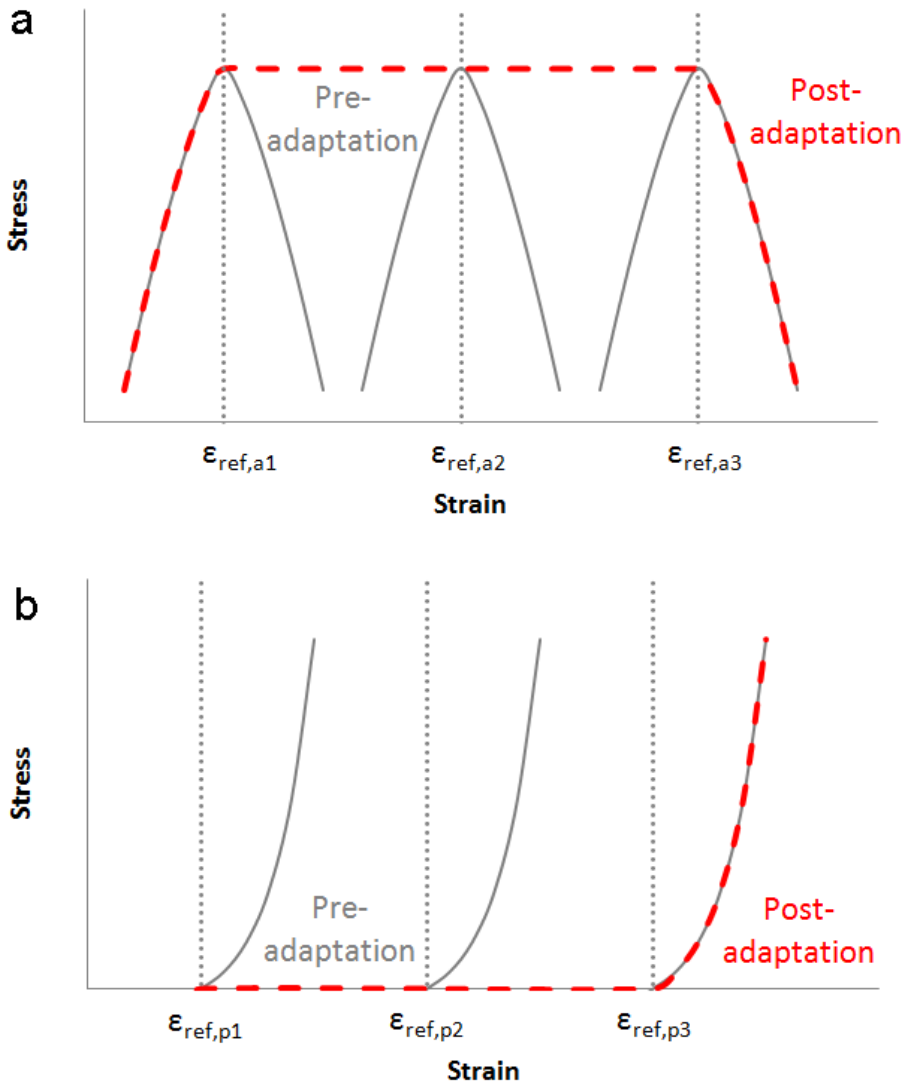

Figure 6.13 Postulated aggregate active and passive stress-strain graphs of adapted smooth muscle. (a) Active stress-strain graph (grey filled curve) at each active stress reference strain ($\varepsilon_{\mathrm{ref,a}}$) (grey dotted axis) represents the pre-adaptive contractile response of smooth muscle. The active stress recovers to the maximum when the smooth muscle has fully adjusted to a new deformation. The overall active stress-strain profile of fully adapted smooth muscle (red broken line) can be deduced if $\varepsilon_{\mathrm{ref,a1}}$ and $\varepsilon_{\mathrm{ref,a3}}$ denote the minimum and maximum strain within which length adaptation is possible. (b) Similarly, passive stress graph (grey filled curve) at each passive stress reference strain ($\varepsilon_{\mathrm{ref,p}}$) (grey dotted axis) represents the pre-adaptive viscoelastic response of smooth muscle. The passive stress decays to the minimum after length adaptation. The aggregate passive stress-strain profile of fully adapted smooth muscle (red broken line) can be deduced when $\varepsilon_{\mathrm{ref,p1}}$ and $\varepsilon_{\mathrm{ref,p3}}$ denote the adaptable length range.

As shown in Figure 6.13a, when the smooth muscle has fully adjusted to its current deformation, $\varepsilon_{\mathrm{ref,a}}$ overlaps with its strain such that maximum contractile stress is

generated. The deformation phase of the cycle starts when the strain of the muscle departs from the fully-adapted position. Therefore, the deformation leads to an immediate decrement of active stress magnitude (grey solid curve) and initiates the length adaptation process. The process is presented in LANVS as a horizontal movement of the active stress-strain relationship. During the adaptive phase, the active mechanics of smooth muscle can be described by different stress-strain relations according to its adaptive state. Eventually, the active stress is restored to the pre-deformation (maximum) magnitude when $\varepsilon_{\mathrm{ref,a}}$ approaches the current strain. The deformation-adaptation cycle is repeated when the geometric and mechanical constraints of smooth muscle are redefined.

The deformation-adaptation cycle can occur over a wide length range in smooth muscle (Pratusevich *et al.*, 1995; Chin *et al.*, 2012). The overall active mechanics of fully-adapted smooth muscle can be deduced by joining all the peaks of pre-adaptive active stress-strain graphs (Figure 6.13a, red broken curve). The contractile stress weakens eventually if the smooth muscle is deformed beyond the adaptable length range.

A similar inference can be drawn for the overall passive mechanics of fully-adapted smooth muscle (Figure 6.13b). Tensile stress is experienced by the smooth muscle when the current strain is greater than $\varepsilon_{\mathrm{ref,p}}$ (grey solid curves and dotted axes). Decay of passive stress occurs within the adaptable length range. By connecting the minimum passive stress of adapted smooth muscle at different strains, the passive mechanics of fully-adapted smooth muscle can be inferred (red broken curve). The passive stress rises considerably when the strain develops outside of the adaptable length range.

The pre-adaptive and post-adaptive stress-strain graphs differentiate the immediate and eventual smooth muscle mechanical responses. The transformation of responses through length adaptation implies a change in the energy requirements. The post-deformation adjustment of contractile apparatus enables generation of stronger contractile force at same level of $[Ca^{2+}]_i$ (Figure 6.9). The $[Ca^{2+}]_i$ waveform originates from energy-consuming electrical and biochemical activities (Paul, 1981). Therefore, the alteration of contractile apparatus enhances energy efficiency in active contraction. Likewise, the area under the passive stress-strain graph denotes the energy exhausted in stretching the smooth muscle. The modification of structural components in smooth muscle leads to reduced energy absorption per unit strain in deformation. It also improves mechanical efficiency of contraction due to weakened passive mechanical resistance.

6.5.3 Smooth muscle length-adaptive mechanism

The length adaptation experimental results shown in this Chapter have proposed that the smooth muscle mechanical response is modifiable by mechanical stimuli. While the underlying mechanism is not fully elucidated, the LANVS provides a feasible hypothesis of the mechanism.

The LANVS schematic in Figure 6.14 illustrates the influence of the applied stress or strain to smooth muscle passive and active mechanics. The deformation response is computed by the model after accounting for tensile or compressive resistance provided by the intra- and extra-cellular components (NVS with symmetric compression). The deformation also initiates the passive stress length adaptation process whose output modulates the viscoelastic response of smooth muscle. The applied stress or strain also affects the mechanics of the cross-bridge-dependent

active contractile component which encapsulates contractile stress generation, bound cross-bridge stiffness and friction due to filament sliding (ACC and strain-dependent activation component). The deformation induces the adaptive process which regulates the active stress recovery.

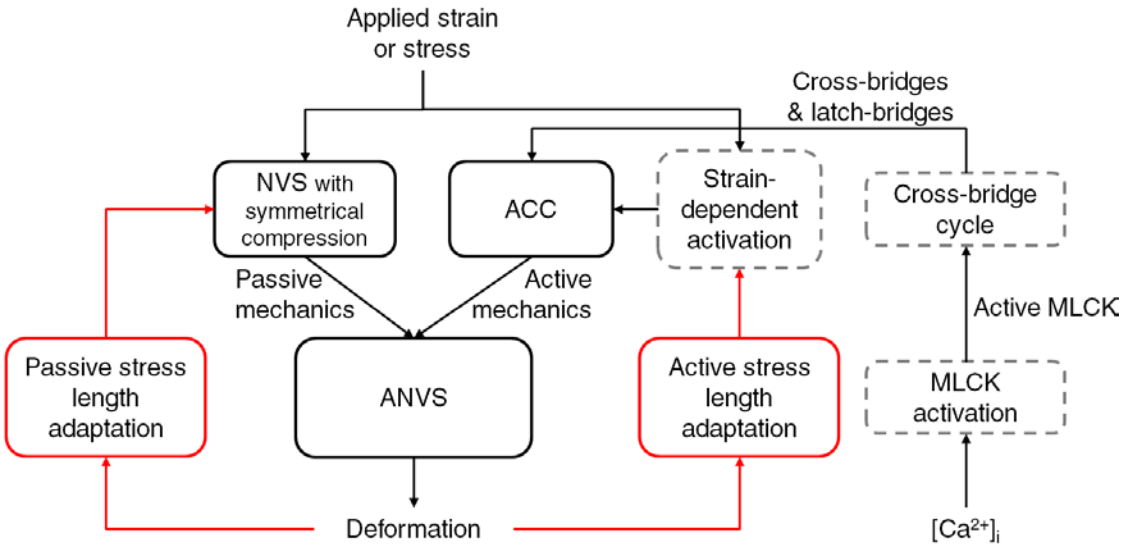

Figure 6.14 Schematic of LANVS GI smooth muscle mechanics model. The model comprises a nonlinear viscoelastic solid (NVS) with symmetrical compression component and an active contractile component (ACC) whose mechanics are aggregated in an active nonlinear viscoelastic solid (ANVS) framework. The active and passive length adaptation components are parts of feedback mechanism which modulates smooth muscle mechanical response (red rectangles and lines). The LANVS is supported by components developed by other investigators (grey rectangles with broken boundary). These components are strain-dependent activation component (Gestrelius and Borgström, 1986), as well as cross-bridge cycle and MLCK activation components (Gajendiran and Buist, 2011).

The LANVS components can be viewed as representatives of biological entities in a mechano-transduction pathway. Cytoskeletal and contractile mechanics are represented by the NVS and ACC, respectively. The model components are connected in ANVS and form a forward pathway which imitates generation of smooth muscle deformation under biomechanical and biochemical perturbations in terms of external stress, strain and $[Ca^{2+}]_i$. Both the passive and active stress length adaptation components are located along the feedback loops. They symbolise the stretch-

sensitive receptors and mechano-sensitive ion channels, which sense the current deformation and modulate the mechanical input signals in a reverse pathway (Kraichely and Farrugia, 2007). These biological entities and pathways cooperate to generate desired smooth muscle mechanical properties and help to maintain its mechanical stability in a dynamic environment. Overall, the LANVS schematic demonstrates the possible principles and communication between biological components in length adaptation.

6.5.4 Investigating mechano-adaptation of GI smooth muscle

The length adaptation phenomenon has not yet been explicitly demonstrated in mammalian GI smooth muscle, however studies have shown that its mechanical properties can be modified through other biological processes. For instance, Jiang *et al*. (2010) have illustrated that the rat oesophagus becomes more compliant after cyclic pressure loading. However, the tissue stiffness can be recovered through contractile activation during which the ruptured inter-filament cross-linking is re-established. The adjustable passive stiffness phenomenon has also been observed in rabbit detrusor smooth muscle (Speich *et al.*, 2007). The same investigators have also demonstrated length adaptation in rabbit detrusor smooth muscle and volume adaptation in mouse bladder (Speich *et al.*, 2009; Speich *et al.*, 2012).

The discovery of mechano-sensitive ion channels, such as L-type Ca^{2+} and $Na_v1.5$, in GI tissue also points to its mechano-adaptive properties (Sanders *et al.*, 2006; Kraichely and Farrugia, 2007). It is hypothesised that physical straining of SMC or ICC leads to deformation of its cytoskeletal network which tethers to ion channel gating mechanisms. The plasma membrane also contains several ion channels which adjust their opening probabilities according to membrane deformation. The modified entry

and release of ionic fluxes affect the electrical and chemical properties of SMC and ICC, and thus regulate the mechanical properties of GI smooth muscle. Similar stretch-activated ion channels and mechano-transduction pathways have also been investigated in mammalian tracheal smooth muscle, which has shown length adaptation phenomena (Grassmann *et al.*, 1999; Ito *et al.*, 2006).

The experimental studies suggest that a common mechanical adaptive mechanism exists in mammalian smooth muscle of different organs. Length adaptation is a feedback mechanism which modulates the mechanical perturbations (applied stress and strain) through sensing the output mechanical signals (smooth muscle deformation). It can be considered as part of a grand scheme of mechano-adaptation in which smooth muscle regulate its biological response according to its physical environment (Huang *et al.*, 2004; Wang and Thampatty, 2006; Lim *et al.*, 2010). The interplay of chemical, electrical and mechanical properties helps to regulate GI smooth muscle biomechanics.

6.6 Summary of LANVS

The discovery of length adaptation fills the gap of knowledge in smooth muscle mechanics. It provides an explanation for uninterrupted GI motility despite a substantial variation of GI organ geometries.

The LANVS provides a mathematical platform for explaining the underlying integrative mechanism of GI smooth muscle mechanics, which includes viscoelasticity, contractile response and length adaptation. It can be used to advance investigations on smooth muscle length adaptation and relating physiological roles in GI organs. The succinct model also facilitates its insertion into simulations which involves higher spatial scales.

Chapter 7 Implications of smooth muscle mechanics on GI physiology

7.1 Overview

The GI smooth muscle models developed in this work capture three important smooth muscle mechanical phenomena. The intrinsic material properties of GI SMC and ECM give rise to the smooth muscle's passive nonlinear viscoelastic behaviour. The active mechanical response allows GI smooth muscle to contract and vary its stiffness depending on cross-bridge cycling and the intra-cellular calcium concentration. The capability of GI smooth muscle to modulate its mechanical response according to deformation implies that its passive and active biomechanics are dynamic and adaptable to changes in physical and geometric constraints. These mechanical phenomena have been well-illustrated in smooth muscle tissues experimentally, to which the parameterised GI smooth muscle mechanics models adhere closely. The models also establish the inter-connections between GI smooth muscle structure, its mechanical properties and its mechanical adaptation capability. Nevertheless, the link between these smooth muscle characteristics and GI physiology has not been completely elucidated, and therefore warrants further discussion.

The notion of structure-property-function has been employed to explain the underlying physiology in biological entities of different sizes (Suresh *et al.*, 2005; Lim *et al.*, 2006a). In experimental studies on GI mechanics, the principle has often been applied to a single spatial scale such as the cell, tissue or organ level (Tasaka and Farrar, 1969; Zhao *et al.*, 2005; Liao *et al.*, 2006b). Although there are papers dedicated to the integration of structure-property-function connections across different length

scales in other smooth muscle organs, such as blood vessel and the urinary bladder, similar discussions are rarely available in the context of GI mechanics (Martinez-Lemus *et al.*, 2009; Speich *et al.*, 2012).

The functions of an organ in the GI tract and its components serve to satisfy the body's changing physiological demands. As such, GI wall tissue constantly modulates its structure and supports the generation of appropriate GI tract properties and functions (Tack, 2006). The remodelling response has also been correlated with GI diseases such as intestinal obstruction, diabetes and systemic sclerosis (Liao *et al.*, 2009a). The attainable evidence suggests that clarifying the biology of smooth muscle's adaptive response is paramount for understanding GI health and disease states.

To elucidate the underlying mechanisms which explain the connection between GI smooth muscle mechanical structure, property, function as well as their adaptive responses towards GI physiology, an adaptive mechanical framework is considered in this chapter. The framework seeks to integrate the biological organisations at different spatial scales, smooth muscle mechanical characteristics, recent knowledge in cell and tissue mechanics, and mechanical signal transduction. The results generated from the computational models are positioned in the framework, and are subsequently examined in association with the physiological functions and adaptive responses of GI tract under healthy and diseased conditions.

7.2 Adaptive mechanical framework

7.2.1 Structure, property and function

Biological structure and hierarchy

The structure of a biological entity refers to the geometric, morphological or anatomical appearance of the entity (Fung, 1993). The biological structure also includes the quantity and quality of constituents, and the ways they are arranged and connected in the construction of the entity.

Biological structures can be classified in accordance to spatial scale (Southern *et al.*, 2008). Particularly, the protein, cell, tissue and organ level structures are relevant to the GI smooth muscle mechanics discussed in this work (Figure 7.1). At different length scales, these biological structures form a morphological hierarchy.

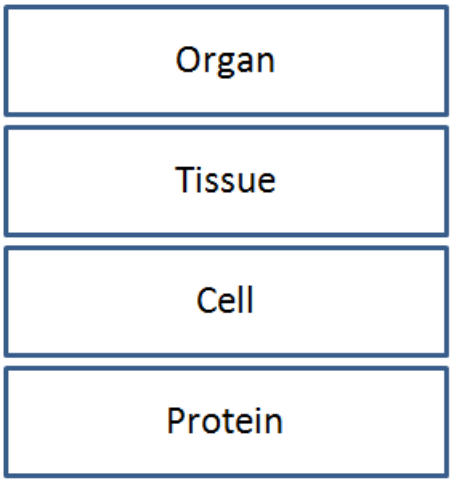

Figure 7.1 Morphological hierarchy of biological organisation. Adapted from Southern *et al.* (2008).

In the morphological hierarchy, smaller entities, such as the cytoskeleton and SMC, are the building blocks of larger entities, such as GI wall tissue and organs. Mechanical couplings exist between entities of the same and different morphological

tiers to provide structural integrity. These mechanical connections allow smaller entities to perceive the macroscopic physical challenges facing the larger entity (Gayer and Basson, 2009). For instance, the tensile stress applied on GI wall tissue is transmitted to the ECM and its constituent fibres, such as collagen. The mechanical signal can be communicated to SMC through different avenues. Firstly, the signal can be perceived by SMC through the transmembrane protein receptor integrin which facilitates the interaction of intra-cellular actin filaments and the ECM (Zhang and Gunst, 2008). In addition, adherent junctions are located between a pair of dense bands in opposing SMC and provide a cell-to-cell mechanical linkage (Kuo and Seow, 2004). Within the SMC, actin filaments connect to both the dense bodies in cytoplasm and dense bands at the cell membrane (Gabella, 1984). Vimentin intermediate filaments link the nucleus to sarcolemma at desmosomes (Tang, 2008). Overall, physical stimulation can be transmitted from the wall tissue to the SMC nucleus and organelles through the morphological hierarchy.

Emergence and propagation of mechanical properties

A mechanical property describes the behaviour of the biological entity and its response towards stimulation as a result of its structure (Gregersen and Kassab, 1996; Lim *et al.*, 2006a; Qin *et al.*, 2010).

Recent studies have revealed that the structure-property connections of biological entities are hierarchical (Figure 7.2). As a case in point, an intermediate filament is constructed by end-to-end connections of basic units called unit length filaments, each having eight tetramers (Qin *et al.*, 2010). The tetramer is a pair of protein dimers which have coiled-coil alpha-helical structures. Molecular dynamics simulation studies have shown that pulling the dimer structures causes transitions from alpha helices to beta sheets, which aggregate to exhibit macroscopic extension of intermediate

filaments (Qin *et al.*, 2009). The result suggests that intrinsic mechanical properties of smaller entities can contribute to the biomechanical response of larger ones.

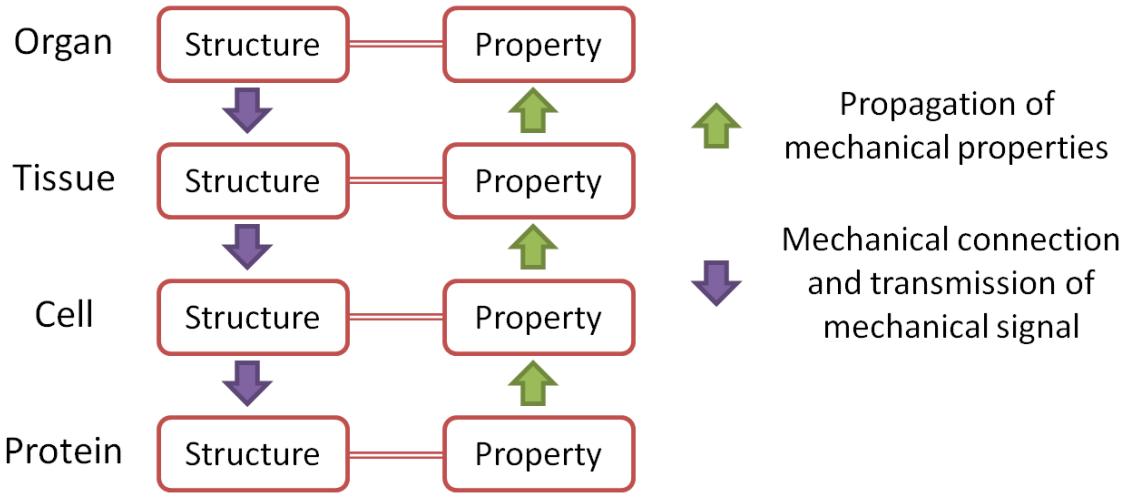

Figure 7.2 Illustration of structure-property linkage and hierarchy. Mechanical couplings exist between different morphological tiers. The connections enable the transmission of mechanical signals which modify the properties of biological entity. The alteration of the mechanical properties propagates through the morphological hierarchy and contributes to the behavioural adjustment of larger entity. As such, structure-property connections exist in each morphological tier which resembles the morphological hierarchy in Figure 7.1.

Emergent mechanical properties, arising from the interaction of smaller and heterogeneous biological entities, also propagate up the morphological hierarchy (Ingber, 2003b). The protein myosin cannot generate contractile force by itself. However, the structure of the intra-myocyte contractile apparatus facilitates the interaction of the myosin head and actin binding sites, and relative sliding of contractile filaments to generate the active force which manifests in SMC contraction.

Functional usage

The term function denotes the role that the biological entity offers in the perspective of a larger system. It is the application of an entity's structure and properties to serve the purpose of a higher tier in the morphological hierarchy. For example, the function of

GI smooth muscle active mechanics is to actuate GI motility which assists in transportation of ingested food, mixing it with digestive juice.

Collectively, the above discussion establishes that the structure-property-function connection in GI mechanics traverses different spatial scales. When the relation is incorporated into the morphological hierarchy, there are intricate associations across the spatial tiers, between the mechanical structure, properties and functions of intra- and extra-cellular filaments, GI SMC, GI wall tissue and the overall alimentary tract. These relations form the backbone of the adaptive mechanical framework which also incorporates the physiological conditions and the adaptive responses of the GI tract.

7.2.2 Physiology and adaptation

Physiological objectives and stimuli

It is important that the functional responses give support to the main GI processes such as food digestion, nutrient absorption and waste ejection. The set of functional responses, which leads to the optimised conditions for GI processes, becomes the physiological objective. It represents the needs of the body that the entity strives to fulfil with its functional roles.

Healthy and diseased physiological processes stimulate the modification of biological structure, properties and function. For instance, the transition from fasting to feeding is accompanied by an accumulation of food materials in the GI tract (Tack, 2006). The GI organs adjust their mechanical structures for bolus containment and transportation. Also, the effect of GI diseases, such as ulcerative colitis, diabetes and systemic sclerosis, on gastrointestinal wall tissue morphology and mechanical properties are well-documented and selected cases have been illustrated previously in Tables 1.3

and 1.4. Overall, the physiological stimulations instigate functional responses from the biological entity (McCain and Parker, 2011).

Transmission of mechanical signals

A biological entity is embedded with mechanisms which respond to the dynamics of mechanical stimuli and deviation from the physiological objectives. Feedback mechanisms, which comprise several components such as mechano-sensitive ion channels and signal transduction pathways, are well-established in studies relating to cardiac physiology (Sachse *et al.*, 2007; McCain and Parker, 2011; Dabiri *et al.*, 2012). The deviation signal, in the form of physiological feedback, is generated from the difference between current function and the physiological goal. The feedback message is a form of regulatory signal driving the biological entity to satisfy the physiological objective.

A mechanical signal is an example of a physiological feedback signal which is communicated across the morphological tiers through mechanical pathways (Kohl *et al.*, 1999; Beyder *et al.*, 2010; Lessey *et al.*, 2012). The cell-cell and cell-ECM mechanical couplings allow the macroscopic mechanical forces experienced by a GI organ to be perceived by its constituent cells (Gayer and Basson, 2009). The mechanical signal also induces a biochemical response through the mechano-transduction components (Ingber, 2003a, 2006). For example, the stretch-sensitive ion channel, SCN5A, can influence the intra-cellular $[Na^{+}]$ and consequently the electrical and contractile activities of GI SMC (Beyder *et al.*, 2010). Various GI cellular processes such as proliferation, migration and adhesion to ECM are also modulated by mechanical stimulation (Gayer and Basson, 2009). Collectively, the mechanical signalling pathways assist in regulating biological response to achieve or maintain the physiological goal.

Adaptive mechanical response

The interactions between stimuli, modulation of a biological entity, physiological objectives and feedback signals constitute an adaptation framework. In this work, adaptation can be defined as the regulation of structure, property and function of the biological entity in response to physiological stimuli and feedback.

The adaptive mechanical response is evident in each biological tier in the morphological hierarchy. Over-expression of extra-cellular collagen has been associated with an increased GI wall tissue elastic modulus in partially obstructed small intestine with increased intra-luminal pressure (Storkholm *et al.*, 2007). The collagen content, and hence stiffness, increased with obstruction duration. The contractile force of activated toad gastric SMC decreased when it was shortened (Harris and Warshaw, 1991). Prolonged deformation could stimulate the adaptive mechanical response such that the active force recovered to the level seen at the reference length. Swelling in both circumferential smooth muscle and submucosa layers have been reported in obstructed jejunum (Zhao *et al.*, 2010). The GI wall tissue thickness is positively correlated with blockage time which implies continuous tissue and organ remodelling (Zhao *et al.*, 2008b).

Apart from different spatial scales, the adaptive mechanical response can be achieved at different rates. As a case in point, one immediate avenue for reinforcing the GI wall tissue is through $[Ca^{2+}]$-dependent SMC active contraction. The process increases cross-linking between myosin and actin filaments, and hence SMC stiffness, within seconds (Warshaw *et al.*, 1988). In the case of the chronically obstructed small intestine, stiffening is accomplished by gradual tissue wall swelling and collagen accumulation (Storkholm *et al.*, 2007).

The above examples impress that these biological entities produce discrete adaptive responses according to different physiological needs. However, these individual mechanical regulatory episodes plausibly belong to a sequence of physiological events, demonstrating a continuously modulating adaptive response. In explaining the regulation of vascular diameter to counteract the intra-luminal pressure, Martinez-Lemus *et al.* (2009) proposed the theory of a remodelling continuum which connects acute vessel contractile response to long-term vessel tissue restructuring. The investigators suggested that initial vasoconstriction is modulated by active SMC contraction while prolonged constriction initiates the adjustment of vascular SMC lengths and positions, causing rearranged cell-cell adhesions and modified cell-ECM connections. Chronic vasoconstriction also influences the transformation of ECM such that the SMC can operate at a reduced diameter. Overall, structural changes help to relieve the mechanical burden carried by ATP-driven active contraction, and consequently reduce energy consumption. A similar sequence of adaptive responses, across both spatial and time scales, is most likely employed by GI smooth muscle in regulating its mechanical structure, property and function. However, there is currently no direct evidence giving support to this notion.

Framework construction

Collectively, an adaptive mechanical framework can be established as shown in Figure 7.3. A physiological stimulus induces modification of the structure, property and function of the entity. The functional response of the entity is evaluated if it deviates from the set physiological goal. The discrepancy generates a physiological feedback signal which influences the subsequent adaptive response.

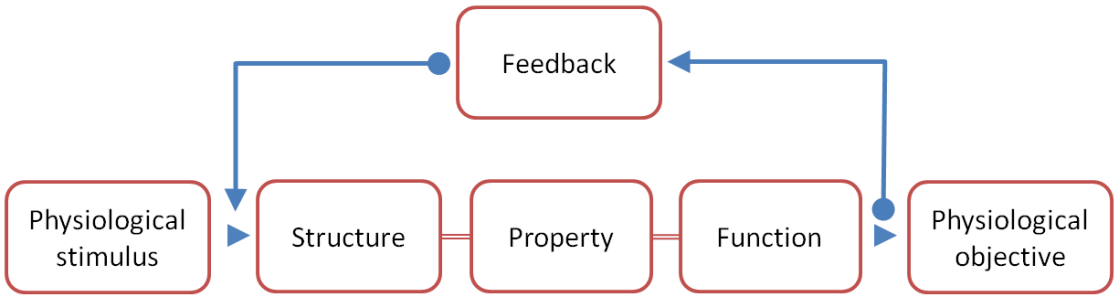

Figure 7.3 Adaptive mechanical framework of a biological entity. A mechanical signal induces changes in structure, property and function of biological entity. The physiological condition created by the function of entity is compared with physiological goal. The resulting physiological feedback modulates the subsequent adaptive behaviour.

The application of the framework is illustrated in terms of achieving mechanical homeostasis, assisting in GI physiological process and responding to GI pathology.

7.3 Mechanical homeostasis

7.3.1 Mechanical equilibrium

Homeostasis is the maintenance of a constant internal environment (Rubinson and Lang, 2008). In the context of vascular adaptation, Humphrey (2008) has postulated that biological entities 'attempt to maintain preferred form and function' through a mechanical homeostatic process. Taken together, the term mechanical homeostasis can thus be inferred as the sustenance of constant mechanical environment, or mechanical equilibrium, through physiological processes.

To achieve mechanical homeostasis, it is hypothesised that each morphological tier needs to attain an internal force balance. Ingber (2003b) explained the mechanical equilibrium within cells, tissues and organs using Fuller's tensegrity principle, which states that continuous transmission of stress between tensile and compressive elements ensures mechanical equilibrium. The investigator inferred that each level of

biological organisation is supported by tensional and compressive components. Actin filaments are postulated to be pre-stretched while microtubules are pre-compressed within a cell. In a tissue, cells are extended and they anchor themselves through focal adhesions to the ECM which is identified as the compressive strut. The existence of residual stress in a no-load state has been illustrated in cutting the radial edge of oesophagus and small intestine cross-sectional rings (Gregersen *et al.*, 1999; Zhao *et al.*, 2002). The transformation of an intact circle to an arc indicated the GI wall tissue was pre-stressed circumferentially. Repeating the opening angle experiment at different tissue layers revealed that the inner mucosa was pre-compressed while the outer submucosa layer was pre-extended in the no-load state. Similar observations, of pre-compressed mucosa and pre-stretched submucosa, were drawn when the tissue layers were separated in the longitudinal direction (Gregersen *et al.*, 2000).

It is important for biological entities, such as GI tract, to preserve mechanical homeostasis while they perform mechanical functions, such as motility. The mechanical homeostasis of GI smooth muscle was considered in the construction of the NVS and ANVS models. The aggregate stress applied on NVS is distributed to the PEC, SEC and SVC elements in accordance to the mechanical equilibrium as shown in Equations (4.4) and (4.5). In ANVS, the sum of stress experienced by the ACC components and NVS components balances with the externally applied stress as shown in Equations (5.5) and (5.6).

Both the NVS and ANVS models can illustrate different equilibrium states at which their constitutive components are either stretched or compressed. As a case in point, applying a step-compression to the ANVS model produces resisting stress which opposes the applied strain, while a simultaneous phasic contraction in the model generates active stress that acts in the same direction as the applied strain (Figure

5.8b). The simulated scenario is comparable to the transmission of stress between compressive elements (presumably the cytoskeleton) and tensile elements (contractile apparatus) suggested in the tensegrity principle. Collectively, our models agree with the tensegrity principle and suggest that pre-stressed components contribute to the mechanical homeostasis of GI smooth muscle tissue.

7.3.2 Mechanical stability

The mechanical equilibrium of the entity is consistently undermined by a dynamic external environment and continuous physical challenge. In order to establish long-term homeostasis, the entity is required to withstand perturbation and, if that fails, enforce regulatory measures for restoring equilibrium. The ability for the entity to retain the state of mechanical equilibrium is termed mechanical stability (Ugural, 1991).

The existence of pre-stress has been suggested to be the signal of mechanical homeostasis being passed from one entity to the other (Ingber, 2003b). It allows the transmission of mechanical signals and mechanical properties across the morphological tiers. Deviations from homeostatic pre-stress levels can act as a feedback signal which initiates corrective measures to restore equilibrium.

The LANVS model presents a succinct illustration of the mechanism that responds to a disturbance of mechanical homeostasis in GI smooth muscle (Figure 6.14). The prescribed stress or strain causes a smooth muscle deformation which deviates from mechanical homeostasis. The transmission of the pre-stress signal in GI tissue is illustrated by the communication of reference strain variables through the passive and active stress length adaptation components in the LANVS model. The subsequent regulations of smooth muscle passive and active mechanical properties are

represented by the translation of stress-strain relations in the NVS and ANVS elements as shown in Figure 6.5.

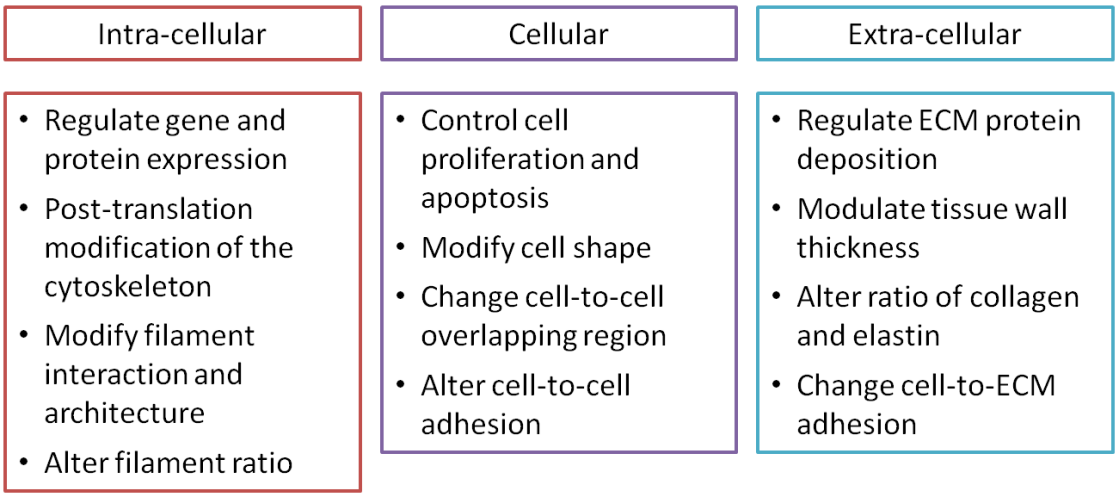

Figure 7.4 Intra-cellular, cellular and extra-cellular measures for regulating mechanical stability of biological entity.

Within a biological entity, mechanical stability can be enforced through different adaptive measures which aim to alter the structure, and hence properties and function, of the entity. The structure of the entity can be modified by regulating the quantity, quality and ratio of the constituents, repositioning and reconnecting the components, and changing their geometric configurations at the intra-cellular, cellular and extra-cellular levels (Figure 7.4).

Within airway SMC, regulation of gene and protein expression influences the polymerisation of actin filaments (Gunst and Zhang, 2008). Phosphorylation of the protein desmin by p21-activated kinase can negate its ability to connect and form filaments to support SMC architecture (Ohtakara *et al.*, 2000; Clemen *et al.*, 2012). Altering the sarcoplasmic F-actin to G-actin ratio can change the stiffness of SMC (Martinez-Lemus *et al.*, 2009). Overall, these intra-cellular biological processes can be adapted by GI SMC and influence their mechanical stability.

To preserve mechanical stability in the circulatory system, it is essential to maintain constant circumferential stress of blood vessels (Wolinsky, 1972). To achieve that, vascular SMC can change their morphology which influences cell-to-cell overlapping and hence cell-cell adhesion in wall tissue (Martinez-Lemus *et al.*, 2004). The modification of inter-cellular connections affects the stiffness of vascular tissue and the ability of blood vessels to withstand different hydrodynamic pressures. The number of cells residing in the tissue can also be regulated by proliferation and apoptosis mechanisms which can affect the mechanical properties of the tissue and organ (Cai *et al.*, 2012).

An example of ECM adaptation can also be found from the vascular system. The degradation of vascular ECM components is promoted by matrix metalloproteinases which is, in turn, regulated by its tissue inhibitors (Kuzuya and Iguchi, 2003). The relative ratio of collagen and elastin fibres also influences the stiffness of blood vessels (VanBavel *et al.*, 2003).

Collectively, biological organisations, including GI tract, seek to maintain a mechanical homeostatic state (Fung, 1993). Deviation from mechanical equilibrium causes a change in pre-stress conditions which is transmitted through the morphological hierarchy. This initiates an adaptive response which modifies the protein, cell, tissue and organ structures and their properties.

7.4 Mechanics and GI physiology

7.4.1 Gastric reservoir function

The stomach serves as storage for the large volume of food ingested at a single meal (Kutchai, 2004). The wall tissue of a fasting stomach is stiffened under the influence of

smooth muscle tonic contraction (Tack, 2006). Swallowing causes distension of the lower sphincter of oesophagus, evokes fast relaxation of stomach through efferent neural pathways (Kutchai, 2004). The phenomenon is called receptive relaxation (Schwizer *et al.*, 2002). The continued entry of ingested food leads to further increments in stomach compliance, which is termed adaptive relaxation. Both the receptive and adaptive relaxations are integral parts of gastric reservoir function which helps to accommodate additional volume while avoiding an excessive built-up of intra-gastric pressure (Lorenzo-Figueras *et al.*, 2005).

The sequence of events that support effective gastric reservoir function can be explained using the adaptive mechanical framework. Distension of oesophagus, as a physiological stimulus, initiates a change in the intra-cellular structures within the stomach. The receptive relaxation of gastric wall tissue can be associated with a reduction of the Ca^{2+}-dependent tonic contraction. Cross-linking between actin and myosin filaments is reduced. Decreased smooth muscle contractile activity leads to quick increment of stomach wall tissue compliance.

The simulation results obtained from the ANVS GI smooth muscle model gives support to the postulated series of events. As shown in Figure 5.16, a decrement of $[Ca^{2+}]_i$ leads to a similar abatement of the smooth muscle elastic modulus. Adjusting the GI wall tissue stiffness through the Ca^{2+}-dependent process can be completed within tens of seconds as illustrated by Figures 5.12a and 5.15a. The notion of fast relaxation is also supported by in-vitro experimental observations which have illustrated that canine smooth muscle relaxation through a reduction of $[Ca^{2+}]_i$ can be completed within 20 seconds (Ozaki *et al.*, 1991b).

The reduction of active stress through [Ca^{2+}]-dependent processes is insufficient to explain the near isobaric expansion of stomach volume which can increase up to 1.5 litres (Kutchai, 2004). While a reduction of tonic contraction can reduce the smooth muscle active stiffness, a continued distension of stomach leads to an inevitable overall stiffening of GI wall tissue due to its passive mechanical properties as predicted by the NVS model (Figure 4.7). As such, further gastric relaxation necessitates the adaptive response of its wall tissue.

The LANVS simulation illustrates an instance of such adaptive response. As shown in Figure 6.12, applying electric field stimulation to a lengthened GI smooth muscle can reduce its initial passive stress by 75% in 35 minutes. The result suggests that persistent lengthening coupled with electrical stimulation can instigate the restructuring of GI smooth muscle. The adjusted intra-cellular architecture eases internal tension and allows further extension of gastric wall tissue without a substantial increment of passive stress and intra-gastric pressure.

7.4.2 Gastric emptying

Gastric emptying is the process of transporting ingested material from stomach to the duodenum through gastric motility. The bolus is encouraged to move to the antrum through periodic circumferential peristaltic activity which starts from mid-corpus (Tack, 2006). The contractile wave, which occurs at a frequency of three waves per minute, transports the chyme out of the stomach when the pyloric splinter is open. When the splinter is closed, the chyme is propelled back to the antrum for further disintegration of large food particles and mixing them with digestive juice (Kutchai, 2004). Simultaneous tonic contraction of the proximal stomach, including fundus and upper half of corpus, also facilitates the movement of the bolus.

The ANVS model can simulate the GI smooth muscle phasic contraction which generates the regular peristaltic movements in the distal stomach. The modelling results illustrate that the magnitude of isometric contraction can be influenced by both $[Ca^{2+}]_i$ and tissue deformation (Figure 5.10d). In particular, the fluctuation of $[Ca^{2+}]_i$ and its magnitude is regulated by SMC electrical activity under the influence of nearby ICC and the ENS (Marieb, 2004). Modulation of GI smooth muscle tonic contraction in the proximal stomach can be explained using the similar Ca^{2+}-dependent mechanism as suggested by the result shown in Figure 5.16. Overall, our simulation results agree with the current understanding that the SMC phasic and tonic contractions are regulated by its $[Ca^{2+}]_i$ and electrical activity, which are influenced by the ICC and ENS. The Ca^{2+}-dependent mechanism is the fundamental principle of GI smooth muscle electro-mechanics and GI motility.

Gastric emptying is stimulated by various neural and hormonal factors (Barrett and Raybould, 2008). It can be postulated that these factors initiate the alteration of mechanical structure and properties of stomach wall tissues. The contribution of phasic and tonic contractions in achieving the physiological objective of stomach emptying is evaluated to generate an appropriate feedback message for further mechanical adjustment. Shear stress is a possible candidate for the mechanical feedback signal. The food bolus pressing against the stomach wall generates viscous stress which can be transmitted from the mucosa to the SMC (Gayer and Basson, 2009). Shear stress can alter the electrical properties of Ca^{2+} and Na^{+} transmembrane ion channels and, in turn, influence the electrical activity of ICC and contractile activity of SMC (Farrugia *et al.*, 1999; Strege *et al.*, 2003). Overall, gastric peristaltic activity and emptying can be influenced by shear stress sensed by the stomach wall tissue. Although shear stress or shear strain is not explicitly represented in the current

LANVS, the model structure can be used as a blueprint for the development of a shear-sensing electro-mechanical model. Overall, a complete analysis of gastric emptying and peristaltic movement of stomach involves the development of a three-dimensional organ model, which is detailed in Section 8.3.

Further modification of stomach wall tissue is needed for effective gastric motility. Expansion of the intra-gastric volume leads to increased organ distension and circumferential SMC lengthening. As a result, the extent of actin and myosin filament overlap diminishes together with magnitude of contractile force (Figures 5.8c and 5.8d). Our simulation results, supported by evidence from in-vitro smooth muscle length adaption experiment, have indicated that chronic tensile stress can stimulate the restoration of active stress to pre-deformation level, probably through rearrangement of contractile elements (Figure 6.8). The results also suggest that gastric emptying can be regulated by this distension-driven adaptive mechanical response.

7.5 Mechanics and GI pathophysiology

GI diseases, such as functional dyspepsia and irritable bowel syndrome, can impair the GI tract's ability to transport food materials which leads to content accumulation (Mizuta *et al.*, 2006). As such, symptoms of intestinal obstruction are observed in the diseased organ without actual occlusion of the lumen (De Giorgio *et al.*, 2011). The term 'pseudo-obstruction' is used to describe the pathological condition.

7.5.1 Morphological remodelling response

Zhao and colleagues (2010) administered a jejunum obstruction by fastening part of the organ with a polyurethane band at the beginning of their experiments. They

reported bowel swelling in the proximity of blockage site starting on the second day of observation. Both the intestinal wall thickness and cross-sectional area increased gradually with the rate of outer wall circumference lengthening occurred faster than that of inner wall circumference.

The chronic internal pressure was translated to intestinal wall distension which served as the physiological stimulus in the adaptive mechanical framework. The increased tension encourages first cell hyperplasia and later cell hypertrophy which together lead to thickening of the wall tissue structure (Gabella, 1979; Storkholm *et al.*, 2007; Zhao *et al.*, 2010). We have fitted the exponential model to the published circumferential passive stress-strain data obtained from healthy individuals and systemic sclerosis patients with expanded small bowel and weakened intestinal motility (Gregersen *et al.*, 2007; Gao *et al.*, 2009). Our results in Table 3.1 show that the model parameter values are higher in patient's model compared to those in healthy individual, indicating a steeper stress-strain relation. The results suggest that disease-driven remodelling strengthens the intestinal wall and enables it to withstand stronger circumferential stress (Gregersen and Kassab, 1996).

7.5.2 Biomechanical remodelling response

In separate experiments performed in obstructed guinea-pig jejunum, a time-dependent leftward shift of circumferential stress-strain and stiffness-strain relations has been observed without altering the exponential shape of the relations (Storkholm *et al.*, 2007). Investigators have also established a positive correlation between the amount of deposited collagen and the tissue elastic modulus. In addition, a reduction of residual strain and opening angle in the affected intestinal segment corresponded to the duration of the obstruction (Zhao *et al.*, 2010). Overall, the evidence suggests

structural modification of the ECM leads to the mechanical stiffening of intestinal tissue in an adaptive manner which is encapsulated by the adaptive mechanical framework.

The exponential stress-strain relation of GI smooth muscle has been demonstrated by the exp-exp-exp NVS model (Figure 4.7). Exponential stiffness-strain relation is the consequence of the exponential stress-strain relation as shown in Section 3.1. Intestinal obstruction instigates translations of these mechanical relations, which mimic the leftward shift of passive stress-strain relation illustrated in the LANVS model (Figure 6.5c). However, the loading condition generated by a sustained increment of lumen pressure in a blocked intestine is likely to be different from that instigated by chronic shortening. Therefore, further investigation is warranted to study the underlying physiology of intestinal obstruction which leads to a change of passive mechanical properties similar to length adaptation.

Both the submucosa and muscle layers expand in the event of chronic intestinal obstruction with the circumferential smooth muscle layer increasing in thickness three-fold after two weeks (Zhao *et al.*, 2010). Furthermore, the reduction of residual strain and opening angle in intestinal wall tissue was largely contributed by circumferential smooth muscle. The results suggest that modulation of smooth muscle passive mechanical properties in response to physical stimulus, as shown in LANVS model simulations, is the major constituent of the adaptive mechanical response of the intestinal wall. These results also illustrate the importance of an understanding of GI smooth muscle mechanics when studying pathophysiological phenomena.

7.5.3 Motility modification response

The thickening of smooth muscle layers in the presence of an obstruction also suggests that the organ attempts to overcome the obstruction by increasing its contractile capability (Zhao *et al.*, 2011b). The contractile stress and pressure were reported to increase with the duration of obstruction but the resulting strain varied inversely. The investigators suggested that the increased stiffness of wall tissue hindered the effectiveness of the contractile process.

Gabella (1979) reported that hypertrophic intestinal smooth muscle has a weaker contractile capability than control tissue. They also observed an increased quantity of intermediate filaments in hypertrophic SMC but no alteration in myosin and actin filament contents. As the intermediate filaments influence the viscoelastic strength of SMC, the result indicates stronger mechanical resistance against the active force in enlarged SMC (Paulin and Li, 2004).

The experimental observations can be explained by the ANVS simulations conducted previously. As shown in Figure 5.11, when the GI smooth muscle was released from an isometric conformation 1.5s after onset of phasic contraction, the maximum shortening displacement decreases with increasing isotonic load. The shortening velocity also varies with the load in a hyperbolic manner, in line with Hill's equation. A similar inverse load-velocity relation can be observed from the tonic contraction simulations (Figure 5.12). Collectively, the results suggested that resistant loads, including those contributed by wall tissue stiffness and cytoskeleton, can impede the smooth muscle contractile performance and, in turn, jeopardise the motility of the obstructed intestine.

The electro-mechanical activity of smooth muscle is driven and coordinated by the constituent ICC, which regulates the $[Ca^{2+}]_i$ and contractile fluctuations in smooth muscle as shown in Figure 5.5. Disruption of the ICC network and electrical activity were observed in obstructed murine intestine (Chang *et al.*, 2001). Together, the results suggested motility in blocked small bowel can also be undermined by crippled electrical activity in smooth muscle.

7.5.4 Sequence of adaptive response

Overall, it can be postulated that a sequence of remodelling events constitutes the collective response of small intestine towards chronic pseudo-obstruction.

Obstruction of intestinal lumen leads to built-up of intra-bowel pressure which is translated to organ distension, tissue extension and cell stretching through the morphological hierarchy. Increasing the tissue stiffness through SMC contraction is possibly the immediate mechanical response to counter the rise of internal pressure. To manage the long-term internal pressure increment and reduce energy consumption, structural remodelling events occur at the intra-cellular, inter-cellular and extra-cellular levels (Figure 7.4). These events lead to morphological and biomechanical changes which affect the intestinal tissue's material and contractile properties. At each level, the ability of the structure in alleviating the syndrome, preventing spillage of intestinal contents, maintaining normal physiological functions and homeostasis, and ultimately protecting the organ and body is assessed. The deviation from the physiological objectives is theorised to feed back through normal (distension) and shear (viscous) stress mechanical signals. The feedback signals influence the subsequent adaptive response of the intestine.

Chapter 8 Conclusions

8.1 Thesis contributions

This thesis aimed to investigate GI smooth muscle mechanics in the context of GI physiology. The method of investigation followed the principle of structure-property-function relationship.

Morphological evidence and experimental results have been presented to support the notion that GI smooth muscle structure contributes to its mechanical properties. The architecture of SMC, the cell-cell connection and ECM were examined and illustrated with microscopic and fluorescent images obtained from the literature. The influence of the cytoskeleton and ECM fibres towards smooth muscle mechanics was illustrated through a series of experiments conducted by other investigators and summarised here. Mechanical responses of both resting and activated smooth muscles under different loading conditions have been reviewed. The length adaptation phenomenon is also closely connected to reorganisations of cytoskeletal network and contractile apparatus. Previous mathematical models developed to simulate smooth muscle mechanics have also been explained and critically assessed.

A NVS model was developed to demonstrate uniaxial passive mechanical properties of GI smooth muscle under isokinetic, isometric and isotonic loading conditions. The simulation results obtained from the selected model variant, which consists of exponential elastic components and exponential viscous component, agrees with experimental results obtained by other investigators. The NVS was also extended to accept piecewise constitutive relations which condense both muscle tensile and

compressive properties into a single model. Overall, the major viscoelastic features of GI smooth muscle can be encapsulated by the compact NVS model.

Built upon the foundation of NVS, an ANVS model was derived to simulate the one-dimensional mechanical properties of active GI smooth muscle. Usage of the ANVS was enhanced by connecting it with strain-dependent active force generation and Ca^{2+}-dependent cross-bridge cycle components, which were developed by other investigators. The collective model has been parameterised using experimental data. The parameterised model was able to simulate both the Ca^{2+}-dependent phasic and tonic contractions at distinct strains, reproduce the Hill's force-velocity relation, and demonstrate the dynamic stiffness of active GI smooth muscle.

The dynamic nature of smooth muscle active and passive mechanics was captured by the LANVS model. The model can simulate the regulation of passive and active stress-strain relations in response to prolonged deformation. It can also exhibit isometric active force recovery and passive tension decay under electrical field stimulation. The model was used to discuss the possible mechanism which enables GI smooth muscle to operate over an extended range of strains. It also demonstrated, mathematically, the possible feedback control mechanism which modulates smooth muscle mechanics under the influence of deformation.

The GI smooth muscle structure, mechanical properties and function are connected to the physiological objectives of the GI tract and stimuli through a postulated adaptive mechanical framework. The framework demonstrated the plausible multi-scale control processes in which GI smooth muscle perceives the mechanical signals, alters its structure and mechanical properties, and influences the effectiveness of gastric reservoir and gastric emptying functions. It also illustrated the way GI smooth muscle

adapts its structure through a sequence of intra-cellular, cellular and extra-cellular measures in response to intestinal pseudo-obstruction. In both cases, it is hypothesised that GI tract and its constituent components seek to achieve mechanical homeostasis.

In conclusion, this work demonstrates the plausible connection that mechanical functions of GI tract are determined by the structure and properties of its constituents. It also establishes that the constituent components, such as cytoskeleton and SMC, regulate their response towards change of physical and chemical factors, which consequently affects the physiology of the GI tract.

8.2 Model limitations

The scarcity of suitable experimental data is a constant challenge in computational modelling. To circumvent the issue, GI smooth muscle cell and tissue mechanical experimental data from a variety of sources has been collected to parameterise and validate the computational models developed here. The data, obtained from both collaborators and peer-reviewed publications, are different in terms of organism, GI tract position and loading condition. For instance, data from cyclic loading of porcine fundus smooth muscle tissue was used for parameterisation of the NVS, while isometric contraction data from active guinea pig corpus circumferential smooth muscle was adapted for validating the ANVS. While the successful inclusion of different data suggests the versatility of the models, the quality of model simulations can be improved if it is parameterised from a series of mechanical experiments conducted on the GI smooth muscle from a fixed location in a single organism. Eventually, more specific GI smooth muscle models can be developed which can assist in physiological study of a particular GI tract location.

The GI smooth muscle developed in this work can be enhanced in various aspects, particularly in model parameterisation, formulation of model mechanism and model validation. As a case in point, the NVS model parameters for simulating stress relaxation and creep are different (Section 4.2.2). While the results suggest alternate NVS components are needed, the discrepancy can be accounted for by the tissue variability and small sample size. The model can be optimised to multiple samples undergoing identical experiments and the model parameters may converge. In another example, the disappearance of the contractile wave after step-extension observed in experiment is not reproduced by ANVS (Figures 5.7a and 5.8a). As the phenomenon has only been demonstrated by Price and colleagues (1977), experimental verification by other research groups is needed to confirm its existence. Nevertheless, it is also possible that the phenomenon is caused by mechano-electrical ion channels which is not considered in the current model (Kraichely and Farrugia, 2007). In length adaptation modelling, the magnitudes of the simulated active and passive stress are different from the experimental results produced by Wang and co-workers (2001). As the experiment is performed on tracheal smooth muscle, the GI smooth muscle LANVS model is not expected to adhere to the empirical results quantitatively. The model can be validated when the data of length adaptation experiments performed on mammalian GI smooth muscle becomes available.

The NVS, ANVS and LANVS models describe the aggregate mechanical behaviour of GI smooth muscle. Although experimental evidence has revealed that the mechanical properties of GI smooth muscle are influenced by biomechanics of cytoskeleton and ECM fibres such as collagen and elastin, the individual contribution of these constituent components has not been elucidated. Qin *et al.* (2011) have recently

reported that the deletion of 50 amino acids from lamin intermediate filament can cause a defective filament morphology which, in turn, causes a premature aging syndrome. The result suggests that knowledge of the individual filament network contributions will be useful in refining the mathematical models for studying the influence of micro-structure in GI wall tissue mechanics under both healthy and diseased conditions.

The NVS, ANVS and LANVS are derived from the SLS framework, which is based on the infinitesimal strain theory. However, the loaded GI tissue can undergo large deformation which deems the application of infinitesimal strain inappropriate. Nevertheless, the results in this work indicate that the installation of exponential and power-law components can compensate for the deficiency of SLS, and simulate the mechanical properties of the GI smooth muscle in wide range of strain. Overall, the models developed in this thesis are viable options for modelling materials with large deformation.

It is important to note that the NVS, ANVS and LANVS models are not frame-invariant, except when linear components are installed in the models. Extending the current one-dimensional constitutive models to higher dimension in the continuum framework is not trivial as the strain measure is not easily identified. Similar issues in cardiac electro-mechanical simulations are circumvented by applying the multi-scale modelling technique, which involves embedding the complex cell/tissue model in a finite element (FE) mesh of the organ (Hunter *et al.*, 2003). The development of GI organ mechanics model is discussed in Section 8.3.

8.3 Future work

The mathematical models presented in this work describe the uniaxial mechanical properties of GI smooth muscle. The usefulness of the models can be enhanced by extending them to higher spatial dimensions. The development of three-dimensional (3D) constitutive GI organ model consists of the construction of finite element mesh, the derivation of mathematical model, model computation and model validation (Liao *et al.*, 2009a; Brook *et al.*, 2010).

Determining the anatomy of GI organ is non-trivial partly due to the structural changes along the alimentary tract, such as wall tissue dimensions (overall thickness and the thickness of the individual layers), tissue constituents (orientation of collagen fibres in submucosa, myocyte arrangements in the circumferential, longitudinal and, in stomach, oblique smooth muscle layers), tissue alignment and tissue folding. Imaging modalities, including ultrasonography, computed tomography (CT) and magnetic resonance (MR), facilitate the capturing of organ anatomy and tissue cross-sections (Gilja *et al.*, 2007; Schreyer and Stroszczynski, 2011). The images can be enhanced, segmented and consolidated into a volume before being translated into a 3D FE mesh. The techniques have been applied in GI, cardiac and airway modelling (Liao *et al.*, 2006a; Brook *et al.*, 2010; Gurev *et al.*, 2011).

The derivation of mathematical model involves the coupling of the organ FE continuum mechanics framework and the muscle contraction model. In building the FE model for rat oesophagus, Liao and colleagues (2004) employed a cylindrical coordinate system with eight-node tri-cubic Hermite interpolation 3D elements to accommodate the tubular shape of the organ and irregular inner boundary. Separate elements were allocated to the non-muscle tissue (mucosa and submucosa) and the

smooth muscle layer. An exponential pseudo-strain density function, with material parameters in longitudinal, circumferential and axial directions, was used to demonstrate the increasing tissue stiffness in large deformation and material anisotropy (Section 3.2.1).

While the organ FE framework accounts for the passive mechanics, the contractile force of smooth muscle can be evaluated by the muscle contraction model such as the parameterised ACC in the ANVS smooth muscle model (Chapter 5). The ACC can be connected to the models developed by Gestrelius and Borgström (1986), and Gajendiran and Buist (2011) to demonstrate strain-dependent and $[Ca^{2+}]$-dependent smooth muscle contraction respectively (Figure 5.17). Similar to its biological counterpart, the muscle contraction model generates uniaxial contractile stress along fibre direction. The ACC are embedded in the FE mesh for computing the local contractile stress at each node

The computation of the multi-scale GI organ model can be initiated by solving the muscle contraction model at each grid point followed by the organ FE model (Nickerson *et al.*, 2005). Briefly, given an initial (global) strain field, the strain for each element (local strain) can be calculated. The local strain and the local calcium concentration are used to compute the contractile stress in the fibre direction using the muscle contraction model. The element stress values are then aggregated to form the global stress tensor. Particularly, the stress is evaluated by summing the contractile stress and the passive stress along the fibre direction, while only passive stress is considered in non-fibre direction. The displacement of each node is then evaluated through conservation of momentum in the organ FE model with boundary conditions. The displacement magnitudes are then translated to strain values which are required for computing the organ deformation in the next time step.

Computational environments and simulation packages such as OpenCMISS (Auckland Bioengineering Institute, New Zealand), CHASTE (University of Oxford, United Kingdom) and FEBio (University of Utah, U.S.A. and Columbia University, U.S.A.) have been developed to facilitate multi-scale modelling. Nevertheless, enormous computational resource is needed to perform a high-resolution simulation of a GI organ. In cardiac modelling, approximately 30 million grid points and 50,000 time steps are required to simulate a single heart beat which lasts for 500 ms. Hunter *et al.* (2003) suggested the implementation of multi-grid technique to reduce the storage requirement, and the application of parallel computing to quicken the simulation. Similar optimisation techniques can be administered in GI organ simulation.

The completed model can be validated against experimental results. For instance, images of organ cross-sections can be obtained from resting and agonist-initiated contractile states (Brook *et al.*, 2010). While the resting state is used as the reference configuration for building the organ model, the contractile state (deformed configuration) can be compared with simulated deformation. Future advance in experimental techniques will aid model validation by providing more accurate measurements and comprehensive results (Hunter *et al.*, 2003).

In addition to the mechanical properties, the contraction of GI smooth muscle is influenced by electrical signals transmitted from ICC, neighbouring SMC and the enteric nervous system. The electro-mechanical behaviour of SMC can be studied by coupling the mechanics models with the electrics counterparts. The connection between GI smooth muscle mechanics and electrics models also enables the computational investigation of GI smooth muscle mechano-electrical behaviour influenced by mechano-sensitive ion channels. The bi-directional interplay of GI smooth muscle electrics and mechanics constitutes the adaptive mechanical

behaviour postulated in this work. Such mathematical model will assist experimentalists to verify the effects of length-adaptation and other regulatory mechanisms in GI smooth muscle.

8.4 Possible clinical applications

The ultimate aim of GI model development is to provide an integrative description of GI physiology and pathophysiology. The models, after validation, can potentially be applied in GI disease detection and medical research.

As illustrated in Tables 1.3 and 1.4, correlations between GI pathology, tissue geometrical and mechanical properties have been reported. This suggests that GI tissue thickness and stiffness can be employed as biomarkers for disease diagnosis and prognosis. Imaging techniques such as CT and MR have been employed to investigate changes in tissue dimensions (Grand *et al.*, 2013). These techniques can be combined with the 3D models suggested in Section 8.3 to monitor deformation and alteration in mechanical properties of GI tissue over time. The new techniques are less invasive compared to traditional methods such as endoscopy and impedance planimetry (Rao *et al.*, 1995; Gregersen *et al.*, 2011). The novel methodology can be used to monitor progression of GI diseases such as intestinal obstruction, ulcerative colitis, and functional dyspepsia.

Selected computational models have been applied to aid the development of novel medical devices such as the Enterra® neuromodulator system (Medtronic, Minnesota, U.S.A.). The device generates electrical signals with desired magnitude and frequency, and transmits them to the electrodes placed on the surface of the stomach. The gastric electrical stimulation technique is an effective therapeutic approach against disorders, such as gastroparesis and functional dyspepsia, originated from

abnormal electrical activities (Gallas and Fetissov, 2011). GI electrophysiological models have been used to predict the optimum electrical signals to effect the positive changes to stomach peristalsis. (Du *et al.*, 2009a; Du *et al.*, 2009b). By incorporating the GI smooth muscle mechanical models developed in this thesis, the effectiveness and efficacy of such devices can be assessed more accurately. Collectively, the cost and risk of developing new medical devices can be reduced.

List of publication and presentations

Part of the work in this thesis has been published in a peer-reviewed journal, and presented in conferences and seminars.

Publication at peer-reviewed journal

Chung CW and Buist ML. A Novel Nonlinear Viscoelastic Solid Model. Nonlinear Analysis: Real World Applications, 13, 1480–1488. (2012).

Presentations in international conferences

Chung CW, Lim CT and Buist ML. Quantification of Soft Tissue Biomechanics Using a Novel Nonlinear Viscoelastic Model. Engineering Mechanics Institute (EMI) 2011 Conference, United State of America. (2011).

Buist ML, **Chung CW** and Gajendiran V. Quantifying Gastrointestinal Smooth Muscle Cell Mechanics. International Symposium on Mechanobiology (5th SICBM), China. (2011).

Buist ML, Gajendiran V and **Chung CW**. Gastrointestinal Smooth Muscle Cell Motility Models. New Advances in Gastrointestinal Motility Meeting, New Zealand. (2011).

Chung CW, Lin M and Buist ML. Quantification of Mammalian Gastrointestinal Tissue Viscoelasticity. 6th World Congress on Biomechanics, Singapore. (2010).

Presentations at student conferences and seminars

Chung CW and Buist ML. Quantification of Gastric Tissue Viscoelasticity. Biomedical Engineering Society 6th Scientific Meeting (BES6SM), Singapore. (2012).

Chung CW and Buist ML. Quantification of Gastric Tissue Viscoelasticity. NUS Bioengineering Showcase, Singapore. (2012).

Chung CW and Buist ML. Quantification of Mammalian Gastrointestinal Tissue Viscoelasticity. NUS Graduate Students' Seminars, Singapore. (2010).

Chung CW, Lim CT and Buist ML. Design of a Micro-Tensile Tester for Probing Smooth Muscle Cell Viscoelasticity. 3rd East Asian Pacific Student Workshop, Singapore. (2009).

Chung CW and Buist ML. Quantification of Smooth Muscle Cell Viscoelasticity. NUS Graduate Students' Seminars, Singapore. (2009).

Bibliography

Agarwal, N. and Spiegel, B. M. (2011). The effect of irritable bowel syndrome on health-related quality of life and health care expenditures. *Gastroenterol Clin North Am* **40**(1): 11-19.

Aitken, K. J. and Bagli, D. J. (2009). The bladder extracellular matrix. Part I: architecture, development and disease. *Nat Rev Urol* **6**(11): 596-611.

Ali, F., Pare, P. D. and Seow, C. Y. (2005). Models of contractile units and their assembly in smooth muscle. *Can J Physiol Pharmacol* **83**(10): 825-831.

Almasri, A. M., Ratz, P. H., Bhatia, H., Klausner, A. P. and Speich, J. E. (2010a). Rhythmic contraction generates adjustable passive stiffness in rabbit detrusor. *J Appl Physiol* **108**(3): 544-553.

Almasri, A. M., Ratz, P. H. and Speich, J. E. (2010b). Length adaptation of the passive-to-active tension ratio in rabbit detrusor. *Ann Biomed Eng* **38**(8): 2594-2605.

Andrews, J. M. and Blackshaw, L. A. (2006). Small Intestinal Motor and Sensory Function and Dysfunction. In: *Sleisenger & Fordtran's gastrointestinal and liver disease : pathophysiology, diagnosis, management. 8th ed*. Edited by: Feldman, M., Friedman, L. S. and Brandt, L. J. Philadelphia, PA, Saunders/Elsevier. Chapter 94.

Andrews, J. M. and Blackshaw, L. A. (2010). Small Intestinal Motor and Sensory Function and Dysfunction. In: *Sleisenger and Fordtran's gastrointestinal and liver disease : pathophysiology, diagnosis, management. 9th ed*. Edited by: Feldman, M., Friedman, L. S. and Brandt, L. J. Philadelphia, PA, Saunders/Elsevier. Chapter 97.

Argyris, J., Stdoltsinis, I. and Dasilva, V. D. (1991). Constitutive Modeling and Computation of Nonlinear Viscoelastic Solids .1. Rheological Models and

Numerical-Integration Techniques. *Computer Methods in Applied Mechanics and Engineering* **88**(2): 135-163.

Arner, A. (1982). Mechanical characteristics of chemically skinned guinea-pig taenia coli. *Pflugers Arch* **395**(4): 277-284.

Bai, T. R., Bates, J. H., Brusasco, V., Camoretti-Mercado, B., Chitano, P., Deng, L. H., Dowell, M., Fabry, B., Ford, L. E., Fredberg, J. J., Gerthoffer, W. T., Gilbert, S. H., Gunst, S. J., Hai, C. M., Halayko, A. J., Hirst, S. J., James, A. L., Janssen, L. J., Jones, K. A., King, G. G., Lakser, O. J., Lambert, R. K., Lauzon, A. M., Lutchen, K. R., Maksym, G. N., Meiss, R. A., Mijailovich, S. M., Mitchell, H. W., Mitchell, R. W., Mitzner, W., Murphy, T. M., Pare, P. D., Schellenberg, R. R., Seow, C. Y., Sieck, G. C., Smith, P. G., Smolensky, A. V., Solway, J., Stephens, N. L., Stewart, A. G., Tang, D. D. and Wang, L. (2004). On the terminology for describing the length-force relationship and its changes in airway smooth muscle. *J Appl Physiol* **97**(6): 2029-2034.

Barrett, K. E. and Raybould, H. E. (2008). Gastrointestinal Physiology. In: *Berne & Levy physiology. 6th ed*. Edited by: Koeppen, B. M. and Stanton, B. A. Philadelphia, PA, Mosby/Elsevier. Section VI.

Basson, M. D. (2003). Paradigms for mechanical signal transduction in the intestinal epithelium. Category: molecular, cell, and developmental biology. *Digestion* **68**(4): 217-225.

Bassotti, G., Germani, U. and Morelli, A. (1995). Human colonic motility: physiological aspects. *Int J Colorectal Dis* **10**(3): 173-180.

Bednarek, M. L., Speich, J. E., Miner, A. S. and Ratz, P. H. (2011). Active tension adaptation at a shortened arterial muscle length: inhibition by cytochalasin-D. *Am J Physiol Heart Circ Physiol* **300**(4): H1166-1173.

Beyder, A., Rae, J. L., Bernard, C., Strege, P. R., Sachs, F. and Farrugia, G. (2010). Mechanosensitivity of Nav1.5, a voltage-sensitive sodium channel. *J Physiol* **588**(Pt 24): 4969-4985.

Black, J. L., Burgess, J. K. and Johnson, P. R. (2003). Airway smooth muscle--its relationship to the extracellular matrix. *Respir Physiol Neurobiol* **137**(2-3): 339-346.

Bosboom, E. M., Hesselink, M. K., Oomens, C. W., Bouten, C. V., Drost, M. R. and Baaijens, F. P. (2001). Passive transverse mechanical properties of skeletal muscle under in vivo compression. *J Biomech* **34**(10): 1365-1368.

Bose, D. and Bose, R. (1975). Mechanics of guinea pig taenia coli smooth muscle during anoxia and rigor. *Am J Physiol* **229**(2): 324-328.

Bosse, Y., Sobieszek, A., Pare, P. D. and Seow, C. Y. (2008). Length adaptation of airway smooth muscle. *Proc Am Thorac Soc* **5**(1): 62-67.

Bosse, Y., Solomon, D., Chin, L. Y., Lian, K., Pare, P. D. and Seow, C. Y. (2009). Increase in passive stiffness at reduced airway smooth muscle length: potential impact on airway responsiveness. *Am J Physiol Lung Cell Mol Physiol* **298**(3): L277-287.

Bredenoord, A. J., Chial, H. J., Camilleri, M., Mullan, B. P. and Murray, J. A. (2003). Gastric accommodation and emptying in evaluation of patients with upper gastrointestinal symptoms. *Clin Gastroenterol Hepatol* **1**(4): 264-272.

Brook, B. S., Peel, S. E., Hall, I. P., Politi, A. Z., Sneyd, J., Bai, Y., Sanderson, M. J. and Jensen, O. E. (2010). A biomechanical model of agonist-initiated contraction in the asthmatic airway. *Respir Physiol Neurobiol* **170**(1): 44-58.

Buehler, M. J. (2008). Nanomechanics of collagen fibrils under varying cross-link densities: atomistic and continuum studies. *J Mech Behav Biomed Mater* **1**(1): 59-67.

Bures, J., Cyrany, J., Kohoutova, D., Forstl, M., Rejchrt, S., Kvetina, J., Vorisek, V. and Kopacova, M. (2010). Small intestinal bacterial overgrowth syndrome. *World J Gastroenterol* **16**(24): 2978-2990.

Bursac, P., Lenormand, G., Fabry, B., Oliver, M., Weitz, D. A., Viasnoff, V., Butler, J. P. and Fredberg, J. J. (2005). Cytoskeletal remodelling and slow dynamics in the living cell. *Nat Mater* **4**(7): 557-561.

Bursztyn, L., Eytan, O., Jaffa, A. and Elad, D. (2007). Mathematical model of excitation-contraction in a uterine smooth muscle cell. *Am J Physiol Cell Physiol* **292**(5): C1816-1829.

Cai, Y., Knight, W. E., Guo, S., Li, J. D., Knight, P. A. and Yan, C. (2012). Vinpocetine suppresses pathological vascular remodeling by inhibiting vascular smooth muscle cell proliferation and migration. *J Pharmacol Exp Ther* **343**(2): 479-488.

Chang, I. Y., Glasgow, N. J., Takayama, I., Horiguchi, K., Sanders, K. M. and Ward, S. M. (2001). Loss of interstitial cells of Cajal and development of electrical dysfunction in murine small bowel obstruction. *J Physiol* **536**(Pt 2): 555-568.

Chaudhuri, O., Parekh, S. H. and Fletcher, D. A. (2007). Reversible stress softening of actin networks. *Nature* **445**(7125): 295-298.

Chen, C., Krishnan, R., Zhou, E., Ramachandran, A., Tambe, D., Rajendran, K., Adam, R. M., Deng, L. and Fredberg, J. J. (2010). Fluidization and resolidification of the human bladder smooth muscle cell in response to transient stretch. *Plos One* **5**(8): e12035.

Cheng, W., Lui, V. C., Chen, Q. M. and Tam, P. K. (2001). Enteric nervous system, interstitial cells of cajal, and smooth muscle vacuolization in segmental dilatation of jejunum. *J Pediatr Surg* **36**(6): 930-935.

Chin, L. Y., Bosse, Y., Pascoe, C., Hackett, T. L., Seow, C. Y. and Pare, P. D. (2012). Mechanical properties of asthmatic airway smooth muscle. *Eur Respir J* **40**(1): 45-54.

Chitano, P., Wang, L. and Murphy, T. M. (2007). Three paradigms of airway smooth muscle hyperresponsiveness in young guinea pigs. *Can J Physiol Pharmacol* **85**(7): 715-726.

Clemen, C. S., Herrmann, H., Strelkov, S. V. and Schroder, R. (2012) Desminopathies: pathology and mechanisms. *Acta Neuropathol* DOI: 10.1007/s00401-012-1057-6.

Clouse, R. E. and Diamant, N. E. (2006). Motor Function of the Esophagus. In: *Physiology of the gastrointestinal tract. 4th ed*. Edited by: Johnson, L. R. Burlington, MA, Elsevier Academic Press. Chapter 36.

Comelekoglu, U. and Ozturk, N. (2008). The stiffness and phase frequency response of taenia coli smooth muscle: comparison of the step and sinusoidal perturbation analysis. *Med Eng Phys* **30**(3): 380-386.

Cook, I. J., Brookes, S. J. and Dinning, P. G. (2010). Colonic Motor and Sensory Function and Dysfunction. In: *Sleisenger and Fordtran's gastrointestinal and liver disease : pathophysiology, diagnosis, management. 9th ed*. Edited by: Feldman, M., Friedman, L. S. and Brandt, L. J. Philadelphia , PA, Saunders/Elsevier. Chapter 98.

Cooke, P. H. and Fay, F. S. (1972). Correlation between fiber length, ultrastructure, and the length-tension relationship of mammalian smooth muscle. *J Cell Biol* **52**(1): 105-116.

Corrias, A. and Buist, M. L. (2007). A quantitative model of gastric smooth muscle cellular activation. *Ann Biomed Eng* **35**(9): 1595-1607.

Craiem, D. O. and Armentano, R. L. (2007). A fractional derivative model to describe arterial viscoelasticity. *Biorheology* **44**(4): 251-263.

Dabiri, B. E., Lee, H. and Parker, K. K. (2012). A potential role for integrin signaling in mechanoelectrical feedback. *Prog Biophys Mol Biol* **110**(2-3): 196-203.

Dahl, J. and Greenson, J. K. (2007). Colon. In: *Histology for pathologists. 3rd ed*. Edited by: Mills, S. E. Philadelphia, Lippincott Williams & Wilkins. Chapter 25.

De Almeida Pdel, V., Gregio, A. M., Machado, M. A., de Lima, A. A. and Azevedo, L. R. (2008). Saliva composition and functions: a comprehensive review. *J Contemp Dent Pract* **9**(3): 72-80.

De Giorgio, R., Cogliandro, R. F., Barbara, G., Corinaldesi, R. and Stanghellini, V. (2011). Chronic intestinal pseudo-obstruction: clinical features, diagnosis, and therapy. *Gastroenterol Clin North Am* **40**(4): 787-807.

Deguchi, S., Ohashi, T. and Sato, M. (2006). Tensile properties of single stress fibers isolated from cultured vascular smooth muscle cells. *J Biomech* **39**(14): 2603-2610.

Deitch, E. A., Bridges, W. M., Ma, J. W., Ma, L., Berg, R. D. and Specian, R. D. (1990). Obstructed intestine as a reservoir for systemic infection. *Am J Surg* **159**(4): 394-401.

Deng, L., Fairbank, N. J., Fabry, B., Smith, P. G. and Maksym, G. N. (2004). Localized mechanical stress induces time-dependent actin cytoskeletal remodeling and stiffening in cultured airway smooth muscle cells. *Am J Physiol Cell Physiol* **287**(2): C440-448.

Deng, L., Fairbank, N. J., Cole, D. J., Fredberg, J. J. and Maksym, G. N. (2005). Airway smooth muscle tone modulates mechanically induced cytoskeletal stiffening and remodeling. *J Appl Physiol* **99**(2): 634-641.

Desprat, N., Richert, A., Simeon, J. and Asnacios, A. (2005). Creep function of a single living cell. *Biophys J* **88**(3): 2224-2233.

Dillon, P. F., Aksoy, M. O., Driska, S. P. and Murphy, R. A. (1981). Myosin phosphorylation and the cross-bridge cycle in arterial smooth muscle. *Science* **211**(4481): 495-497.

Dillon, P. F. and Murphy, R. A. (1982). Tonic force maintenance with reduced shortening velocity in arterial smooth muscle. *Am J Physiol* **242**(1): C102-108.

Doehring, T. C., Freed, A. D., Carew, E. O. and Vesely, I. (2005). Fractional order viscoelasticity of the aortic valve cusp: an alternative to quasilinear viscoelasticity. *J Biomech Eng* **127**(4): 700-708.

Dou, Y., Lu, X., Zhao, J. and Gregersen, H. (2002). Morphometric and biomechanical remodelling in the intestine after small bowel resection in the rat. *Neurogastroenterol Motil* **14**(1): 43-53.

Drozdowski, L. and Thomson, A. B. (2006). Aging and the intestine. *World J Gastroenterol* **12**(47): 7578-7584.

Du, P., Li, S., O'Grady, G., Cheng, L. K., Pullan, A. J. and Chen, J. D. (2009a). Effects of electrical stimulation on isolated rodent gastric smooth muscle cells evaluated via a joint computational simulation and experimental approach. *Am J Physiol Gastrointest Liver Physiol* **297**(4): G672-680.

Du, P., O'Grady, G., Windsor, J. A., Cheng, L. K. and Pullan, A. J. (2009b). A tissue framework for simulating the effects of gastric electrical stimulation and in vivo validation. *IEEE Trans Biomed Eng* **56**(12): 2755-2761.

Du, Y., Al-Jumaily, A. M. and Shukla, H. (2007). Smooth muscle stiffness variation due to external longitudinal oscillations. *J Biomech* **40**(14): 3207-3214.

Eddinger, T. and Meer, D. (2001). Single rabbit stomach smooth muscle cell myosin heavy chain SMB expression and shortening velocity. *Am J Physiol Cell Physiol* **280**(2): C309-316.

Elbrond, H., Tottrup, A. and Forman, A. (1991). Mechanical properties of isolated smooth muscle from rabbit sphincter of Oddi and duodenum. *Scand J Gastroenterol* **26**(3): 289-294.

Eppell, S. J., Smith, B. N., Kahn, H. and Ballarini, R. (2006). Nano measurements with micro-devices: mechanical properties of hydrated collagen fibrils. *J R Soc Interface* **3**(6): 117-121.

Everhart, J. E. (1994). Overview. In: *Digestive diseases in the United States: epidemiology and impact*. Edited by: Everhart, J. E. Washington, DC, US Government Printing Office **NIH publication no. 94-1447.** Chapter 1.

Everhart, J. E. and Ruhl, C. E. (2009). Burden of digestive diseases in the United States part I: overall and upper gastrointestinal diseases. *Gastroenterology* **136**(2): 376-386.

Fabry, B., Maksym, G. N., Butler, J. P., Glogauer, M., Navajas, D. and Fredberg, J. J. (2001). Scaling the microrheology of living cells. *Phys Rev Lett* **87**(14): 148102.

Fabry, B., Maksym, G. N., Butler, J. P., Glogauer, M., Navajas, D., Taback, N. A., Millet, E. J. and Fredberg, J. J. (2003). Time scale and other invariants of integrative mechanical behavior in living cells. *Phys Rev E Stat Nonlin Soft Matter Phys* **68**(4 Pt 1): 041914.

Farrugia, G., Holm, A. N., Rich, A., Sarr, M. G., Szurszewski, J. H. and Rae, J. L. (1999). A mechanosensitive calcium channel in human intestinal smooth muscle cells. *Gastroenterology* **117**(4): 900-905.

Farrugia, G. (2008). Interstitial cells of Cajal in health and disease. *Neurogastroenterol Motil* **20 Suppl 1**: 54-63.

Fay, F. S., Fujiwara, K., Rees, D. D. and Fogarty, K. E. (1983). Distribution of alpha-actinin in single isolated smooth muscle cells. *J Cell Biol* **96**(3): 783-795.

Flügge, W. (1967). *Viscoelasticity*. United States of America, Blaisdell.

Frøkjaer, J. B., Andersen, S. D., Ejskjaer, N., Funch-Jensen, P., Drewes, A. M. and Gregersen, H. (2007). Impaired contractility and remodeling of the upper gastrointestinal tract in diabetes mellitus type-1. *World J Gastroenterol* **13**(36): 4881-4890.

Fudge, D. S., Gardner, K. H., Forsyth, V. T., Riekel, C. and Gosline, J. M. (2003). The mechanical properties of hydrated intermediate filaments: insights from hagfish slime threads. *Biophys J* **85**(3): 2015-2027.

Fung, Y. C. (1967). Elasticity of soft tissues in simple elongation. *Am J Physiol* **213**(6): 1532-1544.

Fung, Y. C. (1993). *Biomechanics : mechanical properties of living tissues*. New York, Springer-Verlag.

Gabbiani, G., Schmid, E., Winter, S., Chaponnier, C., de Ckhastonay, C., Vandekerckhove, J., Weber, K. and Franke, W. W. (1981). Vascular smooth muscle cells differ from other smooth muscle cells: predominance of vimentin filaments and a specific alpha-type actin. *Proc Natl Acad Sci U S A* **78**(1): 298-302.

Gabella, G. (1979). Hypertrophic smooth muscle. IV. Myofilaments, intermediate filaments and some mechanical properties. *Cell Tissue Res* **201**(2): 277-288.

Gabella, G. (1984). Structural apparatus for force transmission in smooth muscles. *Physiol Rev* **64**(2): 455-477.

Gabella, G. (1994). Structure of Smooth Muscles. In: *Pharmacology of Smooth Muscle. ed*. Edited by: Szekeres, L. and Papp, J. G. **Berlin**, Springer-Verlag. Chapter 1.

Gajendiran, V. and Buist, M. L. (2011). A quantitative description of active force generation in gastrointestinal smooth muscle. *International Journal for Numerical Methods in Biomedical Engineering* **27**(3): 450-460.

Gallas, S. and Fetissov, S. O. (2011). Ghrelin, appetite and gastric electrical stimulation. *Peptides* **32**(11): 2283-2289.

Gao, F., Liao, D., Drewes, A. M. and Gregersen, H. (2009). Modelling the elastin, collagen and smooth muscle contribution to the duodenal mechanical behaviour in patients with systemic sclerosis. *Neurogastroenterol Motil* **21**(9): 914-e968.

Gayer, C. P. and Basson, M. D. (2009). The effects of mechanical forces on intestinal physiology and pathology. *Cell Signal* **21**(8): 1237-1244.

Geibel, J. P. (2005). Secretion and absorption by colonic crypts. *Annu Rev Physiol* **67**: 471-490.

Gerthoffer, W. T. and Murphy, R. A. (1983). Myosin phosphorylation and regulation of cross-bridge cycle in tracheal smooth muscle. *Am J Physiol* **244**(3): C182-187.

Gerthoffer, W. T., Murphey, K. A., Mangini, J., Boman, S. and Lattanzio, F. A., Jr. (1991). Myosin phosphorylation and calcium in tonic and phasic contractions of colonic smooth muscle. *Am J Physiol* **260**(6 Pt 1): G958-964.

Gestrelius, S. and Borgström, P. (1986). A dynamic model of smooth muscle contraction. *Biophys J* **50**(1): 157-169.

Gilja, O. H., Hatlebakk, J. G., Odegaard, S., Berstad, A., Viola, I., Giertsen, C., Hausken, T. and Gregersen, H. (2007). Advanced imaging and visualization in gastrointestinal disorders. *World J Gastroenterol* **13**(9): 1408-1421.

Gittes, F., Mickey, B., Nettleton, J. and Howard, J. (1993). Flexural rigidity of microtubules and actin filaments measured from thermal fluctuations in shape. *J Cell Biol* **120**(4): 923-934.

Goh, K. L. (2007). Changing trends in gastrointestinal disease in the Asia-Pacific region. *J Dig Dis* **8**(4): 179-185.

Golenhofen, K. and Mandrek, K. (1991). Phasic and tonic contraction processes in the gastrointestinal tract. *Dig Dis* **9**(6): 341-346.

Gordon, A. R. and Siegman, M. J. (1971). Mechanical properties of smooth muscle. I. Length-tension and force-velocity relations. *Am J Physiol* **221**(5): 1243-1249.

Gosens, R., Mutawe, M., Martin, S., Basu, S., Bos, S. T., Tran, T. and Halayko, A. J. (2008). Caveolae and caveolins in the respiratory system. *Curr Mol Med* **8**(8): 741-753.

Goyal, R. K. and Chaudhury, A. (2008). Physiology of normal esophageal motility. *J Clin Gastroenterol* **42**(5): 610-619.

Gramlich, T. L. and Petras, R. E. (2007). Small Intestine. In: *Histology for pathologists. 3rd ed*. Edited by: Mills, S. E. Philadelphia, Lippincott Williams & Wilkins. Chapter 24.

Grand, D. J., Beland, M. and Harris, A. (2013). Magnetic resonance enterography. *Radiol Clin North Am* **51**(1): 99-112.

Grassmann, C. W., Isken, O. and Behrens, S. E. (1999). Assignment of the multifunctional NS3 protein of bovine viral diarrhea virus during RNA replication: an in vivo and in vitro study. *J Virol* **73**(11): 9196-9205.

Gravesen, F., Behan, N., Drewes, A. and Gregersen, H. (2011). Viscosity of food boluses affects the axial force in the esophagus. *World J Gastroenterol* **17**(15): 1982-1988.

Gregersen, H. and Kassab, G. (1996). Biomechanics of the gastrointestinal tract. *Neurogastroenterol Motil* **8**(4): 277-297.

Gregersen, H., Emery, J. L. and McCulloch, A. D. (1998). History-dependent mechanical behavior of guinea-pig small intestine. *Ann Biomed Eng* **26**(5): 850-858.

Gregersen, H., Lee, T. C., Chien, S., Skalak, R. and Fung, Y. C. (1999). Strain distribution in the layered wall of the esophagus. *J Biomech Eng* **121**(5): 442-448.

Gregersen, H. and Christensen, J. (2000). Gastrointestinal tone. *Neurogastroenterol Motil* **12**(6): 501-508.

Gregersen, H., Kassab, G. S. and Fung, Y. C. (2000). The zero-stress state of the gastrointestinal tract: biomechanical and functional implications. *Dig Dis Sci* **45**(12): 2271-2281.

Gregersen, H., Liao, D., Pedersen, J. and Drewes, A. M. (2007). A new method for evaluation of intestinal muscle contraction properties: studies in normal subjects and in patients with systemic sclerosis. *Neurogastroenterol Motil* **19**(1): 11-19.

Gregersen, H., Villadsen, G. E. and Liao, D. (2011) Mechanical Characteristics of Distension-Evoked Peristaltic Contractions in the Esophagus of Systemic Sclerosis Patients. *Dig Dis Sci* DOI: 10.1007/s10620-011-1777-9.

Gunst, S. J. and Wu, M. F. (2001). Selected contribution: plasticity of airway smooth muscle stiffness and extensibility: role of length-adaptive mechanisms. *J Appl Physiol* **90**(2): 741-749.

Gunst, S. J. and Zhang, W. (2008). Actin cytoskeletal dynamics in smooth muscle: a new paradigm for the regulation of smooth muscle contraction. *Am J Physiol Cell Physiol* **295**(3): C576-587.

Gurev, V., Lee, T., Constantino, J., Arevalo, H. and Trayanova, N. A. (2011). Models of cardiac electromechanics based on individual hearts imaging data: image-based electromechanical models of the heart. *Biomech Model Mechanobiol* **10**(3): 295-306.

Hai, C. M. and Murphy, R. A. (1988a). Regulation of shortening velocity by cross-bridge phosphorylation in smooth muscle. *Am J Physiol* **255**(1 Pt 1): C86-94.

Hai, C. M. and Murphy, R. A. (1988b). Cross-bridge phosphorylation and regulation of latch state in smooth muscle. *Am J Physiol* **254**(1 Pt 1): C99-106.

Hanani, M., Farrugia, G. and Komuro, T. (2005). Intercellular coupling of interstitial cells of cajal in the digestive tract. *Int Rev Cytol* **242**: 249-282.

Hardcastle, J. D. and Mann, C. V. (1970). Physical factors in the stimulation of colonic peristalsis. *Gut* **11**(1): 41-46.

Harris, D. and Warshaw, D. (1990). Slowing of velocity during isotonic shortening in single isolated smooth muscle cells. Evidence for an internal load. *J Gen Physiol* **96**(3): 581-601.

Harris, D. and Warshaw, D. (1991). Length vs. active force relationship in single isolated smooth muscle cells. *Am J Physiol* **260**(5 Pt 1): C1104-1112.

Hasler, W. L. (2006). Small Intestinal Motility. In: *Physiology of the Gastrointestinal Tract. 4th ed*. Edited by: Johnson, L. R., Academic Press. Chapter 38.

Hemmer, J. D., Nagatomi, J., Wood, S. T., Vertegel, A. A., Dean, D. and Laberge, M. (2009). Role of cytoskeletal components in stress-relaxation behavior of adherent vascular smooth muscle cells. *J Biomech Eng* **131**(4): 041001.

Herlihy, J. T. and Murphy, R. A. (1973). Length-tension relationship of smooth muscle of the hog carotid artery. *Circ Res* **33**(3): 275-283.

Herrera, A. M., Martinez, E. C. and Seow, C. Y. (2004). Electron microscopic study of actin polymerization in airway smooth muscle. *Am J Physiol Lung Cell Mol Physiol* **286**(6): L1161-1168.

Herrera, A. M., McParland, B. E., Bienkowska, A., Tait, R., Pare, P. D. and Seow, C. Y. (2005). 'Sarcomeres' of smooth muscle: functional characteristics and ultrastructural evidence. *J Cell Sci* **118**(Pt 11): 2381-2392.

Herrmann, H., Bär, H., Kreplak, L., Strelkov, S. and Aebi, U. (2007). Intermediate filaments: from cell architecture to nanomechanics. *Nat Rev Mol Cell Biol* **8**(7): 562-573.

Hill, A. (1938). The Heat of Shortening and the Dynamic Constants of Muscle. *Proceedings of the Royal Society of London. Series B, Biological Sciences* **126**(843): 136-195.

Himpens, B., Matthijs, G., Somlyo, A. V., Butler, T. M. and Somlyo, A. P. (1988). Cytoplasmic free calcium, myosin light chain phosphorylation, and force in phasic and tonic smooth muscle. *J Gen Physiol* **92**(6): 713-729.

Hong, F., Haldeman, B. D., Jackson, D., Carter, M., Baker, J. E. and Cremo, C. R. (2011). Biochemistry of smooth muscle myosin light chain kinase. *Arch Biochem Biophys* **510**(2): 135-146.

Horowitz, A., Clement-Chomienne, O., Walsh, M. P. and Morgan, K. G. (1996a). Epsilon-isoenzyme of protein kinase C induces a Ca(2+)-independent contraction in vascular smooth muscle. *Am J Physiol* **271**(2 Pt 1): C589-594.

Horowitz, A., Menice, C. B., Laporte, R. and Morgan, K. G. (1996b). Mechanisms of smooth muscle contraction. *Physiol Rev* **76**(4): 967-1003.

Huang, H., Kamm, R. and Lee, R. (2004). Cell mechanics and mechanotransduction: pathways, probes, and physiology. *Am J Physiol Cell Physiol* **287**(1): C1-11.

Huizinga, J. D. and Lammers, W. J. (2009). Gut peristalsis is governed by a multitude of cooperating mechanisms. *Am J Physiol Gastrointest Liver Physiol* **296**(1): G1-8.

Huizinga, J. D., Lammers, W. J., Mikkelsen, H. B., Zhu, Y. and Wang, X. Y. (2010). Toward a concept of stretch coupling in smooth muscle: a thesis by Lars Thuneberg on contractile activity in neonatal interstitial cells of Cajal. *Anat Rec (Hoboken)* **293**(9): 1543-1552.

Humphrey, J. D. (2008). Vascular adaptation and mechanical homeostasis at tissue, cellular, and sub-cellular levels. *Cell Biochem Biophys* **50**(2): 53-78.

Hunter, P. J., Pullan, A. J. and Smaill, B. H. (2003). Modeling total heart function. *Annu Rev Biomed Eng* **5**: 147-177.

Huxley, A. F. and Niedergerke, R. (1954). Structural changes in muscle during contraction; interference microscopy of living muscle fibres. *Nature* **173**(4412): 971-973.

Huxley, A. F. (1957). Muscle structure and theories of contraction. *Prog Biophys Biophys Chem* **7**: 255-318.

Huxley, H. and Hanson, J. (1954). Changes in the cross-striations of muscle during contraction and stretch and their structural interpretation. *Nature* **173**(4412): 973-976.

Imafuku, Y., Emoto, Y. and Tawada, K. (1999). A protein friction model of the actin sliding movement generated by myosin in mixtures of MgATP and MgGTP in vitro. *J Theor Biol* **199**(4): 359-370.

Ingber, D. (2003a). Tensegrity II. How structural networks influence cellular information processing networks. *J Cell Sci* **116**(Pt 8): 1397-1408.

Ingber, D. (2003b). Tensegrity I. Cell structure and hierarchical systems biology. *J Cell Sci* **116**(Pt 7): 1157-1173.

Ingber, D. (2003c). Mechanobiology and diseases of mechanotransduction. *Ann Med* **35**(8): 564-577.

Ingber, D. (2006). Cellular mechanotransduction: putting all the pieces together again. *FASEB J* **20**(7): 811-827.

Ito, S., Kume, H., Oguma, T., Ito, Y., Kondo, M., Shimokata, K., Suki, B. and Naruse, K. (2006). Roles of stretch-activated cation channel and Rho-kinase in the spontaneous contraction of airway smooth muscle. *Eur J Pharmacol* **552**(1-3): 135-142.

Jaksch, W., Dejaco, C. and Schirmer, M. (2008). 4 years after withdrawal of rofecoxib: where do we stand today? *Rheumatol Int* **28**(12): 1187-1195.

Janmey, P. A. and Miller, R. T. (2011). Mechanisms of mechanical signaling in development and disease. *J Cell Sci* **124**(Pt 1): 9-18.

Jarosch, R. (2011). The Different Muscle-Energetics during Shortening and Stretch. *Int J Mol Sci* **12**(5): 2891-2900.

Jiang, H., Liao, D., Zhao, J., Wang, G. and Gregersen, H. (2010). Reversible Stress Softening in Rat Oesophagus in Vitro after KCl Activation. In: *IFMBE Proceedings*. Edited by: Lim, C. T. and Goh, J. C. H. **31**: 1004-1007. Springer Berlin Heidelberg.

Jimenez, M. (2011). Role of peg and socket junctions in stretch coupling in intestinal smooth muscle. *Anat Rec (Hoboken)* **294**(6): 929-930.

Jorgensen, C. S., Ahrensberg, J. M., Gregersen, H. and Flyvberg, A. (2001). Tension-strain relations and morphometry of rat small intestine in experimental diabetes. *Dig Dis Sci* **46**(5): 960-967.

Kahn, E. and Daum, F. (2010). Anatomy, Histology, Embryology, and Developmental Anomalies of the Small and Large Intestine. In: *Sleisenger and Fordtran's*

gastrointestinal and liver disease : pathophysiology, diagnosis, management. 9th ed. Edited by: Feldman, M., Friedman, L. S. and Brandt, L. J. Philadelphia , PA, Saunders/Elsevier. Chapter 96.

Kamada, N., Seo, S. U., Chen, G. Y. and Nunez, G. (2013). Role of the gut microbiota in immunity and inflammatory disease. *Nat Rev Immunol* **13**(5): 321-335.

Kamm, K. E. and Stull, J. T. (1985). Myosin phosphorylation, force, and maximal shortening velocity in neurally stimulated tracheal smooth muscle. *Am J Physiol* **249**(3 Pt 1): C238-247.

Kamm, K. E. and Stull, J. T. (1986). Activation of smooth muscle contraction: relation between myosin phosphorylation and stiffness. *Science* **232**(4746): 80-82.

Kamm, K. E., Gerthoffer, W. T., Murphy, R. A. and Bohr, D. F. (1989). Mechanical properties of carotid arteries from DOCA hypertensive swine. *Hypertension* **13**(2): 102-109.

Kargacin, G. J. and Fay, F. S. (1987). Physiological and structural properties of saponin-skinned single smooth muscle cells. *J Gen Physiol* **90**(1): 49-73.

Kim, H. R., Appel, S., Vetterkind, S., Gangopadhyay, S. S. and Morgan, K. G. (2008). Smooth muscle signalling pathways in health and disease. *J Cell Mol Med* **12**(6A): 2165-2180.

Kindt, S. and Tack, J. (2006). Impaired gastric accommodation and its role in dyspepsia. *Gut* **55**(12): 1685-1691.

Kirton, R. S., Taberner, A. J., Nielsen, P. M., Young, A. A. and Loiselle, D. S. (2004). Strain softening behaviour in nonviable rat right-ventricular trabeculae, in the. *Exp Physiol.* **89**(5): 593-604.

Koch, K. L. (2010). Gastric Neuromuscular Function and Neuromuscular Disorders. In: *Sleisenger and Fordtran's gastrointestinal and liver disease : pathophysiology, diagnosis, management. 9th ed*. Edited by: Feldman, M., Friedman, L. S. and Brandt, L. J. Philadelphia , PA, Saunders/Elsevier. Chapter 48.

Kohl, P., Hunter, P. and Noble, D. (1999). Stretch-induced changes in heart rate and rhythm: clinical observations, experiments and mathematical models. *Prog Biophys Mol Biol* **71**(1): 91-138.

Komuro, T. (2006). Structure and organization of interstitial cells of Cajal in the gastrointestinal tract. *J Physiol* **576**(Pt 3): 653-658.

Kong, F. and Singh, R. P. (2008). Disintegration of solid foods in human stomach. *J Food Sci* **73**(5): R67-80.

Kraichely, R. E. and Farrugia, G. (2007). Mechanosensitive ion channels in interstitial cells of Cajal and smooth muscle of the gastrointestinal tract. *Neurogastroenterol Motil* **19**(4): 245-252.

Kroon, M. (2010). A constitutive model for smooth muscle including active tone and passive viscoelastic behaviour. *Math Med Biol* **27**(2): 129-155.

Kroon, M. (2011). Influence of dispersion in myosin filament orientation and anisotropic filament contractions in smooth muscle. *J Theor Biol* **272**(1): 72-82.

Kunze, W. A. and Furness, J. B. (1999). The enteric nervous system and regulation of intestinal motility. *Annu Rev Physiol* **61**: 117-142.

Kuo, I. Y., Wolfle, S. E. and Hill, C. E. (2011). T-type calcium channels and vascular function: the new kid on the block? *J Physiol* **589**(Pt 4): 783-795.

Kuo, K. H., Wang, L., Pare, P. D., Ford, L. E. and Seow, C. Y. (2001). Myosin thick filament lability induced by mechanical strain in airway smooth muscle. *J Appl Physiol* **90**(5): 1811-1816.

Kuo, K. H., Herrera, A. M., Wang, L., Paré, P. D., Ford, L. E., Stephens, N. L. and Seow, C. Y. (2003). Structure-function correlation in airway smooth muscle adapted to different lengths. *Am J Physiol Cell Physiol* **285**(2): C384-390.

Kuo, K. H. and Seow, C. Y. (2004). Contractile filament architecture and force transmission in swine airway smooth muscle. *J Cell Sci* **117**(Pt 8): 1503-1511.

Kutchai, H. C. (2004). Gastrointestinal Regulation and Motility. In: *Physiology. 5th ed*. Edited by: Berne, R. M., Levy, M. N., Koeppen, B. M. and Stanton, B. A. St. Louis, Mosby**:** x, 1014 p. Chapter 31.

Kuzuya, M. and Iguchi, A. (2003). Role of matrix metalloproteinases in vascular remodeling. *J Atheroscler Thromb* **10**(5): 275-282.

Lakes, R. S. (1999). *Viscoelastic Solids*. Washington, D. C., CRC Press.

Lambert, R. K., Pare, P. D. and Seow, C. Y. (2004). Mathematical description of geometric and kinematic aspects of smooth muscle plasticity and some related morphometrics. *J Appl Physiol* **96**(2): 469-476.

Laudadio, R., Millet, E., Fabry, B., An, S., Butler, J. and Fredberg, J. (2005). Rat airway smooth muscle cell during actin modulation: rheology and glassy dynamics. *Am J Physiol Cell Physiol* **289**(6): C1388-1395.

Lee, G. Y. and Lim, C. T. (2007). Biomechanics approaches to studying human diseases. *Trends Biotechnol* **25**(3): 111-118.

Lenormand, G., Millet, E., Fabry, B., Butler, J. P. and Fredberg, J. J. (2004). Linearity and time-scale invariance of the creep function in living cells. *J R Soc Interface* **1**(1): 91-97.

Lentle, R. G., Janssen, P. W., Goh, K., Chambers, P. and Hulls, C. (2010). Quantification of the effects of the volume and viscosity of gastric contents on antral and fundic activity in the rat stomach maintained ex vivo. *Dig Dis Sci* **55**(12): 3349-3360.

Lessey, E. C., Guilluy, C. and Burridge, K. (2012). From Mechanical Force to RhoA Activation. *Biochemistry* **51**(38): 7420-7432.

Leung, F. P., Yung, L. M., Yao, X., Laher, I. and Huang, Y. (2008). Store-operated calcium entry in vascular smooth muscle. *Br J Pharmacol* **153**(5): 846-857.

Liao, D., Zhao, J., Fan, Y. and Gregersen, H. (2004). Two-layered quasi-3D finite element model of the oesophagus. *Med Eng Phys* **26**(7): 535-543.

Liao, D., Frøkjaer, J. B., Yang, J., Zhao, J., Drewes, A. M., Gilja, O. H. and Gregersen, H. (2006a). Three-dimensional surface model analysis in the gastrointestinal tract. *World J Gastroenterol* **12**(18): 2870-2875.

Liao, D., Sevcencu, C., Yoshida, K. and Gregersen, H. (2006b). Viscoelastic properties of isolated rat colon smooth muscle cells. *Cell Biol Int* **30**(10): 854-858.

Liao, D., Zhao, J. and Gregersen, H. (2006c). Three-dimensional geometry analysis of the stomach in type II diabetic GK rats. *Diabetes Res Clin Pract* **71**(1): 1-13.

Liao, D., Zhao, J. and Gregersen, H. (2009a). Gastrointestinal tract modelling in health and disease. *World J Gastroenterol* **15**(2): 169-176.

Liao, D., Zhao, J., Kunwald, P. and Gregersen, H. (2009b). Tissue softening of guinea pig oesophagus tested by the tri-axial test machine. *J Biomech* **42**(7): 804-810.

Lim, C. T., Zhou, E. H., Li, A., Vedula, S. R. K. and Fu, H. X. (2006a). Experimental techniques for single cell and single molecule biomechanics. *Materials Science & Engineering C* **26**: 1278-1288.

Lim, C. T., Zhou, E. H. and Quek, S. T. (2006b). Mechanical models for living cells--a review. *J Biomech* **39**(2): 195-216.

Lim, C. T., Bershadsky, A. and Sheetz, M. P. (2010). Mechanobiology. *J R Soc Interface* **7 Suppl 3**: S291-293.

Liu, B., Qu, M. J., Qin, K. R., Li, H., Li, Z. K., Shen, B. R. and Jiang, Z. L. (2008). Role of cyclic strain frequency in regulating the alignment of vascular smooth muscle cells in vitro. *Biophys J* **94**(4): 1497-1507.

Liu, J. G. and Qi, H. T. (2010). Dissipated energy function, hysteresis and precondition of a viscoelastic solid model. *Nonlinear Analysis-Real World Applications* **11**(2): 907-912.

Long, J. D. and Orlando, R. C. (2010). Anatomy, Histology, Embryology, and Developmental Anomalies of the Esophagus. In: *Sleisenger and Fordtran's*

gastrointestinal and liver disease : pathophysiology, diagnosis, management. 9th ed. Edited by: Feldman, M., Friedman, L. S. and Brandt, L. J. Philadelphia , PA, Saunders/Elsevier. Chapter 41.

Lorenzo-Figueras, M., Preston, T., Ott, E. A. and Merritt, A. M. (2005). Meal-induced gastric relaxation and emptying in horses after ingestion of high-fat versus high-carbohydrate diets. *Am J Vet Res* **66**(5): 897-906.

Maceri, F., Marino, M. and Vairo, G. (2010). A unified multiscale mechanical model for soft collagenous tissues with regular fiber arrangement. *J Biomech* **43**(2): 355-363.

MacNaughton, W. K. (2006). Mechanisms and Consequences of Intestinal Inflammation. In: *Physiology of the Gastrointestinal Tract. 4th ed*. Edited by: Johnson, L. R., Academic Press. Chapter 45.

Maggio, C. D., Jennings, S. R., Robichaux, J. L., Stapor, P. C. and Hyman, J. M. (2012). A Modified Hai-Murphy Model of Uterine Smooth Muscle Contraction. *Bull Math Biol* **74**(1): 143-158.

Maksym, G. N., Fabry, B., Butler, J. P., Navajas, D., Tschumperlin, D. J., Laporte, J. D. and Fredberg, J. J. (2000). Mechanical properties of cultured human airway smooth muscle cells from 0.05 to 0.4 Hz. *J Appl Physiol* **89**(4): 1619-1632.

Mandrek, K. and Golenhofen, K. (1990). Phasic-rhythmical and tonic components in gastrointestinal motility. *Prog Clin Biol Res* **327**: 463-481.

Manetti, M., Neumann, E., Milia, A. F., Tarner, I. H., Bechi, P., Matucci-Cerinic, M., Ibba-Manneschi, L. and Muller-Ladner, U. (2007). Severe fibrosis and increased expression of fibrogenic cytokines in the gastric wall of systemic sclerosis patients. *Arthritis Rheum* **56**(10): 3442-3447.

Mani, R. J. and Kay, C. M. (1996). Calcium Binding Proteins. In: *Biochemistry of smooth muscle contraction. ed*. Edited by: Bárány, M. San Diego, Academic Press**:** xxvi, 418 p., [412] p. of plates. Chapter 8.

Marieb, E. N. (2004). *Human Anatomy & Physiology*. San Francisco, Pearson Benjamin Cummings.

Martinez-Lemus, L. A., Hill, M. A., Bolz, S. S., Pohl, U. and Meininger, G. A. (2004). Acute mechanoadaptation of vascular smooth muscle cells in response to continuous arteriolar vasoconstriction: implications for functional remodeling. *FASEB J* **18**(6): 708-710.

Martinez-Lemus, L. A., Hill, M. A. and Meininger, G. A. (2009). The plastic nature of the vascular wall: a continuum of remodeling events contributing to control of arteriolar diameter and structure. *Physiology (Bethesda)* **24**: 45-57.

Mashima, H., Okada, T. and Okuyama, H. (1979). The dynamics of contraction in the guinea pig taenia coli. *Jpn J Physiol* **29**(1): 85-98.

McCain, M. L. and Parker, K. K. (2011). Mechanotransduction: the role of mechanical stress, myocyte shape, and cytoskeletal architecture on cardiac function. *Pflugers Arch* **462**(1): 89-104.

McCarron, J. G., Chalmers, S., Bradley, K. N., MacMillan, D. and Muir, T. C. (2006). Ca2+ microdomains in smooth muscle. *Cell Calcium* **40**(5-6): 461-493.

McParland, B. E., Tait, R. R., Pare, P. D. and Seow, C. Y. (2005). The role of airway smooth muscle during an attack of asthma simulated in vitro. *Am J Respir Cell Mol Biol* **33**(5): 500-504.

Meiss, R. A. (1971). Some mechanical properties of cat intestinal muscle. *Am J Physiol* **220**(6): 2000-2007.

Mengheri, E. (2008). Health, probiotics, and inflammation. *J Clin Gastroenterol* **42 Suppl 3 Pt 2**: S177-178.

Meyer, S. L. (1975). *Data analysis for scientists and engineers*. New York,, Wiley.

Mijailovich, S., Butler, J. and Fredberg, J. (2000). Perturbed equilibria of myosin binding in airway smooth muscle: bond-length distributions, mechanics, and ATP metabolism. *Biophys J* **79**(5): 2667-2681.

Miller, A. J. (1982). Deglutition. *Physiol Rev* **62**(1): 129-184.

Mizuta, Y., Shikuwa, S., Isomoto, H., Mishima, R., Akazawa, Y., Masuda, J., Omagari, K., Takeshima, F. and Kohno, S. (2006). Recent insights into digestive motility in functional dyspepsia. *J Gastroenterol* **41**(11): 1025-1040.

Monte, M. J., Marin, J. J., Antelo, A. and Vazquez-Tato, J. (2009). Bile acids: chemistry, physiology, and pathophysiology. *World J Gastroenterol* **15**(7): 804-816.

Moriya, M. and Miyazaki, E. (1982). The differences in contractile response to AC field stimulation between longitudinal and circular muscles of guinea pig stomach. *Jpn J Physiol* **32**(1): 1-12.

Moriya, M. and Miyazaki, E. (1985). Force-velocity characteristics of stomach muscle: a comparison between longitudinal and circular muscle strips. *Comp Biochem Physiol A Comp Physiol* **81**(3): 531-537.

Murphy, R. A. and Rembold, C. M. (2005). The latch-bridge hypothesis of smooth muscle contraction. *Can J Physiol Pharmacol* **83**(10): 857-864.

Nagayama, K., Yanagihara, S. and Matsumoto, T. (2007). A novel micro tensile tester with feed-back control for viscoelastic analysis of single isolated smooth muscle cells. *Med Eng Phys* **29**(5): 620-628.

Nagayama, K. and Matsumoto, T. (2008). Contribution of actin filaments and microtubules to quasi-in situ tensile properties and internal force balance of cultured smooth muscle cells on a substrate. *Am J Physiol Cell Physiol* **295**(6): C1569-1578.

Naghshin, J., Wang, L., Pare, P. D. and Seow, C. Y. (2003). Adaptation to chronic length change in explanted airway smooth muscle. *J Appl Physiol* **95**(1): 448-453.

Nickerson, D., Smith, N. and Hunter, P. (2005). New developments in a strongly coupled cardiac electromechanical model. *Europace* **7 Suppl 2**: 118-127.

Obara, K. and Yabu, H. (1994). Effect of cytochalasin B on intestinal smooth muscle cells. *Eur J Pharmacol* **255**(1-3): 139-147.

Ohama, T., Hori, M. and Ozaki, H. (2007). Mechanism of abnormal intestinal motility in inflammatory bowel disease: how smooth muscle contraction is reduced? *J Smooth Muscle Res* **43**(2): 43-54.

Ohtakara, K., Inada, H., Goto, H., Taki, W., Manser, E., Lim, L., Izawa, I. and Inagaki, M. (2000). p21-activated kinase PAK phosphorylates desmin at sites different from those for Rho-associated kinase. *Biochem Biophys Res Commun* **272**(3): 712-716.

Ozaki, H., Gerthoffer, W. T., Publicover, N. G., Fusetani, N. and Sanders, K. M. (1991a). Time-dependent changes in Ca2+ sensitivity during phasic contraction of canine antral smooth muscle. *J Physiol* **440**: 207-224.

Ozaki, H., Stevens, R. J., Blondfield, D. P., Publicover, N. G. and Sanders, K. M. (1991b). Simultaneous measurement of membrane potential, cytosolic Ca2+, and tension in intact smooth muscles. *Am J Physiol* **260**(5 Pt 1): C917-925.

Pabst, R. (1987). The anatomical basis for the immune function of the gut. *Anat Embryol (Berl)* **176**(2): 135-144.

Paul, R. J. (1981). Smooth Muscle Mechanochemical Energy Conversion: Relations Between Metabolism and Contractility. In: *Physiology of the gastrointestinal tract. 2nd ed*. Edited by: Johnson, L. R. New York, Raven Press. **1:** 483-506. Chapter 14.

Paul, S. M., Mytelka, D. S., Dunwiddie, C. T., Persinger, C. C., Munos, B. H., Lindborg, S. R. and Schacht, A. L. (2010). How to improve R&D productivity: the pharmaceutical industry's grand challenge. *Nat Rev Drug Discov* **9**(3): 203-214.

Paulin, D. and Li, Z. (2004). Desmin: a major intermediate filament protein essential for the structural integrity and function of muscle. *Exp Cell Res* **301**(1): 1-7.

Pedersen, J., Gao, C., Egekvist, H., Bjerring, P., Arendt-Nielsen, L., Gregersen, H. and Drewes, A. M. (2003). Pain and biomechanical responses to distention of the duodenum in patients with systemic sclerosis. *Gastroenterology* **124**(5): 1230-1239.

Pinart, M., Faffe, D. S., Sapina, M. and Romero, P. V. (2011). Dynamic nonlinearity of lung tissue: effects of strain amplitude and stress level. *J Appl Physiol* **110**(3): 653-660.

Pinto, J. G. and Fung, Y. C. (1973). Mechanical properties of the heart muscle in the passive state. *J Biomech* **6**(6): 597-616.

Pratusevich, V. R., Seow, C. Y. and Ford, L. E. (1995). Plasticity in canine airway smooth muscle. *J Gen Physiol* **105**(1): 73-94.

Price, J. M., Patitucci, P. and Fung, Y. C. (1977). Mechanical properties of taenia coli smooth muscle in spontaneous contraction. *Am J Physiol* **233**(1): C47-55.

Price, J. M., Patitucci, P. J. and Fung, Y. C. (1979). Mechanical properties of resting taenia coli smooth muscle. *Am J Physiol* **236**(5): C211-220.

Prosser, C. L. (1995). Rhythmic electrical and mechanical activity in stomach of toad and frog. *Am J Physiol* **269**(3 Pt 1): G386-395.

Qin, Z., Kreplak, L. and Buehler, M. J. (2009). Nanomechanical properties of vimentin intermediate filament dimers. *Nanotechnology* **20**(42): 425101.

Qin, Z., Buehler, M. J. and Kreplak, L. (2010). A multi-scale approach to understand the mechanobiology of intermediate filaments. *J Biomech* **43**(1): 15-22.

Qin, Z., Kalinowski, A., Dahl, K. N. and Buehler, M. J. (2011). Structure and stability of the lamin A tail domain and HGPS mutant. *J Struct Biol* **175**(3): 425-433.

Rana, S. V. and Bhardwaj, S. B. (2008). Small intestinal bacterial overgrowth. *Scand J Gastroenterol* **43**(9): 1030-1037.

Rao, S. S., Hayek, B. and Summers, R. W. (1995). Impedance planimetry: an integrated approach for assessing sensory, active, and passive biomechanical properties of the human esophagus. *Am J Gastroenterol* **90**(3): 431-438.

Rembold, C. M. and Murphy, R. A. (1988). Myoplasmic [Ca2+] determines myosin phosphorylation in agonist-stimulated swine arterial smooth muscle. *Circ Res* **63**(3): 593-603.

Rubinson, K. and Lang, E. J. (2008). The Nervous System. In: *Berne & Levy physiology. 6th ed*. Edited by: Koeppen, B. M. and Stanton, B. A. Philadelphia, PA, Mosby/Elsevier. Section II.

Sachse, F. B., Hunter, G. A., Weiss, D. L. and Seemann, G. (2007). A framework for modeling of mechano-electrical feedback mechanisms of cardiac myocytes and tissues. *Conf Proc IEEE Eng Med Biol Soc* **2007**: 160-163.

Sallam, H., McNearney, T. A. and Chen, J. D. (2006). Systematic review: pathophysiology and management of gastrointestinal dysmotility in systemic sclerosis (scleroderma). *Aliment Pharmacol Ther* **23**(6): 691-712.

Sanders, K. M., Koh, S. D. and Ward, S. M. (2006). Organization and Electrophysiology of Interstitial Cells of Cajal and Smooth Muscle Cells in the Gastrointestinal Tract. In: *Physiology of the Gastrointestinal Tract. 4th ed*. Edited by: Johnson, L. R., Academic Press. Chapter 20.

Sands, B. E. (2004). From symptom to diagnosis: clinical distinctions among various forms of intestinal inflammation. *Gastroenterology* **126**(6): 1518-1532.

Sarna, S. K. and Otterson, M. F. (1989). Small intestinal physiology and pathophysiology. *Gastroenterol Clin North Am* **18**(2): 375-404.

Sarna, S. K. (1993). Gastrointestinal longitudinal muscle contractions. *Am J Physiol* **265**(1 Pt 1): G156-164.

Sarna, S. K. (1999). Tachykinins and in vivo gut motility. *Dig Dis Sci* **44**(8 Suppl): 114S-118S.

Sarna, S. K. and Shi, X.-Z. (2006). Function and Regulation of Colonic Contractions in Health and Disease. In: *Physiology of the gastrointestinal tract. 4th ed*. Edited by: Johnson, L. R. Burlington, MA, Elsevier Academic Press**:** Chapter 39.

Schopferer, M., Bar, H., Hochstein, B., Sharma, S., Mucke, N., Herrmann, H. and Willenbacher, N. (2009). Desmin and vimentin intermediate filament networks: their viscoelastic properties investigated by mechanical rheometry. *J Mol Biol* **388**(1): 133-143.

Schreyer, A. G. and Stroszczynski, C. (2011). Radiological imaging of the small bowel. *Dig Dis* **29 Suppl 1**: 22-26.

Schwizer, W., Steingotter, A., Fox, M., Zur, T., Thumshirn, M., Bosiger, P. and Fried, M. (2002). Non-invasive measurement of gastric accommodation in humans. *Gut* **51 Suppl 1**: i59-62.

Semrin, M. G. and Russo, M. A. (2010). Anatomy, Histology, Embryology, and Developmental Anomalies of the Stomach and Duodenum. In: *Sleisenger and Fordtran's gastrointestinal and liver disease : pathophysiology, diagnosis, management. 9th ed*. Edited by: Feldman, M., Friedman, L. S. and Brandt, L. J. Philadelphia , PA, Saunders/Elsevier. Chapter 47.

Seow, C. Y. (2000). Response of arterial smooth muscle to length perturbation. *J Appl Physiol* **89**(5): 2065-2072.

Seow, C. Y., Pratusevich, V. R. and Ford, L. E. (2000). Series-to-parallel transition in the filament lattice of airway smooth muscle. *J Appl Physiol* **89**(3): 869-876.

Seow, C. Y. and Fredberg, J. J. (2010). Emergence of airway smooth muscle functions related to structural malleability. *J Appl Physiol* **110**(4): 1130-1135.

Shale, M., Kaplan, G. G., Panaccione, R. and Ghosh, S. (2009). Isotretinoin and intestinal inflammation: what gastroenterologists need to know. *Gut* **58**(6): 737-741.

Sharkey, K. A. and Kroese, A. B. (2001). Consequences of intestinal inflammation on the enteric nervous system: neuronal activation induced by inflammatory mediators. *Anat Rec* **262**(1): 79-90.

Shen, Z. L., Kahn, H., Ballarini, R. and Eppell, S. J. (2011). Viscoelastic properties of isolated collagen fibrils. *Biophys J* **100**(12): 3008-3015.

Shmygol, A. and Wray, S. (2004). Functional architecture of the SR calcium store in uterine smooth muscle. *Cell Calcium* **35**(6): 501-508.

Shue, G. H. and Brozovich, F. V. (1999). The frequency response of smooth muscle stiffness during Ca2+-activated contraction. *Biophys J* **76**(5): 2361-2369.

Silveira, P. S., Butler, J. P. and Fredberg, J. J. (2005). Length adaptation of airway smooth muscle: a stochastic model of cytoskeletal dynamics. *J Appl Physiol* **99**(6): 2087-2098.

Silveira, P. S. and Fredberg, J. J. (2005). Smooth muscle length adaptation and actin filament length: a network model of the cytoskeletal dysregulation. *Can J Physiol Pharmacol* **83**(10): 923-931.

Singer, H. A., Kamm, K. E. and Murphy, R. A. (1986). Estimates of activation in arterial smooth muscle. *Am J Physiol* **251**(3 Pt 1): C465-473.

Singer, H. A. and Murphy, R. A. (1987). Maximal rates of activation in electrically stimulated swine carotid media. *Circ Res* **60**(3): 438-445.

Small, J. V. (1977). Studies on isolated smooth muscle cells: The contractile apparatus. *J Cell Sci* **24**: 327-349.

Smith, B. A., Tolloczko, B., Martin, J. G. and Grutter, P. (2005). Probing the viscoelastic behavior of cultured airway smooth muscle cells with atomic force microscopy: stiffening induced by contractile agonist. *Biophys J* **88**(4): 2994-3007.

Smith, J. B., Zhao, J. B., Dou, Y. L. and Gregersen, H. (2005). Time-dependent viscoelastic properties along rat small intestine. *World J Gastroenterol* **11**(32): 4974-4978.

Smith, P. G., Roy, C., Fisher, S., Huang, Q. Q. and Brozovich, F. (2000). Selected contribution: mechanical strain increases force production and calcium sensitivity in cultured airway smooth muscle cells. *J Appl Physiol* **89**(5): 2092-2098.

Somlyo, A. and Himpens, B. (1989). Cell calcium and its regulation in smooth muscle. *FASEB J* **3**(11): 2266-2276.

Sonnenblick, E. H. (1964). Series Elastic and Contractile Elements in Heart Muscle: Changes in Muscle Length. *Am J Physiol* **207**: 1330-1338.

Southern, J., Pitt-Francis, J., Whiteley, J., Stokeley, D., Kobashi, H., Nobes, R., Kadooka, Y. and Gavaghan, D. (2008). Multi-scale computational modelling in biology and physiology. *Prog Biophys Mol Biol* **96**(1-3): 60-89.

Soybel, D. (2005). Anatomy and physiology of the stomach. *Surg Clin North Am* **85**(5): 875-894, v.

Speich, J. E., Quintero, K., Dosier, C., Borgsmiller, L., Koo, H. P. and Ratz, P. H. (2006). A mechanical model for adjustable passive stiffness in rabbit detrusor. *J Appl Physiol* **101**(4): 1189-1198.

Speich, J. E., Dosier, C., Borgsmiller, L., Quintero, K., Koo, H. P. and Ratz, P. H. (2007). Adjustable passive length-tension curve in rabbit detrusor smooth muscle. *J Appl Physiol* **102**(5): 1746-1755.

Speich, J. E., Almasri, A. M., Bhatia, H., Klausner, A. P. and Ratz, P. H. (2009). Adaptation of the length-active tension relationship in rabbit detrusor. *Am J Physiol Renal Physiol* **297**(4): F1119-1128.

Speich, J. E., Wilson, C. W., Almasri, A. M., Southern, J. B., Klausner, A. P. and Ratz, P. H. (2012). Carbachol-Induced Volume Adaptation in Mouse Bladder and

Length Adaptation via Rhythmic Contraction in Rabbit Detrusor. *Ann Biomed Eng* **40**(10): 2266-2276.

Stålhand, J., Klarbring, A. and Holzapfel, G. (2008). Smooth muscle contraction: Mechanochemical formulation for homogeneous finite strains. *Prog Biophys Mol Biol* **96**(1-3): 465-481.

Stålhand, J., Klarbring, A. and Holzapfel, G. A. (2011). A mechanochemical 3D continuum model for smooth muscle contraction under finite strains. *J Theor Biol* **268**(1): 120-130.

Stamenovic, D., Liang, Z., Chen, J. and Wang, N. (2002). Effect of the cytoskeletal prestress on the mechanical impedance of cultured airway smooth muscle cells. *J Appl Physiol* **92**(4): 1443-1450.

Stavropoulou, E. A., Dafalias, Y. F. and Sokolis, D. P. (2009). Biomechanical and histological characteristics of passive esophagus: experimental investigation and comparative constitutive modeling. *J Biomech* **42**(16): 2654-2663.

Stollberger, C., Keller, H. and Finsterer, J. (2007). Disappearance of left ventricular hypertrabeculation/noncompaction after biventricular pacing in a patient with polyneuropathy. *J Card Fail* **13**(3): 211-214.

Storkholm, J. H., Villadsen, G. E., Jensen, S. L. and Gregersen, H. (1998). Mechanical properties and collagen content differ between isolated guinea pig duodenum, jejunum, and distal ileum. *Dig Dis Sci* **43**(9): 2034-2041.

Storkholm, J. H., Zhao, J., Villadsen, G. E., Hager, H., Jensen, S. L. and Gregersen, H. (2007). Biomechanical remodeling of the chronically obstructed Guinea pig small intestine. *Dig Dis Sci* **52**(2): 336-346.

Storkholm, J. H., Zhao, J., Villadsen, G. E. and Gregersen, H. (2008). Spontaneous and bolus-induced motility in the chronically obstructed guinea-pig small intestine in vitro. *Dig Dis Sci* **53**(2): 413-420.

Strege, P. R., Ou, Y., Sha, L., Rich, A., Gibbons, S. J., Szurszewski, J. H., Sarr, M. G. and Farrugia, G. (2003). Sodium current in human intestinal interstitial cells of Cajal. *Am J Physiol Gastrointest Liver Physiol* **285**(6): G1111-1121.

Stull, J. T., Krueger, J. K., Kamm, K. E., Gao, Z., Zhi, G. and Padre, R. (1996). Myosin Light Chain Kinase. In: *Biochemistry of smooth muscle contraction. ed*. Edited by: Bárány, M. San Diego, Academic Press**:** xxvi, 418 p., [412] p. of plates. Chapter 9.

Sung, J. J. (2004). Westernisation of gastrointestinal diseases in Asia. *Gut* **53**(1): 152.

Suresh, S., Spatz, J., Mills, J. P., Micoulet, A., Dao, M., Lim, C. T., Beil, M. and Seufferlein, T. (2005). Connections between single-cell biomechanics and human disease states: gastrointestinal cancer and malaria. *Acta Biomater* **1**(1): 15-30.

Tack, J. (2006). Neurophysiologic Mechanisms of Gastric Reservoir Function. In: *Physiology of the Gastrointestinal Tract. 4th ed*. Edited by: Johnson, L. R., Academic Press. Chapter 37.

Tang, D. (2008). Intermediate filaments in smooth muscle. *Am J Physiol Cell Physiol* **294**(4): C869-878.

Tasaka, K. and Farrar, J. T. (1969). Mechanics of small intestinal muscle function in the dog. *Am J Physiol* **217**(4): 1224-1229.

Thuneberg, L. and Peters, S. (2001). Toward a concept of stretch-coupling in smooth muscle. I. Anatomy of intestinal segmentation and sleeve contractions. *Anat Rec* **262**(1): 110-124.

Toghanian, S., Wahlqvist, P., Johnson, D. A., Bolge, S. C. and Liljas, B. (2010). The burden of disrupting gastro-oesophageal reflux disease: a database study in US and European cohorts. *Clin Drug Investig* **30**(3): 167-178.

Tsai, M. A., Frank, R. S. and Waugh, R. E. (1993). Passive mechanical behavior of human neutrophils: power-law fluid. *Biophys J* **65**(5): 2078-2088.

Ugural, A. C. (1991). *Mechanics of materials*. New York, McGraw-Hill.

Van Loocke, M., Lyons, C. G. and Simms, C. K. (2006). A validated model of passive muscle in compression. *J Biomech* **39**(16): 2999-3009.

Van Loocke, M., Lyons, C. G. and Simms, C. K. (2008). Viscoelastic properties of passive skeletal muscle in compression: stress-relaxation behaviour and constitutive modelling. *J Biomech* **41**(7): 1555-1566.

Van Loocke, M., Simms, C. K. and Lyons, C. G. (2009). Viscoelastic properties of passive skeletal muscle in compression-cyclic behaviour. *J Biomech* **42**(8): 1038-1048.

VanBavel, E., Siersma, P. and Spaan, J. A. (2003). Elasticity of passive blood vessels: a new concept. *Am J Physiol Heart Circ Physiol* **285**(5): H1986-2000.

Vaziri, A. and Gopinath, A. (2008). Cell and biomolecular mechanics in silico. *Nat Mater* **7**(1): 15-23.

Wagenseil, J. E., Ciliberto, C. H., Knutsen, R. H., Levy, M. A., Kovacs, A. and Mecham, R. P. (2010). The importance of elastin to aortic development in mice. *Am J Physiol Heart Circ Physiol* **299**(2): H257-264.

Wang, I., Politi, A., Tania, N., Bai, Y., Sanderson, M. and Sneyd, J. (2008). A mathematical model of airway and pulmonary arteriole smooth muscle. *Biophys J* **94**(6): 2053-2064.

Wang, J. H. and Thampatty, B. P. (2006). An introductory review of cell mechanobiology. *Biomech Model Mechanobiol* **5**(1): 1-16.

Wang, L., Pare, P. D. and Seow, C. Y. (2001). Selected contribution: effect of chronic passive length change on airway smooth. *J Appl Physiol* **90**(2): 734-740.

Wang, L., Chitano, P. and Murphy, T. M. (2005). A maturational model for the study of airway smooth muscle adaptation to mechanical oscillation. *Can J Physiol Pharmacol* **83**(10): 817-824.

Warshaw, D. and Fay, F. (1983a). Cross-bridge elasticity in single smooth muscle cells. *J Gen Physiol* **82**(2): 157-199.

Warshaw, D. and Fay, F. (1983b). Tension transients in single isolated smooth muscle cells. *Science* **219**(4591): 1438-1441.

Warshaw, D. (1987). Force: velocity relationship in single isolated toad stomach smooth muscle cells. *J Gen Physiol* **89**(5): 771-789.

Warshaw, D., Rees, D. and Fay, F. (1988). Characterization of cross-bridge elasticity and kinetics of cross-bridge cycling during force development in single smooth muscle cells. *J Gen Physiol* **91**(6): 761-779.

Watras, J. (2004). Smooth Muscle Physiology. In: *Physiology. 5th ed*. Edited by: Berne, R. M., Levy, M. N., Koeppen, B. M. and Stanton, B. A. St Louis, Mosby. Chapter 13.

Watras, J. M. (2008). Muscle. In: *Berne & Levy physiology. 6th ed*. Edited by: Koeppen, B. M. and Stanton, B. A. Philadelphia, PA, Mosby/Elsevier. Section III.

Weems, W. A. (1981). The intestine as a fluid propelling system. *Annu Rev Physiol* **43**: 9-19.

Weisbrodt, N. W. (1981). Patterns of intestinal motility. *Annu Rev Physiol* **43**: 21-31.

Wess, T. J. (2008). Collagen Fibrillar Structure and Hierarchies. In: *Collagen : structure and mechanics. ed*. Edited by: Fratzl, P. New York, Springer. Chapter 3.

Woda, A., Mishellany, A. and Peyron, M. A. (2006). The regulation of masticatory function and food bolus formation. *J Oral Rehabil* **33**(11): 840-849.

Wognum, S., Schmidt, D. E. and Sacks, M. S. (2009). On the mechanical role of de novo synthesized elastin in the urinary bladder wall. *J Biomech Eng* **131**(10): 101018.

Wolinsky, H. (1972). Long-term effects of hypertension on the rat aortic wall and their relation to concurrent aging changes. Morphological and chemical studies. *Circ Res* **30**(3): 301-309.

Won, K. J., Suzuki, T., Hori, M. and Ozaki, H. (2006). Motility disorder in experimentally obstructed intestine: relationship between muscularis inflammation and disruption of the ICC network. *Neurogastroenterol Motil* **18**(1): 53-61.

Wray, S. and Burdyga, T. (2010). Sarcoplasmic reticulum function in smooth muscle. *Physiol Rev* **90**(1): 113-178.

Yamakawa, M., Harris, D., Fay, F. and Warshaw, D. (1990). Mechanical transients of single toad stomach smooth muscle cells. Effects of lowering temperature and extracellular calcium. *J Gen Physiol* **95**(4): 697-715.

Yang, J., Clark, J. W., Jr., Bryan, R. M. and Robertson, C. S. (2003a). The myogenic response in isolated rat cerebrovascular arteries: vessel model. *Med Eng Phys* **25**(8): 711-717.

Yang, J., Clark, J. W., Jr., Bryan, R. M. and Robertson, C. S. (2003b). The myogenic response in isolated rat cerebrovascular arteries: smooth muscle cell model. *Med Eng Phys* **25**(8): 691-709.

Yang, J., Zhao, J., Nakaguchi, T. and Gregersen, H. (2009). Biomechanical changes in oxazolone-induced colitis in BALB/C mice. *J Biomech* **42**(7): 811-817.

Yang, W., Fung, T. C., Chian, K. S. and Chong, C. K. (2006). Viscoelasticity of esophageal tissue and application of a QLV model. *J Biomech Eng* **128**(6): 909-916.

Yin, F. C. and Fung, Y. C. (1971). Mechanical properties of isolated mammalian ureteral segments. *Am J Physiol* **221**(5): 1484-1493.

Yu, S. N., Crago, P. E. and Chiel, H. J. (1997). A nonisometric kinetic model for smooth muscle. *Am J Physiol* **272**(3 Pt 1): C1025-1039.

Zhang, J., Herrera, A. M., Pare, P. D. and Seow, C. Y. (2010). Dense-body aggregates as plastic structures supporting tension in smooth muscle cells. *Am J Physiol Lung Cell Mol Physiol* **299**(5): L631-638.

Zhang, W. and Gunst, S. J. (2008). Interactions of airway smooth muscle cells with their tissue matrix: implications for contraction. *Proc Am Thorac Soc* **5**(1): 32-39.

Zhao, J., Sha, H., Zhou, S., Tong, X., Zhuang, F. Y. and Gregersen, H. (2002). Remodelling of zero-stress state of small intestine in streptozotocin-induced diabetic rats. Effect of gliclazide. *Dig Liver Dis* **34**(10): 707-716.

Zhao, J., Liao, D., Yang, J. and Gregersen, H. (2003). Viscoelastic behavior of small intestine in streptozotocin-induced diabetic rats. *Dig Dis Sci* **48**(12): 2271-2277.

Zhao, J., Liao, D. and Gregersen, H. (2005). Tension and stress in the rat and rabbit stomach are location- and direction-dependent. *Neurogastroenterol Motil* **17**(3): 388-398.

Zhao, J., Chen, X., Yang, J., Liao, D. and Gregersen, H. (2007). Opening angle and residual strain in a three-layered model of pig oesophagus. *J Biomech* **40**(14): 3187-3192.

Zhao, J., Liao, D., Chen, P., Kunwald, P. and Gregersen, H. (2008a). Stomach stress and strain depend on location, direction and the layered structure. *J Biomech* **41**(16): 3441-3447.

Zhao, J., Liao, D. and Gregersen, H. (2008b). Phasic and tonic stress-strain data obtained in intact intestinal segment in vitro. *Dig Dis Sci* **53**(12): 3145-3151.

Zhao, J., Liao, D., Yang, J. and Gregersen, H. (2010). Biomechanical remodelling of obstructed guinea pig jejunum. *J Biomech* **43**(7): 1322-1329.

Zhao, J., Liao, D., Yang, J. and Gregersen, H. (2011a). Stress and strain analysis of contractions during ramp distension in partially obstructed guinea pig jejunal segments. *J Biomech* **44**(11): 2077-2082.

Zhao, J., Liao, D., Yang, J. and Gregersen, H. (2011b). Phasic and tonic smooth muscle function of the partially obstructed guinea pig intestine. *J Biomed Biotechnol* **2011**: 489720.

Zhou, E. H., Quek, S. T. and Lim, C. T. (2010). Power-law rheology analysis of cells undergoing micropipette aspiration. *Biomech Model Mechanobiol* **9**(5): 563-572.

Appendix A Linear viscoelastic models

A.1 Overview

Linear viscoelastic models are generally applied to describe the viscoelastic responses of materials (Flügge, 1967; Fung, 1993). All models in this group contain some combination of two types of components, spring and dashpot, as illustrated in Figure A.1.

(a)  (b) 

Figure A.1 Basic elements of viscoelastic models. (a) Linear spring and (b) linear dashpot.

The spring represents the Hookean elastic solid. Its deformation stress, σ, is proportional to the applied strain, ε, such that

$$\sigma = E\varepsilon \tag{A.1}$$

where E is the elastic spring constant.

The dashpot symbolises a movable piston fixed to a gas container. A Newtonian viscous fluid is assumed to exist between the wall of container and the side of piston. The force per unit area or stress (σ) applied to the piston for altering its position is proportional to the velocity of piston. The velocity can be normalised by the initial length of the dashpot to obtain the strain rate ($\dot{\varepsilon}$). The constitutive relation of a linear dashpot with viscosity coefficient M is thus

$$\sigma = M\dot{\varepsilon}. \tag{A.2}$$

Note that both E and M are independent, while only σ and ε are time-dependent in the derivation of linear viscoelastic models. Different arrangements of springs and dashpots, through serial and/or parallel connections, produce a variety of linear viscoelastic models, the simplest of these are the Maxwell body and the Kelvin body.

A.2 Maxwell and Kelvin models

A.2.1 Maxwell model

The Maxwell model consists of a spring with stiffness E serially connected to a dashpot with viscosity M as shown in Figure A.2.

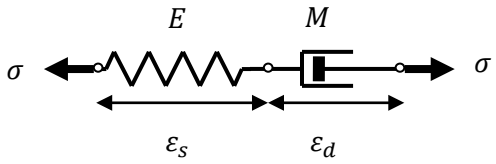

Figure A.2 Illustration of the Maxwell model. E is the elastic modulus of the linear spring while M is the coefficient of viscosity of linear dashpot. σ is the applied stress, and ε_s and ε_d are the resulting strains in the series spring and dashpot, respectively.

Due to the serial linkage, the applied stress, σ, is identical for both elements. From Equations (A.1) and (A.2),

$$\sigma = E\varepsilon_s \tag{A.3}$$

$$\sigma = M\dot{\varepsilon_d}. \tag{A.4}$$

The total strain, ε, is the sum of individual strains, ε_s and ε_d. Therefore,

$$\varepsilon = \varepsilon_s + \varepsilon_d. \tag{A.5}$$

Differentiating Equations (A.3) and (A.5) with respect to time gives

$$\dot{\sigma} = E\dot{\varepsilon}_s \tag{A.6}$$

$$\dot{\varepsilon} = \dot{\varepsilon}_s + \dot{\varepsilon}_d. \tag{A.7}$$

Inserting Equations (A.4) and (A.6) into (A.7), and then rearranging, produces the governing equation for the Maxwell body

$$\sigma + \frac{M}{E}\dot{\sigma} = M\dot{\varepsilon}. \tag{A.8}$$

Let p_i be the coefficient of i^{th} time-derivative of σ, and q_j be the coefficient of j^{th} time-derivative of ε. Equation (A.8) can be redefined as

$$\sigma + p_1\dot{\sigma} = q_1\dot{\varepsilon} \tag{A.9}$$

where $p_1 = M/E$ and $q_1 = M$. Equation (A.9) is also the governing equation of Maxwell body expressed in the general form of a linear viscoelastic model constitutive equation (Equation (3.4)) (Flügge, 1967).

A.2.2 Kelvin model

The Kelvin model comprises a spring with stiffness E which is arranged in parallel to a dashpot with viscosity M as shown in Figure A.3.

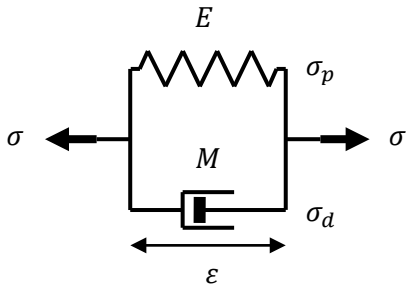

Figure A.3 Illustration of the Kelvin model. E is the elastic modulus of parallel spring while M is the coefficient of viscosity of linear dashpot. σ and ε are the applied stress and strain. σ_p and σ_d are the stresses in the parallel spring and dashpot, respectively.

The strains are equal for both elements. Their respective constitutive equations are therefore

$$\sigma_p = E\varepsilon \tag{A.10}$$

$$\sigma_d = M\dot{\varepsilon}. \tag{A.11}$$

Aggregating σ_p and σ_d gives the total stress, σ, such that

$$\sigma = \sigma_p + \sigma_d. \tag{A.12}$$

Substituting Equations (A.10) and (A.11) into Equation (A.12) and rearranging produces the governing equation for the Kelvin model

$$\sigma = E\varepsilon + M\dot{\varepsilon}. \tag{A.13}$$

Alternatively, it can be expressed in the form specified by Equation (3.4), that is

$$\sigma = q_0\varepsilon + q_1\dot{\varepsilon} \tag{A.14}$$

where $q_0 = E$ and $q_1 = M$.

A.2.3 Assessment of the Maxwell and Kelvin models

The main objective of deriving the aforementioned models is to simulate a material's viscoelastic responses, such as stress relaxation and creep. In stress relaxation, the tensile stress of the material decreases at a diminishing rate when it is kept at constant positive strain. Conversely, the strain of material increases at a decreasing rate when an isotonic tensile stress is applied and produces the creep phenomenon.

In a stress relaxation test, a step strain is applied to a Maxwell body (Figure A.2) at $t = 0$ in the manner

$$\varepsilon(t) = \varepsilon_0 H(t) \tag{A.15}$$

where $H(t)$ is the Heaviside step function and ε_0 is the magnitude of the applied strain. As a result,

$$\dot{\varepsilon}(t) = 0, t \neq 0. \tag{A.16}$$

Substituting Equation (A.16) to Equation (A.9) produces

$$\sigma + p_1 \dot{\sigma} = 0 \tag{A.17}$$

Solving Equation (A.17) analytically gives

$$\sigma(t) = A \exp\left(-\frac{t}{p_1}\right) \tag{A.18}$$

where A is an arbitrary constant.

When a sudden stress is applied to the Maxwell body, the spring element deforms immediately while the dashpot remains unaltered at that instant. Therefore, with reference to Equation (A.5) and the assumption that equal stress is applied to both elements in Figure A.2,

$$\varepsilon(0) = \varepsilon_s(0) = \varepsilon_0 \tag{A.19}$$

$$\sigma(0) = \sigma_s(0) = \sigma_0. \tag{A.20}$$

The initial condition can thus be written as

$$\sigma_0 = E\varepsilon_s(0) = E\varepsilon_0 = \frac{q_1}{p_1}\varepsilon_0 \tag{A.21}$$

Applying Equation (A.21) to Equation (A.18) with $t = 0$ determines A,

$$A = \frac{q_1}{p_1}\varepsilon_0. \tag{A.22}$$

The stress relaxation function of Maxwell model is therefore

$$\sigma(t) = \frac{q_1}{p_1}\varepsilon_0 \exp\left(-\frac{t}{p_1}\right). \tag{A.23}$$

The creep response of the Maxwell body can be determined in a similar manner. Instead of a step strain, a step stress is applied such that

$$\sigma(t) = \sigma_0 H(t) \tag{A.24}$$

$$\dot{\sigma}(t) = 0, t \neq 0. \tag{A.25}$$

Applying Equations (A.24) and (A.25) in Equation (A.9) and solving the resulting formulation gives

$$\sigma_0 = q_1\dot{\varepsilon} \tag{A.26}$$

$$\varepsilon(t) = \frac{1}{q_1}t\sigma_0 + B \tag{A.27}$$

where B is an arbitrary constant.

Similar to the previous case, the spring responds instantaneously in a sudden application of stress. Applying Equation (A.21) with $t = 0$ determines B, such that

$$B = \frac{p_1}{q_1}\sigma_0. \tag{A.28}$$

The creep function of Maxwell body is thus

$$\varepsilon(t) = \frac{1}{q_1}(t + p_1)\sigma_0. \tag{A.29}$$

As shown in Equation (A.23), the stress decreases exponentially if a stress relaxation test is performed on the Maxwell model. However, its creep response function in Equation (A.29) shows that its strain increases linearly with time in an unbounded manner. The creep simulation is therefore does not agree with experimental observations on cells and tissues (Fung, 1993; Desprat *et al.*, 2005). The indefinite strain increment resembles the property of a pure fluid. Thus, the Maxwell model is also known as a Maxwell fluid.

With reference to Figure A.3 and Equations (A.14) to (A.16), performing a stress relaxation test on the Kelvin model gives

$$\sigma(t) = q_0 \varepsilon_0. \tag{A.30}$$

Equation (A.30) is the relaxation function of the Kelvin model.

Testing the creep response of Kelvin model using Equations (A.14) and (A.24) gives

$$\sigma_0 = q_0 \varepsilon + q_1 \dot{\varepsilon}. \tag{A.31}$$

The solution of Equation (A.31) is

$$\varepsilon(t) = \frac{1}{q_0}\sigma_0 + C \exp\left(-\frac{q_0}{q_1}t\right) \tag{A.32}$$

where C is an arbitrary constant.

In the Kelvin model, the spring cannot react to the sudden stress immediately as its extension is restricted by the dashpot in parallel. Therefore, the length is initially unaltered, that is,

$$\varepsilon(0) = 0. \tag{A.33}$$

Substituting Equation (A.33) into (A.32) with $t = 0$ gives C,

$$C = -\frac{1}{q_0}\sigma_0. \tag{A.34}$$

Hence, the creep response function of Kelvin model is

$$\varepsilon(t) = \frac{1}{q_0}\sigma_0\left[1 - \exp\left(-\frac{q_0}{q_1}t\right)\right]. \tag{A.35}$$

Equation (A.35) shows that the strain of Kelvin model increases at a reducing rate when it is under constant stress. However, its time-independent stress relaxation function, shown in Equation (A.30), does not match the experimental results obtained from cell or tissue (Herlihy and Murphy, 1973; Warshaw and Fay, 1983b).

In summary, neither the Maxwell model nor the Kelvin model has the constitutive properties necessary to represent the viscoelasticity of cells or tissues.

A.3 Standard linear solid

The standard linear solid (SLS) comprises a spring connected in parallel to a Maxwell model. The resulting layout is shown in Figure A.4.

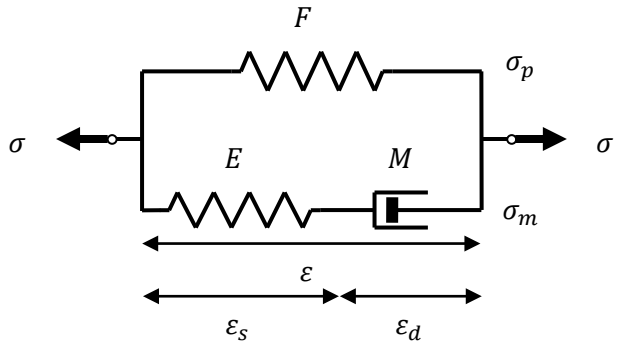

Figure A.4 Illustration of the standard linear solid (SLS) model. F and E are the elastic moduli of parallel and series springs while M is the viscosity of the linear dashpot. σ and ε are the applied stress and strain. σ_p and σ_m are the stresses in the parallel spring and the Maxwell element, respectively. ε_s and ε_d are the corresponding strains in the serial spring and the dashpot.

To derive the constitute equation of the SLS, Equations (A.1) and (A.8) are employed such that

$$\sigma_p = F\varepsilon \tag{A.36}$$

$$\sigma_m + \frac{M}{E}\dot{\sigma}_m = M\dot{\varepsilon}. \tag{A.37}$$

The total stress σ for the SLS is

$$\sigma = \sigma_p + \sigma_m \tag{A.38}$$

and its time-derivative is

$$\dot{\sigma} = \dot{\sigma}_p + \dot{\sigma}_m. \tag{A.39}$$

Substituting Equations (A.38) and (A.39) into Equation (A.37) gives

$$\sigma - \sigma_p + \frac{M}{E}\left(\dot{\sigma} - \dot{\sigma}_p\right) = M\dot{\varepsilon}. \tag{A.40}$$

Differentiating Equation (A.36) with respect to time produces

$$\dot{\sigma}_p = F\dot{\varepsilon}. \tag{A.41}$$

Inserting Equations (A.36) and (A.41) to Equation (A.40) and rearranging to give

$$\sigma + \frac{M}{E}\dot{\sigma} = F\varepsilon + M\left(1 + \frac{F}{E}\right)\dot{\varepsilon}. \tag{A.42}$$

Equation (A.42) is the constitutive equation for the SLS. An alternative form that compiles with the general form shown in Equation (3.4) is

$$\sigma + p_1\dot{\sigma} = q_0\varepsilon + q_1\dot{\varepsilon} \tag{A.43}$$

where $p_1 = M/E$, $q_0 = F$ and $q_1 = M(1 + F/E)$.

Applying a step strain on the SLS as defined by Equations (A.15) and (A.16), Equation (A.43) becomes

$$\sigma + p_1\dot{\sigma} = q_0\varepsilon_0. \tag{A.44}$$

Solving the differential equation analytically gives

$$\sigma(t) = q_0\varepsilon_0 + D\exp\left(-\frac{t}{p_1}\right) \tag{A.45}$$

where D is an arbitrary constant.

When the step strain is applied, both springs respond immediately but the dashpot does not. The springs are extended by a similar magnitude, that is, $\varepsilon(0) = \varepsilon_s(0) = \varepsilon_0$, and stress is only accumulated in the springs. Therefore, the initial condition is given by

$$\sigma_0 = F\varepsilon(0) + E\varepsilon_s(0) = (E+F)\varepsilon_0 = \frac{q_1}{p_1}\varepsilon_0. \tag{A.46}$$

Applying the initial condition to Equation (A.45) solves for D, that is,

$$D = \left(\frac{q_1}{p_1} - q_0\right)\varepsilon_0. \tag{A.47}$$

Thus, the SLS stress relaxation function is given by

$$\sigma(t) = q_0\varepsilon_0 + \left(\frac{q_1}{p_1} - q_0\right)\varepsilon_0\exp\left(-\frac{t}{p_1}\right). \tag{A.48}$$

To elucidate the SLS creep response, a step stress perturbation, as defined by Equations (A.24) and (A.25), can be applied to the SLS. Equation (A.43) becomes

$$\sigma_0 = q_0\varepsilon + q_1\dot{\varepsilon}. \tag{A.49}$$

Solving the differential equation gives

$$\varepsilon(t) = \frac{\sigma_0}{q_0} + G \exp\left(-\frac{q_0}{q_1}t\right) \tag{A.50}$$

where G is an arbitrary constant.

The initial condition is similarly defined by Equation (A.46). It is then inserted to Equation (A.50) with $t = 0$ to solve for G such that

$$G = \left(\frac{p_1}{q_1} - \frac{1}{q_0}\right)\sigma_0. \tag{A.51}$$

Overall, the SLS creep response function is given by

$$\varepsilon(t) = \frac{\sigma_0}{q_0} + \left(\frac{p_1}{q_1} - \frac{1}{q_0}\right)\sigma_0 \exp\left(-\frac{q_0}{q_1}t\right). \tag{A.52}$$

As F, E and M are all positive, so are p_1, q_0 and q_1. In Equation (A.48), note that $q_1/p_1 - q_0 = E > 0$, the stress decreases from peak stress $q_1\varepsilon_0/p_1$ at a decreasing rate to reach a steady state at $\sigma = q_0\varepsilon_0$. In Equation (A.52), the strain increases from $p_1\sigma_0/q_1$ to an upper bound at σ_0/q_0 as $p_1/q_1 - 1/q_0 = -E/[F(F+E)] < 0$. Overall, the SLS model is able to illustrate the stress relaxation and creep phenomena observed in mammalian cells and tissues (Fung, 1993; Desprat *et al.*, 2005; Nagayama *et al.*, 2007).

A.4 Alternative configuration for standard linear solid

There is another linear viscoelastic model which is also termed the SLS. The alternative layout of the SLS model is shown in Figure A.5.

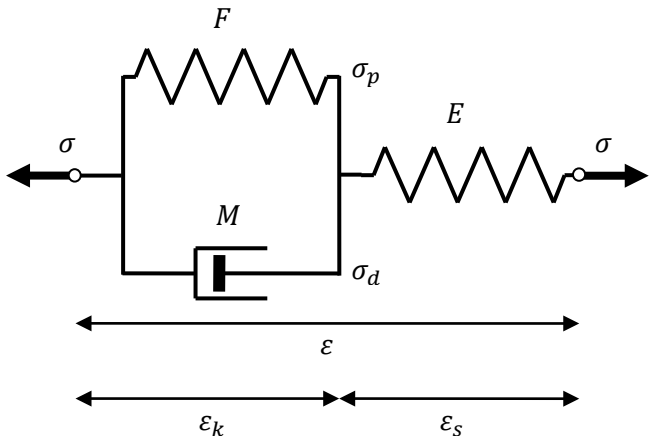

Figure A.5 Alternative configuration of the standard linear solid model. E and F are the elastic moduli of the series and parallel springs while M is the viscosity of the linear dashpot. σ and ε are the applied stress and strain. σ_p and σ_d are the stresses in the parallel spring and the linear dashpot, respectively. ε_k and ε_s are the corresponding strains in the Kelvin element and the series spring.

The arrangement shown in Figure A.5 resembles the serial connection of a linear spring to a Kelvin body. Therefore, Equations (A.1) and (A.13) can be applied to this configuration, such that

$$\sigma = E\varepsilon_s \tag{A.53}$$

$$\sigma = F\varepsilon_k + M\dot{\varepsilon}_k. \tag{A.54}$$

This configuration is also governed by the equation

$$\varepsilon = \varepsilon_k + \varepsilon_s. \tag{A.55}$$

Replacing ε_k and ε_s in Equation (A.55) with Equations (A.53) and (A.54) gives

$$\varepsilon = \frac{\sigma}{E} + \frac{\sigma - M\dot{\varepsilon}_k}{F}. \tag{A.56}$$

Differentiating Equations (A.53) and (A.55) with respect to time gives

$$\dot{\sigma} = E\dot{\varepsilon}_s \tag{A.57}$$

$$\dot{\varepsilon} = \dot{\varepsilon}_k + \dot{\varepsilon}_s. \tag{A.58}$$

Substituting Equation (A.57) into Equation (A.58) produces

$$\dot{\varepsilon}_k = \dot{\varepsilon} - \frac{\dot{\sigma}}{E}. \tag{A.59}$$

Substituting Equation (A.59) into Equation (A.56) and rearranging gives

$$\sigma + \frac{M}{E+F}\dot{\sigma} = \frac{EF}{E+F}\varepsilon + \frac{EM}{E+F}\dot{\varepsilon}. \tag{A.60}$$

Equation (A.60) is the constitutive equation of SLS model with configuration shown in Figure A.5. It can be reduced to the form shown in Equation (A.43) with $p_1 = M/(E+F)$, $q_0 = EF/(E+F)$ and $q_1 = EM/(E+F)$.

A.5 Concluding remarks

This appendix illustrates the derivations of simple linear viscoelastic models such as the Kelvin body, the Maxwell fluid and the SLS. Complex models consisting of multiple springs and dashpots can be constructed using a similar methodology (Flügge, 1967; Fung, 1993). The resulting constitutive equations contain higher order time-derivatives of stress and strain which conform to Equation (3.4).

Stress relaxation and creep are a subset of viscoelastic properties found in mammalian cells and tissues. Other viscoelastic features and the limitations of SLS models in illustrating them are discussed in Chapters 3 and 4 of this thesis.

Appendix B Alternate NVS configuration

The alternate configuration of the SLS framework consists of a serial spring connecting to a Kelvin body, which is a parallel combination of a linear spring and a linear dashpot. In view of this, an alternate NVS constitutive equation can be derived by generalising the SLS framework as illustrated in Figure B.1. The parallel elastic component (PEC), serial elastic component (SEC) and serial viscous component (SVC) are represented by subscripts p, s and v respectively. The combination of the two parallel components forms a Kelvin element, denoted here by the k subscript.

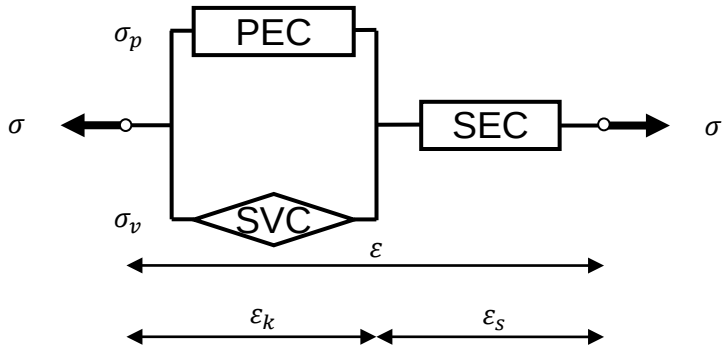

Figure B.1 Alternative configuration of the NVS model. The parallel elastic component (PEC) and the series viscous component (SVC) form a Kelvin element, which is connected serially with the series elastic component (SEC). The configuration is identical to that of the SLS model when linear springs are used in place of the PEC and SEC, and a linear dashpot replaces the SVC. σ and ε represent stress and strain while subscripts p, v, s and k indicate the quantities belonging to the PEC, the SEC, the SVC and the Kelvin element.

The general stress-strain relationships for the three components are identical to Equations (4.1)-(4.3). However, a separate set of constraints applies, replacing Equations (4.4)-(4.7) with

$$\sigma = \sigma_s = \sigma_k \tag{B.1}$$

$$\sigma_k = \sigma_p + \sigma_v \tag{B.2}$$

$$\varepsilon = \varepsilon_k + \varepsilon_s \tag{B.3}$$

$$\varepsilon_k = \varepsilon_p = \varepsilon_v. \tag{B.4}$$

Differentiating Equation (B.3) with respect to time gives

$$\dot{\varepsilon} = \dot{\varepsilon}_k + \dot{\varepsilon}_s. \tag{B.5}$$

Equation (B.5) can be rewritten using Equation (4.9) such that

$$\dot{\varepsilon} = \dot{\varepsilon}_k + \frac{\dot{\sigma}_s}{\left(\frac{df_s}{d\varepsilon_s}\right)}. \tag{B.6}$$

Applying the constraints given in Equations (B.1) & (B.4) and rearranging gives

$$\dot{\sigma} = \frac{df_s}{d\varepsilon_s}(\dot{\varepsilon} - \dot{\varepsilon}_v) \tag{B.7}$$

which is the governing equation for the NVS model shown in Figure B.1.

Appendix C NVS with piecewise constitutive relations

In Chapter 4, the tri-exponential NVS model was derived for the case when the constitutive relations of the PEC, SEC and SVC can each be described by a single mathematical function. If the mechanical properties of a NVS component are defined by two or more functions in piecewise manner, the deformation for this NVS element needs to be considered in the construction of NVS governing equation.

C.1 Derivation of NVS with piecewise constitutive relations

Assuming that the stresses in PEC, SEC and SVC (σ_p, σ_s and σ_v) are defined in piecewise fashions such that

$$\sigma_p = \begin{cases} f_-(\varepsilon_p) = f_{p-}, & \varepsilon_p < 0 \\ f_+(\varepsilon_p) = f_{p+}, & \varepsilon_p \geq 0 \end{cases} \tag{C.1}$$

$$\sigma_s = \begin{cases} f_-(\varepsilon_s) = f_{s-}, & \varepsilon_s < 0 \\ f_+(\varepsilon_s) = f_{s+}, & \varepsilon_s \geq 0 \end{cases} \tag{C.2}$$

$$\sigma_v = \begin{cases} f_-(\dot{\varepsilon}_v) = f_{v-}, & \dot{\varepsilon}_v < 0 \\ f_+(\dot{\varepsilon}_v) = f_{v+}, & \dot{\varepsilon}_v \geq 0 \end{cases}. \tag{C.3}$$

Here, the piecewise functions are assumed to be invertible and continuous over the considered range of deformation.

Differentiating Equations (C.1) and (C.2) with respect to their strains obtains

$$\frac{d\sigma_p}{d\varepsilon_p} = \frac{df_p}{d\varepsilon_p} = \begin{cases} \dfrac{df_{p-}}{d\varepsilon_p}, & \varepsilon_p < 0 \\ \dfrac{df_{p+}}{d\varepsilon_p}, & \varepsilon_p \geq 0 \end{cases} \tag{C.4}$$

$$\frac{d\sigma_s}{d\varepsilon_s} = \frac{df_s}{d\varepsilon_s} = \begin{cases} \dfrac{df_{s-}}{d\varepsilon_s}, & \varepsilon_s < 0 \\ \dfrac{df_{s+}}{d\varepsilon_s}, & \varepsilon_s \geq 0 \end{cases}. \tag{C.5}$$

Taking the inverse of Equation (C.3) determines $\dot{\varepsilon}_v$ such that

$$\dot{\varepsilon}_v = f^{-1}(\sigma_v) = \begin{cases} {f_-}^{-1}(\sigma_v) = g_{v-}(\sigma_v), & \sigma_v < 0 \\ {f_+}^{-1}(\sigma_v) = g_{v+}(\sigma_v), & \sigma_v \geq 0 \end{cases}. \tag{C.6}$$

The NVS constitutive equation shown in Equation (4.17) can be modified to facilitate the implementation of piecewise functions such that

$$\dot{\sigma} = \frac{df_{p-/+}}{d\varepsilon_p}\dot{\varepsilon} + \frac{df_{s-/+}}{d\varepsilon_s}\left[\dot{\varepsilon} - g_{v-/+}(\sigma_v)\right]. \tag{C.7}$$

Overall, a set of eight NVS equations can be derived from Equation (C.7) depending on the values (or signs) of ε_p, ε_s and σ_v at different states of deformation. For instance, the NVS equation for $\varepsilon_p \geq 0$, $\varepsilon_s < 0$ and $\sigma_v < 0$ is

$$\dot{\sigma} = \frac{df_{p+}}{d\varepsilon_p}\dot{\varepsilon} + \frac{df_{s-}}{d\varepsilon_s}\left[\dot{\varepsilon} - g_{v-}(\sigma_v)\right]. \tag{C.8}$$

C.2 NVS with symmetrical compression

As a case in point, the tri-exponential NVS model in Chapter 4 was extended to encompass compressive deformation. The passive mechanics of smooth muscle

compression was assumed to be symmetrical to that in tension. Additional expressions for negative strain are inserted to the constitutive equations of exponential PEC, SEC and SVC in Equations (4.38) to (4.40) such that

$$\sigma_p = \begin{cases} -\beta\left[\exp\left(-\alpha\varepsilon_p\right) - 1\right] = f_{p-}, & \varepsilon_p < 0 \\ \beta\left[\exp\left(\alpha\varepsilon_p\right) - 1\right] = f_{p+}, & \varepsilon_p \geq 0 \end{cases} \tag{C.9}$$

$$\sigma_s = \begin{cases} -\delta[\exp(-\gamma\varepsilon_s) - 1] = f_{s-}, & \varepsilon_s < 0 \\ \delta[\exp(\gamma\varepsilon_s) - 1] = f_{s+}, & \varepsilon_s \geq 0 \end{cases} \tag{C.10}$$

$$\sigma_v = \begin{cases} -\mu[\exp(-\lambda\dot{\varepsilon}_v) - 1] = f_{v-}, & \dot{\varepsilon}_v < 0 \\ \mu[\exp(\lambda\dot{\varepsilon}_v) - 1] = f_{v+}, & \dot{\varepsilon}_v \geq 0 \end{cases}. \tag{C.11}$$

Differentiating Equations (C.9) with respect to ε_p,

$$\frac{d\sigma_p}{d\varepsilon_p} = \frac{df_p}{d\varepsilon_p} = \begin{cases} \alpha\beta\,\exp\left(-\alpha\varepsilon_p\right) = \dfrac{df_{p-}}{d\varepsilon_p}, & \varepsilon_p < 0 \\ \alpha\beta\,\exp\left(\alpha\varepsilon_p\right) = \dfrac{df_{p+}}{d\varepsilon_p}, & \varepsilon_p \geq 0 \end{cases}. \tag{C.12}$$

Similarly, differentiating Equations (C.10) with respect to ε_s, and apply Equations (4.4), (4.5) & (4.43) to obtain

$$\frac{d\sigma_s}{d\varepsilon_s} = \frac{df_s}{d\varepsilon_s} = \begin{cases} \gamma\delta\,\exp(-\gamma\varepsilon_s) = \dfrac{df_{s-}}{d\varepsilon_s}, & \varepsilon_s < 0 \\ \gamma\delta\,\exp(\gamma\varepsilon_s) = \dfrac{df_{s+}}{d\varepsilon_s}, & \varepsilon_s \geq 0 \end{cases} \tag{C.13}$$

$$= \begin{cases} \gamma\left(\delta - \sigma + \sigma_p\right), & \varepsilon_s < 0 \\ \gamma\left(\delta + \sigma - \sigma_p\right), & \varepsilon_s \geq 0 \end{cases}. \tag{C.14}$$

Taking the inverse of Equation (C.11), and apply Equations (4.4) & (4.5) determines $\dot{\varepsilon}_v$ such that

$$\dot{\varepsilon}_v = f^{-1}(\sigma_v) = \begin{cases} -\frac{1}{\lambda}\ln\left(1-\frac{\sigma-\sigma_p}{\mu}\right) = g_{v-}(\sigma_v), & \sigma_v < 0 \\ \frac{1}{\lambda}\ln\left(1+\frac{\sigma-\sigma_p}{\mu}\right) = g_{v+}(\sigma_v), & \sigma_v \geq 0 \end{cases}. \quad \text{(C.15)}$$

With reference to Equation (4.5), both SEC and SVC experience the same magnitude of stress during deformation ($\sigma_s = \sigma_v$). This implies that the SEC and the SVC are compressed concurrently, or extended simultaneously in tri-exponential NVS (that is $\varepsilon_s < 0$ when $\sigma_v < 0$, and vice versa). As a result, it is sufficient to identify a set of four equations to define the tri-exponential model for both compressive and extensive deformations.

When all the NVS components are compressed, that is $\varepsilon_p < 0$, $\varepsilon_s < 0$ and $\sigma_v < 0$, applying Equation (C.7) gives

$$\dot{\sigma} = \alpha\beta\exp(-\alpha\varepsilon)\dot{\varepsilon} + \gamma\{\delta - \sigma - \beta[\exp(-\alpha\varepsilon) - 1]\} \times \left[\dot{\varepsilon} + \frac{1}{\lambda}\ln\left(1 - \frac{\sigma + \beta[\exp(-\alpha\varepsilon) - 1]}{\mu}\right)\right]. \quad \text{(C.16)}$$

When PEC is compressed while SEC and SVC are extended ($\varepsilon_p < 0$, $\varepsilon_s \geq 0$ and $\sigma_v \geq 0$),

$$\dot{\sigma} = \alpha\beta\exp(-\alpha\varepsilon)\dot{\varepsilon} + \gamma\{\delta + \sigma + \beta[\exp(-\alpha\varepsilon) - 1]\} \times \left[\dot{\varepsilon} - \frac{1}{\lambda}\ln\left(1 + \frac{\sigma + \beta[\exp(-\alpha\varepsilon) - 1]}{\mu}\right)\right]. \quad \text{(C.17)}$$

Conversely, when PEC is extended and the Maxwell element is compressed ($\varepsilon_p \geq 0$, $\varepsilon_s < 0$ and $\sigma_v < 0$),

$$\dot{\sigma} = \alpha\beta \exp(\alpha\varepsilon)\dot{\varepsilon} + \gamma\{\delta - \sigma + \beta[\exp(\alpha\varepsilon) - 1]\}$$
$$\times \left[\dot{\varepsilon} + \frac{1}{\lambda} \ln\left(1 - \frac{\sigma - \beta[\exp(\alpha\varepsilon) - 1]}{\mu}\right)\right]. \tag{C.18}$$

Finally, for $\varepsilon_p \geq 0$, $\varepsilon_s \geq 0$ and $\sigma_v \geq 0$, the equation is identical to Equation (4.48) such that

$$\dot{\sigma} = \alpha\beta \exp(\alpha\varepsilon)\dot{\varepsilon} + \gamma\{\delta + \sigma - \beta[\exp(\alpha\varepsilon) - 1]\}$$
$$\times \left[\dot{\varepsilon} - \frac{1}{\lambda} \ln\left(1 + \frac{\sigma - \beta[\exp(\alpha\varepsilon) - 1]}{\mu}\right)\right]. \tag{C.19}$$

For ease of computation, Equations (C.16) to (C.19) can be unified such that

$$\dot{\sigma} = \alpha\beta \exp(\alpha|\varepsilon|)\dot{\varepsilon} + \gamma\{\delta + |\sigma - \beta \operatorname{sgn}(\varepsilon)[\exp(\alpha|\varepsilon|) - 1]|\}$$
$$\times \left[\dot{\varepsilon} - \frac{\operatorname{sgn}(\sigma_v)}{\lambda} \ln\left\{1 + \frac{|\sigma - \beta \operatorname{sgn}(\varepsilon)[\exp(\alpha|\varepsilon|) - 1]|}{\mu}\right\}\right] \tag{C.20}$$

where $\operatorname{sgn}(\bullet)$ is the signum function whose definition is

$$\operatorname{sgn}(\bullet) = \begin{cases} -1 \text{ if } \bullet < 0 \\ 0 \text{ if } \bullet = 0 \\ 1 \text{ if } \bullet > 0 \end{cases}. \tag{C.21}$$

Equation (C.20) is identical to Equation (4.70).

Appendix D Modelling Ca^{2+}-dependent cross-bridge cycling

The Gajendiran and Buist (2011) GI smooth muscle active force generation model has been adopted in ANVS to describe the Ca^{2+}-dependent cross-bridge cycling.

D.1 Myosin light chain kinase activation

Intra-cellular [Ca^{2+}] regulates smooth muscle contraction by modulating the activity of myosin filaments. The process is initiated by their interaction with calmodulin (CaM). Each CaM contains four Ca^{2+} binding sites and the increment of $[Ca^{2+}]_i$ raises the possibility of CaM-Ca^{2+} binding (Mani and Kay, 1996). However, CaM is transformed to its functional conformation only if all of its Ca^{2+} binding sites are filled. The reactions are illustrated by the middle row in Figure D.1.

Myosin light chain kinase (MLCK) assumes an inactive state naturally and its catalytic functions can be resumed by interaction with CaM (Hong *et al.*, 2011). In the Gajendiran and Buist (2011) model, CaM can bind to MLCK regardless the number of calcium ions it is attached to (Figure D.1 top row). However, only the activated form, or Ca_4CaM, is able to trigger the kinase for its rapid phosphorylation on myosin light chain (Stull *et al.*, 1996) (Figure D.1 top right corner).

A buffering protein (BP) species, which competes with Ca^{2+} for CaM binding, was also added to the model. A rise in [Ca^{2+}] can displace BP from the CaM-BP complexes. The diagonal reactions at the left bottom of Figure D.1 illustrate the BP-related processes.

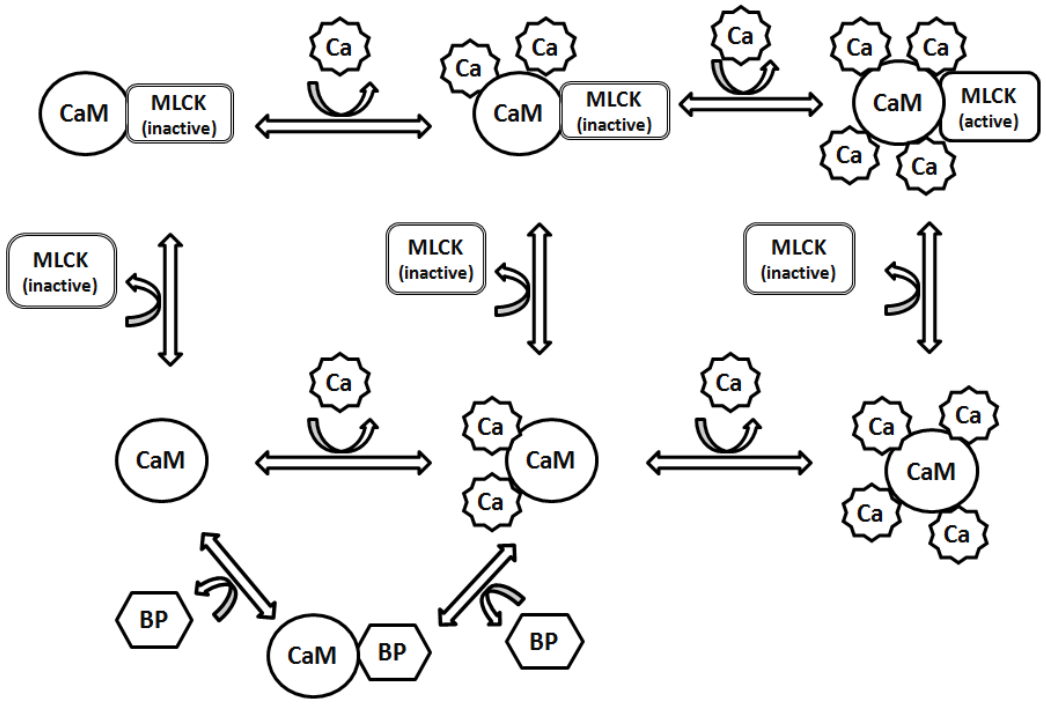

Figure D.1 Detailed illustration of GI SMC MLC_{20} phosphorylation in the Gajendiran and Buist (2011) model. The above reactions are formulated as a MLC_{20} phosphorylation module which supplements k_1 in the latch-bridge model (Figure D.2). MLCK is activated only when Ca_4CaM binds to it (top right corner). CaM: calmodulin; MLCK: myosin light chain kinase; Ca: calcium ion; BP: binding protein.

For each reaction illustrated in Figure D.1, the forward (K_f) and reverse (K_r) reaction rate constants are listed in Table D.1. The reactions are then formulated using a system of first order differential equations (Table D.2). The initial conditions of the simulation are stated in Table D.3.

Table D.1 Forward and reverse reaction constants in GI SMC MLCK activation model. K_f: forward reaction constant; K_r: reverse reaction constant.

No.	Reactions	K_f	K_r
1	CaM + $2Ca^{2+}$ ↔ $(Ca^{2+})_2$CaM	12 $\mu M^{-2}s^{-1}$	12 s^{-1}
2	$(Ca^{2+})_2$CaM + $2Ca^{2+}$ ↔ $(Ca^{2+})_4$CaM	480 $\mu M^{-2}s^{-1}$	1200 s^{-1}
3	CaM + MLCK ↔ CaM–MLCK	5 $\mu M^{-1}s^{-1}$	135 s^{-1}

No.	Reactions	K_f	K_r
4	$(Ca^{2+})_2CaM$+ MLCK ↔ $(Ca^{2+})_2CaM$–MLCK	840 $\mu M^{-1}s^{-1}$	45.4 s^{-1}
5	$(Ca^{2+})_4CaM$ + MLCK ↔ $(Ca^{2+})_4CaM$–-MLCK	28 $\mu M^{-1}s^{-1}$	0.0308 s^{-1}
6	CaM-MLCK + $2Ca^{2+}$ ↔ $(Ca^{2+})_2CaM$–MLCK	120 $\mu M^{-2}s^{-1}$	4 s^{-1}
7	$(Ca^{2+})_2CaM$-MLCK + $2Ca^{2+}$ ↔ $(Ca^{2+})_4CaM$–MLCK	7.5 $\mu M^{-2}s^{-1}$	3.75 s^{-1}
8	CaM + BP ↔ CaM-BP	5 $\mu M^{-1}s^{-1}$	25 s^{-1}
9	CaM-BP + $2Ca^{2+}$ ↔ $(Ca^{2+})_2CaM$ + BP	7.6 $\mu M^{-2}s^{-1}$	22.8 s^{-1}

Table D.2 Chemical kinetic equations in GI SMC MLCK activation model.

Reactions	Equations	
1	$\frac{\mathrm{d}[\mathrm{Ca_2CaM}]}{\mathrm{dt}} = K_{f1}[\mathrm{CaM}][\mathrm{Ca}]^2 - K_{r1}[\mathrm{Ca_2CaM}] = -\frac{\mathrm{d}[\mathrm{CaM}]}{\mathrm{dt}} = -\frac{\mathrm{d}[\mathrm{Ca}]}{\mathrm{dt}}$	(D.1)
2	$\frac{\mathrm{d}[\mathrm{Ca_4CaM}]}{\mathrm{dt}} = K_{f2}[\mathrm{Ca_2CaM}][\mathrm{Ca}]^2 - K_{r2}[\mathrm{Ca_4CaM}] = -\frac{\mathrm{d}[\mathrm{Ca_2CaM}]}{\mathrm{dt}} = -\frac{\mathrm{d}[\mathrm{Ca}]}{\mathrm{dt}}$	(D.2)
3	$\frac{\mathrm{d}[\mathrm{CaM\_MLCK}]}{\mathrm{dt}} = K_{f3}[\mathrm{CaM}][\mathrm{MLCK}] - K_{r3}[\mathrm{CaM\_MLCK}] = -\frac{\mathrm{d}[\mathrm{CaM}]}{\mathrm{dt}} = -\frac{\mathrm{d}[\mathrm{MLCK}]}{\mathrm{dt}}$	(D.3)

Reactions	Equations	
4	$\frac{\mathrm{d}[\mathrm{Ca_2CaM\_MLCK}]}{\mathrm{dt}} = K_{f4}[\mathrm{Ca_2CaM}][\mathrm{MLCK}] - K_{r4}[\mathrm{Ca_2CaM\_MLCK}] = -\frac{\mathrm{d}[\mathrm{Ca_2CaM}]}{\mathrm{dt}} = -\frac{\mathrm{d}[\mathrm{MLCK}]}{\mathrm{dt}}$	(D.4)
5	$\frac{\mathrm{d}[\mathrm{Ca_4CaM\_\_MLCK}]}{\mathrm{dt}} = K_{f5}[\mathrm{Ca_4CaM}][\mathrm{MLCK}] - K_{r5}[\mathrm{Ca_4CaM\_\_MLCK}] = -\frac{\mathrm{d}[\mathrm{Ca_4CaM}]}{\mathrm{dt}} = -\frac{\mathrm{d}[\mathrm{MLCK}]}{\mathrm{dt}}$	(D.5)
6	$\frac{\mathrm{d}[\mathrm{Ca_2CaM\_MLCK}]}{\mathrm{dt}} = K_{f6}[\mathrm{CaM\_MLCK}][\mathrm{Ca}]^2 - K_{r6}[\mathrm{Ca_2CaM\_MLCK}] = -\frac{\mathrm{d}[\mathrm{CaM\_MLCK}]}{\mathrm{dt}} = -\frac{\mathrm{d}[\mathrm{Ca}]}{\mathrm{dt}}$	(D.6)
7	$\frac{\mathrm{d}[\mathrm{Ca_4CaM\_MLCK}]}{\mathrm{dt}} = K_{f7}[\mathrm{Ca_2CaM\_MLCK}][\mathrm{Ca}]^2 - K_{r7}[\mathrm{Ca_4CaM\_MLCK}] = -\frac{\mathrm{d}[\mathrm{Ca_2CaM\_MLCK}]}{\mathrm{dt}} = -\frac{\mathrm{d}[\mathrm{Ca}]}{\mathrm{dt}}$	(D.7)
8	$\frac{\mathrm{d}[\mathrm{CaM\_BP}]}{\mathrm{dt}} = K_{f8}[\mathrm{CaM}][\mathrm{BP}] - K_{r8}[\mathrm{CaM\_BP}] = -\frac{\mathrm{d}[\mathrm{CaM}]}{\mathrm{dt}} = -\frac{\mathrm{d}[\mathrm{BP}]}{\mathrm{dt}}$	(D.8)
9	$\frac{\mathrm{d}[\mathrm{Ca_2CaM}]}{\mathrm{dt}} = \frac{\mathrm{d}[\mathrm{BP}]}{\mathrm{dt}} = K_{f9}[\mathrm{CaM\_BP}][\mathrm{Ca}]^2 - K_{r9}[\mathrm{Ca_2CaM}][\mathrm{BP}] = -\frac{\mathrm{d}[\mathrm{CaM\_BP}]}{\mathrm{dt}} = -\frac{\mathrm{d}[\mathrm{Ca}]}{\mathrm{dt}}$	(D.9)

Table D.3 Initial concentrations of ions and proteins in GI SMC MLCK activation model.

Variables	Descriptions	Initial concentrations (μM)
$[\mathbf{CaM}]$	Concentration of CaM	0.9285
$[\mathbf{Ca_2CaM}]$	Concentration of $(Ca^{2+})_2$CaM	0.0015
$[\mathbf{Ca_4CaM}]$	Concentration of $(Ca^{2+})_4$CaM	0.0000
$[\mathbf{CaM\_MLCK}]$	Concentration of CaM–MLCK (inactive MLCK)	0.3332
$[\mathbf{Ca_2CaM\_MLCK}]$	Concentration of $(Ca^{2+})_2$CaM –MLCK (inactive MLCK)	0.2713
$[\mathbf{Ca_4CaM\_MLCK}]$	Concentration of $(Ca^{2+})_4$CaM –MLCK (active MLCK)	0.0130
$[\mathbf{BP}]$	Concentration of BP	2.8207
$[\mathbf{Ca}]$	Concentration of Ca^{2+}	15.1793

D.2 Myosin light chain phosphatase and cross-bridge cycle

Myosin light chain phosphatase (MLCP) catalyses the removal of phosphate ions from phosphorylated myosin and cross-bridges. In the Gajendiran and Buist (2011) model, the intra-cellular MLCP concentration is assumed to be unchanged in the absence of an agonist. The quantity of activated MLCK ($MLCK_{active}$) and MLCP is then used to evaluate the amount of unattached myosin (M), phosphorylated myosin (M_p), cross-bridges (AM_p) and dephosphorylated latch-bridges (AM) according to the extended Hai and Murphy model shown in Figure D.2.

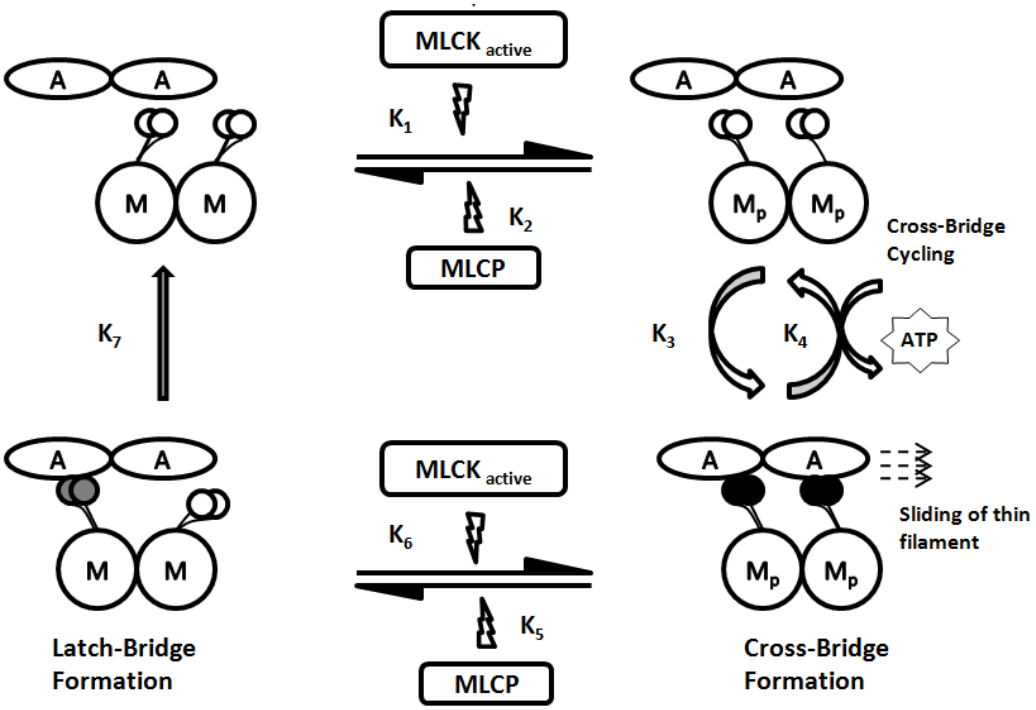

Figure D.2 Modification of Hai and Murphy (1988b) smooth muscle latch-bridge model as shown by Gajendiran and Buist (2011). The phosphorylation and dephosphorylation of myosin are driven by the enzymatic reactions of active myosin light chain kinase ($MLCK_{active}$) and myosin light chain phosphate (MLCP). A: actin; M: dephosphorylated myosin; M_p: phosphorylated myosin.

The rate constant K_3 illustrates the rate of cross-bridge formation while K_4 and K_7 determines the speed of cross-bridge and latch-bridge dissociations, respectively. The $MLCK_{active}$- and MLCP-driven reactions replace the phosphorylation (K_1 and K_6) and dephosphorylation (K_2 and K_5) rate constants from the Hai and Murphy (1988b) model. Both the phosphorylation and dephosphorylation of myosin light chain are modelled to follow Henri-Michaelis-Menten enzyme kinetics. As such, the reaction rate is influenced by the maximum reaction rate per unit concentration of enzyme (k_{cat}) and the substrate concentration at which a half-maximal reaction rate is achieved (K_m).

The concentrations of M, M_p, AM and AM_p are evaluated by the following system of differentiate equations:

$$\frac{d[M]}{dt} = -\frac{k_{cat\_MLCK_{active}}[MLCK_{active}][M]}{K_{m\_MLCK_{active}} + [M]} + \frac{k_{cat\_MLCP}[MLCP][M_p]}{K_{m\_MLCP} + [M_p]} + K_7[AM] \quad \text{(D.10)}$$

$$\frac{d[M_p]}{dt} = \frac{k_{cat\_MLCK_{active}}[MLCK_{active}][M]}{K_{m\_MLCK_{active}} + [M]} - \frac{k_{cat\_MLCP}[MLCP][M_p]}{K_{m\_MLCP} + [M_p]} - K_3[M_p] + K_4[AM_p] \quad \text{(D.11)}$$

$$\frac{d[AM_p]}{dt} = K_3[M_p] - K_4[AM_p] + \frac{k_{cat\_MLCK_{active}}[MLCK_{active}][AM]}{K_{m\_MLCK_{active}} + [AM]} - \frac{k_{cat\_MLCP}[MLCP][AM_p]}{K_{m\_MLCP} + [AM_p]} \quad \text{(D.12)}$$

$$\frac{d[AM]}{dt} = -\frac{k_{cat\_MLCK_{active}}[MLCK_{active}][AM]}{K_{m\_MLCK_{active}} + [AM]} + \frac{k_{cat\_MLCP}[MLCP][AM_p]}{K_{m\_MLCP} + [AM_p]} - K_7[AM]. \quad \text{(D.13)}$$

The quantity of cross-bridges and latch-bridges determined by Equations (D.12) and (D.13) are adapted for the calculation of contractile stress, active stiffness, friction coefficients and their time-derivatives in ANVS. The parameters for Equations (D.10) to (D.13) are shown in Table D.4. The initial concentrations of the ions and proteins listed in Tables D.5 were used in simulations illustrated in this thesis.

Table D.4 Parameters of active force generation model for calculating the quantities of unattached and attached myosin.

Symbols	Descriptions	Values
$\mathbf{k_{cat\_MLCK_{active}}}$	Maximum reaction rate per unit concentration of active MLCK	27 s^{-1}

Symbols	Descriptions	Values
$\mathbf{K_{m\_MLCK_{active}}}$	Substrate concentration of active MLCK at which a half-maximal reaction rate is achieved	10 μM
$\mathbf{k_{cat\_MLCP}}$	Maximum reaction rate per unit concentration of active MLCP	16 s^{-1}
$\mathbf{K_{m\_MLCP}}$	Substrate concentration of MLCP at which a half-maximal reaction rate is achieved	15 μM
$\mathbf{K_3}$	Rate of cross-bridge formation	15 s^{-1}
$\mathbf{K_4}$	Rate of cross-bridge dissociation	5 s^{-1}
$\mathbf{K_7}$	Rate of latch-bridge dissociation	10 s^{-1}
$[\mathbf{MLCP}]$	Concentration of MLCP	7.5 μM

Table D.5 Initial concentrations of attached and unattached myosin in GI SMC cross-bridge cycling.

Variables	Descriptions	Initial concentrations
$[\mathbf{M}]$	Concentration of unattached and unphosphorylated myosin	23.9558 μM
$[\mathbf{M_p}]$	Concentration of dissociated cross-bridges	0.0144 μM
$[\mathbf{AM_p}]$	Concentration of attached cross-bridges	0.0166 μM
$[\mathbf{AM}]$	Concentration of attached latch-bridges	0.0132 μM

Appendix E Parameters and initial conditions in smooth muscle mechanics models

E.1 Intra-cellular calcium transient in GI smooth muscle

Table E.1 Parameters of intra-cellular calcium concentration transient ($[Ca^{2+}]_i$) formulation, which is used to illustrate the canine antral circumferential smooth muscle phasic contractions examined by Ozaki *et al.* (1991a). The formulation is constructed by Gajendiran and Buist (2011). Refer to Equations (5.44) and (5.45) for details.

Variables	Descriptions	Values
t_{start}	Starting time of $[Ca^{2+}]_i$ transient	0.0 s
t_{peak}	Time at which peak $[Ca^{2+}]_i$ occurs	3.0 s
t_{end}	Ending time of $[Ca^{2+}]_i$ transient	20.0 s
$[Ca^{2+}]_{rest}$	Non-stimulated or resting $[Ca^{2+}]_i$	0.15 μM
$[Ca^{2+}]_{peak}$	Peak $[Ca^{2+}]_i$	0.72 μM
k_{decay}	Exponential decay rate that $[Ca^{2+}]_i$ recovers from $[Ca^{2+}]_{peak}$ to $[Ca^{2+}]_{rest}$	0.5 s^{-1}

Table E.2 Parameters of intra-cellular calcium concentration transient ($[Ca^{2+}]_i$) formulation, which is used to illustrate the guinea pig corpus circumferential smooth muscle phasic contractions examined by Moriya and Miyasaki (1982). Refer to Equation (5.46) for details.

Variables	Descriptions	Values
t_{start}	Starting time of $[Ca^{2+}]_i$ transient	0.0 s
t_{peak}	Time at which peak $[Ca^{2+}]_i$ occurs	5.0 s
t_{end}	Ending time of $[Ca^{2+}]_i$ transient	10.0 s
$[\mathbf{Ca^{2+}}]_{rest}$	Non-stimulated or resting $[Ca^{2+}]_i$	0.15 μM
$[\mathbf{Ca^{2+}}]_{peak}$	Peak $[Ca^{2+}]_i$	1.5 μM

Table E.3 Parameters of intra-cellular calcium concentration transient ($[Ca^{2+}]_i$) formulation, which is used to illustrate the canine proximal colonic circumferential smooth muscle tonic contractions examined by Gerthoffer *et al.* (1991). Refer to Equation (5.47) for details.

Variables	Descriptions	Values
t_{start}	Starting time of $[Ca^{2+}]_i$ transient	0.0 s
$[\mathbf{Ca^{2+}}]_{rest}$	Non-stimulated or resting $[Ca^{2+}]_i$	0.15 μM
$[\mathbf{Ca^{2+}}]_{peak}$	Peak $[Ca^{2+}]_i$	0.777 μM
k_{rise}	Exponential increment rate that $[Ca^{2+}]_i$ rises from $[Ca^{2+}]_{peak}$ to $[Ca^{2+}]_{rest}$	0.07 s^{-1}

Table E.4 Parameters of intra-cellular calcium concentration transient ($[Ca^{2+}]_i$) formulation, which is used to illustrate the rabbit tracheal smooth muscle contractions and length adaptation examined by Wang *et al.* (2001). Refer to Equations (6.15) and (6.16) for details.

Variables	Descriptions	Values
t_{start}	Starting time of $[Ca^{2+}]_i$ transient cycle	0.0 s
t_{delay}	Starting time of $[Ca^{2+}]_i$ transient after t_{start}	90.0 s
t_{peak}	Time at which peak $[Ca^{2+}]_i$ occurs	150.0 s
t_{end}	Ending time of $[Ca^{2+}]_i$ transient cycle	300.0 s
$[\mathbf{Ca^{2+}}]_{rest}$	Non-stimulated or resting $[Ca^{2+}]_i$	0.15 μM
$[\mathbf{Ca^{2+}}]_{peak}$	Peak $[Ca^{2+}]_i$	0.72 μM
k_{rise}	Exponential increment rate that $[Ca^{2+}]_i$ rises from $[Ca^{2+}]_{peak}$ to $[Ca^{2+}]_{rest}$	0.07 s^{-1}

E.2 GI smooth muscle passive mechanics

Table E.5 Parameters of PEC, SEC and SVC in ANVS model which describe the passive mechanical properties of GI smooth muscle. All values were obtained by fitting the porcine fundus tissue cyclic stretching data from Zhao *et al.* (2008a).

Symbols	Descriptions	Values
α	Coefficient of PEC strain	5.59
β	Coefficient of exponential PEC	0.222 kPa
γ	Coefficient of SEC strain	17.3
δ	Coefficient of exponential SEC	0.367 kPa
λ	Coefficient of SVC strain rate	234 s
μ	Coefficient of exponential SVC	0.443 kPa

E.3 GI smooth muscle active mechanics

Table E.6 Parameters of CCC, BCC and FCC in ANVS model which describe the active mechanical properties of mammalian stomach circumferential smooth muscle in phasic contraction.

Symbols	Descriptions	Values	References
F_{cc}	Maximum active stress generated by all the cross-bridges in smooth muscle	45.0 kPa	Gajendiran and Buist (2011)
γ_{bc}	Coefficient of cross-bridge and latch-bridge strain in smooth muscle	126	Moriya and Miyasaki (1982, 1985)
δ_{bc}	Maximum active stiffness generated by all the cross-bridges and the latch-bridges in smooth muscle	40.6 kPa	Moriya and Miyasaki (1982, 1985)
M_{fc}	Maximum frictional stress generated by all the cross-bridges and the latch-bridges in smooth muscle	4.90×10^3 kPa s	Moriya and Miyasaki (1982, 1985)

Table E.7 Parameters of CCC, BCC and FCC in ANVS model which describe the active mechanical properties of mammalian colonic circumferential smooth muscle in tonic contraction.

Symbols	Descriptions	Values	References
F_{cc}	Maximum active stress generated by all the cross-bridges in smooth muscle	1.24×10^3 kPa	Gerthoffer *et al.* (1991)
γ_{bc}	Coefficient of cross-bridge and latch-bridge strains in smooth muscle	765	Gerthoffer *et al.* (1991)
δ_{bc}	Maximum active stiffness generated by all the cross-bridges and the latch-bridges in smooth muscle	1.43×10^3 kPa	Gerthoffer *et al.* (1991)
M_{fc}	Maximum frictional stress generated by all the cross-bridges and the latch-bridges in smooth muscle	5.03×10^5 kPa s	Gerthoffer *et al.* (1991)

Table E.8 Parameters of strain-dependent activation mechanism in ANVS model which are used to evaluate the number of available cross-bridges and latch-bridges. The values were obtained from Gestrelius and Borgström (1986) in which the authors modelled the data from mammalian portal vein smooth muscle.

Symbols	Descriptions	Values
a_n	Coefficient of difference between tissue strain (ε) and optimum strain ($\varepsilon_{\mathrm{opt}}$)	1.4
b_n	Exponent of difference between ε and $\varepsilon_{\mathrm{opt}}$	1.8

Table E.9 Initial values of ANVS model.

Variables	Descriptions	Initial values
σ	Applied stress on smooth muscle	0.0 kPa
σ_{mc}	Stress in the Maxwell cross-bridge element	0.0 kPa
ε	Applied strain on smooth muscle	0.0
$\varepsilon_{\mathrm{opt}}$	Optimum strain	0.0

E.4 Smooth muscle length adaptation

Table E.10 Parameters of length-adaptive mechanism in LANVS model which are used to evaluate the active and passive stress reference strains under electrical field stimulation (60 Hz AC). All values were obtained by fitting the rabbit tracheal tissue strip data from Wang *et al.* (2001).

Symbols	Descriptions	Values
τ_a	Active stress reference strain time constant	768 s
τ_p	Passive stress reference strain time constant	6030 s

Table E.11 Initial active and passive stress reference strains in LANVS model.

Variables	Descriptions	Initial values
$\varepsilon_{\mathrm{ref,a}}$	Active stress reference strain	0.0
$\varepsilon_{\mathrm{ref,p}}$	Passive stress reference strain	0.0